Dissertation

submitted to the

Combined Faculties of the Natural Sciences and Mathematics

of the Ruperto-Carola-University of Heidelberg, Germany

for the degree of

Doctor of Natural Sciences

Put forward by

Peter Lysakovski

Born in Göppingen, Germany

Oral examination: 03.06.2024

MonteRay: A Fast Monte Carlo Dose Engine for Protons, Helium Ions and Carbon Ions

Referees

Prof. Dr. Dr. Jürgen Debus

Prof. Dr. Oliver Jäkel

Abstract

Radiation therapy is one of the cornerstones of modern cancer treatment, and at the Heidelberg Ion Beam Therapy Centre, tumors are treated with protons, helium ions and carbon ions. For this, the precise delivery of thousands of individual beamlets is necessary. Planning such complex treatments is unthinkable without dose calculation algorithms, and in terms of accuracy, Monte Carlo (MC) algorithms like FLUKA are seen as the gold standard. However, due to their long runtimes, they are limited to nonurgent applications.

To meet the demand of clinicians and researchers for fast dose estimation, the focus in recent years has been on the development of fast MC algorithms that combine speed and accuracy. While many fast proton MC codes exist, there is a lack of fast MC algorithms capable of supporting the full range of ions used at HIT. The aim of this thesis, which is a cumulative work consisting of three publications, is to provide an overview of the development and validation of MonteRay, a fast and precise MC dose calculation engine for protons, helium ions, and carbon ions.

In the accompanying publications, MonteRay is compared against a wide range of measurements and other dose engines, achieving excellent results in terms of accuracy while being significantly faster than FLUKA, with speedups between approximately 15 and 70, depending on the energy and ion type.

Zusammenfassung

Die Strahlentherapie ist einer der Eckpfeiler der modernen Krebsbehandlung, und am Heidelberger Ionentherapiezentrum werden Tumore mit Protonen, Heliumionen und Kohlenstoffionen behandelt. Hierfür ist die präzise Bestrahlung mit Tausenden einzelner "beamlets" erforderlich. Die Planung solch komplexer Behandlungen ist ohne Dosisberechnungsalgorithmen undenkbar, und was die Genauigkeit angeht, gelten Monte Carlo (MC) Algorithmen wie FLUKA als Goldstandard. Aufgrund ihrer langen Laufzeiten ist ihre Verwendung jedoch auf nicht dringliche Anwendungen beschränkt.

Um dem klinischen und akademischen Bedarf nach schneller Dosisberechnung gerecht zu werden, lag der Schwerpunkt in den letzten Jahren auf der Entwicklung sogenannter schneller MC Algorithmen, die Geschwindigkeit und Genauigkeit vereinen. Obwohl es viele schnelle Protonen MC Codes gibt, existieren keine schnellen MC Algorithmen, die die gesamte Palette der Ionen unterstützen, die am HIT klinisch verwendet werden. Das Ziel dieser Arbeit, die aus drei Publikationen besteht, ist es, einen Überblick über die Entwicklung und Validierung von MonteRay zu geben, einem schnellen und präzisen MC Dosisberechnungsalgorithmus für Protonen, Heliumionen und Kohlenstoffionen.

In den begleitenden Veröffentlichungen wird MonteRay mit einer Vielzahl von Messungen und anderen Dosisalgorithmen verglichen und erzielt hervorragende Ergebnisse in Bezug auf Genauigkeit. Gleichzeitig ist MonteRay ungefähr 15 bis 70 mal schneller als FLUKA, je nach Energie und Ionenart.

Contents

List of Acronyms

HIT	Heidelberg Ion Beam Therapy Center 1, 2, 3, 5, 6, 7, 14, 26, 31, 34, 99, 101, 102, 103, 108, 111
TPS	Treatment Planning System 1, 2
LET	Linear Energy Transfer 2
MC	Monte Carlo 2, 3, 8, 9, 10, 12, 14, 15, 16, 18, 23, 24, 27, 30, 35, 99, 100, 101, 104, 105, 106, 107, 108, 110, 111, 112
QA	Quality Assurance 3, 99, 108
BP	Bragg Peak 5, 6, 12, 14, 16, 26, 34, 99, 101
SOBP	Spread Out Bragg Peak 8, 36, 45, 61, 79, 99, 101, 102, 103, 108
mMKM	modified Microdosimetric Kinetic Model 8, 102
MCS	Multiple Coulomb Scattering 12, 13, 18, 19, 23, 101, 102
SPR	Stopping Power Ratio 14, 32, 33, 35
CT	Computed Tomography 15, 18, 32, 33, 99, 100
COM	center-of-mass 28, 29
RQMD	Relativistic Quantum Molecular Dynamics Model 31
BME	Boltzmann Master Equation 31
HU	Hounsfield Unit 32, 33, 35
FWHM	Full Width at Half Maximum 101
GPU	Graphics Processing Unit 106

Chapter 1

Motivation & Outline

1.1 Motivation

In 1946, around 30 years after Rutherford's discovery of protons [1], Wilson, in his paper titled "Radiological Use of Fast Protons" [2], highlighted that the localized dose deposition of protons would be a favorable property for the treatment of tumors, and in 1954, the first attempts to treat patients with protons were made. To this day, proton beam therapy remains an important modality for the treatment of cancer, with almost one hundred proton therapy facilities worldwide and almost 200 000 treated patients [3]. Particle therapy is not limited to protons, and at some facilities, the Heidelberg Ion Beam Therapy Center (HIT) for example, certain cancers are treated with carbon ions due their favorable properties over protons, namely higher biological effectiveness and dose conformality [4]. Additionally, HIT recently treated the first patient with helium ions [5], and comprehensive clinical trials are underway to investigate whether helium ions, with properties somewhere between protons and carbon ions, could be a viable treatment modality for certain indications.

Ideally, radiotherapy treatment would destroy cancerous cells without damaging the surrounding healthy tissue. In reality, patients may experience severe and life-altering side effects [6]. The goal of the radiotherapy treatment planning process is to minimize these side effects, while still delivering adequate dose to the tumor. Among other things, this process involves the right choice of particle type, irradiation directions and particle energies [7]. To aid physicians in their choice of these, a computer program called a Treatment Planning System (TPS) is employed. In the case of raster scanned particle therapy, thousands of individual scan spots must be positioned to adequately cover the tumor; an optimization

problem that is intractable without the help of a TPS.

To understand the effect of radiation on various tissue types, researchers have established the probability of tumor control and the probabilities of normal tissue complications through in-vivo and in-vitro experiments. These probabilities are not trivially related to the energy deposited, but are influenced by complex biological mechanisms which depend on the particle type, the fractionation scheme and the time for dose application [8]. These biological effects of radiation must be taken into account when planning a treatment, especially when using heavier particles like helium or carbon ions [9, 10, 11].

In order to judge both the physical and biological effect of radiation, the interaction of radiation with matter must be modeled in detail. In a TPS, this task is handled by so-called dose calculation algorithms. The primary aim of these codes is to predict energy deposition but also other quantities like the Linear Energy Transfer (LET), used in biological modelling. Today, broadly three classes of dose calculation algorithms exist: Monte Carlo (MC), analytical, and AI based algorithms. While AI based dose calculation algorithms are promising in terms of computation time [12], they have so far not seen use in clinical practice.

To compute the deposited dose, MC algorithms simulate the trajectories and energy depositions of millions of particles in the patient's body, eventually converging to a statistical estimate of the dose. They are generally accepted to be the most accurate, while also offering a wide range of other benefits such as broad applicability, adaptability and the ability to estimate a wide range of quantities of interest besides dose, much easier than analytical algorithms could [13]. Further, there is evidence that analytical algorithms perform poorly in certain conditions [14, 15, 16, 17]. Yet, analytical algorithm remain a strong presence in clinical routine. For example, at HIT, treatment planning with helium and carbon ions is based on an analytical dose calculation algorithm by RaySearch Laboratories. This is not due to a lack of availability of MC algorithms for these particles. Classical particle transport codes like FLUKA [18, 19], Geant4 [20] or PHITS [21] have existed for many years and have been used for radiotherapy purposes [9, 19, 22]. What makes the use of these codes problematic in regular clinical practice are their long runtimes. Using Geant4 for example, Grevillot et al. [23] report computation times between 18 and 33 hours for carbon ion plans using 48 physical CPU cores[1].

To make clinical use of MC engines viable, many so-called fast MC engines for

[1] In 2024, 48 cores is a realistic hardware requirement. For example, IBA lists an 48 core CPU under their recommended hardware requirements for their myQA iON software [24].

proton dose calculation have been developed in recent years [25, 26, 27, 28, 29, 30, 31, 32, 33]. They are typically based on the same principles as traditional MC engines, but they achieve speedups via approximations of physical interactions, specialization to radiotherapy purposes or hardware acceleration. For protons, fast MC based algorithms are already commercialy available and in clinical use [34]. For helium and carbon ions, the range of available MC codes is much more limited, in part due to the complexity of the nuclear interactions involved [11]. No fast MC algorithms for helium ions exists and only two algorithms for carbon ions have been presented [35, 36]. So far, no clinically used commercial solution exists.

Fast MC engines for these modalities may prove beneficial both in a clinical and research context. The former may benefit from more accurate dose calculation results and, to name one example relevant to the HIT facility, daily Quality Assurance (QA) measurements of patient plans could in the future be replaced by fast MC simulations, thus freeing up both beam and personnel time. In a research context, fast MC engines could be used to accelerate research workflows, which are currently hampered by long computation times. For example, at HIT, a dedicated cluster with hundreds of CPUs is used, primarily for running FLUKA simulations. However, even with this high core count, researchers frequently contend for cluster resources.

1.2 Outline

Motivated by this, the development of the fast MC dose engine MonteRay started in 2020. In this thesis, put forward as a cumulative thesis consisting of three publications [37, 38, 39], the process of developing this MC engine will be described, and the speed and accuracy of it demonstrated.

In chapter 2, an overview of the fundamentals of particle therapy from the perspective of MC simulations will be given. Following this, the three publications will be presented, each detailing different aspects of the development and validation of MonteRay. All three publications will be tied together in chapter 4, where the results of the publications will be discussed and put into context.

Finally, the development and use of MonteRay has already expanded beyond the scope of the publications included in this cumulative thesis. This includes finished work, like the implementation of electrons & photons in MonteRay [40, 41], but also ongoing work like the development of an GPU accelerated dose optimization framework coupled to MonteRay [42], or the use of MonteRay to study the viability of very high energy electron beams for radiotherapy. In chapter 5,

a brief overview over some of this work and the author's vision for the future of MonteRay will be given.

Chapter 2

Fundamentals

2.1 The Heidelberg Ion Beam Therapy Center

Since the work presented in this thesis was carried out at HIT, a brief overview of the facility will be given here. While the particle transport inside MonteRay is facility agnostic, a basic understanding of the beam generation and raster scanning process is important when it comes to initializing the simulation and modeling of the beamline.

The Heidelberg Ion Beam Therapy Center was constructed following a pilot study at the GSI Helmholtz Centre for Heavy Ion Research [43], which proved the feasibility of active raster scanning for the treatment of tumors. Between 1998 and 2008, 440 patients were treated there [44]. With active raster scanning, the goal of achieving conformal dose distributions is achieved by scanning a narrow beam, called a pencil beam, across the tumor. This principle is shown in Figure 2.1. Two scanning magnets deflect the beam in the horizontal and vertical direction and steer it towards the desired scan spot position. By changing the beam's energy, the depth of the Bragg Peak (BP) can be adjusted. In this way, the tumor can be "painted", energy layer by energy layer.

To accurately paint the tumor in this way, narrow particle beams with adjustable energies are needed. At HIT, this is achieved through the use of a synchrotron accelerator, labeled (2) in the schematic overview in Figure 2.2. It is fed by a linear pre-accelerator, labeled (1), which provides the particles with the necessary energy to be injected into the synchrotron. The synchrotron with a radius of 10 meters (2), then accelerates protons, helium ions, carbon ions and oxygen ions to variable energies covering the full therapeutic range, i.e. the energy range allows the depth of the BP to be varied from 20 mm to 300 mm in water [46]. The

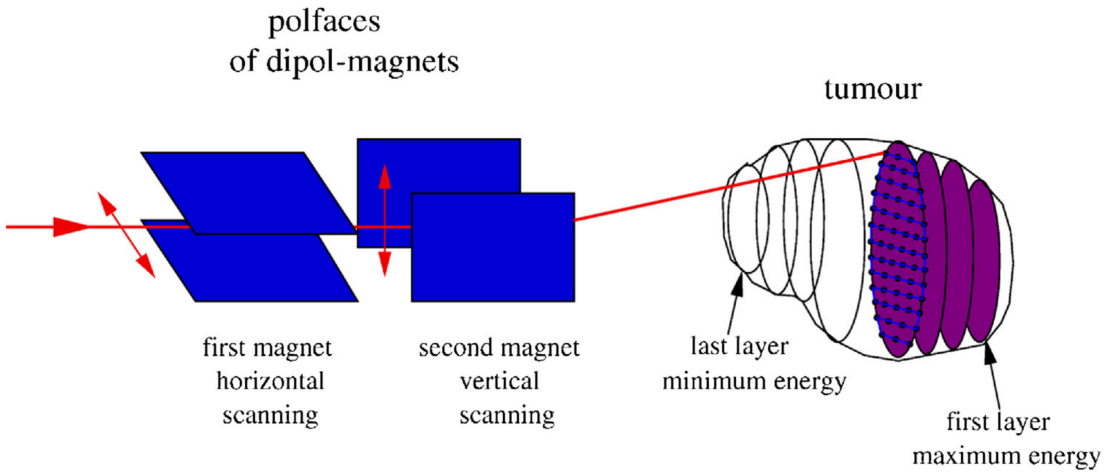

Figure 2.1: Example of how a tumor can be "painted" using the raster scanning principle. Scanning magnets deflect the beam horizontally and vertically, while changing the beam's energy allows to move the depth of the BP. Figure taken from Jäkel et al. [45].

particles are then guided to one of the three treatment rooms or the experimental room (5). Two of the treatment rooms (3) feature a horizontal beam, i.e. the beam is stationary, but rotation of the patient can be achieved through a rotating table. The third treatment room features a rotating gantry (4), which at the time of construction of HIT, was the world's first carbon ion gantry.

2.2 Physical and Biological Dose

Dose is a key quantity in radiotherapy. It is a measure for the energy deposited by ionizing radiation in a certain amount of matter and has the unit of Gy (Gray), or $\frac{J}{kg}$ in SI units.

Dose deposition by ionizing radiation is not homogeneous but has a spatial dependency that depends on the radiation's energy, the radiation's type and the traversed material itself. This is exemplified in Figure 2.3, where dose distributions of different monoenergetic particle beams (photons, electrons, protons, helium ions and carbon ions) in water are displayed. As visible there, electrons deposit their dose primarily at the surface, while photons, after a short buildup, show an exponentially fall-of in the dose. Ions on the other hand, show a sharp peak in their dose distribution at the end of their range, the so called Bragg Peak. Wilson [2] was the first to point out that this feature could allow the targeted irradiation of tumors within the body. Further, the sharpness of the BP increases with the

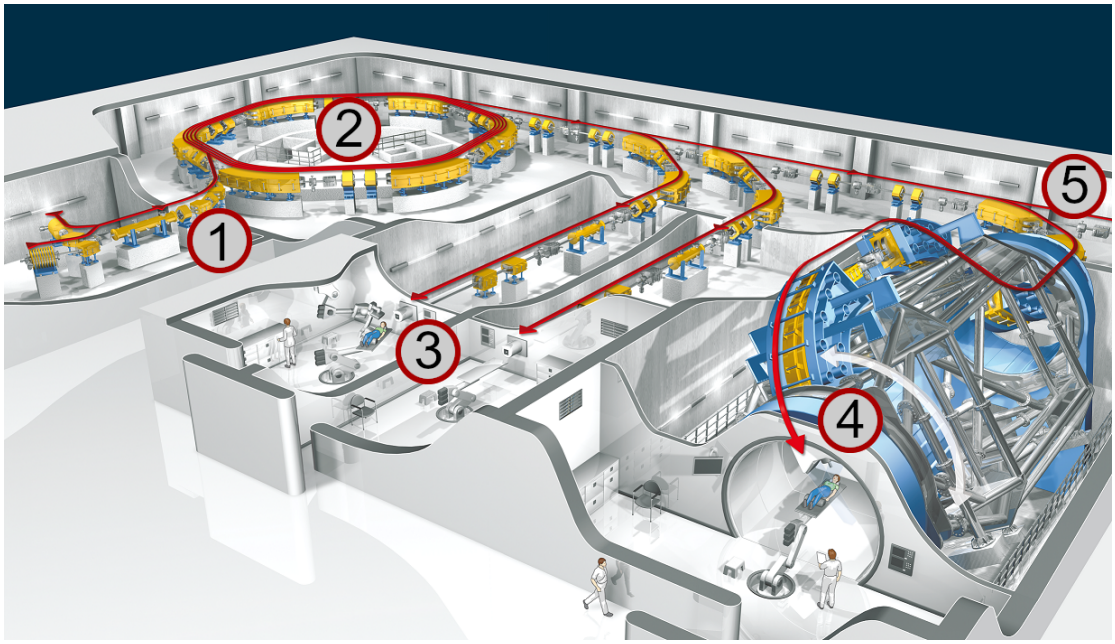

Figure 2.2: Numbered overview of the HIT facility. (1) Particle source and linear accelerator (2) Synchrotron accelerator (3) Horizontal treatment rooms (4) Gantry (5) beamline towards experimental room (not shown). Adapted from [47].

particle's mass, one of the reasons why helium and carbon ions are of interest for radiotherapy.

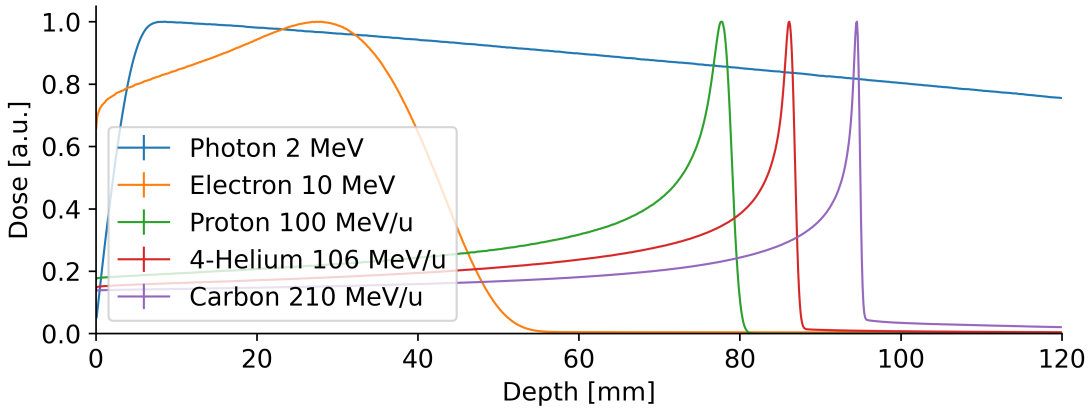

Figure 2.3: Integrated depth dose distributions of different particle types used in radiotherapy as computed by MonteRay. The energies for protons, helium ions, carbon ions, electrons and photons were 100 MeV, 106 MeV/u, 210 MeV/u, 10 MeV and 2 MeV, respectively. The dose distributions were computed in water.

For well collimated beams such as those at HIT, a single pencil beam may not be enough to achieve full coverage of the tumor. For this, multiple beams with

different energies and positions must be combined to form a uniform dose. This principle, already introduced in section 2.1, is exemplified in Figure 2.4 where multiple individual monoenergetic proton beams (blue curves) and their superposition (red curve) are shown. While individual beams have highly inhomogeneous dose distributions, the superposition of individual beams produces a nearly uniform plateau, called a Spread Out Bragg Peak (SOBP).

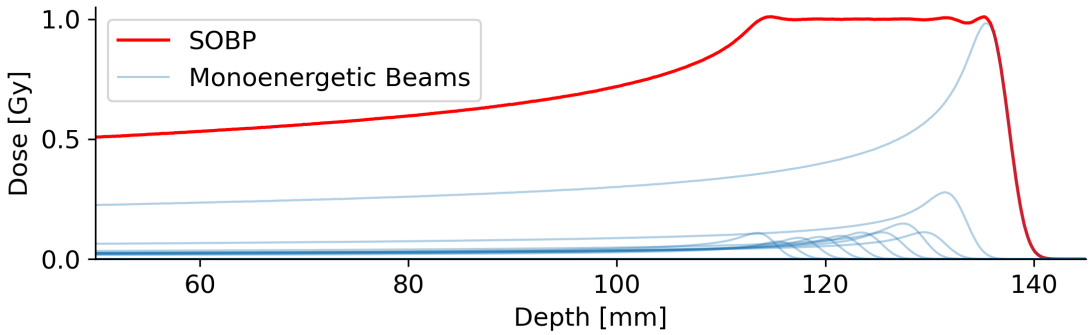

Figure 2.4: The combined dose of multiple monoenergetic proton beams incident on a water target (blue curves) results in a dose distribution with a nearly homogeneous region, called a Spread Out Bragg Peak (red curve).

The above defined quantity "dose" is also referred to as physical dose, to distinguish it from the clinically more relevant quantity of biological dose. For the ultimate goal of radiotherapy is not to deposit dose, but to treat the patient's tumor. To do this, the biological effect of the deposited dose must be taken into account, and one must understand how energy deposition of particles eventually leads to cell death through DNA damage. This is a complex process, involving physical, chemical and biological components, each acting on different timescales, ranging from attoseconds for physical process to hours or years for biological ones [8].

While MC particle simulations tailored to this purpose exist (e.g. Geant4-DNA [48]), the computational cost of such simulations is far too high to be used for full dose calculation. Instead, one must rely on models that relate the physical properties of a particle, like its energy, it's stopping power and the particle type itself to the biological effect of the particle. Many models exist for this purpose, e.g. the local effect model [49] or the modified Microdosimetric Kinetic Model (mMKM) [50]. The later model was used for the calculations presented in the third publication. A thorough description of biological models would go beyond the scope of this thesis and only a brief summary of the implementation of the mMKM, based on the summary of Mairani et al. [51], will be given here.

First, let the total physical dose D_j received by the voxel with index j be defined as

$$D_j = \sum_i d_{ji}. \tag{2.1}$$

In this equation, d_{ji} is the dose deposited by the i-th particle in the j-th voxel. Following Mairani et al. [51], the biological dose D_j^{bio} can then be calculated via

$$D_j^{bio} = \sqrt{\frac{\ln(S_j)}{\beta_{ph}} + \left(\frac{\alpha_{ph}}{2\beta_{ph}}\right)^2} - \frac{\alpha_{ph}}{2\beta_{ph}}. \tag{2.2}$$

Here, α_{ph} and β_{ph} are the tissue specific parameters of the linear-quadratic-model [52], and S_j is the survival fraction of cells in the j-th voxel, predicted by

$$-\ln(S_j) = (\alpha_{ph} + \beta_{ph} z^*_{1\mathrm{D}j}) D_j + \beta_{ph} D_j^2. \tag{2.3}$$

The quantity $z^*_{1\mathrm{D}j}$ is the saturation-corrected dose-mean specific energy and is computed using

$$z^*_{1\mathrm{D}j} = \frac{\sum_{i=0}^{N} d_{ji} \cdot z_i(E, Z)}{D_j}. \tag{2.4}$$

Here, z_i are tabulated values of the dose-mean specific energy, which depends on the particle's energy and atomic number.

2.3 Monte Carlo Simulations for Particle Therapy

In this section, the basics behind MC particle simulations will be explained so that the next section can give an overview of the underlying physics, specifically with MC simulations in mind.

The development of MC transport of charged particles as it is known today is often [53, 54] attributed to Berger and his work on numerically solving electron and proton transport problems [55]. Berger pointed out that due to the large number of individual collisions electrons or protons experience, a direct MC method where each individual collision is simulated would be computationally costly. Instead, he introduced the "condensed random walk" approach, wherein multiple individual interactions are grouped together, thereby "condensing" the action of many smaller interactions into one big interaction. The variables of interest of this step, like energy loss or deflection angle, must then be described by some adequate probability distribution.

Based on this principle, many MC particle transport codes have been developed over the years. The most prominent ones in the realm of hadron therapy being

FLUKA [18, 19], GEANT4 [20] and PHITS [21]. But, these codes are general purpose codes supporting a wide range of applications, allowing the simulation of particle types, physical processes or energy ranges irrelevant to radiotherapy. They are not optimized for radiotherapy and their long execution times make their adoption in clinical routine difficult. Nonetheless, traditional MC engine have served as important research tools (e.g. [9, 22, 56]). Striving to overcome these limitations, many fast MC engines have been developed in recent years. These programs aim to solve the radiation transport problem with sufficient accuracy while significantly reducing runtime. For protons, the list of fast MC algorithms is long [25, 26, 27, 28, 29, 30, 31, 37, 32, 33], with commercial solutions like RayStation [34] or IBA's myQA iON [24] making use of MC algorithms as well.

For helium or carbon ions, the list is much shorter. To the best of the author's knowledge, no fast MC algorithms for helium ions exist[1]. For carbon ions, the list is limited to goCMC [35, 58] and FRED [36].

MC algorithms based on the condensed history scheme were further separated into two classes in Berger's work:

- Class I: All possible interactions a particle can undergo are grouped together and condensed into probability distributions.

- Class II: Only a subset of interactions are grouped together. Some interactions, so called "catastrophic" events, e.g. large energy losses producing delta rays (high energy electrons) or nuclear interactions, are simulated directly.

The majority of fast MC algorithms for radiotherapy purposes are Class II algorithms, but as pointed out by Wan Chan Tseung et al. [27], a few Class I algorithms have been developed as well [15, 59]. Class II MC algorithms typically use what is known as the random-hinge method to transport particle from one multiple-scattering event to the next. An example of a particle track simulated with the class II random hinge method is shown in Figure 2.5. There, the track of a single carbon ion with 430 MeV/u incident on water, simulated by MonteRay, is shown. Besides the primary carbon ion track in black, the tracks of secondary particles are shown in blue. For visual purposes, the size of the scoring grid was set to 4 mm along the z-axis (parallel to the beam's direction), 0.4 mm along the x-axis (perpendicular to the beam's direction) and a large step size of 16 mm was

[1] There exists one code for the fast simulation of helium ion transport by Peralta et al. [57], but with maximum energies of only 12 MeV, it is not suited for radiotherapy purposes.

chosen. At every dot along the track, the particle loses energy and is deflected by a certain angle (sampled from the distributions introduced in subsubsection 2.4.1.2 and subsubsection 2.4.1.3). Between two dots, the particle is assumed to travel in a straight line, and energy is deposited along this line using the rasterization algorithm of Amanatides & Woo [60]. In the example shown, an inelastic nuclear interaction (subsection 2.4.2) occurred in which multiple secondary particles were created. These secondaries are transported using the same principles as the primary particle.

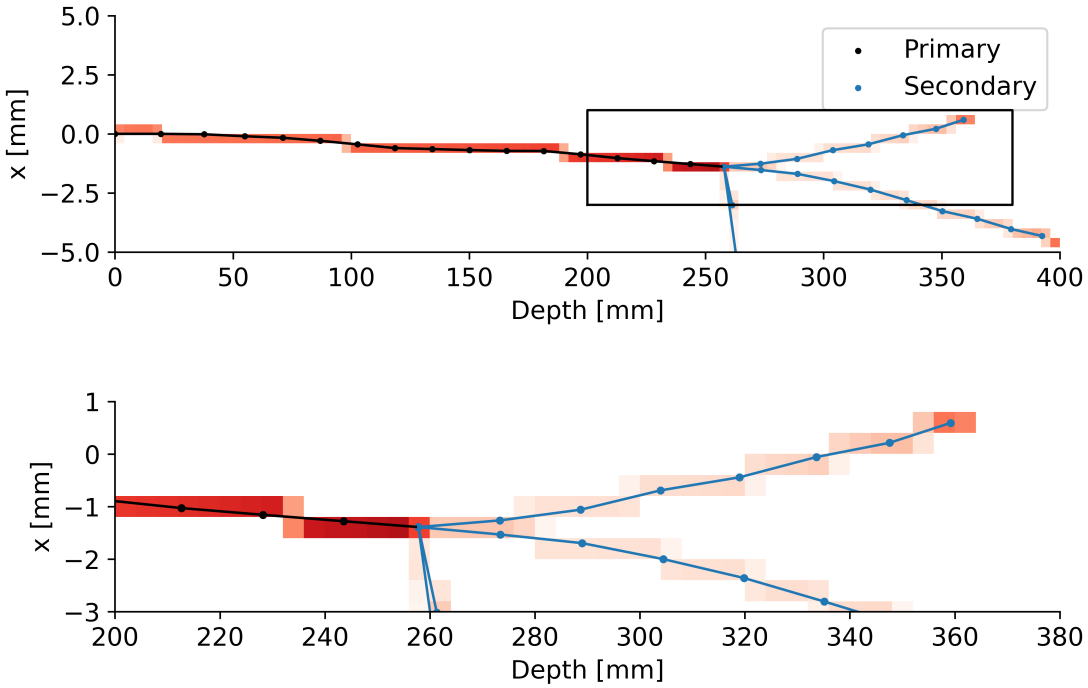

Figure 2.5: Sample track of a single 430 MeV/u carbon ion incident on water. Each random hinge step performed in MonteRay is shown as a dot. Besides the primary carbon ion in black, the tracks of secondaries are shown with blue dots. In the top panel, a zoomed out view of the track is shown. The bottom panel shows a zoom into the region of the inelastic nuclear interaction. The dose deposition is shown in shades of red. Darker colors indicating more dose. The resolution of the scoring grid was 4 mm along the z-axis and 0.4 mm axis along the x-axis, resulting in square voxels at the plot's aspect ratio of 10:1.

Discrete interactions, are those that are not condensed into probability distributions. In the case of light ions, these are typically nuclear interactions, but for other particle types, they may include processes like pair production or bremsstrahlung. Deciding when to simulate such an interaction is usually done

using macroscopic cross sections. From the macroscopic cross section, the mean free path λ_{disc} can be computed, which describes the average distance a particle will travel before undergoing an interaction. The distance to the next discrete interaction Δx_{disc} is then sampled from an exponential distribution

$$P(\Delta x_{\text{disc}}) = \frac{1}{\lambda_{\text{disc}}} \exp(-\frac{\Delta x_{\text{disc}}}{\lambda_{\text{disc}}}). \tag{2.5}$$

2.4 Interactions of Light Ions With Matter

For a MC engine to accurately estimate dose deposition, it must accurately model the interactions of particles with matter. As discussed in section 2.3, MonteRay is a class II MC engine, i.e. it doesn't simulate every single interaction of the particle with the target's electrons and nuclei but groups some of them together, describing their combined action through appropriate probability distributions. Indeed, MonteRay treats all interactions of the particle with the target's electrons in a condensed fashion approach. However, both elastic and inelastic nuclear interactions are treated individually. In the following sections, an overview of the physical processes relevant for light ion radiotherapy will be given with a focus on MC simulations. Particularly, the simplifications implemented inside MonteRay will be presented, together with the rigorous physical theory.

2.4.1 Electromagnetic Interactions

When fast charged particles traverse matter, they lose energy predominantly through their interactions with atomic electrons [61] and these interactions are ultimately responsible for the characteristic BP shape. This can be seen when one visualizes the depth dose distributions of light ions with different interaction types switched on or off. In Figure 2.6 this is shown for 300 MeV/u carbon ions incident on water for three configurations. For configuration a), the only physical process modelled in MonteRay is the mean energy loss $\left\langle \frac{dE}{dx} \right\rangle$ after equation Equation 2.6. Already here, the characteristic BP emerges. Enabling further interactions b): energy loss straggling (subsubsection 2.4.1.2) & Multiple Coulomb Scattering (MCS) (subsubsection 2.4.1.3) and c): nuclear interactions (subsection 2.4.2), only serves to broaden the BP. Additionally, nuclear interactions lead to a low dose tail after the BP, also known as the fragmentation tail. Figure 2.6 is suggestive of the fact that the process behind the energy loss of the particle is typically divided into two parts. The first part is the mean energy loss $\left\langle \frac{dE}{dx} \right\rangle$ and the second part is the

energy loss straggling, i.e. the random fluctuation of the energy loss around the mean due to the stochastic nature of particle collisions.

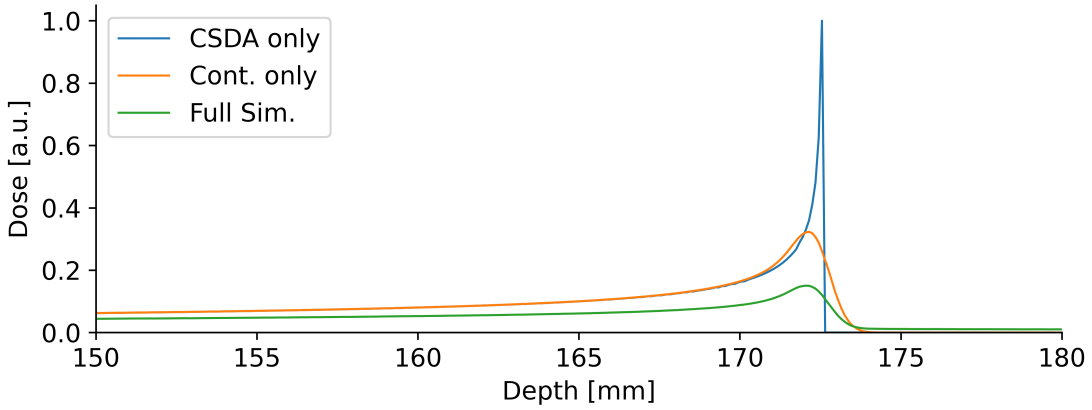

Figure 2.6: Depth-dose distributions of 300 MeV/u carbon ions incident on water are shown for three different settings. For the blue curve, only energy deposition according to Equation 2.6 was considered, for the orange curve both energy loss straggling (subsubsection 2.4.1.2) and MCS (subsubsection 2.4.1.3) were enabled. For the green curve all physical processes, including nuclear interactions (subsection 2.4.2), were enabled.

2.4.1.1 The Average Energy Loss

Determination of the energy loss as the particle travels a certain distance is usually divided into two steps. First, a mean energy loss is computed and then a random variation around this mean is sampled from a probability distribution. The mean energy loss per unit length $\left\langle \frac{dE}{dx} \right\rangle$ due to electromagnetic interactions is given by the Bethe-Bloch equation [62, 63] (see [64] or [65] for a summary)

$$S(E) = \left\langle \frac{dE}{dx} \right\rangle = 0.1535 \frac{\mathrm{cm}^2 \mathrm{MeV}}{\mathrm{g}} \frac{\rho z^2 Z}{\beta^2 A} \left(\log \left(\frac{2 m_e c^2 \beta^2 T_{\max}}{I^2 (1-\beta^2)} \right) - 2\beta^2 - 2\frac{C}{Z} - \delta \right). \tag{2.6}$$

Here, z is the incident particle's charge, β its relativistic velocity, Z is the target atom's charge and A its mass number. The quantity $T_{\max}$ is the maximum possible energy transfer to an electron in a single collision. With the electron mass m_e and the Lorentz factor γ, it is given by

$$T_{\max} = \frac{2 m_e \beta \gamma^2}{1 + 2\gamma m_e + m_e^2}. \tag{2.7}$$

The terms $\frac{C}{Z}$ and δ in Equation 2.6, not included in the original work of Bethe, are corrections to the Bethe-Bloch equation. The term $\frac{C}{Z}$ is the so-called shell correction and becomes relevant for particles with low energy. The term δ is the density correction and takes into account the polarization of the target's atoms induced by the incident particle. It becomes relevant for highly energetic particles.

The quantity I is the mean ionization potential of the target material. The determination of this quantity is not straightforward and as Sabin et al. [66] have pointed out, reported mean ionization potentials for water vary widely from 68 eV [67] to 81.1 eV [68]. This is reflected in an uncertainty of the particle's range. Using FLUKA, the R_{80} range, i.e. the point after the BP where the dose has fallen to 80 % of the maximum value, of 250 MeV protons in water is 37.6 cm when using $I = 68$ eV and 38.5 cm when using $I = 81.1$ eV. A difference of 8 mm, roughly in line with the uncertainty of 1.5 % given in [16]. In the context of radiotherapy, this uncertainty is not so relevant because the absolute energies of particles produced in particle accelerators are typically not measured [56] and consistency is achieved by commissioning the MC engine to match measured data in terms of range.

Evaluation of Equation 2.6 including the correction terms is computationally costly. However, it is one of the most used quantities for MC dose calculation and must be evaluated every time the particle is advanced by a step. Due to this, the stopping power for different particles in water is tabulated in MonteRay instead of computing it on the fly. This is similar to the approach of Schiavi et al. [30], where stopping powers from PSTAR [69] were used. Since MonteRay was initially developed for the use at HIT, where previous work was based on FLUKA simulations [70, 71, 9], stopping powers were also extracted from FLUKA. In Figure 2.7, $\left\langle \frac{dE}{dx} \right\rangle$ as it is tabulated in MonteRay is shown for carbon ions in water. The stopping powers in materials other than water are computed using a per-material scaling factor that is nearly independent of energy or particle type, the so called Stopping Power Ratio (SPR). This is discussed in more detail in section 2.5.

When performing a MC simulation using the random hinge method as described in section 2.3, one frequently wants to compute the energy loss ΔE as a particle traverses a certain length Δx of a material. The need for this arises since a limit on the step size might be imposed trough:

- The distance to the next discrete interaction event (e.g. nuclear interactions).

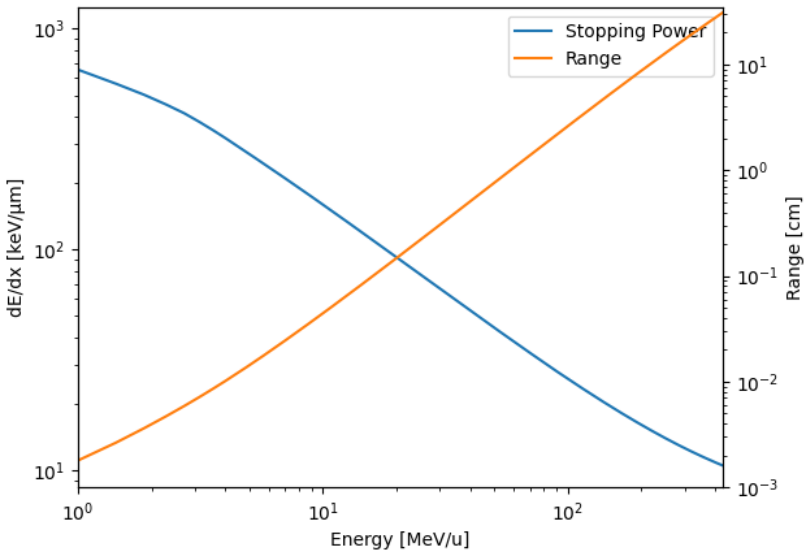

Figure 2.7: Stopping power (blue) and remaining range (orange) of carbon ions in water as a function of the particle's energy.

- The distance to a region interface.
- The distance to the next voxel (Computed Tomography (CT) grid or scoring grid).
- The maximum step size allowed by the user.

If Δx is small, the energy loss can be approximated by $\Delta E = S(E_0)\Delta x$, where E_0 is the particle's energy at the beginning of the step. This assumes that the stopping power is constant over the step. In reality, this is not true. To correctly account for this, the energy loss should be computed as

$$E(x_0 + \Delta x) = E(x_0) - \int_{x_0}^{x_0+\Delta x} S(E(x'))dx'. \tag{2.8}$$

To the best of the author's knowledge, there exist no analytical solutions to this integro-differential equation. While an approximate solution has been derived by Grimes et al. [72], it includes the exponential integral function which makes this approach unsuitable for fast MC dose calculation purposes, where this function must be evaluated many times. At the same time, a tabulation would require a two-dimensional table in E_0 and Δx. Instead, MonteRay never guarantees steps with a fixed step-size but only with a fixed energy loss such that the resulting step size is close to the requested one. This step size is computed as

$$\Delta x = \int_{E_0}^{E_0-\Delta E} \frac{dE'}{S(E')} = R(E_0) - R(E_0 - \Delta E) \tag{2.9}$$

where $R(E)$ is the range of the particle with energy E and given through

$$R(E) = \int_0^E \frac{dE'}{S(E')}. \tag{2.10}$$

In Figure 2.7, this quantity is shown as a function of the particle's energy for carbon ions incident on water. In MonteRay, this quantity is tabulated for all transported particles.

2.4.1.2 Energy loss straggling

The quantity $\left\langle \frac{dE}{dx} \right\rangle$, as per equation Equation 2.6, describes the average energy loss of a particle, and in MC simulations it is used as a substitute for the otherwise computationally expensive task of simulating each individual collision of the projectile. But, as its name suggests, it only describes the mean energy loss and for an accurate description of the particle, the stochastic nature of collisions must be taken into account. These fluctuations are commonly referred to as energy loss straggling. As can be seen in Figure 2.6, they serve to broaden the BP.

Energy loss straggling is a direct result of the random nature of the projectile's interaction with the target's electrons and for a MC simulation, a distribution function that we can sample from is needed. Loosely following the notation of Landau [73], let Δx be the traversed material's thickness and let ΔE be the energy the particle loses, then we are interested in the distribution $f(\Delta x, \Delta E)$ which describes the probability that a particle with some initial energy E_0 will experience an energy loss within ΔE and $\Delta E + d\Delta E$. It is useful to define the quantity $\kappa = \frac{\xi}{T_{\max}}$, where $T_{\max}$ was defined in Equation 2.7 and ξ is given by

$$\xi = \frac{Z}{A} \frac{2\pi N_a m_e r_e^2 z^2 \rho \Delta x}{\beta^2}, \tag{2.11}$$

where N_a is Avogadro's numbers, $r_e = 2.818E-15$ m the classical electron radius and ρ the target's density. After Uehling [74], the physical meaning of ξ is that it is, on average, the maximum energy loss a particle experiences in an individual collision when traversing a material of thickness Δx. Based on κ, the scattering process can be divided into several regimes for which different approximations are used. For very small κ, the so-called Landau distribution [73] is a good approximation to the particle's energy loss distribution. Its derivation is based on

the assumption that the maximum possible energy transfer in a single collision is infinite and the non-relativistic Rutherford cross-section $\omega(\epsilon)$ is used

$$\omega(\epsilon) = \frac{\xi}{\Delta x \epsilon^2}. \tag{2.12}$$

Based on this, Landau obtained the following expression for the energy loss distribution

$$f(\Delta x, \Delta E) = \frac{1}{\xi}\psi(\lambda), \tag{2.13}$$

with

$$\psi(\lambda) = \frac{1}{2\pi i}\int_{\sigma-i\infty}^{\sigma+i\infty} \exp\left(uln(u) + \lambda u\right)du. \tag{2.14}$$

The variable λ is known as the universal Landau variable and is given by

$$\lambda = \frac{\Delta}{\xi} - \log\frac{\xi}{\epsilon'} + 1 - C_E, \tag{2.15}$$

where $C_E = 0.577$ is the Euler-Mascheroni constant and ϵ' is the minimum possible energy transfer in a single collision, given by

$$\log\epsilon' = \log\left(\frac{I^2}{2mc^2\beta^2\gamma^2}\right) + \beta^2 \tag{2.16}$$

where I is the mean ionization potential of the target material. As already pointed out, using Landau's distribution is only valid when κ is small. Typically, $\kappa < 0.01$ is used as the threshold criterion [75]. For larger values of κ, the appropriate distribution is the Vavilov distribution. In Vavilov's work [75], he expanded on Landau's work by using the relativistic version of the Rutherford scattering cross section $\omega_{rel}(\epsilon)$ which notably also included an upper limit on the maximum transferable energy in a single scattering event, $T_{\max}$

$$\omega_{\text{rel}}(\epsilon) = \begin{cases} \frac{\xi}{\Delta x\epsilon^2}\left(1 - \frac{\beta^2\epsilon}{T_{\max}}\right) & \epsilon \leq T_{\max} \\ 0 & \epsilon > T_{\max} \end{cases}. \tag{2.17}$$

The solution obtained by Vavilov under these assumptions is a complicated equation and, as already pointed out by Seltzer et al. [76], the evaluation of Vavilov's distribution is computationally expensive, making numerical approximations necessary. For a thorough definition of Vavilov's distribution, the reader is encouraged to consult Vavilov's original publication [75], the summary given by Seltzer [76] or the work of Chibani [77]. The latter also describes a method for sampling from an approximation of the Vavilov distribution which MonteRay employs. Before describing this method in more detail the third regime of κ should be mentioned.

For very large values of κ, typically $\kappa > 10$, the distribution is well approximated by a Gaussian distribution [75], whose mean is given by Equation 2.6 and after [76], its standard deviation can be computed as

$$\sigma^2 = T_{\max}\xi(1 - 0.5\beta^2). \tag{2.18}$$

For the purpose of radiotherapy MC calculations, κ can reach values across all three regimes. For small step sizes or low target material densities, κ can be very small, while large step sizes or high densities lead to large values of κ. The sampling scheme proposed by Chibani [77] is based on a partitioning of the distribution into four regimes based on the value of κ:

- $\kappa > 10$: The distribution is assumed to be Gaussian and Equation 2.18 is used.
- $0.3 < \kappa < 10$: The distribution is approximated through a log-normal distribution.
- $0.01 < \kappa < 0.3$: Chibani proposed to use a log-normal distribution, which models multiple scattering due to many small energy losses, convoluted with a log-normal distribution which models individual high energy losses.
- $\kappa < 0.01$ Landau's distribution from Equation 2.13 can be used.

In the current version of MonteRay, this scheme is used, but for $0.01 < \kappa < 0.3$ the single scattering approximation is not included, and instead this regime is treated with a log-normal distribution like for $0.3 < \kappa < 10$.

For the sampling of Landau's distribution, an adoption of the CERNLIB routine RANLAN [78] is used to sample the landau random variable λ, and then Equation 2.15 is used to convert it into an energy loss ΔE. The parameters of the log-normal distribution are computed as proposed by Chibani [77].

To provide an insight into which regimes are relevant for MC simulations in the context of radiotherapy purposes, Figure 2.8 shows κ values extracted from MonteRay for protons (223 MeV/u), helium ions (223 MeV/u) and carbon ions (430 MeV/u) as a function of depth. The simulations were performed with energy loss straggling, MCS and nuclear interactions disabled. To showcase the effect of step size on κ, two different step size policies are shown. For the solid lines, a constant fractional energy loss of 4 % was used while for the dashed lines, a constant step size of 1 mm was forced. As can be seen, the step size policy has a significant effect on κ. Forcing 1 mm steps, a typical resolution of a CT, leads to

minimum kappa values of 0.04, 0.2 and 0.5 for protons, helium ions and carbon ions, respectively. Especially for protons, the simulation is then frequently in a regime where neither the Landau, nor the log-normal approximation of Chibani are particularly adequate. Taking bigger steps, i.e. 4 % of the particle's energy, leads to minimum kappa values of no less than one for all three particle types. This pushes the shape of the energy straggling distribution further towards a Gaussian distribution, and together with the gain in performance, this is a reason to prefer a bigger step size rather than a smaller one. This comes with the caveat of requiring a more complex scoring algorithm to account for energy loss in multiple voxels, as opposed to a single voxel when taking steps of 1 mm.

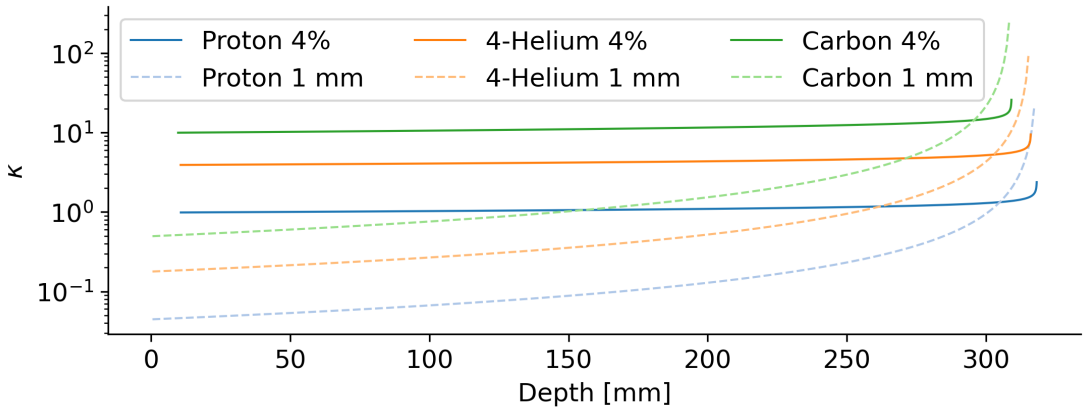

Figure 2.8: Visualization of κ as a function of the depth in water for protons, helium ions and carbon ions with energies of 223 MeV/u, 223 MeV/u and 400 MeV/u respectively. The energies roughly result in equal ranges. Simulations were performed with all physical processes but the mean energy loss disabled. For each particle type, two different step size policies were used. The first one uses a fixed energy loss fraction of 4 % (solid lines) while the second uses a fixed step size of 1 mm (dashed lines).

2.4.1.3 Angular Deflection

Besides losing energy, light ions interacting with matter also get deflected through their interactions with atomic nuclei. When treated in the condensed history scheme, this process is called Multiple Coulomb Scattering (MCS). Like with energy loss straggling, this is a stochastic process that can be described using an adequate probability distribution. The work presented here makes use of the scattering theory developed by Molière [79], but other theories exist [80, 81, 82]. As shown by Bethe [83], the distribution derived by Molière, which is expressed as an

infinite series, is in good agreement with experimental data already when one takes into account only the first three terms of the distribution. Indeed, as pointed out by Bethe [83], also the sum of the first two terms of Molière's distribution already is a good approximation at all angles.

Based on his derivation of single scattering [84], Molière derived a series expansion for the scattering angle distribution for multiple scattering. For this, he introduced the scaled angle

$$\vartheta = \chi_c^{-1} B^{-1/2} \theta, \tag{2.19}$$

where θ is the polar scattering angle, B is a measure for the average number of single scattering events and χ_c is called the characteristic angle. Following the summary of Gottschalk et al. [85], we can compute these quantities as follows. Let p be the particle's momentum in MeV c^{-1}, β its relativistic velocity and z its charge as a multiple of the elementary charge e. Further, let the target material be described by its density ρ in g/cm^3, the atomic numbers Z_i and atomic weights A_i of its N constituent elements with associated weight fractions w_i (see section 2.5). The step size is denoted by Δx. Using these quantities one first computes

$$c_i = \frac{\rho K_{\mathrm{M}} z^2 Z_i^2 w_i}{A_i} \tag{2.20}$$

where K_M is a constant given by

$$K_M = \frac{4\pi N_a (\hbar c)^2}{\alpha^2} = 0.1569\,\mathrm{rad}^2, \tag{2.21}$$

and α being the fine-structure constant. $\sqrt{K_M} = 22.7°$ corresponds to the numerical constant introduced in Equation (III) of Molière's original work [79]. Defining

$$c_{\mathrm{tot}} = \sum_{i=1}^{N} c_i \tag{2.22}$$

one can then compute the characteristic angle as

$$\chi_c^2 = \frac{c_{\mathrm{tot}} \Delta x}{p^2 \beta^2}. \tag{2.23}$$

For B, we begin by computing $\chi_{a_i}^2$

$$\chi_{a_i}^2 = \chi_i^2 \left(1.13 + 3.76 \alpha_i^2\right) \tag{2.24}$$

where α_i^2 and χ_i^2 are given by

$$\alpha_i^2 = \frac{z^2 Z_i^2}{\alpha^2 \beta^2} \tag{2.25}$$

and

$$\chi_i^2 = \frac{0.004215^2}{p^2 \sqrt[3]{Z_i^2}}, \tag{2.26}$$

respectively. Fano [86] derived a correction term to account for the scattering of the incident particle from atomic electrons. This correction term is given by

$$F_i = \frac{1}{Z_i}\left(\log\frac{1130(\gamma^2-1)}{\sqrt[3]{Z_i^2}} - U_{\text{in}} - 0.5\beta^2\right) \tag{2.27}$$

where the constant U_{in} was set to -5 as suggested by Fano. Continuing, we compute χ_a^2 as

$$\chi_a^2 = \frac{\Delta x \sum_{i=0}^{N} \log(\chi_{a_i}^2) - F_i}{\chi_c^2 p^2 \beta^2}, \tag{2.28}$$

and $\log_{10}\Omega$ as

$$\log_{10}\Omega = \frac{\log(\chi_c^2) - \chi_a^2}{\log(10)}. \tag{2.29}$$

Finally, B is given as the solution of the transcendental equation

$$B = \log(B) - 0.1544 + \log(\Omega), \tag{2.30}$$

which can be solved using the linear approximation by Scott [87]

$$B = 1.153 + 2.583\log_{10}\Omega. \tag{2.31}$$

Now that the scaled angle can be computed, Molière's distribution can be given. In terms of the scaled angle, Molière expressed the distribution of the scattering angles $f(\vartheta)$ as an infinite sum of terms $f^n(\vartheta)$:

$$f(\vartheta) = \sum_{n=0}^{\infty} \frac{\vartheta}{B^n} f^n(\vartheta). \tag{2.32}$$

with

$$f^n(\vartheta) = \frac{1}{n!}\int_0^\infty y J_0(\vartheta y)\exp\left(-\frac{y^2}{4}\right)\left(\frac{y^2}{4}\log\frac{y^2}{4}\right)^n dy, \tag{2.33}$$

where J_0 is the zeroth oder Bessel function of the first kind. For the first two terms, Molière provides the following analytical expressions, but to the best of the author's knowledge, no analytical expression for $f^2(\vartheta)$ exists:

$$f^0(\vartheta) = 2\exp\left(-\frac{\vartheta^2}{2}\right) \tag{2.34}$$

$$f^1(\vartheta) = 2\exp\left(-\frac{\vartheta^2}{2}\right)\left(\left(\vartheta^2-1\right)\left(\text{Ei}(\vartheta^2) - \log(\vartheta^2)\right) + 2 - \exp(-\vartheta^2)\right). \tag{2.35}$$

In Figure 2.9, Molière's distribution is shown together with the first three terms of the series, and since B influences the shape of Molière's distribution, it is shown for two values of it, $B = 5$ and $B = 15$. The terms f^n of Molière's distributions were tabulated up to f^{10} by numerically integrating Equation 2.33. As can be seen, the first term already provides a good approximation to the distribution at small angles, especially when B is large.

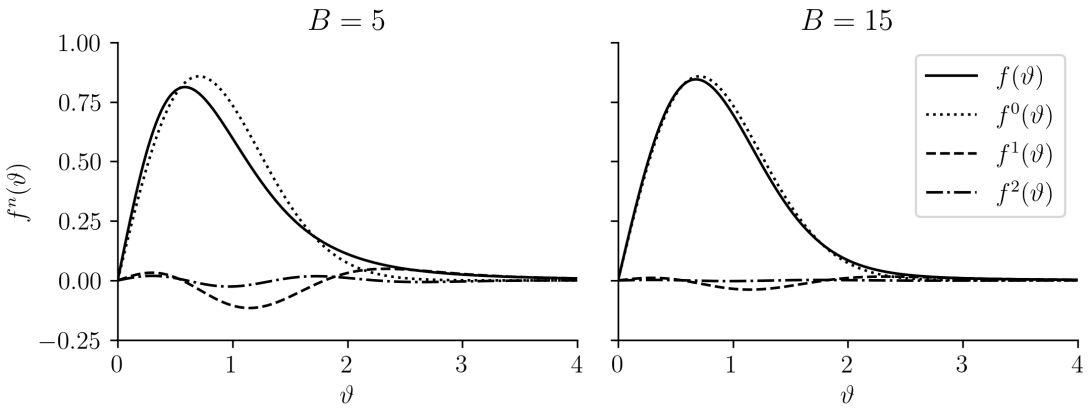

Figure 2.9: Molière's distribution $f(\vartheta)$ is shown (solid line) together with the first three terms $f^0(\vartheta)$ (dotted), $f^1(\vartheta)$ (dashed) and $f^2(\vartheta)$ (dot-dashed). B was set to 5 in the left panel and 15 in the right panel.

Molière's treatment is complicated both in terms of the resulting probability distribution $f(\vartheta)$ and in terms of the calculations required to compute B and χ_c. But, as put by Gottschalk [85], a huge shortcut in the form of a Gaussian[2] approximation exists. The standard deviation of this approximation, in this form attributed to Highland [89], can be written as [90]

$$\sigma_{\text{Highland}} = \frac{E_s z}{\beta p}\sqrt{\frac{\Delta x}{\rho X_0}}\left(1 + \frac{1}{9}\log_{10}\left(\frac{\Delta x}{\rho X_0}\right)\right), \tag{2.36}$$

where the radiation length X_0 is the single parameter Highland has condensed Molière's formalism to. Due to its simplicity, many fast MC codes work with Highland's approximation [25, 36, 35]. A similar simplification by Rossi and Greisen [91] is also sometimes used [28, 37]. The width of the Gaussian after Rossi and Greisen [91] is given by

[2]The reason why the approximation to Molière's distribution is called a Gaussian even if Molière's distribution (see Figure 2.9) is clearly not a Gaussian, is that the distribution of the projected angles θ_x and θ_y is Gaussian, and under the small angle approximation, we can write $\theta = \sqrt{\theta_x^2 + \theta_y^2}$ and if θ_x and θ_y are Gaussian, θ follows a Rayleigh distribution, corresponding to the first term of Molière's series. A detailed explanation of this has been given by Beilai [88].

$$\sigma_{\text{Rossi}} = \frac{E_s z}{\beta p}\sqrt{\frac{\Delta x}{\rho X_0}}. \tag{2.37}$$

The exact value of the constant E_s varies in literature. In the original publication of Highland [89], a value of 17.5 MeV was used, while Rossi & Greisen [91] set $E_s = 21$ MeV. In the context of fast MC simulations, its value is often determined through fits to reference simulations with traditional MC engines like Geant4 or FLUKA. For example, Fippel and Soukup [25] reported optimal values of 12.4 MeV, 12.0 MeV and 12.9 MeV when using Geant4 version 5.1, Geant4 version 5.2 and FLUKA version 2002.4, respectively. In developing their fast carbon ion MC engine, Simoni et al. [36] found it necessary to include an energy, particle type and depth dependent scaling factor f_{mcs} by which Equation 2.36 was multiplied. This factor was determined from fits to FLUKA simulation in water and ranged from 1.29 to 1.43. Qin et al. [35], also developing a fast carbon ion MC engine, found it sufficient to use an empirical, energy dependent, parametrization:

$$E_s = 19.8 \text{ MeV} + 0.0023E. \tag{2.38}$$

Using Rossi's & Greisen's formula, the first publication for MonteRay [37] used a value of $E_s = 11.6$ MeV. Such a low value was necessary because a mixed Gaussian-Rutherford distribution was used. Souris et al. [28], also using Rossi's & Greisen's approximation, wrote that "E_s is a coefficient tuned to reproduce other simulated or experimental results". While they did not specify the value of E_s in their publication, their code is open source [92] and at the time of accessing (01.03.2024) the value used was 18.3 MeV.

As evident from these examples, the description of MCS through a single Gaussian is widely used. However, while the distribution is easy to compute, there exists no consensus on the exact value of the constant E_s. And since this is merely an approximation of the true distribution, there likely is no one best value. This forces authors to introduce empirical and finely tuned scaling factors.

One possible explanation for the issues behind this approximation is that it was never meant to be used in a MC calculation, but as a way to estimate the spatial distribution of particles after passing through a target with certain thickness. The difference is subtle but important: In a MC simulation we sample the distribution over and over again, several hundreds of times, to simulate the particle's path through the target. When estimating the spatial distribution of particles, the distribution is used only once. This issue was also encountered during the development of MonteRay and the observation made is that the consecutive effect

of multiple scattering events does not converge nicely to a Gaussian distribution. This observation is backed up by a passage in a textbook by Roe [93] where in a section titled "Failures of the Central Limit Theorem" the author writes "Does the central limit theorem ever fail for real physical cases? The answer is yes! Consider the multiple scattering of a particle (...)".

MonteRay's approach on the other hand, similar to the work of Kuhn & Dodge for electron MC simulations [94], is based on an approximation to Molière's distribution which requires no additional finely tuned parameters. This approximation makes use the asymptotic behaviour of $f^1(\vartheta)$ which, as pointed out by Molière, tends to $f^1(\vartheta) \approx \frac{2}{\vartheta^4} + O(\vartheta^-6)$ for large ϑ. Together with the $f^0(\vartheta)$ term, this leads to the following approximation:

$$f_{\text{approx}}(\vartheta) = \begin{cases} 2\vartheta \exp\left(-\frac{\vartheta^2}{2}\right) & \vartheta \leq \sqrt{2} \\ 2\vartheta \exp\left(-\frac{\vartheta^2}{2}\right) + \frac{2}{B\vartheta^3} & \vartheta > \sqrt{2} \end{cases} \tag{2.39}$$

The threshold of $\sqrt{2}$, where the large angle tail comes into play, was also used by Kuhn & Dodge and was found to work well for this approximation, too.

The quality of this approximation depends on the value of B. Since the weight of the n-th term in Equation 2.39 is proportional to B^{-n}, the approximation becomes more accurate for larger B. In Figure 2.9 b), the distribution of B is shown for two exemplary prostate plans, one with protons and one with carbon ions. The energy ranges of the particles in the two plans were 147-189 MeV/u and 284-370 MeV/u, respectively. The distributions were computed using MonteRay's MC engine with the settings described in [39]. As can be seen, typical values of B range from approximately 5 to 17.

In the left column of Figure 2.11, MonteRay's approximation is shown together with Molière's distribution for two different values of B, 5 (top row) and 15 (bottom row). Additionally, a Gaussian fit to Moliere's distribution, i.e. not simply the term $f^0(\vartheta)$, is shown in green. The approximation provides a good fit to Molière's distribution for large angles and small angles but fails at intermediate angles. Notably this approximation has a discontinuity at $\vartheta = \sqrt{2}$ which is not present in Molière's distribution. While this discontinuity appears for a single scattering event, it is not present when looking at the result of multiple steps of the MC simulation. This is shown in the middle and right columns of Figure 2.11 b). There, the scaled angle ϑ of the particle relative to its initial direction is shown, i.e. let $\vec{d_0}$ be the initial direction and $\vec{d_n}$ be the particle's direction after n scattering events, then the polar scattering angle after n scattering events is given

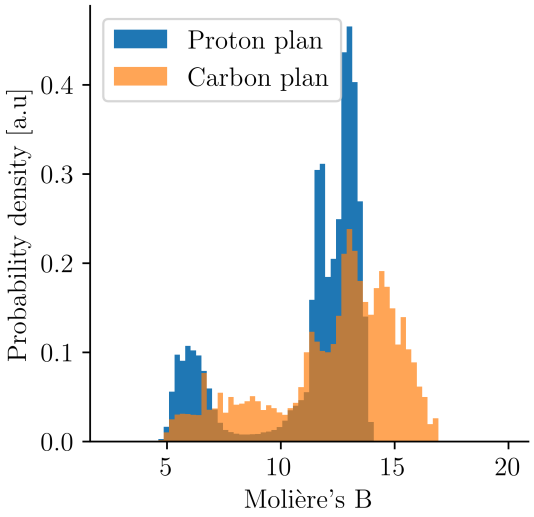

Figure 2.10: The distribution of Molière's parameter B for two patient plans, exemplary of a prostate patient, computed in MonteRay are shown. The step size settings (see [39]) were: minimum energy loss fraction 2 %, maximum energy loss fraction 25 %, step size target 2 mm. B was recorded for both primary and secondary particles.

by

$$\theta_n = \arccos\left(\frac{\vec{d_0}\cdot\vec{d_n}}{||\vec{d_0}||\cdot||\vec{d_n}||}\right), \tag{2.40}$$

and ϑ is computed after Equation 2.19. In the middle column, the distributions for $n = 2$ and in the right column, the distributions for $n = 4$ are shown. With increasing number of scattering events, the approximation used in MonteRay more closely follows Molière's distribution. The Gaussian fit on the other hand, does not improve with the number of scattering events, and fails to capture the large angle tail of Molière's distribution.

2.4.2 Nuclear Interactions

The electromagnetic interactions introduced in subsection 2.4.1 were treated in the condensed history scheme (see section 2.3), however inelastic and elastic nuclear interactions are treated as individual events. While elastic nuclear interactions only modify the projectile's and target's energy and direction, inelastic interactions may also produce secondary particles. As could be seen in Figure 2.6 for carbon ions, this has a significant impact on the dose distribution. A more detailed look at the fragmentation spectrum of carbon ions is given in Figure 2.12. There, the depth dose distribution of carbon ions with an energy of 430 MeV/u, the

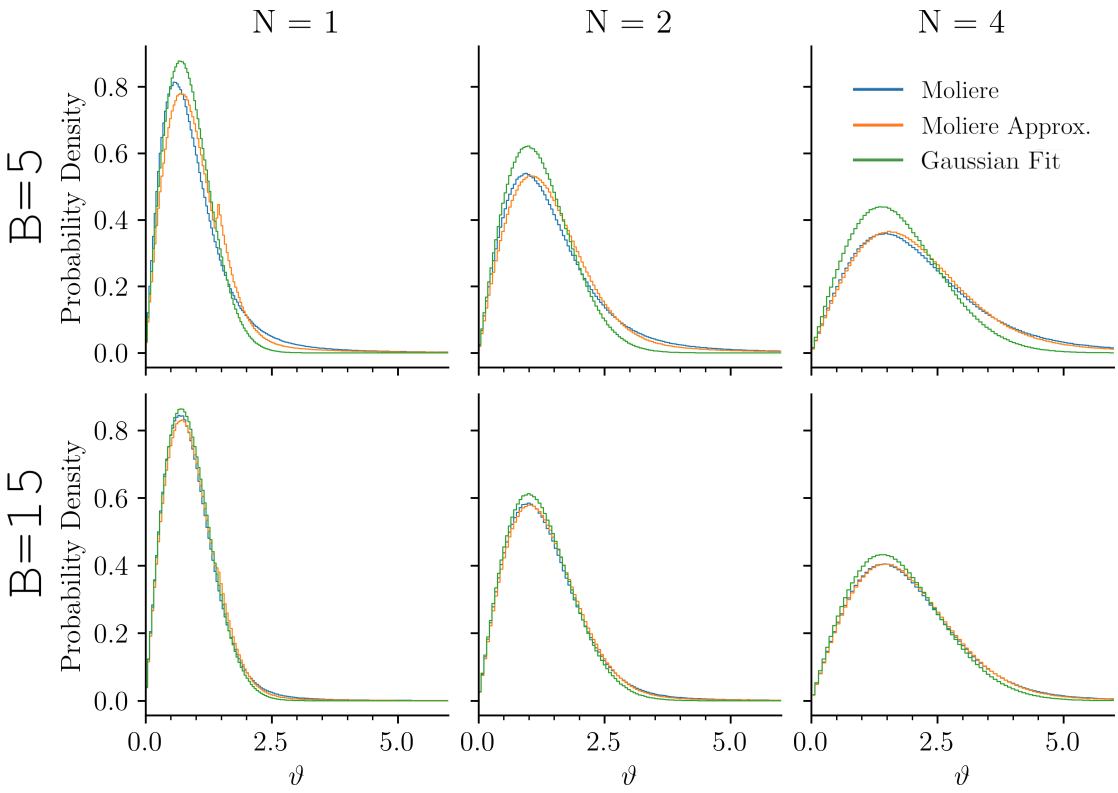

Figure 2.11: Angular distributions of a particle are shown when using Molière's distribution (Equation 2.32), the approximation employed in MonteRay (Equation 2.39) or a Gaussian fit to Molière's distribution. In the top row, the distribution is shown for $B = 5$, while in the bottom row $B = 15$ was used. The panels are labeled with the number of consecutive convolutions N, i.e. the angular distributions after N identical scattering events are shown.

highest energy at HIT, is shown for a water target. In addition to the total dose, the contributions of different nuclear fragments, grouped by their atomic number Z, are shown. As can be seen, the contribution of other particle species is significant, and dominates in the region behind the BP. This part is called the fragmentation tail. For heavier ions like carbon, a significant number of primary particles undergoes a nuclear interaction before they reach the BP. For 350 MeV/u carbon ions incident on water this number is $\approx 50\%$ [95].

2.4.2.1 Macroscopic Cross Sections

While a particle is traversing a material, there is a certain probability that it will undergo a nuclear interaction, either elastic or inelastic. Unlike electromagnetic interactions, nuclear interactions are rare events. As a consequence, they are not treated in the condensed history scheme but as individual events and their

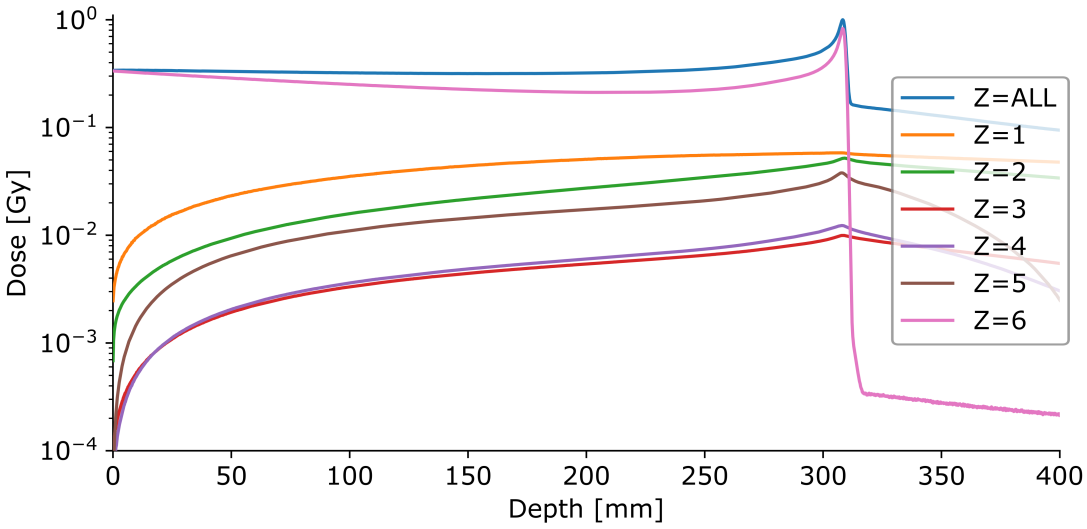

Figure 2.12: Contributions of different nuclear fragments to the depth dose distribution of a 430 MeV/u carbon ion beam incident on water are shown. The contributions are grouped by atomic numbers and the sum of all contributions is additionally shown in blue. The simulation was performed with MonteRay. Figure adapted from [39].

occurrence along the track is simulated via the inverse of the macroscopic cross section, the mean free path λ_{nuc} (see also section 2.3). Sampling of the distance to the next discrete event is done using an exponential distribution (Equation 2.5).

In reality, λ_{nuc} is not a constant but varies with the particle's energy and the material it is traversing. For example, if the particle crosses into a much denser material during its step, the probability of a nuclear interaction will have been underestimated when using the cross section at the beginning of the step. It is not trivial to avoid this in a MC engine since a look-ahead would be required to determine the materials the particle will encounter during its step. Instead, MonteRay defines a maximum allowed density variation of 5 % relative to the material at the beginning of the hinge step. If this threshold is crossed, the hinge step is aborted and the cross section is re-evaluated.

For all particles and compounds included in MonteRay, macroscopic cross sections for elastic and inelastic nuclear interactions were extracted from FLUKA. No cross sections for proton-proton inelastic nuclear interactions are tabulated since they are low and can be neglected [96, Table 11]. Elastic nuclear interactions of nuclei heavier than protons are only tabulated for cases where the target nucleus is a proton. This is inline with the approach taken by other fast MC engines for their treatment of carbon ions [36, 35]. For all particles that undergo nuclear

interactions, cross sections were tabulated with 500 bins in the energy range of 1 MeV/u to 500 MeV/u.

2.4.2.2 Elastic Nuclear Interactions

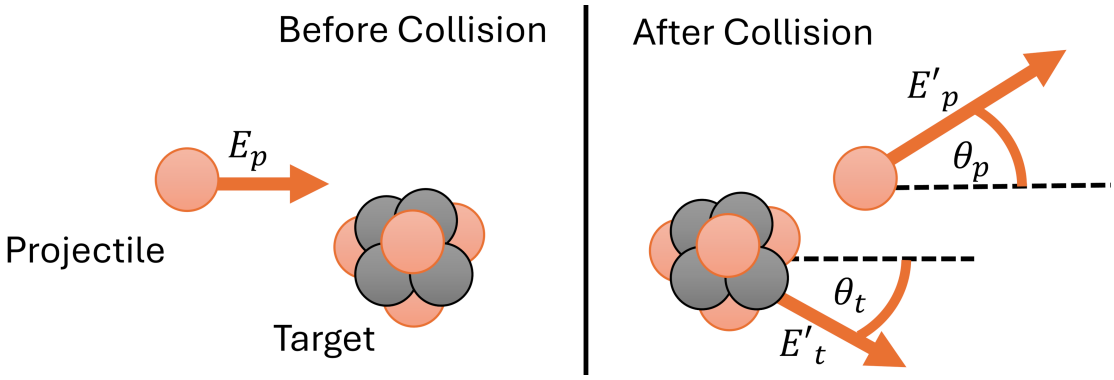

Figure 2.13: Schematic of the elastic nuclear interaction process.

In elastic nuclear interactions, the compositions of the projectile and target nucleus don't change. Merely their energies and directions are changed, similar to how two billiard balls would interact in a collision. A schematic of this process is shown in Figure 2.13. There, the projectile and target nucleus together with their respective directions of motion are shown. Before the collision, the target is at rest and the projectile has a certain kinetic energy E_p. After the collision, the projectile has kinetic energy E'_p and the target kinetic energy E'_t. Since the interaction is elastic, the total energy is conserved and we have $E_p = E'_p + E'_t$. Conservation of momentum further puts a restriction on the possible values of the deflection angles θ_p and θ_t, and the whole scattering process can be characterized through a single free variable. In this description, based on [97], this variable will be the square of the four-momentum transfer t_{com}. As a function of the center-of-mass (COM) scattering angle θ_{com}, the scattering angles in the laboratory frame can be computed via

$$\tan(\theta_p) = \frac{\sin(\theta_{\mathrm{com}})}{\mathrm{G}(\cos(\theta_{\mathrm{com}}) + \mathrm{f})} \tag{2.41}$$

$$\tan(\theta_t) = \frac{\tan(\pi - \theta_{\mathrm{com}})}{2\mathrm{G}} \tag{2.42}$$

with

$$\mathrm{G} = \frac{m_p\gamma + m_t}{\sqrt{m_p^2 + m_t^2 + 2m_p m_t \gamma}} \tag{2.43}$$

and

$$\mathrm{f} = \frac{m_p^2 + m_p m_t \gamma}{m_t^2 + m_p m_t \gamma}. \tag{2.44}$$

If $m_t > m_p$, one must be careful when evaluating Equation 2.41 as the divisor can become negative for high enough values of θ_{com}. Using the simple atan function leads to incorrect results, and one should use the atan2 function instead. This is not of concern for Equation 2.42 as the divisor is always positive. The COM scattering angle θ_{com} is given by

$$\theta_{\text{com}} = \arccos\left(1 - \frac{t_{\text{com}}}{2p_{\text{com}}^2}\right), \tag{2.45}$$

where p_{com} is the COM momentum, given by

$$p_{\text{com}}^2 = \frac{(s_{\text{com}} - (m_p - m_t)^2)(s_{\text{com}} - (m_p + m_t)^2)}{4s_{\text{com}}} \tag{2.46}$$

and s_{com} is the square of the COM energy, defined as

$$s_{\text{com}} = m_p^2 + m_t^2 + 2m_t(m_p + E_p). \tag{2.47}$$

The equations so far are general to relativistic elastic scattering and no assumptions about the nature of the scattering potential have been made. They enter the calculation through the yet undefined variable t_{com}, which is the square of the four-momentum transfer. No single value for t_{com} can be given as it is a random variable. Instead, we must sample it from a probability distribution, $P(t_{\text{com}})$. As pointed out by [25], this distribution is almost uniform for proton-proton collisions and consequently, MonteRay samples t_{com} from a uniform distribution with maximum value $4p_{\text{com}}^2$. For target nuclei other than protons, the distribution proposed by Ranft et al. [98] is used:

$$P(t_{\text{com}}) = A_t^{1.63}\exp(14.5A_t^{0.66}t_{\text{com}}) + 1.4A_t^{0.33}\exp(10t_{\text{com}}). \tag{2.48}$$

Here, A_t is the target's atomic weight. This has also been used by several fast MC engines for proton transport, like pGPUMCD [31], gPMC [29] or the work of Wan et al. [27]. Unlike Qin et al. [29], MonteRay does not use rejection sampling to sample t_{com} but instead uses the inverse transform sampling method. This is possible since the inverse cumulative distribution function of an exponential distribution, and consequently also the sum of two exponential functions, can be computed easily.

For the elastic scattering of ions other than protons with a proton, the same formalism is used after shifting the frame of reference such that the ion is at rest, and the proton can be considered to be the projectile. For this, the Lorentz

transformation

$$\Lambda = \begin{bmatrix} \gamma & -\gamma\beta_x & -\gamma\beta_y & -\gamma\beta_z \\ -\gamma\beta_x & 1+(\gamma-1)\frac{\beta_x^2}{\beta^2} & 1+(\gamma-1)\frac{\beta_x\beta_y}{\beta^2} & 1+(\gamma-1)\frac{\beta_x\beta_z}{\beta^2} \\ -\gamma\beta_y & 1+(\gamma-1)\frac{\beta_x\beta_y}{\beta^2} & 1+(\gamma-1)\frac{\beta_y^2}{\beta^2} & 1+(\gamma-1)\frac{\beta_y\beta_z}{\beta^2} \\ -\gamma\beta_z & 1+(\gamma-1)\frac{\beta_x\beta_z}{\beta^2} & 1+(\gamma-1)\frac{\beta_y\beta_z}{\beta^2} & 1+(\gamma-1)\frac{\beta_z^2}{\beta^2} \end{bmatrix}, \tag{2.49}$$

is used. After the scattering has taken place, the frame of reference is shifted back to the original one, and transport can continue.

2.4.2.3 Inelastic Nuclear Interactions

Unlike elastic nuclear interactions, inelastic nuclear interactions may cause the projectile and target nucleus to break up into fragments. This process is frequently described through the abrasion-ablation model, whose origin is usually, e.g. by [99], attributed to the work of Serber [100]. Serber pointed out, that the interaction between nuclei can be divided into two processes acting at different time scales. The first process, ablation, can be understood as the collision between the two nuclei themselves while the second process, working on longer time scales, describes the interaction of nucleons within the nuclei after the collision. This is visualized in Figure 2.14. As put by Gaimard and Schmidt [99], in the abrasion stage, the particles collide, which modifies their composition and possibly leaves them in an excited state. In the ablation stage, the resulting system thermalizes and deexcites, by emitting smaller fragments, like protons or light ions.

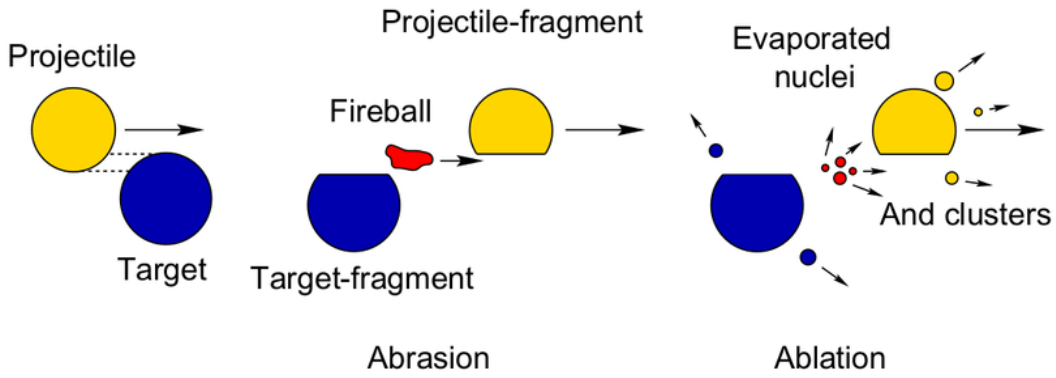

Figure 2.14: Abrasion-ablation model as described by Serber [100]. Figure taken from [101].

In MC engines, there must exist models to treat these nuclear interactions. For the developments in this thesis, the nuclear interaction model of FLUKA was

of particular interest due to previous work with FLUKA at HIT. For example, as described by Arico et al. [102], nuclear interactions of helium ions have recently been tuned to better match new data collected at HIT with the aim of improving dose predictions for helium ion beam therapy.

The nuclear models inside FLUKA are complex and cover a wide range of particles and energies. For protons, FLUKA uses the so-called PEANUT model [103]. For nucleus-nucleus interactions above 150 MeV per nucleon, a code [104] based on the Relativistic Quantum Molecular Dynamics Model (RQMD) model [105] is used, while below 100 MeV/n a model based on Boltzmann Master Equation (BME) theory is used [106]. Between 100 MeV per nucleon and 150 MeV per nucleon, a gradual transition from the BME to the RQMD model is made.

2.4.2.4 Nuclear Database Generation and Sampling

The nuclear interaction model of MonteRay is based on the nuclear interaction model contained within FLUKA. While different versions of this model have existed over the three publications, the final version used in the third publication [39], is the most complete and allows the simulation of proton, helium ion and carbon ion beams. The nuclear interaction databases were generated using a custom executable, called PREY, which was kindly provided by the FLUKA development team. With this executable, the sampling of nuclear interactions is possibly without invoking the full FLUKA executable, speeding up the process. The PREY executable was linked against the libraries of FLUKA version 2021.2 and this version was used to generate all the databases used in the final version of MonteRay.

The nuclear database files generated by PREY are stored in a FLUKA native, binary format that, for normal FLUKA runs, is used for the scoring of boundary crossing events with the so called USRBDX option [107]. As per the FLUKA manual [107], these files contain the double-differential current in units of $\mathrm{cm}^{-1}\mathrm{GeV}^{-1}\mathrm{sr}^{-1}$. One such file was generated for every possible ejectile, projectile and target combination; resulting in ≈ 60000 tables in total. The scoring of currents was done with 100 energy bins and 100 bins in solid angle, the latter ranging from 0 to 4π. During initial development of MonteRay for protons, a linear binning in solid angle was found to be adequate when comparing native FLUKA runs against FLUKA runs using the generated database for sampling. However, when extending the model to helium and carbon ions, this was found to be insufficient. As a result, MonteRay now uses a logarithmic binning in solid angle for all projectile types besides protons. The energy binning on the other hand, is linear for all particle types. For $i = 0, \ldots, 100$, the edges of the linear

bins in energy E_i, and solid angle Ω_i are defined as

$$E_i = \frac{E_{\max} i}{N_E} \tag{2.50}$$

$$\Omega_i^{\text{lin}} = \frac{4\pi i}{N_\Omega} \tag{2.51}$$

Per the convention used in FLUKA, the edges of the 100 logarithmic bins $\Omega_i^{\log}$ are given by

$$\Omega_0^{\log} = 0 \tag{2.52}$$

$$\Omega_1^{\log} = \frac{\pi}{10000} \tag{2.53}$$

$$\Omega_i^{\log} = g\Omega_{i-1} \tag{2.54}$$

with

$$g = \left(\frac{4\pi}{\Omega_1^{\log}}\right)^{1/99}. \tag{2.55}$$

Since the so tabulated probability distributions are not analytical functions, sampling of them at runtime is done by sampling a uniform random number $U \in [0, 1)$, and performing a binary search on the cumulative distribution. The so found 1D-Index $j = 0, \ldots, 9999$ is converted into an index tuple (i_E, i_Ω) that corresponds to an energy and angular bin.

2.5 Elements and Compounds

In order to evaluate the equations for energy loss, energy loss straggling, multiple coulomb scattering and nuclear interactions, the target material must be defined. When transporting particles in a voxelized patient geometry based on 3D CT images, no exact information on the material of a given voxel is available. Instead, each voxel is assigned a single value, the Hounsfield Unit (HU). It is a measure for the attenuation of X-rays, and defined as

$$\text{HU} = 1000 \times \frac{\mu - \mu_{\text{water}}}{\mu_{\text{water}}}, \tag{2.56}$$

where μ is the linear attenuation coefficient of the material in question and μ_{water} is the linear attenuation coefficient of water [8]. Therefore, the information encoded in a CT is only a measure for the attenuation of X-rays, and does not directly provide the necessary quantities for the evaluation of the equations introduced in subsection 2.4.1 or subsection 2.4.2. Consequently, a mapping from HUs to the voxel's elemental composition, density and SPR is needed. The list of elements

included in MonteRay for which inelastic nuclear databases have been simulated, is given in Table 2.1, and matches the one used by Schneider et al., in their work on the relation of HUs to elemental compositions [108]. These elements make up over 99.9 % of the human body by mass [109], and titanium is included for the possibility of modelling titanium implants. By mixing these elements, so-called compounds are defined. For example, the compound "Water" is defined as a mixture of 11% hydrogen and 89% oxygen. A visualization of the elemental composition of all compounds included in Monteray is given in the bottom panel of Figure 2.15. For a limited number of compounds, most notably water, PMMA (Polymethyl methacrylate) and air, not only the elemental composition is stored but also the density and SPR. In terms of their elemental composition, all other compounds are either defined according to [108, Table 4], or using the extension of Parodi et al. [110, 71]. In total 35 compounds mapping the HU value range from -995 to 3070 are defined. For the compounds corresponding to certain HU values, densities and SPR values are computed on a per-voxel basis before the simulation begins. For the density, the approach described in [108] is used, and again the extensions of Parodi et al. [110, 71] are included. SPR values are computed using a lookup table which is specific to the CT-scanner [111]. In the top panel of Figure 2.15, the function mapping HU to density, and an example of a function mapping HU to SPR are shown.

Element	Atomic Mass (u)	Atomic Number
Oxygen	15.999	8
Carbon	12.011	6
Nitrogen	14.007	7
Argon	39.948	18
Titanium	47.867	22
Sodium	22.99	11
Phosphorus	30.97376	15
Sulfur	32.066	16
Chlorine	35.453	17
Potassium	39.0983	19
Calcium	40.078	20
Magnesium	24.305	12
Hydrogen	1.008	1

Table 2.1: The names, atomic masses and atomic numbers of all elements currently supported in MonteRay are shown.

2.6 Beam Shaping Devices

Even in actively scanned radiotherapy, passive beam shaping devices are used. At HIT, this includes an optional range shifter and a ripple filter that is always used in helium and carbon ion irradiation, but not for protons. The range shifter is a uniform slab of PMMA with a thickness of 19.7 mm, located between the patient and the nozzle. Its effect on the beam are to broaden it slightly and to reduce its energy. This reduction in energy is uniform across the beam and causes a backwards shift of the BP. This is helpful in the treatment of shallow seated tumors, since the minimum range at HIT without the range shifter is 2 cm [112].

The ripple filter serves to filter away ripples in the dose distribution caused by the small width of the BP's of helium and carbon ions, paired with a low number of energy layers [113]. This principle is shown in Figure 2.16 where dose distributions for two identical plans are shown, once with a ripple filter (dotted line) and once without a ripple filter (solid line). The ripple filter allows for a much more homogeneous dose distribution, without increasing the number of energy layers, thereby reducing irradiation time. Unlike the ranger shifter, its thickness is not constant. In the case of the HIT, this structure is periodic and

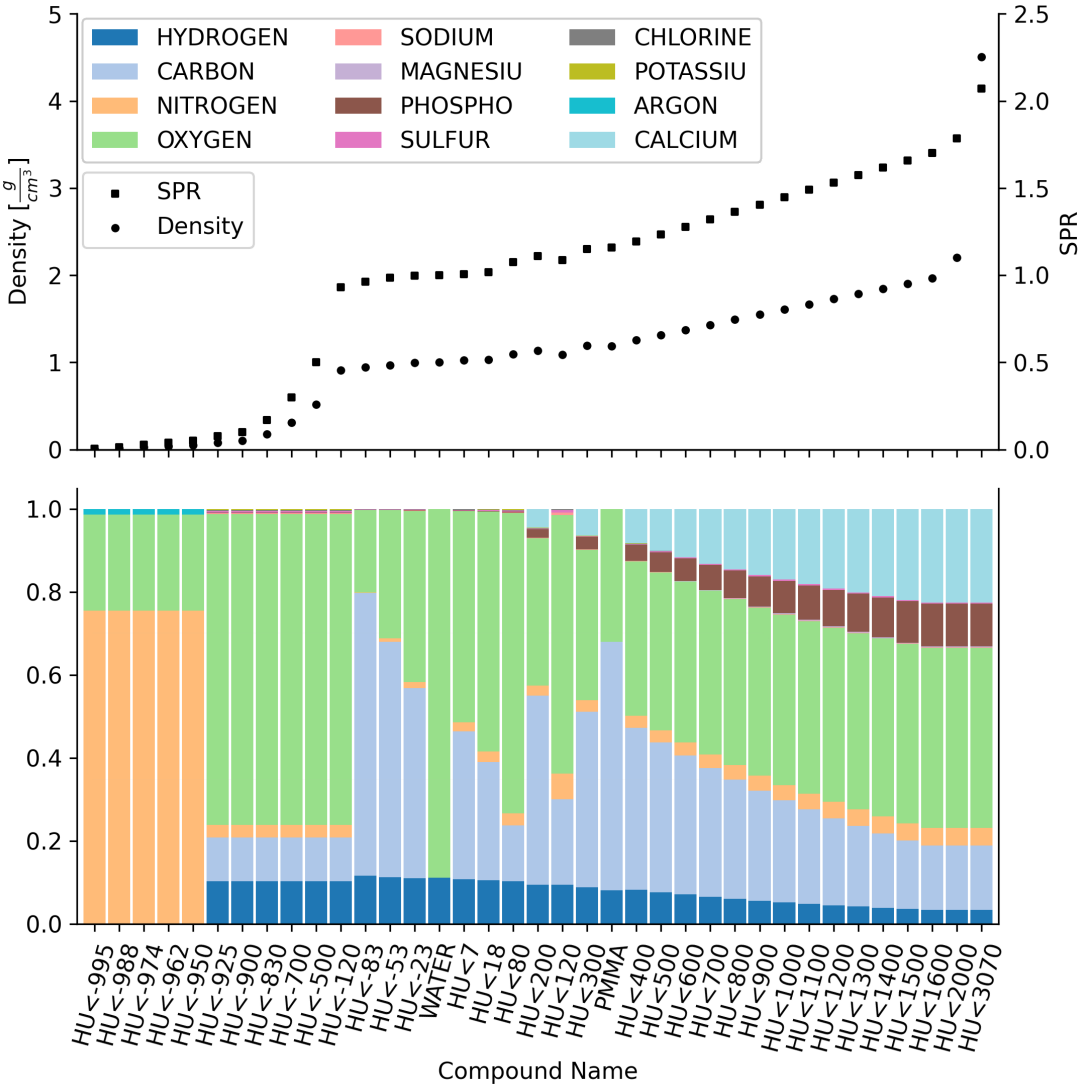

Figure 2.15: In the top panel, the conversion of HUs to density and SPR values is shown. In the bottom panel, the elemental compositions of compounds defined in MonteRay are shown. For density, the approach by Schneider et al. [108] is used with the extensions proposed by Parodi et al. [110, 71]. The SPR conversion is done with a CT-scanner specific lookup table [111]. The definition of compounds and their relation to HUs is done according to [108, 110, 71].

only two-dimensional, simplifying the treatment of it.

Ripple filter and range shifters are also used at other facilities [114, 115], and consequently it is a necessity for a MC engine to be able to incorporate them. For this, MonteRay uses an approach based on ray tracing through geometrical representations of these elements. During the simulation of particles, as pointed out in subsection 2.4.1, one of the limits on the particle's step size is the distance

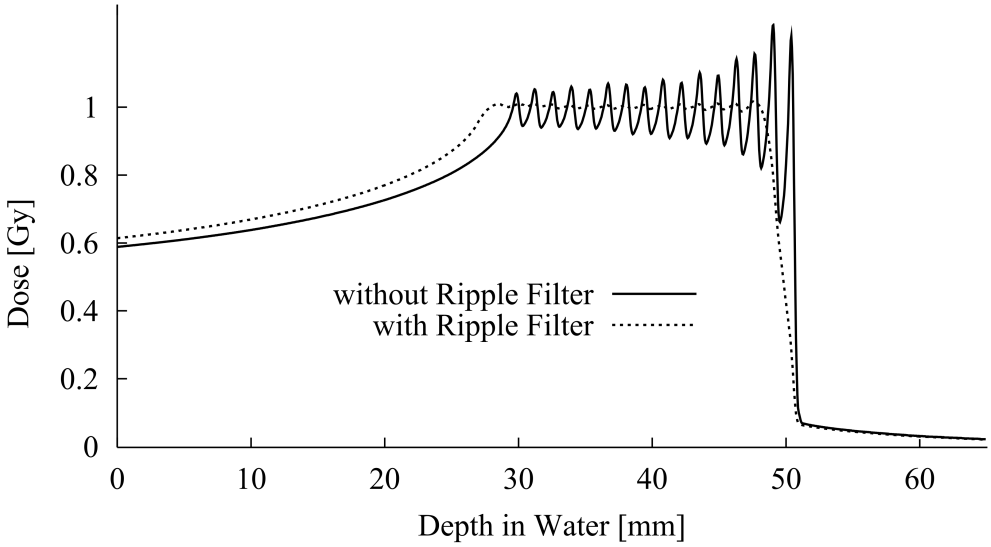

Figure 2.16: The effect of a ripple filter on an SOBP is shown. Without the ripple filter (solid line), the dose distribution features prominent ripples due to an insufficient number of energy layers. With the ripple filter (dotted line), a much more homogeneous dose distribution is achieved with the same energy layer spacing. Figure adapted from [113].

to a region interface. This means, that one has to define functions that determine the distance of the particle, taking into account its direction, to the ripple filter and the range shifter. In the case of the range shifter, this is simply a ray-box intersection as, for example, described in [116]. For the ripple filter, MonteRay makes use of its periodic, quasi two-dimensional shape, displayed in Figure 2.17. With this, finding the distance to any of the ripple filter's sides, becomes equivalent to finding the intersection of a ray with a polygon in two dimensions. Since this is also required for the generation of masks from RT structure sets described in section 2.7, the algorithm used shall be briefly described here.

Let $\vec{p} = (p_x, p_z)$ be the particle's position, and $\vec{d} = (d_x, d_z)$ its direction, with $||\vec{d}|| = 1$. Now let the ripple filter be described by a set of N vertices $\vec{v}_i = (v_{i,x}, v_{i,z})$ with $i = 1, \ldots, N$. Due to the periodicity of the ripple filter along the x-direction, the algorithm begins by mapping the coordinate p_x into the interval $[x_{\min}, x_{\max}]$ where $x_{\min}$ and $x_{\max}$ are the minimum and maximum x-coordinates of a single ripple of the filter.

$$p'_x = x_{\min} + \phi(p_x - x_{\min}) \tag{2.57}$$

Where ϕ is a modulo function that only returns positive values. Now, let the i-th edge number be defined through the vertices (x_i, z_i) and (x_{i+1}, z_{i+1}). Whether the

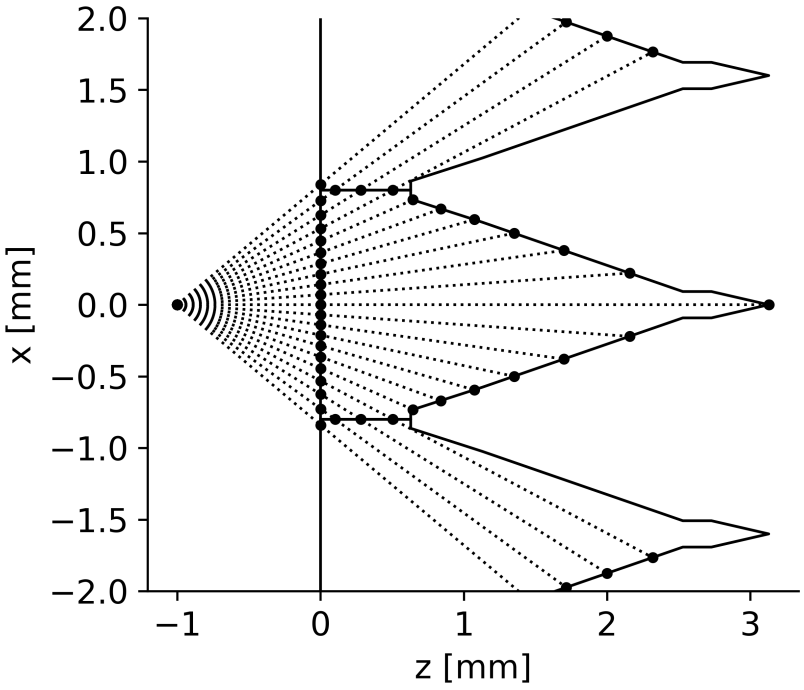

Figure 2.17: Schematic view of the ripple filter's profile. The ripple filter is periodic along the x-direction and has a polygonal base that extends into the image plane. Besides the ripple filter (solid lines), the trajectories of several rays originating behind it, traveling at different angles, are shown (dotted lines). Their intersections with the ripple filter are marked with dots.

particle intersects with this edge can be determined by computing t_i and s_i, with

$$t_i = \frac{(z_1 - p_z)(x_2 - x_1) - (x_1 - p_x)(z_2 - z_1)}{c_p} \tag{2.58}$$

$$s_i = \frac{(z_1 - p_z)d_x - (x_1 - p_x)d_z}{c_p} \tag{2.59}$$

with

$$c_p = (x_2 - x_1)d_z - (z_2 - z_1)d_x. \tag{2.60}$$

In essence, this is an adaptation of the 3D line intersection algorithm presented in [117]. If $t_i > 0$, i.e. the intersection is in front of the particle, and $0 \leq s_i \leq 1$, i.e. the intersection lies within the two vertices defining the edge, the particle intersects with the edge. Finally, the closest intersection of the particle with the ripple filter is given by the minimum of all t_i for which these conditions are fulfilled. In Figure 2.17, the trajectories of 10 exemplary particles through the ripple filter are shown, with intersection marked through dots.

2.7 Mask Generation

For treatment planning, structures inside the patient like the tumor or organs at risk must be delineated. This data is stored in the form of contours that can be thought of as two-dimensional polygons. For dose calculation, RT structures have relevance since they may encode material overwrites, i.e. the dose calculation engine may have to overwrite certain CT voxels with a given material. For example, this could be the treatment table on which the patient is positioned, or in the case of plan verification on a water tank, the whole verification geometry may be defined in this way. In addition, RT structure sets are essential for dose optimization purposes, where per-region optimization goals may be specified. For these purposes, one must correctly decide whether the voxel of a CT lies inside a structure set or not. This process is called mask generation and the exact algorithm used can have a significant impact on the computed dose. Besides creating binary masks, the algorithm should also be able to create decimal masks, based on the fraction of a voxel covered by the structure set. This may be important since structure sets are not necessarily aligned with the CT grid.

The algorithm for structure sets to masks implemented inside MontRay is based on the scanline approach, and can be thought of a combination of the rasterization algorithm of Amanatides & Woo [60], and the polygon intersection algorithm presented in section 2.6. For this, a set of parallel rays is generated and their intersections with the structure set polygon are computed. In section 2.6, an algorithm for finding the intersection of a generalized ray with a polygon has already been described. For the purpose of mask generation, we may assume that rays are parallel to the x-axis, simplifying the algorithm. For each of N rays per voxel, we compute all intersection points with the polygon. The intersection points are sorted by their x-coordinate and the resulting list of points is interpreted as a list of point-pairs, where each pair marks the start and end of a section of the ray inside the polygon. For each pair, start and end voxels are computed. All voxels between these two voxels are then marked as being inside the polygon, and the edge voxels are assigned a value that is equal to the fraction of the voxel inside the polygon.

An example of the mask generation process is shown in Figure 2.18. There, a mask is created from a randomly generated polygon. In the left panel, the polygon and resulting mask are shown. In the right panel, a zoomed-in view is shown with the scanlines overlaid.

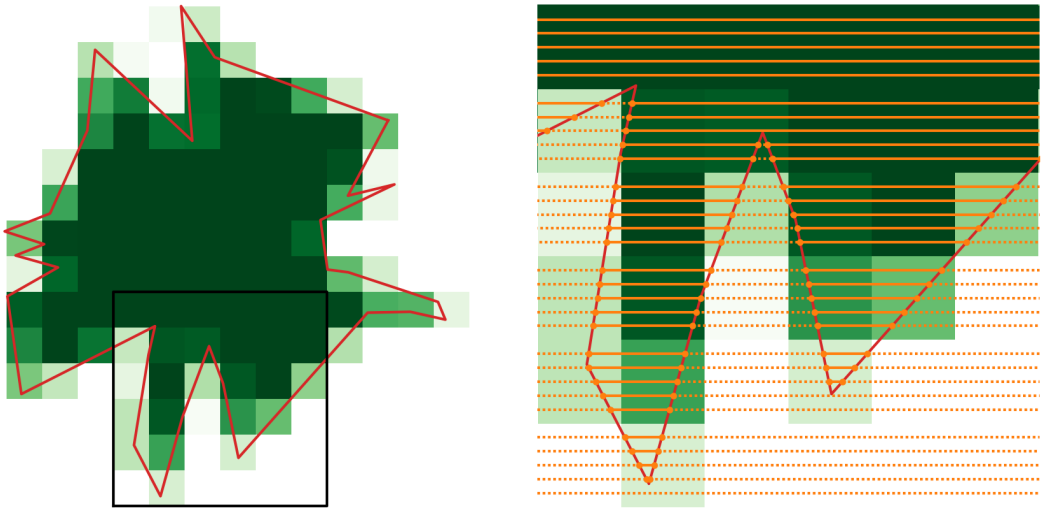

Figure 2.18: The mask-generation algorithm used in MonteRay is visualized for a random Polygon. In the left panel, the polygon is shown in red and the generated mask in various shades of green. The darker the shade, the more of a voxel is inside the mask. A black rectangle in the left panel indicates the region shown in the zoomed-in view in the right panel. Beside the polygon and the mask, the scanlines used for the mask generation are shown in orange. Solid scanlines indicate sections where the algorithm determined them to be inside the polygon, while dotted scanline indicate sections of the scanline outside the polygon.

2.8 Third-Party Dependencies

For the development and testing of MonteRay, several third-party libraries have been used. Additionally, several libraries are required to run MonteRay. A brief overview of these will be given in this section.

GoogleTest

GoogleTest [118] is an open-source unit testing framework for C++ applications. It can be used to test individual pieces of code, so-called "units", for correctness. It provides an easy-to-use interface for writing and executing tests, making it straight forward to ensure that all parts of the code function correctly, at least when tested in isolation. An example of such a test can be seen in Figure 2.19, where the correctness of a polygon's area calculation is tested for a simple triangular shape. This allows developers to quickly verify that the code is working as intended, guarding against errors during installation (e.g. missing files) and changes to the code base with unforeseen consequences.

```
TEST(TestPolygon, TestAreaCalc2){
    const std::vector<float> contour_data_triangle{
        -2., -0.5, 0,
        2., 6, 0,
        -6., 23., 0,
        -2, -0.5, 0
    };
    const Polygon<double> poly_triangle(contour_data_triangle);
    ASSERT_FLOAT_EQ(poly_triangle.ComputeAreaShoelace(), 60);
}
```

Figure 2.19: Example test contained inside MonteRay. It asserts that the function "ComputeAreaShoelace", which is a member of the "Polygon" class, correctly computes the area of a polygon by comparing it to the value obtained by hand.

Boost

The Boost libraries [119] provide a wide range of support libraries for C++ development. In MonteRay, only the Boost "filesystem" and "program options" libraries are used. The filesystem library is used for convenience and for backwards compatibility with GCC 7.5.0. The program options library is used to provide a command line and configuration file interface to the user. Using this, the user can provide a variety of options to the program, e.g. the number of particles, the beam particle type, the geometry to be used, the scorer to be used, etc. An example of such a configuration file is shown in Figure 2.20.

```
num_particles = 100000
Beamtype = 0
particle_type = 2
energy = 430
num_threads = 8
output_dir = /tmp/exampledir
seed = 080816
scorer = -0.1 -0.1 0. 0.1 0.1 0.5 1 1 500
water_region

rectangle = -0.1 -0.1 -0.5 0.1 0.1 0.5 sbb
zplane = 0.0 divider
region = 0 !sbb BLACKBOX BB
region = 1 +sbb + divider AIR air_region
region = 2 +sbb + !divider WATER water_region
```

Figure 2.20: Example configuration file for MonteRay.

Insight Toolkit

The Insight Toolkit [120] is an open-source library for image analysis. In MonteRay, it is used to read CT image series and to convert them to 3D arrays. Additionally, it is used to interpolate the CT image to the scoring grid's resolution.

DICOM Toolkit

The DICOM Toolkit [121] is an open-source library for the handling of DICOM files. It allows MonteRay to directly read DICOM files, the file format a clinical TPS uses, without the need for prior conversion to a MonteRay specific format. This includes the reading and parsing of RTDose, RTStructureSet and RTPlan files, and the writing of RTDose files after dose calculation.

SQLite3

A database is used to manage the data required for running MonteRay, for example particle data, material data, nuclear interaction cross section or beamline information. Since the data is not accessed by more than one process at a time, a simple SQLite3 [122] database, stored in a single file, is used. This allows for easy access to the data and the use of SQL queries to retrieve the desired information.

Chapter 3

List of Publications

Per the regulations of the Department of Physics and Astronomy of Heidelberg University, this thesis is presented as a cumulative thesis. In the following, three publications which were published in international peer reviewed journals will be presented. Besides the publications themselves, a detailed description of the author's contribution to each of the publication is included. The author of this thesis is the sole first author of all three publications and contributed significantly to each. None of the publications have been used in another cumulative thesis before.

3.1 Development and Benchmarking of a Monte Carlo Dose Engine for Proton Radiation Therapy

Authors: **Peter Lysakovski**, Alfredo Ferrari, Thomas Tessonnier, Judith Besuglow, Benedikt Kopp, Stewart Mein, Thomas Haberer, Jürgen Debus, Andrea Mairani

Publication status: Published (03 November 2021)

Journal reference: Frontiers in Physics

DOI: https://doi.org/10.3389/fphy.2021.741453

Authors' contributions: **PL** is the first author of this publication. **PL**, AM and AF were responsible for the conceptual design of the Monte Carlo engine. **PL**, BK, and AM developed the source code of the Monte Carlo engine. **PL**, TT, and AM worked on the analysis of data and **PL** created all Figures. AM generated the material database, including elastic and inelastic nuclear cross sections. AF provided the code for the generation of inelastic nuclear databases from FLUKA. JB generated the inelastic nuclear databases. TT, AM, and SM collected and provided experimental data used in this work. TT computed and provided the patient plan and SOBP plans. JD and TH provided clinical direction during project development, manuscript writing and project administration and funding acquisition.

frontiers in Physics

ORIGINAL RESEARCH
published: 03 November 2021
doi: 10.3389/fphy.2021.741453

Development and Benchmarking of a Monte Carlo Dose Engine for Proton Radiation Therapy

Peter Lysakovski[1,2], *Alfredo Ferrari*[1], *Thomas Tessonnier*[1], *Judith Besuglow*[1,2,3,4,5], *Benedikt Kopp*[1], *Stewart Mein*[1,3,4,5], *Thomas Haberer*[1], *Jürgen Debus*[1,5,6] *and Andrea Mairani*[1,7,3,8]*

[1]*Department of Radiation Oncology, Heidelberg Ion Beam Therapy Center (HIT), Heidelberg University Hospital, Heidelberg, Germany,* [2]*Faculty of Physics and Astronomy, Heidelberg University, Heidelberg, Germany,* [3]*Clinical Cooperation Unit Translational Radiation Oncology, German Cancer Consortium (DKTK) Core-Center Heidelberg, National Center for Tumor Diseases (NCT), Heidelberg University Hospital (UKHD) and German Cancer Research Center (DKFZ), Heidelberg, Germany,* [4]*Division of Molecular and Translational Radiation Oncology, Heidelberg Faculty of Medicine (MFHD) and Heidelberg University Hospital (UKHD), Heidelberg, Germany,* [5]*Heidelberg Faculty of Medicine (MFHD) and German Cancer Research Center (DKFZ), Heidelberg Institute of Radiation Oncology (HIRO), National Center for Radiation Oncology (NCRO), Heidelberg University Hospital (UKHD), Heidelberg, Germany,* [6]*Clinical Cooperation Unit Radiation Oncology, German Cancer Consortium (DKTK) Core-Center Heidelberg, National Center for Tumor Diseases (NCT), Heidelberg University Hospital (UKHD) and German Cancer Research Center (DKFZ), Heidelberg, Germany,* [7]*Medical Physics, National Centre of Oncological Hadrontherapy (CNAO), Pavia, Italy,* [8]*Medical Faculty, Heidelberg University, Heidelberg, Germany*

OPEN ACCESS

Edited by:
Miguel Antonio Cortés-Giraldo, Sevilla University, Spain

Reviewed by:
Adam Aitkenhead, The Christie National Health Service Foundation Trust, United Kingdom
Matteo Duranti, Istituto Nazionale di Fisica Nucleare di Perugia, Italy

***Correspondence:**
Andrea Mairani
Andrea.Mairani@med.uni-heidelberg.de

Specialty section:
This article was submitted to Radiation Detectors and Imaging, a section of the journal Frontiers in Physics

Received: *14 July 2021*
Accepted: *15 October 2021*
Published: *03 November 2021*

Citation:
Lysakovski P, Ferrari A, Tessonnier T, Besuglow J, Kopp B, Mein S, Haberer T, Debus J and Mairani A (2021) Development and Benchmarking of a Monte Carlo Dose Engine for Proton Radiation Therapy. Front. Phys. 9:741453. doi: 10.3389/fphy.2021.741453

Dose calculation algorithms based on Monte Carlo (MC) simulations play a crucial role in radiotherapy. Here, the development and benchmarking of a novel MC dose engine, MonteRay, is presented for proton therapy aiming to support clinical activity at the Heidelberg Ion Beam Therapy center (HIT) and the development of MRI (magnetic resonance imaging)-guided particle therapy. Comparisons against dosimetric data and gold standard MC FLUKA calculations at different levels of complexity, ranging from single pencil beams in water to patient plans, showed high levels of agreement, validating the physical approach implemented in the dose engine. Additionally, MonteRay has been found to match satisfactorily to FLUKA dose predictions in magnetic fields both in homogeneous and heterogeneous scenarios advocating its use for future MRI-guided proton therapy applications. Benchmarked on 150 MeV protons transported on a $2 \times 2 \times 2\,mm^3$ grid, MonteRay achieved a high computational throughput and was able to simulate the histories of more than 30,000 primary protons per second on a single CPU core.

Keywords: Monte Carlo (MC), dose calculation, radiotherapy, magnetic field, proton

INTRODUCTION

Image guided radiotherapy is at the forefront of innovative treatment delivery techniques. It has the potential to improve treatment efficacy via on-board imaging procedures such as adaptive planning and/or live monitoring, for instance via magnetic resonance (MR)-guided radiation therapy (MRgRT) [1, 2]. Over the last decade, clinical prototypes have combined low-field-strength MR and radioactive cobalt-60 sources for photon treatment, followed by linear accelerators and higher field-strength MR fields for improved image resolution [3–5].

Particle therapy (PT), a cancer treatment modality achieving superior dose conformity to solid tumours compared to conventional photon techniques [6, 7], would greatly benefit from on-board MR-guided treatment delivery [8]. For instance, at the Heidelberg Ion Beam Therapy Center (HIT) over 5,000 patients have been treated with proton and carbon ions since 2009 [9]. While ^{16}O ions have so far only been used for research purposes, HIT has treated the first patient with raster scanning ^{4}He ion beams in July 2021.

For all clinically administered ion beams, on-board MR-guided treatment delivery is currently not feasible. However, system developments for treatment planning and delivery of MR-guided particle therapy are underway at HIT. Here, we begin with considerations in dose calculation for MR-guided particle therapy. During MRgRT using photons, for example, the MR field (due to Lorentz forces) can impact the dose deposition of ionized electrons/delta-rays, with severity depending on patient anatomy and MR field strength [10, 11]. Hence, dose calculation corrections are introduced in clinical practice for improving accuracy [12]. Similarly, trajectories of fast charged particles like protons are altered by the MR field [13–15] and consequently, proper consideration must be given for accurate dose calculation.

With the aim of providing dose computations at various levels of accuracy and speed for current and future treatment in particle therapy with light and heavy ions, various systems have been introduced at HIT to support clinical deployment of PT. Initially, as a gold standard, a MC environment based on the MC code FLUKA [16, 17] has been developed and extensively benchmarked [18] for allowing database generation for clinical analytical treatment planning system (TPS) and patient recalculations. This framework required long computation times (hours to days depending on the number of CPUs available) which limited its usage in the analysis of large patient cohorts and for any adaptive/on-line planning.

In order to overcome these limitations, FRoG (Fast dose* Recalculation on GPU) has been introduced, an advanced analytical code capable of calculating dose, LET_d (dose-weighted Linear Energy Transfer) and biological dose for the four particle beams available at HIT [19–21] and which is in use at other PT facilities in Europe (Centro Nazionale di Adroterapia Oncologica [21], Danish Centre for Particle Therapy [22]. High levels of agreement within 1–2% [19, 21, 23] were found comparing FLUKA and FRoG recalculated dose-volume-histograms (DVH) of proton and other light ion patient plans even for complex cases such as lung irradiation [23]. However, analytical codes are usually designed for a specific task, making the introduction of new features such as MR-guidance [14, 24], positron emission tomography [25, 26] and prompt gammas [27] require large development effort and substantial changes in the physics engine. Fast MC engines have been introduced for proton beams [28–33] and helped streamline the development while reaching various levels of agreement when compared against gold standard MC codes such as FLUKA and TOPAS/Geant [34].

Several recent works have investigated the impact of MR-guidance on particle beam physics and modelling distortion due to the Lorentz force [13, 35–38]. Despite these characterizations however, no fast MC engine has been presented in literature which is able to perform clinically relevant particle therapy calculations in magnetic fields. In this work, a CPU-based fast MC dose engine for proton beams (MonteRay) was developed and benchmarked for supporting ongoing clinical activity and introducing novel treatment modalities, particularly within the MRI-guided particle therapy program at HIT.

MATERIALS AND METHODS

Programming Languages and Libraries

With performance and extensibility to GPUs in mind, the MonteRay MC engine was written in C++. Several external libraries were used either during development or execution of the MC code. The frameworks GoogleTest [39] and Benchmark [40] are used for testing and microbenchmarking the source code. The Boost library [41] is used for filesystem operations and parsing of configuration files. RapidXml [42] is used for reading of irradiation plans in XML format. ITK [43] and DCMTK [44] are used for reading CT images. FLUKA simulations were performed using FLUKA version 2020 0.6.

Geometry and Materials

Voxelized water phantom and patient geometries are implemented from computed tomography (CT) scans using the approach described in [45, 46], i.e. the Hounsfield Unit (HU) of each voxel is converted to a water equivalent path length, density and elemental composition. In total, 36 different materials, covering an HU range between -1000 HU and 3070 HU are used. HU values larger than 3070 are assumed to be metallic implants made from titanium. Each material is modeled as a combination of up to ten elements. Additionally, five extra materials (water, RW3, PMMA, air and carbon fiber) can be defined by the user for dosimetric studies. For the calculation of nuclear interactions, only the most abundant isotope of each element is considered: ^{1}H, ^{12}C, ^{14}N, ^{16}O, ^{23}Na, ^{24}Mg, ^{31}P, ^{32}S, ^{35}Cl,^{40}Ar, ^{39}K, ^{40}Ca and ^{48}Ti. However, just H, C, O and Ca already constitute more than 90% of a human's weight [47]. Including more materials in MonteRay is trivial if they consist only of the ten base elements already defined. Adding additional elements requires the generation of additional inelastic nuclear interaction databases (***Inelastic Nuclear Interactions***).

Handling the HIT-specific Beamline

The HIT beamline consists of various layers of different materials, including tungsten [48], with which the particle beam interacts before reaching the patient, resulting in a unique phase-space of particles. To avoid modelling and simulating the whole beamline in MonteRay, the approach described in [49] was used, i.e., sampling from a phase-space for each of the 255 quasi-monoenergetic proton beams available at the HIT facility. Each file contains the location, direction and energy of 10 million particles sampled on a plane perpendicular to the beam's direction before the patient's entrance. The phase space was generated using FLUKA and besides primary protons, secondary protons generated due to the primary particle's

interactions with the beamline are also considered. For now, however, all other secondary particles (deuterons, tritons, ^{3}He, ^{4}He and neutrons) are neglected. During simulation, our MC code randomly samples individual particles from these phase space files.

Transport

For the simulation of proton beams, MonteRay performs the transport of protons, deuterons, tritons, 3-Helium and 4-Helium. Of these particles, only protons undergo elastic and ***Inelastic Nuclear Interactions*** as described in ***Nuclear Interactions***. All transported particles experience energy loss and scattering through electromagnetic interactions as described in ***Electromagnetic Interactions***.

Energy is deposited either on a Cartesian or a cylindrical grid. Energy depositions from heavy nuclear recoils are recorded locally while energy lost through electromagnetic interactions are deposited along a track via the method described in [50]: given the particle's location at the beginning of the transport step $\overrightarrow{x_i}$ and its position at the end of the transport step $\overrightarrow{x_f}$, the point of energy deposition is chosen randomly *via*

$$\overrightarrow{x_{dep}} = \overrightarrow{x_i} \cdot (1 - \boldsymbol{U}) + \overrightarrow{x_f} \cdot \boldsymbol{U}, \tag{1}$$

where $\boldsymbol{U}$ is a random number uniformly distributed on the interval $[0, 1)$. This is an efficient method of avoiding aliasing effects due to floating-point inaccuracies at grid boundaries and mismatches between the CT and the scoring grid. To avoid discontinuities in the deposited dose, the particles are transported on a grid with spacing equal to or less than the requested scoring grids spacing. If a CT is loaded, this will be the CT grid. All simulations shown here, unless otherwise noted, were performed on a $1 \times 1 \times 1\,\mathrm{mm}^3$ Cartesian grid. At the beginning of each step, the distance to the next voxel's boundary $\boldsymbol{dx_{vox}}$ is calculated and the distance to the next nuclear interaction $\boldsymbol{dx_{nuc}}$ is sampled based on the total nuclear cross section introduced in ***Nuclear Interactions***. The smaller of these two values is chosen as the current iteration's step length $\boldsymbol{dx}$, i.e.

$$\boldsymbol{dx} = \boldsymbol{min}(\boldsymbol{dx_{vox}}, \boldsymbol{dx_{nuc}}). \tag{2}$$

The energy loss over the distance $\boldsymbol{dx}$ is calculated and the scattering angle is sampled after the approaches described in ***Electromagnetic Interactions***. In the presence of a magnetic field $\vec{\boldsymbol{B}}$, an additional deflection $\overrightarrow{\boldsymbol{\Delta u_m}}$ due to the Lorentz force is calculated after [51] using

$$\overrightarrow{\boldsymbol{\Delta u_m}} = \frac{\left(\vec{\boldsymbol{u}} \times \vec{\boldsymbol{B}}\right) \cdot \boldsymbol{z} \cdot \boldsymbol{c} \cdot \boldsymbol{dx}}{\boldsymbol{m} \cdot \boldsymbol{\gamma} \cdot \boldsymbol{\beta}}, \tag{3}$$

where $\boldsymbol{m}$ is the particle's rest mass, z is the particle's charge in units of the elementary charge, $\boldsymbol{\beta}$ is its velocity relative to the speed of light $\boldsymbol{c}$, $\vec{\boldsymbol{u}}$ is its normalized direction and $\boldsymbol{\gamma}$ is the Lorentz factor.

After updating the particle's position, energy and direction, if a nuclear interaction occurred, the type of nuclear interaction is determined, and the nuclear interaction performed as will be described in ***Nuclear Interactions***. The transport step is repeated until the particle's energy falls below a threshold of 1 MeV. The remaining energy is deposited in a single step. During transport, only protons undergo nuclear interactions. For all other particles, only electromagnetic energy losses are considered.

Angular deflections due to nuclear or electromagnetic interactions, expressed through a polar angle $\boldsymbol{\theta}$ and an azimuthal angle $\boldsymbol{\phi}$, are applied to the particle's initial direction $\vec{\boldsymbol{u}}$ to obtain the particle's final direction $\overrightarrow{\boldsymbol{u'}}$ *via*:

$$\overrightarrow{\boldsymbol{u'}} = \vec{\boldsymbol{v}} \cdot \boldsymbol{sin}(\boldsymbol{\theta}) \cdot \boldsymbol{cos}(\phi) + \vec{\boldsymbol{w}} \cdot \boldsymbol{sin}(\boldsymbol{\theta}) \cdot \boldsymbol{sin}(\phi) + \vec{\boldsymbol{u}} \cdot \boldsymbol{cos}(\boldsymbol{\theta}) \tag{4}$$

where the vectors $\vec{\boldsymbol{v}}$ and $\vec{\boldsymbol{w}}$ are chosen such that together with $\vec{\boldsymbol{u}}$, they form an orthonormal basis. Since all physical interactions considered in the simulation are independent of $\boldsymbol{\phi}$, any orthonormal basis can be used for this purpose. To find $\vec{\boldsymbol{v}}$, a run-time efficient algorithm described in [52] is used. The last constituent of the orthonormal basis is then computed using the cross product $\vec{\boldsymbol{w}} = \vec{\boldsymbol{u}} \times \vec{\boldsymbol{v}}$.

Electromagnetic Interactions

Interactions with electrons cause charged particles to continuously lose energy while travelling through matter. The mean energy loss per unit distance due to this process is called the stopping power $\boldsymbol{S}$, which is a function of energy and dependent on the projectile's mass and charge [53, 54]. FLUKA was used to tabulate the energy loss of the transported particles in water from 0.1 MeV/ u to 1,000 MeV/ u with 2000 linearly spaced intervals. To obtain the stopping power in materials other than water, the stopping power table for water was multiplied by a factor dependent on the materials HU value [45]. Since the step size $\boldsymbol{dx}$ is fixed at the beginning of each transport step, the mean energy loss $\overline{\boldsymbol{dE}}$ that the particle experiences during the step must be calculated. This problem is equivalent to solving the following equation:

$$\boldsymbol{E}(\boldsymbol{dx}) = \boldsymbol{E}_0 - \int_0^{\boldsymbol{dx}} \boldsymbol{S}(\boldsymbol{E}(\boldsymbol{y}))\boldsymbol{dy} \tag{5}$$

where $\boldsymbol{E}(\boldsymbol{x})$ is the particles energy after having travelled a distance $\boldsymbol{x}$ and $\boldsymbol{E}_0$ is the particle's energy at the beginning of the step. While this equation is in principle solvable under the assumption that $\boldsymbol{S}$ is linear along the step, a numerical approximation was used instead. This approximation is based on the following recurrence relation:

$$\overline{\mathbf{dE}_0} = \mathbf{dx} \cdot \mathbf{S}(\mathbf{E}_0) \tag{6}$$

$$\overline{\mathbf{dE}_\mathbf{n}} = \mathbf{dx} \cdot \mathbf{S}\left(\mathbf{E}_0 - \frac{\overline{\mathbf{dE}_{\mathbf{n}-1}}}{2}\right). \tag{7}$$

This recurrence relation is evaluated up to a depth of n = 3 to arrive at an accurate estimate of $\overline{\boldsymbol{dE}}$.

Scattering is a statistical process, so the stopping power only describes the mean energy loss per unit distance traveled. Theoretical treatments of this process have for example been done in [55, 56]. The distributions derived therein are complex and their sampling costly. But in the limit were $\mathbf{dx}$ is

large, the energy loss is approximately distributed normally around $\overline{dE}$. If dx is small on the other hand, the Gaussian approximation is inadequate and the distribution is skewed towards high energy losses [54]. Whether a Gaussian approximation is appropriate can be judged through the parameter κ given by

$$\kappa = \frac{\xi}{T_{max}}, \tag{8}$$

where ξ is given by

$$\xi = 2\pi \cdot N_a m_e r_e \rho \cdot dx \cdot \frac{q^2}{e^2}\frac{Z}{A} \cdot \frac{1}{\beta^2} \tag{9}$$

and T_{max} is given by

$$\mathrm{T_{max}} = \frac{2\mathrm{m_e}\beta^2\gamma^2}{1 + 2\gamma\frac{\mathrm{m_e}}{\mathrm{m}} + \frac{\mathrm{m_e^2}}{\mathrm{m^2}}}, \tag{10}$$

where N_a is Avogadro's number, m_e is the electron's mass, r_e is the classical electrons radius, q is the particles charge in Coulomb, Z is the target's atomic charge and A is the target's atomic number. Following [57], the energy loss distribution is approximated through a normal distribution if $\kappa \geq 10$ and a log-normal distribution if $\kappa < 10$. The normal distribution has mean $\overline{dE}$ and standard deviation σ as given for example in [53]:

$$\sigma = \sqrt{\xi \cdot T_{max}\left(1 - 0.5\beta^2\right)}. \tag{11}$$

The log-normal distribution's parameters are determined through a fit, matching the first four moments of the Vavilov distribution [57]. For very small $\kappa < 0.3$ [57], propose the use of a different distribution, but with step sizes of 1 mm it was found that adequate agreement can be achieved by sampling from a log-normal distribution even when $\kappa < 0.3$. During the simulations, care had to be taken here since occasionally, especially for very low-density materials like air, the energy loss sampled according to the log-normal approximation could become negative. In this case the approximation $dE = \overline{dE}$ was used.

Besides inelastic collisions with atomic electrons, charged particles also undergo elastic collisions with atomic nuclei. These interactions do not contribute to the particle's energy loss but deflect the particle. This too, is a statistical process. Commonly, MC simulations base their scattering model on Moliere's theoretical treatment [58]. The formula derived by Moliere is a series of functions

$$f(\vartheta) = \sum_n \frac{\vartheta f_n(\vartheta)}{B^n}, \tag{12}$$

where the reduced angle ϑ is related to the polar scattering angle θ used in **Eq. 1** *via*

$$\vartheta = \frac{\theta}{\chi_c\sqrt{B}} \tag{13}$$

and where χ_c and B are constants dependent on the target material, the incoming particle's energy and charge. These constants are defined in [58] together with an integral representation of the functions f_n. To clear up possible confusions, we note that in literature, frequently not the scattering angle ϑ is considered but instead the projected angle φ is used. This angle arises when one considers the projection of ϑ onto an axis perpendicular to the beam's direction. For a rigorous definition of ϑ and φ, we refer to [58, 59] and here we will only work with the angle ϑ.

Sampling from higher order terms of the Moliere distribution is computationally expensive, but approximations can be made. Perhaps the simplest is dropping higher order terms, i.e. terms where $n \geq 2$. Since B is a measure for the average number of single scattering events occurring along a step, when the step size dx is large the weight of the higher order terms decreases and the distribution can be approximated through a Rayleigh distribution in ϑ

$$\mathrm{f}(\vartheta) \approx \vartheta\exp\left(-\vartheta^2\right) \tag{14}$$

or a Gaussian distribution in φ

$$\mathrm{f}(\varphi) \approx \exp\left(-\varphi^2\right). \tag{15}$$

Single Gaussian approximations of the scattering angle have for example been introduced by Rossi [60] or Highland [61]. For the width σ of this Gaussian [60], provide the following empirical formula:

$$\sigma = \frac{E_s z}{\beta p}\sqrt{\frac{\rho dx}{\chi_0}}, \tag{16}$$

where z is the particle's charge in units of the elementary charge, ρ is the target's density, χ_0 is the target's radiation length and p is the particle's momentum in MeV/c. Originally, the value of E_s was given as 21 MeV but with the mixed Rayleigh-Rutherford approach that will be presented here, a value of 11.6 MeV was found to be better and was used throughout all simulations presented in ***Results***.

For small dx, the single Gaussian approximation does not adequately reproduce the large angle tails of Moliere's distribution. As a result, authors have proposed different modifications to the pure Gaussian probability distribution such as double or triple Gaussian parametrizations [62, 63] or parametrizations that use a Rutherford distribution to model the tail [31, 53, 64–66]. Generally, even when using fits of Gaussian mixture models, the large-angle tails of the Moliere distribution are not reproduced adequately. In this work, a parametrization similar to [64] was used, combining a Rutherford-like tail with a Rayleigh distribution at the center

$$P(\theta) = \begin{cases} \frac{\theta}{N\sigma^2}exp\left(-\frac{\theta}{2\sigma^2}\right), & \theta \leq \mathrm{k} \\ \frac{\alpha}{N\theta^3}, & \theta > \mathrm{k}. \end{cases} \tag{17}$$

For the simulations, the value $k = 3.5\sigma$ was used, the constant α was determined such that $P(\theta)$ is continuous at the boundary $\theta = \mathrm{k}$ and N was determined such that the probability density function is normalized, i.e.

$$\alpha = \frac{k^4}{\sigma^2} exp\left(-\frac{k^2}{2\sigma^2} \right) \text{and} \tag{18}$$

$$N = N_G + N_R. \tag{19}$$

Here, N_G and N_R are the integral of the Rayleigh and the Rutherford-like part respectively, given by

$$\mathrm{N_G} = 1 - \exp\left(-\frac{\mathrm{k}^2}{2\sigma^2} \right) \text{and} \tag{20}$$

$$\mathrm{N_R} = \frac{\mathrm{k}^2}{2\sigma^2} \exp\left(-\frac{\mathrm{k}^2}{2\sigma^2} \right). \tag{21}$$

Sampling of an angle θ is then done via inverse transform sampling using only a single uniformly distributed random number **U** after

$$\theta = \begin{cases} \sigma\sqrt{-2\,log\,(1 - U \cdot N)}, & U \le N_G \\ \dfrac{1}{\sqrt{\dfrac{1}{k^2} - \dfrac{2}{\alpha}\,(U \cdot N - N_G)}}, & U > N_G \cdot \end{cases} \tag{22}$$

Nuclear Interactions

Elastic Nuclear Interactions

The kinematics involved in elastic nuclear interactions are implemented fully relativistically. The total elastic cross section σ_{el} is calculated starting from the work of [67] and was tabulated in 500 evenly spaced bins ranging from 0.1 to 500.1 MeV for all 10 nuclei listed in ***Geometry and Materials***. The scattering angle in the center of mass frame is sampled according to a parametrization proposed in [68]. First, the momentum transfer t is sampled after

$$P(t) = A^{1.63}\, exp\left(14.5A^{0.66}t\right) + 1.4A^{0.33}\, exp\,(10t), \tag{23}$$

where, A is the target nucleus atomic number. Then, the center of mass scattering angle is calculated via

$$\cos\left(\theta_{\mathrm{CM}}\right) = 1 - \frac{\mathrm{t}}{2\mathrm{p_{CM}}}. \tag{24}$$

With p_{CM} being the center of mass momentum. From θ_{CM}, the laboratory frame polar scattering angles are computed and, together with a uniformly distributed azimuthal angle, applied to the resulting scattered particles.

Inelastic Nuclear Interactions

In particle therapy, inelastic nuclear scattering events generate the mixed radiation field, i.e. photons, protons, neutrons, deuterons, tritons, ^{3}He, ^{4}He and heavier fragments (nuclear recoils). In MonteRay, similarly to other works in literature [31, 32], photons and neutrons are assumed to be dosimetrically irrelevant and they are neither transported nor produced. The total inelastic cross section σ_{ine} for protons was calculated starting from the work of [69, 70]. To model the production of secondary particles, a database of nuclear event probabilities was generated based on nuclear models used internally by FLUKA. The database covers a primary proton energy T_{in} ranging from 10 to 300 MeV, in steps of 10 MeV. Tables were generated for each of the 10 elements defined in and for each of the five possible product particles considered: protons, tritons, deuterons, 3-Helium and 4-Helium. Each table (of the $30 \cdot 10 \cdot 5 = 1500$ tables) is divided into 100 bins in the kinetic energy T_{sec} and 100 bins in the solid angle Ω_{sec} of the secondaries. The 100 energy bins divide the range **0** to T_{in} into evenly spaced intervals and the 100 angular bins evenly divide the interval **0** to $4\,\pi$. If an inelastic nuclear event occurs during simulation, all possible products for the current target nucleus are created but assigned weights corresponding to their relative multiplicity (**Figure 1A**). Secondary particle energy (**Figure 1B**) and direction are chosen via a binary search on a cumulative probability distribution, generated at the beginning of the simulation by summing up the tables values. Additionally, the mean kinetic recoil energy is stored for each table and deposited on the spot following a nuclear event.

Benchmarking of the Developed Dose Engine

To benchmark MonteRay, its predictions were compared against experimental data acquired at HIT over the last years, published in [71, 72]. For scenarios where experimental data was not available, e.g. in presence of magnetic fields and for patient calculations, FLUKA predictions were used as a reference.

Comparison Metrics

To judge MonteRay's agreement with measurements or against other TPS, several common radiotherapy metrics were used. The relative error

$$\varepsilon_{\mathrm{rel}} = 200\,\frac{\mathrm{d_1} - \mathrm{d_2}}{(\mathrm{d_1} + \mathrm{d_2})}\,[\%] \tag{25}$$

was used to quantify the relative disagreement between two dose profiles, d_1 and d_2. Measured and calculated beam ranges were compared in terms of their R_{80} value which is defined as the depth distal to the Bragg peak (BP) where the dose falls to 80% of the BP value. The difference in range for two dose distributions was quantified through $\Delta R_{80} = |R^1_{80} - R^2_{80}|$. Agreement between lateral profiles was judged using the full width at half maximum (FWHM) value and the full width at 10% of the maximum (FW10%M) value. For the comparison of 3D dose distributions, the 3D local gamma pass rate was calculated. For this the python package pymedphys version 0.37.1 was used. For the calculation, similar to previous proton MC engines [28, 31, 73, 74], the dose percentage threshold was set to 2%, the distance threshold to 2 mm and the dose cutoff to 5% of the maximum dose. During the calculation of the gamma pass rate, dose outside the patient was not considered as it is clinically irrelevant. Another metric used to evaluate patient plans is the D_x value. For a given region of interest (ROI), it is defined as the minimum dose that x percent of the ROIs volume is exposed to.

To judge the deflection of a single beam in a magnetic field, we introduce the center of mass (COM) of the beam. Given a lateral profile scored in N bins at locations x_i with corresponding scored doses $d(x_i)$, we define it as

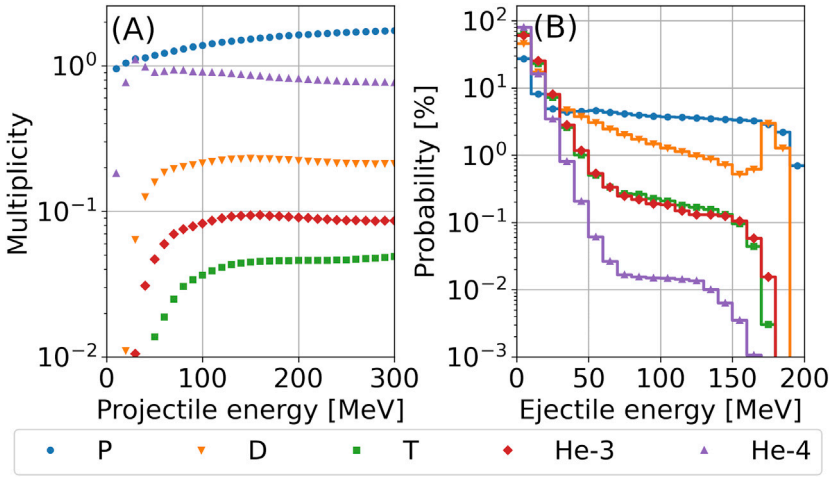

FIGURE 1 | (A) Average number of particles produced per p + ^{16}O collision as a function of the energy of the incoming proton. **(B)** For 200 MeV p + ^{16}O collisions, the angularly integrated probability (in %) of a secondary particle being produced in a certain energy bin (bin size: 10 MeV) is shown. Abbreviations stand for Protons (P), Deuterons (D), Tritons (T), Helium-3 (^{3}He) and Helium-4 (^{4}He).

$$COM = \frac{1}{N} \sum x_i \cdot d(x_i). \tag{26}$$

Dosimetric Data

Various experimental data that was previously recorded at HIT was used to evaluate MonteRay's performance in terms of dosimetric accuracy. This data, included pencil-beam depth-dose distributions [71], lateral profiles of vertically scanned line profiles [75] and Spread-Out Bragg Peak (SOBP) plans [72]. Details on the measurement procedures were given in the mentioned references so only a quick overview will be given here.

Pencil beam depth-dose distributions in water were recorded using a PeakFinder water column (PTW, Freiburg) with a diameter of 8.16 cm. In total, 17 Bragg curves with beam energies spanning the entire energy range available at HIT (from 48.5 to 222.6 MeV) have been measured. The measurements took place in a clinical room at HIT. The resolution was 0.05 mm in the region of the BP.

Measurements of lateral profiles of vertically scanned irradiation lines in a water phantom were obtained at three energies (81.5, 158.5 and 222.6 MeV) using an array of 24 motorized pinpoint chambers (PTW, 0.03 cm^3) arranged in a block of six rows and four columns. The profiles were recorded perpendicularly to the direction of the vertically scanned line. Each scanned line consisted of 101 pencil beams ranging from -50 mm to +50 mm with a 1 mm spacing. The horizontal profiles were recorded starting from about 16 mm in water to 30 mm after the BP. For each energy, profiles at 42 depths were recorded. The distance between consecutive profiles was between 0.5 and 10 mm.

Three SOBP plans centered around 5 cm, 12.5 and 20 cm in water were created using a FLUKA-based treatment planning tool. The planned dose was 1 Gy within the 3 × 3 × 3 cm target region. Delivery of the plans happened in the experimental room at HIT with measurements being done with the same block of pinpoint ionization chambers used for acquiring the lateral profiles described earlier. The profiles were recorded starting at a depth of 16 mm to approximately 20 mm after the end of the SOBP. The step size between measurements in regions of high gradient and in regions of high dose was 1 mm.

FLUKA Calculations

Due to the lack of dosimetric data in magnetic fields, the transport in magnetic fields was benchmarked by comparing MonteRay against FLUKA. For this the effect of homogenous magnetic fields, applied perpendicular to the beam's direction, was studied for field strengths of 0.5, 1.0 and 2 T. In FLUKA, magnetic fields were enabled using the MGNFIELD card with default settings. The DEFAULTS card with value PRECISIO was enabled during FLUKA simulations to ensure high precision simulations.

Patient Planning

Patient planning was performed in the clinical TPS RayStation 10 A (RaySearch Laboraries, Stockholm, Sweden) on an anonymized DICOM patient data set representative of a meningioma treatment. A proton treatment plan using a single beam at 90° was optimized for evaluation of dose calculation accuracies in a patient anatomy. The initial spot positioning (hexagonal grid with spot spacing of 3.6 mm, energy spacing of 2.1 mm) and minimum number of particles (580.000 particles) settings follow clinical practice at HIT. Optimization was made on the planning target volume (PTV, ~112 cm^3) for 49.1 Gy/ 54 GyRBE in 30 fractions using a constant radiobiological effectiveness of 1.1. The resultant energy range spanned from ~78 to 151 MeV. The dose grid was set to 2 × 2 × 2 mm^3 in RayStation with a dose uncertainty of 0.5%. The treatment plan was exported in FLUKA and MonteRay for forward calculation with and without a magnetic field. The statistical uncertainty of the MonteRay and FLUKA runs was 1%. The dose uncertainty was estimated using the batch method. Dose cubes stemming

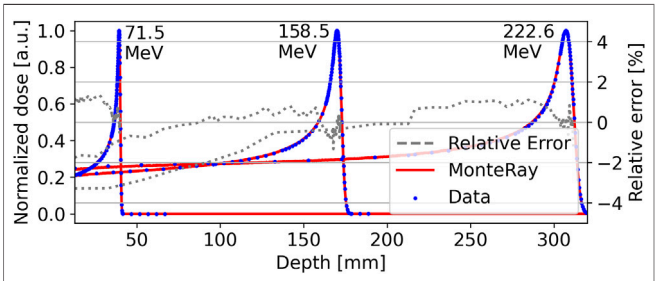

FIGURE 2 | Integrated depth-dose profiles of quasi-monoenergetic beams with energies of 71 MeV, 158.5, and 222.6 MeV are shown. Peakfinder measurements are indicated by blue points and MonteRay simulations as solid red lines. The relative error, after correcting for a lateral shift, between measurements and MonteRay simulations is shown with grey dotted lines after correcting for the lateral shift.

from FLUKA MC and MonteRay were ultimately imported in RayStation for dosimetric analysis (DVH and line profile evaluation). All doses were computed as dose-to-water and dose comparisons were made in Gy.

RESULTS

Pristine Bragg Peaks in Water

To evaluate the accuracy of MonteRay, we first compare the simulated dose in water $\boldsymbol{d_{MR}}$ to the dose measured at HIT $\boldsymbol{d_{HIT}}$ for 17 quasi-monoenergetic beams. The beam energies ranged from 71.5 to 222.6 MeV. **Figure 2** shows a comparison of the dose obtained with MonteRay with measured values for three exemplary energies of 71.5, 158.5 and 222.6 MeV. Due to the high resolution of the measured data (up to 0.05 mm in the BP region), the transport was performed on a Cartesian grid with $0.1 \times 0.1 \times 0.1\,\mathrm{mm}^3$ resolution. Scoring likewise was done in 0.1 mm thick slices. To match the physical dimension of the detector, scoring was performed in a cylindrical volume with a radius of 4.08 cm. Both measurements and simulations were normalized to one at the BP. Across all the energies, the maximum, minimum and mean $\boldsymbol{\Delta R_{80}}$ values were 0.16, 0.06 and 0.10 mm, respectively. Once the MC calculations were shifted by $\Delta \boldsymbol{R_{80}}$, $\boldsymbol{d_{MC}}$ and $\boldsymbol{d_{HIT}}$ were quantitively compared using the relative error $\boldsymbol{\varepsilon_{rel}}$. The dose threshold for calculating $\boldsymbol{\varepsilon_{rel}}$ was set to 20% of maximum. The mean absolute $\boldsymbol{\varepsilon_{rel}}$ over all the investigated energies was 0.56 %.

For the verification of the lateral parametrization in water, measurements of vertically scanned proton beam lines, as described in ***Dosimetric Data***, were compared against MonteRay simulations. Lateral relative dose profiles at three energies, 81.5, 158.5 and 222.6 MeV, and at 40 different depths were compared. In **Figure 3** and for each energy, lateral profiles at three depths are visualized: at the entrance (top row), in the BP region (bottom row) and in the middle of these two (middle row). The depths are reported in each panel of **Figure 3**. The corresponding energy is given at the top of each column. After correcting for the error in FWHM already present at the entrance due to daily variations in the beam's shape, on average, the simulated FWHM matched the experimental data's FWHM within 0.1, 0.3 and 0.5 mm for the three energies, respectively. Likewise, the FW10%M values matched to within 0.1, 0.3 and 0.9 mm.

Spread Out Bragg Peaks in Water

Next, MonteRay's simulated dose was compared with dosimetric data from SOBP plans. The measurement process was described in ***Dosimetric Data***. The resulting depth-dose distributions are displayed in **Figure 4**, together with the measured values. The mean absolute relative error between measurements and predictions (excluding data in regions of high dose gradients, as performed in clinical routine) was (0.69%, 0.74%, 1.0%) with a standard deviation of (0.7%, 0.6%, 1.0%). The $\Delta \boldsymbol{R_{80}}$ values were 0.5, 0.3 and 0.3 mm, respectively. In the lower panels of **Figure 4**, lateral profiles at the entrance and at in the middle of the SOBP are shown. Here, the simulated SOBP widths matched the experimental ones on to within about 1 mm.

Magnetic Field Deflection in Homogenous Fields

To judge the accuracy of MonteRay when dealing with homogenous magnetic fields, MonteRay's simulations were first compared to FLUKA's for monoenergetic proton beams incident on water. The magnetic field was applied perpendicular to the beam's direction and four field strengths of 0 T, 0.5 T, 1 T and 2 T were compared. Planar profiles were scored with a resolution of $1 \times 1 \times 1\,\mathrm{mm}^3$ but were afterwards integrated along 1 cm in the direction of the magnetic field axis to provide higher statistics. In **Figures 5A,B**, 2D dose distributions, perpendicular to the magnetic field, are shown for the case where the magnetic field strength was 2 T. In panel **(A)**, MonteRay's results are shown while FLUKA's results are displayed in panel **(B)**. For all tested field strengths, the gamma passing rate (as defined in ***Comparison Metrics***) was above 99.8%

In **Figure 5C**, lateral profiles at the BP position for the four field strengths are shown. From lateral profiles, COM, FWHM and FW%10M were computed at each depth up to the BP. The maximum differences in COMs (ΔCOM), FWHM (ΔFW_{50}) and FW10%M (ΔFW_{10}) between MonteRay and FLUKA are summarized in **Table 1**. For all tested field strengths and at all depths, the maximum distances between the COMs stayed below 0.15 mm, the maximum disagreements in the FWHM reached 0.21 mm while the maximum disagreements in the FW10%M reached 0.31 mm. Comparing integrated depth-dose profiles, the R_{80} values between MonteRay and FLUKA were found to agree to within 0.14, 0.18, 0.10 and 0.07 mm. The maximum relative errors in dose, after correcting for these shifts, was 1.2%.

Patient Case

In **Figure 6** panels **(A)** and **(B)**, the doses for a patient plan, calculated with FLUKA and MonteRay are shown in the axial plane. The gamma passing rate between MonteRay and FLUKA was computed to be 99.8%. In panel **(C)**, longitudinal profiles and in panel **(D)**, lateral profiles are shown. The profiles are shown for

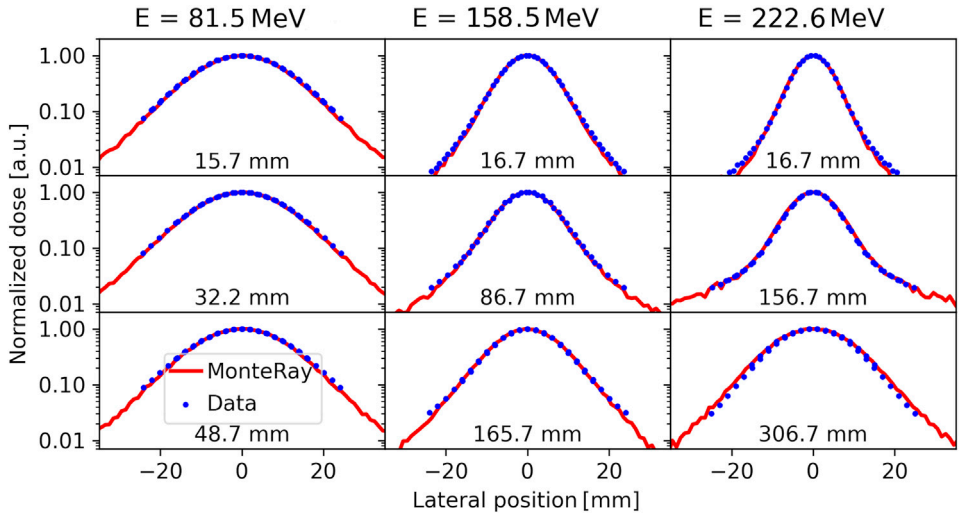

FIGURE 3 | Lateral dose profiles of vertically scanned proton lines at 81.5 MeV **(left column)**, 158.5 MeV (central column) and 222.6 MeV **(right column)** at different depths as reported in the panels. Measurements (blue points) are compared against MonteRay simulations (red lines).

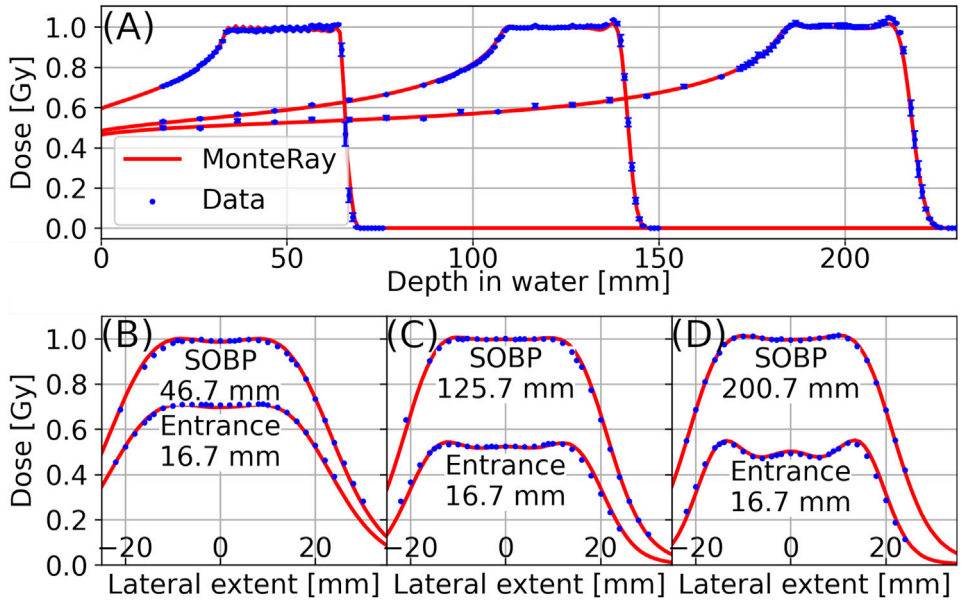

FIGURE 4 | In panel **(A)**, Longitudinal dose distributions of three proton SOBP plans in water with plateau depths of approximately 5 cm, 12.5, and 20 cm are shown. In panels **(B)**, **(C)**, and **(D)**, lateral profiles corresponding to the three SOBP plans are displayed. For each SOBP, one lateral profile at the entrance and one lateral profile in the middle of the SOBP is shown. Measurements (points) are compared against MonteRay's simulated values (lines).

simulated doses obtained from RayStation, FLUKA and MonteRay, and their locations are indicated in panel **(A)** through red horizontal (longitudinal) and vertical (lateral) lines. For RayStation, FLUKA and MonteRay, the lateral profile's FWHMs were 67.6, 68.1, and 68.3 mm. The widths at 10% of the maximum were 85.3, 86.1, and 85.9 mm. The differences in range between MonteRay/FLUKA and RayStation/FLUKA were calculated from the longitudinal profiles and found to be 0.4 and 0.6 mm, respectively. Both in terms of lateral and longitudinal profiles, MonteRay agrees well with FLUKA.

In **Figure 7A**, DVHs calculated for several regions of interest (ROI) are displayed: the CTV, the brain, the brainstem and the right optical nerve. The $\boldsymbol{D}_2$, $\boldsymbol{D}_{50}$ and $\boldsymbol{D}_{98}$ values were computed for the CTV and $\boldsymbol{D}_2$ values were computed for the organs at risk (OAR). To judge the quality of MonteRay, the relative difference in $\boldsymbol{D}_x$ values between MonteRay and FLUKA is compared to those between RayStation and FLUKA. Overall, the agreement

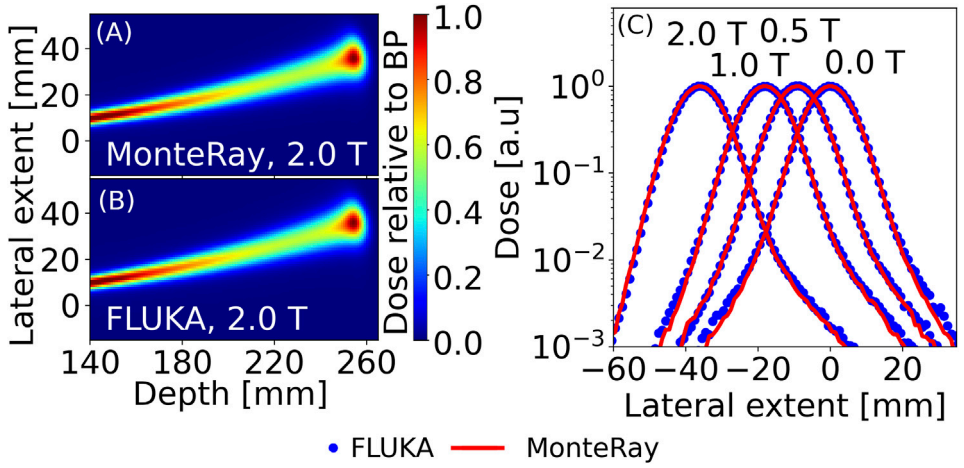

FIGURE 5 | For 200 MeV protons in water, 2D dose distributions calculated with MonteRay **(A)** and FLUKA **(B)** are shown in a plane perpendicular to the 2 T magnetic field. In **(C)**, Lateral profiles for 200 MeV protons in water and with magnetic field strengths of 0 T, 0.5 T, 1 T, and 2 T are displayed at the location of the BP. MonteRay's results are indicated by a red line while FLUKA's results are displayed as blue dots.

TABLE 1 | Comparison of MonteRay against Fluka for a 200 MeV proton beam incident on water with different homogenous magnetic fields applied perpendicular to the beam. The maximum differences in the COM (ΔCOM), FWHM (ΔFW_{50}) and FW10%M (ΔFW_{10}) across all depths up to the BP are reported.

Field strength [T]	ΔCOM [mm]	ΔFW_{50} [mm]	ΔFW_{10} [mm]
0	0.018	0.17	0.24
0.5	0.043	0.21	0.30
1.0	0.072	0.19	0.23
2.0	0.14	0.21	0.31

between MonteRay and FLUKA was of the same magnitude as the agreement between RayStation and FLUKA. For the CTV, good agreement in the D_2 value of 0.25%, the D_{50} value of 0.38% and the D_{98} value to within 0.58% was found. For the considered OARs the computed D_2 values matched within 0.50% for the brain, within 0.44% for the brainstem and to within 0.49% for the right optical nerve.

Patient Case With a Magnetic Field

To benchmark our magnetic field implementation, the previous patient plan was reused but for the dose calculation in MonteRay and FLUKA, a homogenous magnetic field of 1 T was applied throughout the CT volume. In **Figure 8**, the calculated doses in FLUKA (Panel **(A)**) and MonteRay (Panel **(B)**) are displayed. With the magnetic field enabled, the gamma passing rate between MonteRay and FLUKA was found to be 98.8%.

In panel **(C)**, longitudinal profiles and in panel **(D)**, lateral profiles are shown, and their locations are indicated in panel **(A)** through horizonal (longitudinal) and vertical (lateral) lines. Profiles are shown for simulated doses obtained with MonteRay and FLUKA. Additionally, in panel **(D)**, the lateral profile obtain d from RayStation without an applied magnetic field is shown. The deflection observed at the lateral profile's position was ~5 mm. Computed for FLUKA and MonteRay, the lateral profile's FWHMs were 67.4 mm, 67.5 mm. The widths at 10% of the maximum were 86.0 and 85.0 mm. The difference in range between MonteRay and FLUKA, calculated from the longitudinal profiles, was found to be 0.4 mm.

In **Figure 7B**, DVHs calculated on the same ROIs as in the previous section are shown. D_x values were computed for FLUKA and MonteRay. For the CTV we found agreement in the D_2 value of 2%, in the D_{50} value of 0.53% and in the D_{98} value of 1.2%. For the OARs, the computed D_2 values matched within 0.76% for the brain, within 2.1% for the brainstem and within 2.3% for the right optical nerve.

Runtime Benchmarks

The performance of MonteRay was evaluated for various test cases. All tests were performed on a six-core AMD Ryzen 5,3600 processor. The transport grid's resolution was set to 2 × 2 × 2 mm^3. This resolution is used clinically at HIT and other fast MC codes have used this resolution for benchmarking [31]. For 150 MeV monoenergetic Protons in water with a FWHM of 1 cm, a throughput of 31 k primaries per second on a single core and 180 k primaries per second when using all six cores of the CPU, was measured. Under parallel load, the throughput therefore was 30 k primaries per second per core. In comparison, the computational throughput of FLUKA on the same problem on the same hardware was 1.1 k primaries per second.

For the patient plan, benchmarks were run on a 2 × 2 × 2 mm^3 grid with 5,000 particles per pencil beam per core. In total, the plan consisted of 8313 pencil beams. On a single core, a throughput of 33 k particles per second was observed while the throughput on six core was measured to be 193 k primaries per second which corresponds to 32 k primaries per seconds per core.

DISCUSSION

The comparison of MonteRay predictions against dosimetric data and FLUKA simulations confirms that the implemented

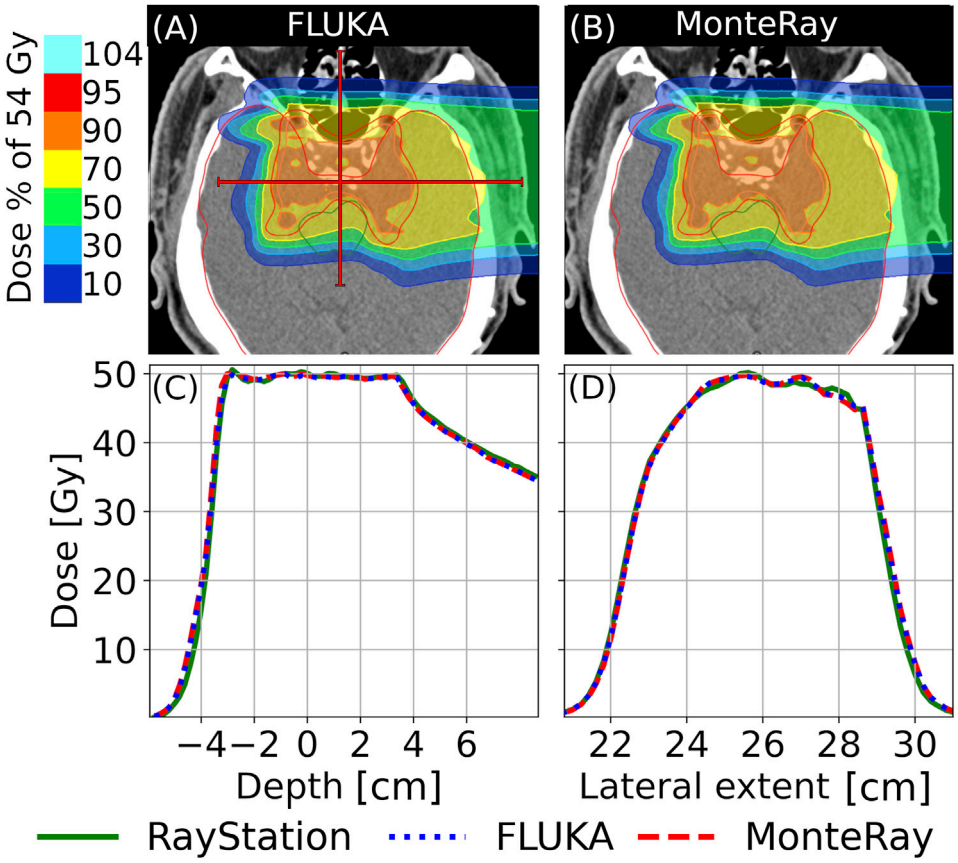

FIGURE 6 | Axial views of calculated doses for the plan described in Section 2.2.4 are shown for **(A)** FLUKA and **(B)** MonteRay. In panels **(C)** and **(D)**, longitudinal and lateral profiles are shown, respectively. The locations of the profiles relative to the 2D plots are indicated trough red lines in panel **(A)**. RayStation profiles are indicated by a solid green line, FLUKA profiles by a dotted blue line and MonteRay profiles by a dashed red line.

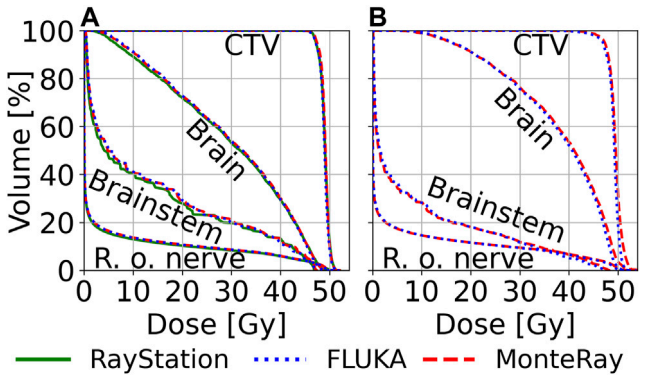

FIGURE 7 | Computed DVHs for the CTV, the brain, the brainstem and the right optical nerve (r. o. nerve) are shown. DVHs were computed for RayStation (green, solid line), FLUKA (blue, dotted line) and MonteRay (red, dashed line). In panel **(A)**, DVHs for the patient case without a magnetic field are shown while in panel **(B)** DVHs calculated for the case with an applied magnetic field are shown.

electromagnetic and nuclear models correctly reproduce the underlying physics. In terms of depth-dose distributions for pencil beams in water (***Pristine Bragg Peaks in Water***), the mean absolute relative error over all 17 compared energies was 0.56%, ranging from 0.33 to 0.60% for 102.6 and 222.6 MeV protons, respectively. The depth-dependent maximum absolute relative error varied from 0.95% (48.5 MeV) to 3.4% (222.6 MeV). The latter is located at the entrance channel of the highest energy (222.6 MeV) which is typically not used for clinical purpose. This underestimation could in part be explained through the fact that the current approach for sampling the initial particles neglects secondary d, t, ^{3}He and ^{4}He particles produced in the beamline. Our predictions are in line with other fast MC engines available in literature, for example [73], using FRED have found relative differences of up to about 3% for 200 MeV protons in water.

In terms of lateral evolution as function of depth, MonteRay matched satisfactorily the experimental data in terms of FWHM/FW10%M within on average 0.1, 0.3, and 0.9 mm for low, medium and high energies. The largest difference has been found in the Bragg peak region for 222.6 MeV protons with a maximum variation of the FW10%M of 2 mm. To evaluate possible shortcomings in the scattering model, we have compared FLUKA and MonteRay predictions for 200 MeV proton beams in water without the HIT beamline. The maximum FWHM(FW10%M) variation found was

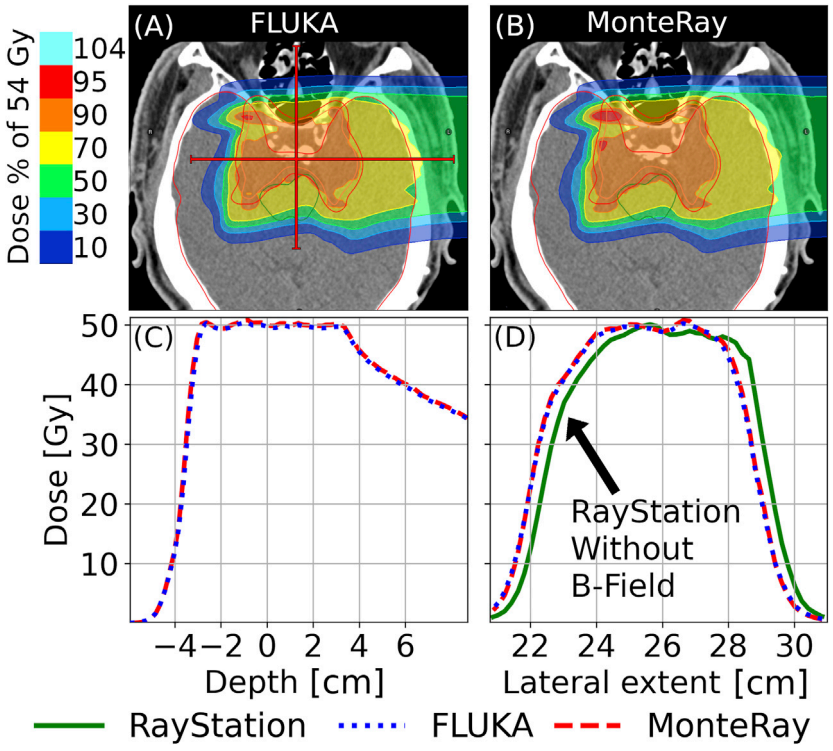

FIGURE 8 | Axial views of calculated doses for the plan described in Section 2.2.4 with an added perpendicular magnetic field of 1 T are shown for **(A)** FLUKA and **(B)** MonteRay. In panels **(C)** and **(D)**, longitudinal and lateral profiles are shown, respectively. Besides the lateral profiles obtained from FLUKA and MonteRay, we also show the lateral profile of the RayStation dose calculated without a magnetic field. The locations of the profiles relative to the 2D plots are indicated trough red lines in panel **(A)**. RayStation profiles are indicated by a solid green line, FLUKA profiles by a dotted blue line and MonteRay profiles by a dashed red line.

0.17 mm (0.24 mm) and the 3D gamma pass rate was 99.8% confirming the quality of the implemented model.

Prediction of SOBPs centered at different depths confirmed MonteRay's beam-model with an average agreement of 1% when compared against experimental data, well fulfilling clinical criteria. MonteRay's results have been found to be in line with FLUKA results for the same set of experimental SOBP data [71], with average FLUKA dose deviations of 0.9%.

Evaluation of MonteRay on a patient plan showed good agreement against simulations performed with FLUKA. In terms of D2, D50, and D98 we achieved similar agreement to FLUKA as RayStation did. The 3D gamma pass rate was calculated to be 99.8% showing that the implemented models and approximations for electromagnetic and nuclear interactions approximate the underlying physics well, also in a clinical setting. Computed 3D gamma pass rates were in line with those obtained by other fast MC engines [28, 33, 73].

Similarly, we evaluated the quality of our simulation when an additional magnetic field was applied to an irradiation plan. Compared to FLUKA, we found adequate agreement in terms of D2, D50, and D98 between 0.5 and 2.3%. The 3D gamma pass rate was 98.9%, showing that a simple approximation of the Lorentz force is adequate at describing the transport of charged particles in homogenous magnetic fields.

In terms of computational throughput, MonteRay was able to simulate 31 k primaries per second for a 150 MeV proton beam incident on water, transported on a $2 \times 2 \times 2$ mm^3 grid. Parallel execution on six cores was found to scale linearly, achieving a throughput of 180 k primaries per second. When benchmarked on a patient plan containing ~8300 pencil beams with energies ranging from ~78 to ~150 MeV, we measured a throughput of 33 k particles per seconds on a single core and 193 k particles on six cores. Again, linear scaling was observed which demonstrates that reading the phase space from disk is not a bottleneck, even when multiple cores are competing for random read access.

CONCLUSION AND OUTLOOK

In this work we have presented a novel MC engine, specialized for proton therapy calculations, currently under development at HIT. Good agreement with measured data and a full-fledged MC engine (FLUKA) has been found. MonteRay achieved fast tracking rates of more than 30 k proton primaries per second at 150 MeV on a $2 \times 2 \times 2$ mm^3 grid. In a next step, work will begin on porting our fast CPU engine onto GPUs. Following a heterogenous approach, i.e. using both CPUs and GPUs, we hope to achieve sub-minute runtimes even for large irradiation plans.

A custom Monte Carlo engine will also allow us to easily implement custom features such as computing the linear energy transfer or to add imaging capabilities by producing positrons or prompt gammas.

With helium beam treatment commencing at HIT, inclusion of helium beams in MonteRay is underway with inelastic nuclear databases having already been generated.

With the aim of MR guided ion therapy, we are the first fast MC engine to include magnetic field support. In the future we will expand our evaluation to inhomogeneous fields with a focus on simulating MRIs which are being installed at HIT for the purpose of MR guided ion therapy.

DATA AVAILABILITY STATEMENT

The raw data supporting the conclusions of this article will be made available by the authors, without undue reservation.

AUTHOR CONTRIBUTIONS

AM, AF, and PL were responsible for the conceptual design of the Monte Carlo engine. PL, BK, and AM developed the source code of the Monte Carlo engine. AM generated the materials database, including elastic and inelastic nuclear cross sections. AF developed the code for the generation of inelastic nuclear databases from FLUKA. JB generated the inelastic nuclear databases. PL, TT, and AM worked on the analysis of data. TT, AM, and SM collected and provided experimental data used in this work. TT computed and provided the patient plan and SOBP plans. JD and TH provided clinical direction during project development, manuscript writing and project administration and funding acquisition. All authors read and contributed to the preparation of the manuscript.

FUNDING

The authors acknowledge financial support through the German Federal Ministry of Education and Research (BMBF) within the project (Grant number: 13GW0436A).

ACKNOWLEDGMENTS

The authors would like to acknowledge Eric Heim's work on the initial setup of the C++ code base and unit testing framework. The authors would like to acknowledge Ahmad Neishabouri for his help with performing Fluka calculations and Eric Heim for his work on the initial setup of the C++ code base and the unit testing framework.

REFERENCES

1. Chandarana H, Wang H, Tijssen RHN, and Das IJ Emerging Role of MRI in Radiation Therapy. *J Magn Reson Imaging* (2018) 48:1468–78. doi:10.1002/jmri.26271
2. Pollard JM, Wen Z, Sadagopan R, Wang J, and Ibbott GS The Future of Image-Guided Radiotherapy Will Be MR Guided. *Bjr* (2017) 90:20160667. doi:10.1259/bjr.20160667
3. Mutic S, and Dempsey JF The ViewRay System: Magnetic Resonance-Guided and Controlled Radiotherapy. *Semin Radiat Oncol* (2014) 24:196–9. doi:10.1016/j.semradonc.2014.02.008
4. Liney GP, Whelan B, Oborn B, Barton M, and Keall P MRI-linear Accelerator Radiotherapy Systems. *Clin Oncol* (2018) 30:686–91. doi:10.1016/j.clon.2018.08.003
5. Acharya S, Fischer-Valuck BW, Kashani R, Parikh P, Yang D, Zhao T, et al. Online Magnetic Resonance Image Guided Adaptive Radiation Therapy: First Clinical Applications. *Int J Radiat Oncology*Biology*Physics* (2016) 94:394–403. doi:10.1016/j.ijrobp.2015.10.015
6. Durante M, and Loeffler JS Charged Particles in Radiation Oncology. *Nat Rev Clin Oncol* (2010) 7:37–43. doi:10.1038/nrclinonc.2009.183
7. Durante M, Orecchia R, and Loeffler JS Charged-particle Therapy in Cancer: Clinical Uses and Future Perspectives. *Nat Rev Clin Oncol* (2017) 14:483–95. doi:10.1038/nrclinonc.2017.30
8. Hoffmann A, Oborn B, Moteabbed M, Yan S, Bortfeld T, Knopf A, et al. MR-guided Proton Therapy: a Review and a Preview. *Radiat Oncol* (2020) 15:129. doi:10.1186/s13014-020-01571-x
9. Haberer T, Debus J, Eickhoff H, Jäkel O, Schulz-Ertner D, and Weber U The heidelberg Ion Therapy center. *Radiother Oncol* (2004) 73:S186–S190. doi:10.1016/s0167-8140(04)80046-x
10. Rankine LJ, Mein S, Cai B, Curcuru A, Juang T, Miles D, et al. Three-Dimensional Dosimetric Validation of a Magnetic Resonance Guided Intensity Modulated Radiation Therapy System. *Int J Radiat Oncol Biol Phys* (2017) 97:1095–104. doi:10.1016/j.ijrobp.2017.01.223
11. Klüter S Technical Design and Concept of a 0.35 T MR-Linac. *Clin Translational Radiat Oncol* (2019) 18:98–101. doi:10.1016/j.ctro.2019.04.007
12. Chamberlain M, Krayenbuehl J, van Timmeren JE, Wilke L, Andratschke N, Garcia Schüler H, et al. Head and Neck Radiotherapy on the MR Linac: a Multicenter Planning challenge Amongst MRIdian Platform Users. *Strahlenther Onkol* (2021) 1–11. doi:10.1007/s00066-021-01771-8
13. Raaijmakers AJE, Raaymakers BW, and Lagendijk JJW Magnetic-field-induced Dose Effects in MR-Guided Radiotherapy Systems: Dependence on the Magnetic Field Strength. *Phys Med Biol* (2008) 53:909–23. doi:10.1088/0031-9155/53/4/006
14. Wolf R, and Bortfeld T An Analytical Solution to Proton Bragg Peak Deflection in a Magnetic Field. *Phys Med Biol* (2012) 57:N329–N337. doi:10.1088/0031-9155/57/17/N329
15. Moteabbed M, Schuemann J, and Paganetti H Dosimetric Feasibility of Real-Time MRI-Guided Proton Therapy. *Med Phys* (2014) 41:111713. doi:10.1118/1.4897570
16. Ferrari A, Sala PR, Fasso A, and Ranft J *FLUKA: A Multi-Particle Transport Code*. Stanford: Stanford linear accelerator center (2005). doi:10.2172/877507
17. Böhlen TT, Cerutti F, Chin MPW, Fassò A, Ferrari A, Ortega PG, et al. The FLUKA Code: Developments and Challenges for High Energy and Medical Applications. *Nucl Data Sheets* (2014) 120:211–4. doi:10.1016/j.nds.2014.07.049
18. Bauer J, Sommerer F, Mairani A, Unholtz D, Farook R, Handrack J, et al. Integration and Evaluation of Automated Monte Carlo Simulations in the Clinical Practice of Scanned Proton and Carbon Ion Beam Therapy. *Phys Med Biol* (2014) 59:4635–59. doi:10.1088/0031-9155/59/16/4635
19. Mein S, Choi K, Kopp B, Tessonnier T, Bauer J, Ferrari A, et al. Fast Robust Dose Calculation on GPU for High-Precision 1H, 4He, 12C and 16O Ion Therapy: the FRoG Platform. *Sci Rep* (2018) 8:14829. doi:10.1038/s41598-018-33194-4
20. Mein S, Kopp B, Tessonnier T, Ackermann B, Ecker S, Bauer J, et al. Dosimetric Validation of Monte Carlo and Analytical Dose Engines with Raster-Scanning 1H, 4He, 12C, and 16O Ion-Beams Using an Anthropomorphic Phantom. *Physica Med* (2019) 64:123–31. doi:10.1016/j.ejmp.2019.07.001
21. Choi K, Mein S, Kopp B, Magro G, Molinelli S, Ciocca M, et al. FRoG-A New Calculation Engine for Clinical Investigations with Proton and Carbon Ion Beams at CNAO. *Cancers* (2018) 10:395. doi:10.3390/cancers10110395

22. Kopp B, Fuglsang Jensen M, Mein S, Hoffmann L, Nyström H, Falk M, et al. FRoG: An Independent Dose and LET D Prediction Tool for Proton Therapy at ProBeam Facilities. *Med Phys* (2020) 47:5274–86. doi:10.1002/mp.14417
23. Magro G, Mein S, Kopp B, Mastella E, Pella A, Ciocca M, et al. FRoG Dose Computation Meets Monte Carlo Accuracy for Proton Therapy Dose Calculation in Lung. *Physica Med* (2021) 86:66–74. doi:10.1016/j.ejmp.2021.05.021
24. Fuchs H, Moser P, Gröschl M, and Georg D Magnetic Field Effects on Particle Beams and Their Implications for Dose Calculation in MR-Guided Particle Therapy. *Med Phys* (2017) 44:1149–56. doi:10.1002/mp.12105
25. Parodi K Vision 20/20: Positron Emission Tomography in Radiation Therapy Planning, Delivery, and Monitoring. *Med Phys* (2015) 42:7153–68. doi:10.1118/1.4935869
26. Parodi K, Paganetti H, Shih HA, Michaud S, Loeffler JS, DeLaney TF, et al. Patient Study of *In Vivo* Verification of Beam Delivery and Range, Using Positron Emission Tomography and Computed Tomography Imaging after Proton Therapy. *Int J Radiat Oncol Biol Phys* (2007) 68:920–34. doi:10.1016/j.ijrobp.2007.01.063
27. Parodi K, and Polf JC *In Vivo* range Verification in Particle Therapy. *Med Phys* (2018) 45:e1036–e1050. doi:10.1002/mp.12960
28. Jia X, Schümann J, Paganetti H, and Jiang SB GPU-based Fast Monte Carlo Dose Calculation for Proton Therapy. *Phys Med Biol* (2012) 57:7783–97. doi:10.1088/0031-9155/57/23/7783
29. Jia X, Pawlicki T, Murphy KT, and Mundt AJ Proton Therapy Dose Calculations on GPU: Advances and Challenges. *Translational Cancer Res* (2012) 1:207–16. doi:10.3978/j.issn.2218-676X.2012.10.03
30. Giantsoudi D, Schuemann J, Jia X, Dowdell S, Jiang S, and Paganetti H Validation of a GPU-Based Monte Carlo Code (gPMC) for Proton Radiation Therapy: Clinical Cases Study. *Phys Med Biol* (2015) 60:2257–69. doi:10.1088/0031-9155/60/6/2257
31. Schiavi A, Senzacqua M, Pioli S, Mairani A, Magro G, Molinelli S, et al. Fred: a GPU-Accelerated Fast-Monte Carlo Code for Rapid Treatment Plan Recalculation in Ion Beam Therapy. *Phys Med Biol* (2017) 62:7482–504. doi:10.1088/1361-6560/aa8134
32. Deng W, Younkin JE, Souris K, Huang S, Augustine K, Fatyga M, et al. Technical Note: Integrating an Open Source Monte Carlo Code "MCsquare" for Clinical Use in Intensity-modulated Proton Therapy. *Med Phys* (2020) 47:2558–74. doi:10.1002/mp.14125
33. Tian Z, Shi F, Folkerts M, Qin N, Jiang SB, and Jia X A GPU Opencl Based Cross-Platform Monte Carlo Dose Calculation Engine (Gomc). *Phys Med Biol* (2015) 60:7419–35. doi:10.1088/0031-9155/60/19/7419
34. Faddegon B, Ramos-Méndez J, Schuemann J, McNamara A, Shin J, Perl J, et al. The TOPAS Tool for Particle Simulation, a Monte Carlo Simulation Tool for Physics, Biology and Clinical Research. *Physica Med* (2020) 72:114–21. doi:10.1016/j.ejmp.2020.03.019
35. Oborn BM, Dowdell S, Metcalfe PE, Crozier S, Mohan R, and Keall PJ Proton Beam Deflection in MRI fields: Implications for MRI-Guided Proton Therapy. *Med Phys* (2015) 42:2113–24. doi:10.1118/1.4916661
36. Padilla-Cabal F, Georg D, and Fuchs H A Pencil Beam Algorithm for Magnetic Resonance Image-Guided Proton Therapy. *Med Phys* (2018) 45:2195–204. doi:10.1002/mp.12854
37. Schellhammer SM, Hoffmann AL, Gantz S, Smeets J, van der Kraaij E, Quets S, et al. Integrating a Low-Field Open MR Scanner with a Static Proton Research Beam Line: Proof of Concept. *Phys Med Biol* (2018) 63:23LT01. doi:10.1088/1361-6560/aaece8
38. Schellhammer SM, and Hoffmann AL Prediction and Compensation of Magnetic Beam Deflection in MR-Integrated Proton Therapy: a Method Optimized Regarding Accuracy, Versatility and Speed. *Phys Med Biol* (2017) 62:1548–64. doi:10.1088/1361-6560/62/4/1548
39. GitHub, *Google/Googletest* (2021) Available from: https://github.com/google/googletest. (Accessed July 08, 2021).
40. GitHub, *Google/Benchmark* (2021) Available from: https://github.com/google/benchmark (Accessed July 08, 2021).
41. Boost C++ Libraries (2021) Available from: https://www.boost.org/ (Accessed July 09, 2021).
42. RapidXml (2009) Available from: http://rapidxml.sourceforge.net/ (Accessed July 08, 2021).
43. McCormick M, Liu X, Jomier J, Marion C, and Ibanez L ITK: Enabling Reproducible Research and Open Science. *Front Neuroinform* (2014) 8:13. doi:10.3389/fninf.2014.00013
44. Wilkens T dicom.offis.de - Home (2018). [cited 2021 Jul 10]. Available from: https://dcmtk.org/.
45. Schneider U, Pedroni E, and Lomax A The Calibration of CT Hounsfield Units for Radiotherapy Treatment Planning. *Phys Med Biol* (1996) 41:111–24. doi:10.1088/0031-9155/41/1/009
46. Parodi K, Ferrari A, Sommerer F, and Paganetti H Clinical CT-based Calculations of Dose and Positron Emitter Distributions in Proton Therapy Using the FLUKA Monte Carlo Code. *Phys Med Biol* (2007) 52:3369–87. doi:10.1088/0031-9155/52/12/004
47. Qin N, Pinto M, Tian Z, Dedes G, Pompos A, Jiang SB, et al. Initial Development of goCMC: a GPU-Oriented Fast Cross-Platform Monte Carlo Engine for Carbon Ion Therapy. *Phys Med Biol* (2017) 62:3682–99. doi:10.1088/1361-6560/aa5d43
48. Parodi K, Mairani A, and Sommerer F Monte Carlo-Based Parametrization of the Lateral Dose Spread for Clinical Treatment Planning of Scanned Proton and Carbon Ion Beams. *J Radiat Res* (2013) 54(1):i91–i96. doi:10.1093/jrr/rrt051
49. Tessonnier T, Marcelos T, Mairani A, Brons S, and Parodi K Phase Space Generation for Proton and Carbon Ion Beams for External Users' Applications at the Heidelberg Ion Therapy Center. *Front Oncol* (2015) 5:297. doi:10.3389/fonc.2015.00297
50. Seltzer SM An Overview of ETRAN Monte Carlo Methods. In: *Monte Carlo Transport of Electrons and Photons*. Boston, MA: Springer (1988). p. 153–81. doi:10.1007/978-1-4613-1059-4_7
51. Alex F Bielajew. "Electron Transport in E and B Fields. In: *Monte Carlo Transport of Electrons and Photons*. Boston, MA: Springer (1988). p. 421–34.
52. Duff T, Burgess J, Christensen P, Hery C, Kensler A, Liani M, et al. Building an Orthonormal Basis, Revisited. *J Comp Graphics Tech* (2017) 6:1–8.
53. Jackson JD *Classical Electrodynamics*. New York, NY: Wiley (1975).
54. Fano U Penetration of Protons, Alpha Particles, and Mesons. *Annu Rev Nucl Sci* (1963) 13:1–66. doi:10.1146/annurev.ns.13.120163.000245
55. Landau LD On the Energy Loss of Fast Particles by Ionization. *J Phys* (1944) 8:201–5.
56. Vavilov PV Ionization Losses of High-Energy Heavy Particles. *Soviet Phys JETP* (1957) 5:749–51.
57. Chibani O New Algorithms for the Vavilov Distribution Calculation and the Corresponding Energy Loss Sampling. *IEEE Trans Nucl Sci* (1998) 45:2288–92. doi:10.1109/23.725266
58. Moliere G Theorie der Streuung schneller geladener Teilchen II Mehrfach-und Vielfachstreuung. *Z für Naturforschung A* (1948) 3:78–97. doi:10.1515/zna-1948-0203
59. Scott WT The Theory of Small-Angle Multiple Scattering of Fast Charged Particles. *Rev Mod Phys* (1963) 35:231–313. doi:10.1103/RevModPhys.35.231
60. Rossi B, and Greisen K Cosmic-Ray Theory. *Rev Mod Phys* (1941) 13:240–309. doi:10.1103/RevModPhys.13.240
61. Highland VL Some Practical Remarks on Multiple Scattering. *Nucl Instr Methods* (1975) 129:497–9. doi:10.1016/0029-554x(75)90743-0
62. Frühwirth R, and Regler M On the Quantitative Modelling of Core and Tails of Multiple Scattering by Gaussian Mixtures. *Nucl Instr Methods Phys Res Section A: Acc Spectrometers, Detectors Associated Equipment* (2001) 456:369–89. doi:10.1016/s0168-9002(00)00589-1
63. Bellinzona VE, Ciocca M, Embriaco A, Fontana A, Mairani A, Mori M, et al. On the Parametrization of Lateral Dose Profiles in Proton Radiation Therapy. *Physica Med* (2015) 31:484–92. doi:10.1016/j.ejmp.2015.05.004
64. Kuhn SE, and Dodge GE A Fast Algorithm for Monte Carlo Simulations of Multiple Coulomb Scattering. *Nucl Instr Methods Phys Res Section A: Acc Spectrometers, Detectors Associated Equipment* (1992) 322:88–92. doi:10.1016/0168-9002(92)90361-7
65. Adelmann A, Calvo P, Frey M, Gsell A, Locans U, Metzger-Kraus C, et al. *OPAL a Versatile Tool for Charged Particle Accelerator Simulations*. arxiv: 1905.06654 (2019).
66. Bellinzona VE *A Non Gaussian Model for the Lateral Dose Evaluation in Hadrontherapy*. [PhD thesis]. Ludwig-Maximillians-University Munich (2017).

67. Tripathi RK, Wilson JW, and Cucinotta FA A Method for Calculating Proton-Nucleus Elastic Cross-Sections. *Nucl Instr Methods Phys Res Section B: Beam Interactions Mater Atoms* (2002) 194:229–36. doi:10.1016/s0168-583x(02)00690-0
68. Ranft J Estimation of Radiation Problems Around High-Energy Accelerators Using Calculations of the Hadronic cascade in Matter. *Part Accel* (1972) 3: 129–61.
69. Tripathi RK, Cucinotta FA, and Wilson JW Accurate Universal Parameterization of Absorption Cross Sections. *Nucl Instr Methods Phys Res Section B: Beam Interactions Mater Atoms* (1996) 117:347–9. doi:10.1016/0168-583X(96)00331-X
70. Tripathi RK, Cucinotta FA, and Wilson JW Accurate Universal Parameterization of Absorption Cross Sections III - Light Systems. *Nucl Instr Methods Phys Res Section B: Beam Interactions Mater Atoms* (1999) 155:349–56. doi:10.1016/s0168-583x(99)00479-6
71. Tessonnier T, Mairani A, Brons S, Haberer T, Debus J, and Parodi K Experimental Dosimetric Comparison of1H,4He,12C and16O Scanned Ion Beams. *Phys Med Biol* (2017) 62:3958–82. doi:10.1088/1361-6560/aa6516
72. Tessonnier T, Böhlen TT, Ceruti F, Ferrari A, Sala P, Brons S, et al. Dosimetric Verification in Water of a Monte Carlo Treatment Planning Tool for Proton, Helium, Carbon and Oxygen Ion Beams at the Heidelberg Ion Beam Therapy Center. *Phys Med Biol* (2017) 62:6579–94. doi:10.1088/1361-6560/aa7be4
73. Gajewski J, Garbacz M, Chang C-W, Czerska K, Durante M, Krah N, et al. Commissioning of GPU-Accelerated Monte Carlo Code FRED for Clinical Applications in Proton Therapy. *Front Phys* (2021) 8:403. doi:10.3389/fphy.2020.567300
74. Garbacz M, Battistoni G, Durante M, Gajewski J, Krah N, Patera V, et al. Proton Therapy Treatment Plan Verification in CCB Krakow Using Fred Monte Carlo TPS Tool. In: *World Congress on Medical Physics and Biomedical Engineering 2018*. Singapore: Springer (2019). p. 783–7. doi:10.1007/978-981-10-9035-6_144
75. Tessonnier T *Treatment of Low-Grade Meningiomas with Protons and Helium Ions*. [PhD thesis]. Ludwig-Maximillians-University Munich (2017).

Conflict of Interest: The authors declare that the research was conducted in the absence of any commercial or financial relationships that could be construed as a potential conflict of interest.

3.2 Development and benchmarking of the first fast Monte Carlo engine for helium ion beam dose calculation: MonteRay

Authors: **Peter Lysakovski**, Judith Besuglow, Benedikt Kopp, Stewart Mein, Alfredo Ferrari, Thomas Tessonnier, Thomas Haberer, Jürgen Debus, Andrea Mairani

Publication status: Published (21 December 2022)

Journal reference: Medical Physics

DOI: https://doi.org/10.1002/mp.16178

Authors' contributions: **PL** is the first author of this publication. **PL**, BK and AM were responsible for the conceptual design of the Monte Carlo engine. **PL**, BK, and AM developed the source code of the Monte Carlo engine. **PL** developed the scattering model. **PL**, TT, and AM worked on the analysis of data. **PL** generated all Figures besides Figure 4 which was generated by SM. AM generated the materials database, including elastic and inelastic nuclear cross sections. AF developed the code for the generation of inelastic nuclear databases from FLUKA. JB generated the inelastic nuclear databases. TT, JB, AM, and SM collected and provided experimental data used in this work. TT computed and provided the patient plan and SOBP plans. JD and TH provided clinical direction during project development, manuscript writing and project administration and funding acquisition.

Received: 10 May 2022 | Revised: 4 December 2022 | Accepted: 5 December 2022

DOI: 10.1002/mp.16178

RESEARCH ARTICLE

MEDICAL PHYSICS

Development and benchmarking of the first fast Monte Carlo engine for helium ion beam dose calculation: MonteRay

Peter Lysakovski[1,2] | **Judith Besuglow**[1,2,3,4,5] | **Benedikt Kopp**[1] | **Stewart Mein**[1,3,4,5] | **Thomas Tessonnier**[1,3] | **Alfredo Ferrari**[1] | **Thomas Haberer**[1] | **Jürgen Debus**[1,5,6] | **Andrea Mairani**[1,3,7]

[1]Heidelberg Ion-Beam Therapy Center (HIT), Department of Radiation Oncology, Heidelberg University Hospital, Heidelberg, Germany

[2]Faculty of Physics and Astronomy, Heidelberg University, Heidelberg, Germany

[3]Clinical Cooperation Unit Translational Radiation Oncology, German Cancer Consortium (DKTK) Core-Center Heidelberg, National Center for Tumor Diseases (NCT), Heidelberg University Hospital (UKHD) and German Cancer Research Center (DKFZ), Heidelberg, Germany

[4]Division of Molecular and Translational Radiation Oncology, Heidelberg Faculty of Medicine (MFHD) and Department of Radiation Oncology, Heidelberg University Hospital (UKHD), Heidelberg, Germany

[5]Heidelberg Institute of Radiation Oncology (HIRO), National Center for Radiation Oncology (NCRO), Heidelberg University Hospital (UKHD), Heidelberg Faculty of Medicine (MFHD) and German Cancer Research Center (DKFZ), Heidelberg, Germany

[6]Clinical Cooperation Unit Radiation Oncology, German Cancer Consortium (DKTK) Core-Center Heidelberg, National Center for Tumor Diseases (NCT), Department of Radiation Oncology, Heidelberg University Hospital (UKHD) and German Cancer Research Center (DKFZ), Heidelberg, Germany

[7]Medical Physics, National Centre of Oncological Hadrontherapy (CNAO), Pavia, Italy

Correspondence
Andrea Mairani, Heidelberg Ion-Beam Therapy Center (HIT), Department of Radiation Oncology, Heidelberg University Hospital, Heidelberg, Germany.
Email: Andrea.Mairani@med.uni-heidelberg.de

Funding information
German Federal Ministry of Education and Research (BMBF), Grant/Award Number: 13GW0436A

Abstract

Background: Monte Carlo (MC) simulations are considered the gold-standard for accuracy in radiotherapy dose calculation; however, general purpose MC engines are computationally demanding and require long runtimes. For this reason, several groups have recently developed fast MC systems dedicated mainly to photon and proton external beam therapy, affording both speed and accuracy.

Purpose: To support research and clinical activities at the Heidelberg Ion-beam Therapy Center (HIT) with actively scanned helium ion beams, this work presents MonteRay, the first fast MC dose calculation engine for helium ion therapy.

Methods: MonteRay is a CPU MC dose calculation engine written in C++, capable of simulating therapeutic proton and helium ion beams. In this work, development steps taken to include helium ion beams in MonteRay are presented. A detailed description of the newly implemented physics models for helium ions, for example, for multiple coulomb scattering and inelastic nuclear interactions, is provided. MonteRay dose computations of helium ion beams are evaluated using a comprehensive validation dataset, including measurements of spread-out Bragg peaks (SOBPs) with varying penetration depths/field sizes, measurements with an anthropomorphic phantom and FLUKA simulations of a patient plan. Improvement in computational speed is demonstrated in comparison against reference FLUKA simulations.

Results: Dosimetric comparisons between MonteRay and measurements demonstrated good agreement. Comparing SOBPs at 5, 12.5, and 20 cm depth, mean absolute percent dose differences were 0.7%, 0.7%, and 1.4%, respectively. Comparison against measurements behind an anthropomorphic head phantom revealed mean absolute dose differences of about 1.2% (FLUKA: 1.5%) with per voxel errors ranging from -4.5% to 4.1% (FLUKA: -6% to 3%). Computed global 3%/3 mm 3D-gamma passing rates of ∼99% were achieved, exceeding those previously reported for an analytical dose engine. Comparisons against FLUKA simulations for a patient plan revealed local 2%/2 mm 3D-gamma passing rates of 98%. Compared to FLUKA in voxelized geometries, MonteRay saw run-time reductions ranging from 20× to 60×, depending on the beam's energy.
Conclusions: MonteRay, the first fast MC engine dedicated to helium ion therapy, has been successfully developed with a focus on both speed and accuracy. Validations against dosimetric measurements in homogeneous and heterogeneous scenarios and FLUKA MC calculations have proven the validity of the physical models implemented. Timing comparisons have shown significant speedups between 20 and 60 when compared to FLUKA, making MonteRay viable for clinical routine. MonteRay will support research and clinical practice at HIT, for example, TPS development, validation and treatment design for upcoming clinical trials for raster-scanned helium ion therapy.

KEYWORDS
dose calculation, fast monte carlo, helium ions, radiotherapy

1 | INTRODUCTION

Since the shutdown of the Lawrence Berkeley National Laboratory (LBNL) cancer treatment trials,[1–3] helium ion beams have remained clinically unexploited worldwide, with few facilities hosting ion sources and acceleration/beam delivery systems for experimentation (HIT, NIRS-QST, GANIL, LNS, CNAO). However, interest in helium ion therapy is rising, due to their favorable physical and radio-biological properties intermediate of the major clinical ion beams, for instance, reduced lateral scattering, sharper penumbra, enhanced linear energy transfer (LET) and targeting compared to protons or a reduced fragmentation tail compared to carbon ions.[4] Helium ion therapy could potentially improve clinical outcomes in terms of local control or toxicity rates for sensitive cases such as in pediatrics.[5,6]

In July 2021, the Heidelberg Ion-Beam Therapy Center (HIT) began the world's first helium ion-beam therapy program by initiating the first patient treatment using active scanning delivery.[7] Prior to program initiation, extensive beam characterization and development, validation and benchmarking of a physics engine dedicated to helium ion dose calculation were necessary.[4,6,8] Monte Carlo (MC) codes are the preferred method for most accurately simulating the physics of particle interactions with matter. Helium ion beams produce a complex mixed radiation field, consisting of helium ions (^{4}He), protons, deuterons, tritons, ^{3}He particles and neutrons. Accurate modeling of this spectrum is critical to predict physical dose in both simple (e.g., water phantom for QA) and complex geometries like patients. For instance, FLUKA[9,10] MC is used at the HIT facility since start-up and supports clinical practice, providing a particle transport framework for a wide range of materials, particles and energies. When it comes to accuracy and flexibility, MC simulations like FLUKA MC, GEANT,[11] or PHITS[12] provide the gold standard. However, this comprehensive modeling of particle interactions with matter comes at the cost of increased runtime. Recent works have developed fast analytical dose engines for helium ions for both research and/or clinical investigations[13,14]; however, accuracy of these systems may be limited in highly heterogeneous anatomy and/or complex clinical scenarios.[15] Therefore, MC codes which provide both fast and accurate predictions are needed for research and clinical use.

In this work, we present the development and validation of MonteRay, the first rapid MC dose engine for helium ions, suitable for the energies available at HIT, covering an energy range from 0.1 MeV/u to 230 MeV/u. MonteRay provides dose predictions for proton[16] and helium ion therapy within an adaptable in-house framework. In detail, we outline the implemented physics models for electromagnetic (energy loss and scattering) and nuclear (elastic and inelastic) interactions. Benchmarking against measurements, for example, depth and lateral dose distributions, spread-out Bragg peaks (SOBPs), was performed with various dosimetric metrics. Validation of MonteRay was conducted

versus FLUKA MC on a patient case, as well as against measurements to test the accuracy in heterogeneous settings using an anthropomorphic head phantom.

2 | METHODS AND MATERIALS

The main features of MonteRay for proton beams have already been summarized in Lysakovski et al.[16] For the extension to helium ion beams, several changes and additions were made to the original code. Below, these will be described in detail and a general overview of the code will be given.

2.1 | Transport

During the simulation, helium ions (^{4}He) as well as protons, deuterons, tritons, ^{3}He particles (produced during nuclear interactions) are transported. In MonteRay, all particles undergo energy loss and scattering due to electromagnetic interactions, while only protons and helium ions undergo nuclear interactions. Nuclear interactions are not limited to primary particles but also take place for protons and helium ions which themselves were generated in nuclear interactions. MonteRay allows particle transport in either simple geometries, such as a homogenous water tank, or in voxelized geometries defined by importing a CT. Regardless of the chosen geometry, the transport of particles is always performed on a rectilinear grid and in each iteration the particle is transported to the beginning of the next grid cell. For protons and helium ions, this step can be cut short if a nuclear interaction is determined to take place along the way. Sampling of nuclear interactions is based on interaction cross sections defined for each material as described in Section 2.4. During each step, the particle loses energy (Section 2.3.1) and is deflected (Section 2.3.2) due to electromagnetic interactions. At the end of each step, the energy loss is recorded in one or multiple user-defined scoring geometries. To allow arbitrary combinations of transport and scoring grid sizes, the energy is deposited in a random location on the line connecting start and end position of the particle, avoiding aliasing effects due to grid mismatches or floating-point precision issues. Particle (protons, deuterons, tritons, 3-Helium and 4-Helium) transport is interrupted if a particle's kinetic energy falls below a user defined threshold (for this work 0.1 MeV/u), at which point the particle's remaining energy is deposited in one final step.

2.2 | Geometry and materials

The material classification of MonteRay can be divided into a discrete and a continuous part. For the discrete part we follow an approach similar to previous work.[17,18] Elemental compositions and nuclear interaction cross sections are defined for 40 materials including, among others, water, air and 35 compounds corresponding to Hounsfield Units (HU) in the range of −995 to 3070. Each material is composed of up to ten different elements (^{1}H, ^{12}C, ^{14}N, ^{16}O, ^{23}Na, ^{24}Mg, ^{31}P, ^{32}S, ^{35}Cl, ^{40}Ar, ^{39}K, ^{40}Ca and ^{48}Ti) and material compositions are given in terms of mass fractions, e.g. water is defined to consist of 11% hydrogen and 89% oxygen by mass. During simulation, each point in space is assigned exactly one of the available materials, that is, the elemental compositions of voxels are discretized. On the other hand, the density and stopping power ratio (SPR), are computed in a continuous manner from the HU values. For the density, the approach by Schneider et al.[19] is used. Like in clinical treatment planning systems, lookup tables are used for the conversion of HU values to SPR values. For some select materials, for example, air or PMMA, the SPR ratios were determined based on FLUKA simulations.

To summarize, for a given point in space we thus obtain:

- Nuclear interaction cross sections used to calculate the distance to the next nuclear event.
- A material and its corresponding elemental composition, used in the calculation of quantities needed for coulomb scattering and in the selection of per-element inelastic nuclear interaction tables.
- A density and a SPR, which are either derived from a HU value or specified by hand.

2.3 | Electromagnetic interactions

2.3.1 | Energy loss

The continuous energy loss of charged particles due to the interaction with atomic electrons is modeled via the mean stopping power of water. For each of the transported particles, the mean stopping power in water was obtained from FLUKA and stored between 0.01 MeV/n and 300 MeV/n. The stopping power in materials other than water is determined through the SPR. Energy loss straggling is simulated based on the method described in Chibani et al.[20] In our simulations, we only implement the Gaussian, the log-normal and the Landau distribution, that is, we do not implement the mixed-distribution approach described by Chibani et al.[20] We found that an exact reproduction of the single step energy loss distribution is not critical in practice. After less than 10 iterations, the convolution of multiple steps accurately reproduces the energy loss distribution when compared against FLUKA. In Figure 1a, the energy loss distribution of 150 MeV/u ^{4}He particles is shown for MonteRay

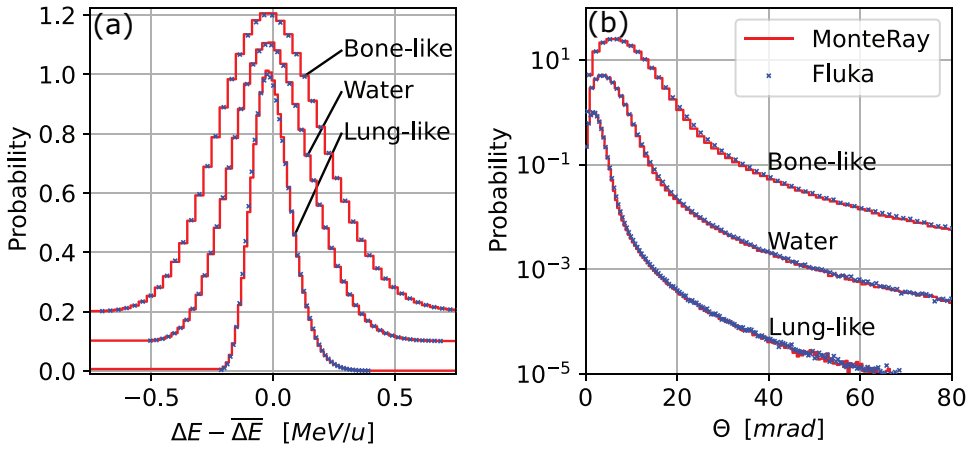

FIGURE 1 For 1 cm of three materials (Bone-like, Water and Lung-Like), the (a) Energy loss distributions relative to the mean energy loss of the respective materials and (b) distributions for the polar scattering angle Θ are shown. To avoid overlap, that is, for visual purposes, the curves in panel (a) are offset by 0.1 from another while the maxima of the curves in panel b) are normalized to 1, 5, and 25 (Lung-Like, Water, Bone-like)

and FLUKA. Three different materials with a thickness of 1 cm with MonteRay step sizes of 1 mm are shown.

2.3.2 | Multiple coulomb scattering

Elastic collisions of beam particles with atomic electrons lead to a broadening of the beam. The distribution of polar scattering angles θ after a particle has traversed a certain thickness dx of matter can be described by a distribution derived by Molière.[21] For simplicity, Molière introduced the scaled angle $\vartheta = \theta/(\chi_c B^{1/2})$, where B is a measure for the average number of collisions occurring along the path dx and χ_c is called the characteristic angle. Molière expressed the distribution of scattering angles $f(\vartheta)$ as an infinite sum of functions $f^n(\vartheta)$

$$f\ (\vartheta) = \sum \frac{\vartheta}{B^n} f^n(\vartheta)\ . \tag{1}$$

The first two terms of this expansion are f^0 and f^1 with

$$f^0\ (\vartheta) = \ 2\exp\left(-\vartheta^2\right) \tag{2}$$

and

$$f^1\ (\vartheta) = \ 2\cdot\exp\left(-\vartheta^2\right)\cdot\left(\left(\vartheta^2-1\right)\cdot\left(\mathrm{Ei}\left(\vartheta^2\right)\right.\right.$$
$$\left.\left.-\log\left(\vartheta^2\right)\right)+2-\exp\left(\vartheta^2\right)\right), \tag{3}$$

where Ei is the exponential integral function. While higher order terms become increasingly more complex to evaluate, their weight also decreases. Computing B for particle, material and energy configurations typical for radiotherapy MC simulations, one finds values of B between 5 and 20, resulting in a suppression factor of >100 for f^2.

MonteRay's approximation to Molière's distribution is similar to the one by Kuhn and Dodge[22] in that we use two separate functions to approximate the small angle and asymptotic large angle parts of Molière's distribution, corresponding to f^0 and f^1, respectively,

$$f\left(\vartheta\right) \approx f_{\mathrm{ray}}\left(\vartheta\right) + f_{\mathrm{ruth}}\left(\vartheta\right). \tag{4}$$

The small angle part of Molière's distribution can be approximated by a Rayleigh distribution, corresponding to the first term in Molière's expansion

$$f_{\mathrm{ray}}\ \left(\vartheta\right) = \ 2\vartheta\exp\left(-\vartheta^2\right). \tag{5}$$

Our choice of the asymptotic part differs from the one used by Kuhn and Dodge and is motivated by the behavior of Molière's distribution at large angles. According to Molière, the asymptotic behavior of the distribution for large angles is mostly determined by f^1, and since at large angles $f^1(\vartheta) \approx 2\vartheta^{-4} + O(\vartheta^{-6})$, we use

$$f_{\mathrm{ruth}}\left(\vartheta\right) = \begin{cases} \frac{2}{B\vartheta^3}, & \vartheta \geq k \\ 0, & \vartheta < k \end{cases}. \tag{6}$$

The exact choice of the cutoff k appears to be relatively unimportant for the shape of the distribution. Following Kuhn and Dodge, a value of $\sqrt{2}$ is used for k.

The angle ϑ can be sampled from this distribution using inverse transform sampling but to convert ϑ to the true polar angle θ, the material, particle and path length dependent quantities χ_c and B must be computed. MonteRay's computation of these constants is based on the summary given by Gottschalk et al.[23] The quantities relating to the incoming particle are the momentum p in units of MeV/c, the relativistic velocity β and its

charge z, given as a multiple of the elementary charge. The quantities relating to the traversed material are the density ρ in g/cm^3, the atomic numbers Z_i and relative atomic mass A_i of its constituent atoms and the mass fractions w_i of these atoms. Finally, the thickness of the material is denoted by dx. To compute χ_c and B for a given scattering event, the constants c_i are first computed for every elemental constituent of the traversed material

$$c_i = \frac{4\pi N_A (\hbar c)^2}{\alpha^2} \frac{z^2 Z_i^2 \rho}{w_i A_i} \approx 0.157 \text{ MeV}^2\text{cm}^2 \frac{z^2 Z_i^2 \rho}{w_i A_i}. \quad (7)$$

With N_A being Avogadro's number, $\alpha \approx 137^{-1}$ being the fine-structure constant and where $\hbar c$ is expressed in units of MeV cm. By defining the sum over all c_i as

$$c_{\text{tot}} = \sum c_i \,, \quad (8)$$

the characteristic angle χ_c can be computed via

$$\chi_c^2 = \frac{c_{\text{tot}} dx}{p^2 \beta^2} \,. \quad (9)$$

To compute B, the constants χ_a^i are first computed for every element via

$$\chi_a^{i\,2} = \chi_0^{i\,2} \left(1.13 + 3.76\alpha_i^2\right), \quad (10)$$

$$\alpha_i = \frac{z Z_i}{137\beta} \text{ and} \quad (11)$$

$$\chi_0^i = \frac{C_2 \sqrt[3]{Z_i}}{p} \,, \quad (12)$$

with $C_2 = 0.00421$ MeV/c. To account for the scattering of the incident particle from atomic electrons the correction term derived by Fano[25] is used

$$F_i = \frac{1}{Z_i} \left(\log \frac{1130 Z_i^{-\frac{4}{3}}}{\left(\frac{1}{\beta^2} - 1\right)} - u_{\text{in}} - \frac{1}{2}\beta^2 \right). \quad (13)$$

As suggested by Fano,[24] a value of -5 is used for u_{in}. With this,

$$\chi_a^{\text{tot}\,2} = \sum c_i \cdot \left(\log \left(\chi_a^{i\,2} \right) - F_i \right) \,, \quad (14)$$

$$\chi_a^2 = \frac{\chi_a^{\text{tot}\,2} dx}{\chi_c^2 p^2 \beta^2} \text{ and} \quad (15)$$

$$\log_{10}\Omega = \frac{\log\left(\chi_c^2\right) - \chi_a^2}{\log(10)} \quad (16)$$

and finally, the linear approximation by Scott[26] is used to compute B

$$B = 1.153 + 2.583 * \log_{10}\Omega. \quad (17)$$

The strength of the presented approach lies in the fact that it does not rely on the introduction of ad-hoc finely tuned empirical constants or pre-computed lookup tables. In Figure 1b, the angular distributions of 150 MeV/u helium ions traversing 1 cm of Water, a Lung-Like material and a Bone-like material are shown. The MonteRay simulations were performed with a fixed step size of 1 mm and a total of 10^7 particles histories were followed.

2.4 | Nuclear interactions

In MonteRay, protons and helium ions can undergo nuclear interactions. These are treated separately from the electromagnetic interactions mentioned in the previous chapter. As nuclear interactions happen infrequently, they are not grouped together like electromagnetic interactions are. Instead, each nuclear interaction is treated as a point like event. The distance to the next nuclear event is sampled at each transport step and if this distance is less than the distance to the next voxel, the step is cut short and we enter the nuclear interaction routine.

2.4.1 | Elastic nuclear interactions

Like FLUKA, MonteRay only considers elastic nuclear interactions of helium ions with hydrogen atoms. Similarly, De Simoni et al.[26] report that their carbon dose engine FRED only considers carbon-hydrogen elastic nuclear interactions. Protons on the other hand, as described previously,[16] undergo elastic nuclear interactions with all ten available elements.

The elastic cross section of helium ions was extracted from FLUKA and tabulated for energies ranging from 0.1 MeV/u to 500.1 MeV/u. For the elastic nuclear interaction itself, helium ions that interact with hydrogen atoms are first boosted into a frame of reference where the helium ion is at rest and the hydrogen atom is considered as the projectile. With this, the interaction process can use the same formalism as previously presented for protons,[16] based on the work of Ranft et al.[27] Afterwards, the resulting particles are boosted back into the initial frame of reference and transport continues.

2.4.2 | Inelastic nuclear interactions

In particle therapy, inelastic nuclear scattering events generate the mixed radiation field, that is, photons, protons, neutrons, deuterons, tritons, ^{3}He particles, helium

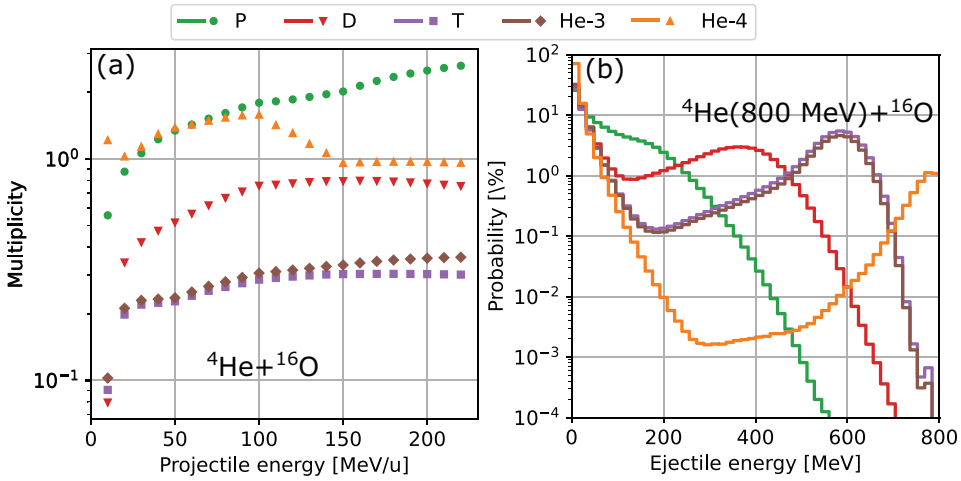

FIGURE 2 Panel (a) Weights of secondary particles produced in MonteRay as a function of projectile energy for inelastic collisions between ^{4}He and ^{16}O. Panel (b) For an incoming 800 MeV ^{4}He projectile and a ^{16}O target the energy distributions of produced secondaries are shown. Blue, orange, green, red and violet points/curves represent protons, deuterons, tritons, ^{3}He particles and helium ions, respectively

ions (^{4}He) and heavier fragments (nuclear recoils). For the handling of proton beams, photons and neutrons were assumed to be dosimetrically irrelevant and they were neither transported nor produced.[16] To verify that the same could be applied for helium ion beams, FLUKA simulations were run for an energy range of 50–220 MeV/u, and it was found that the contribution of photons and neutrons to the integrated depth dose distribution in water was smaller than 0.03% and therefore they are also neglected for helium ion beams.

Like the elastic cross section, the total inelastic cross sections of helium ions are tabulated from 0.1 MeV/u to 500.1 MeV/u, however they are tabulated for all ten elements inside MonteRay, and not just for hydrogen. The tabulated inelastic cross sections are calculated based on the work by Tripathi et al.,[28,29] but with the corrections proposed by Horst et al.,[30] which are based on measurements performed at HIT.

To model the production of secondary particles, a database of nuclear event probabilities was generated based on nuclear models used internally by FLUKA. The database covers a helium ion energy range from 10 MeV/u to 230 MeV/u, in steps of 10 MeV/u. For projectiles below 10 MeV/u, MonteRay randomly choses whether a nuclear interaction takes place (using the 10 MeV/u database) or not. For each available element and product particle, a 100 × 100 large table stores the production probabilities as a function of the produced particles solid angle and kinetic energy. While for protons, both the energy and the angular binning was linear, for helium a logarithmic binning for the storage of solid angles was chosen. The resulting 100 angular bins divide the interval 0 to 4π such that the ratio of two subsequent angular bins is constant, that is, $\frac{\Omega_{i+1}}{\Omega_i} = 1.139$. This convention is adopted from how FLUKA scores boundary crossing events.

If an inelastic nuclear event occurs during simulation, all possible products for the current target nucleus are created but assigned weights corresponding to the probability that they would occur in any given interaction. For example, in Figure 2a these weights are shown for a ^{16}O target as a function of the incoming helium ion's energy. Energy and direction of the secondary particles are chosen according to the probabilities encoded in the database and in Figure 2b, the energy distributions of produced secondary particles for 800 MeV helium ions are shown.

The effect of the resulting mixed radiation field is shown in Figure 3. Here, MonteRay and FLUKA simulated doses of 200 MeV/u helium ions incident on water are shown with the total dose broken up into the individual contributions of the available ions.

2.5 | Benchmarks

2.5.1 | Pristine Bragg peaks – depth dose distributions

To evaluate the accuracy of implemented energy loss and nuclear interaction models, measured integral depth dose distributions (IDDD) were compared against MonteRay simulations. Measurements were recorded at HIT using a PEAKFINDER water column (PTW, Freiburg) with the measurement setup previously described by Tessonnier et al.[31] For this comparison, 15 recorded IDDDs with energies ranging from 50 MeV/u to 200 MeV/u were available. Each individual IDDD consisted of between 90 and 300 individual measurements with the highest density of measurements around the BP region (step sizes down to 0.05 mm). The detectors radius of 4.08 cm was taken into account in MonteRay

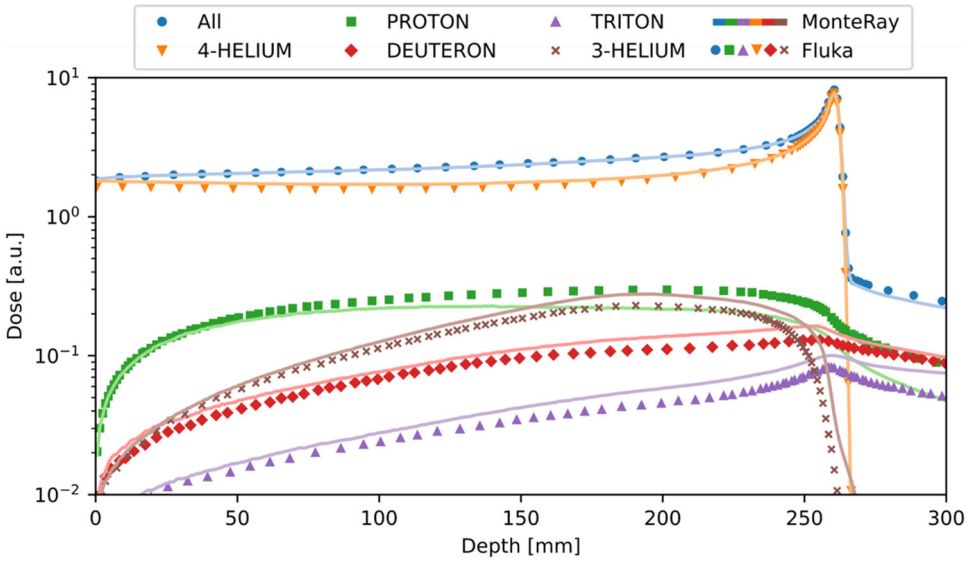

FIGURE 3 Comparison of integrated depth-dose distributions (IDDD) of 200 MeV/u ^{4}He ions incident on water computed with FLUKA and MonteRay. The total IDDDs (blue) are broken down by particle type: ^{4}He (orange), Proton(green), Deuteron(red), Triton(purple) and 3-Helium(brown). FLUKA runs are indicated through symbols while MonteRay runs are displayed as solid lines

when scoring the simulated dose. Particle tracking and scoring were performed on a $0.1 \times 0.1 \times 0.1$ mm^3 grid. The grids high resolution was necessary to accurately capture the IDDDs in high gradient regions, especially for low energies. For each beam, 10^6 primaries were simulated.

For the comparisons of measured dose to simulated dose, the IDDDs were normalized to 1 in the BP and relative errors calculated according to

$$\epsilon = 200 \left| \frac{d_{sim} - d_{meas}}{d_{sim} + d_{meas}} \right| [\%]. \quad (18)$$

2.5.2 | Pristine Bragg peaks – lateral dose distributions

As the comparison of IDDDs provides very limited information about the validity of the scattering model implemented, measured lateral dose distributions in water were compared against MonteRay simulations. The measurement process was described by Besuglow et al.[32] in detail. Briefly: A 2D-ionization chamber array (OCTAVIUS, PTW Freiburg) was used to obtain 2D dose distributions at multiple depths in water. The 2D detector consists of an array of 977 ionization chambers with a size of $2.3 \times 2.3 \times 0.5$ mm^3. Irradiation was performed with approximately 10^9 helium ions incident on a water tank equipped with a PMMA sleave for housing the detector. Lateral dose distributions obtained at 10 different energies ranging from 82 to 201 MeV/u were recorded with the number of different positions recorded per energy ranging from 3 to 42. For comparison with simulations, 1D dose distributions were extracted from the measurements and corresponding simulated dose distributions were scored in MonteRay for comparison, using 10^7 primary particles per run.

2.5.3 | Spread out Bragg peaks

MonteRay was compared against measured SOBPs in water, planned doses of 1 Gy were delivered to a cubic region of $6 \times 6 \times 6$ cm^3, centered at depths of 5, 12.5 and 20 cm in water. The energies of the three SOBPs ranged from 52 MeV/u to 107 MeV/u, 115 MeV/u to 151 MeV/u and 158 MeV/u to 190 MeV/u, respectively. Data acquisition was carried out using a three-dimensional array of 24 PinPoint ionization chambers (TM31015, PTW Freiburg). A detailed description of the array of ionization chambers was given by Karger et al.,[33] and the same measurement setup has previously been used for verification purposes.[16,34]

2.5.4 | Anthropomorphic phantom

For verification in heterogeneous conditions, an anthropomorphic head phantom (Alderson phantom Radiology Support Devices, Long Beach, CA, USA) was used. Generation of the irradiation plan and data collection has been described by Mein et al.[35] In short, the plan was optimized using a FLUKA-based treatment planning tool with a target dose of 1 Gy in a $6 \times 6 \times 6$ cm^3 cubic volume centered 7 cm behind the phantoms backplate. The plan included energies ranging from 115 MeV/u to 180 MeV/u. Delivery of the plan was performed in HITs experimental room. Behind the phantom, PMMA

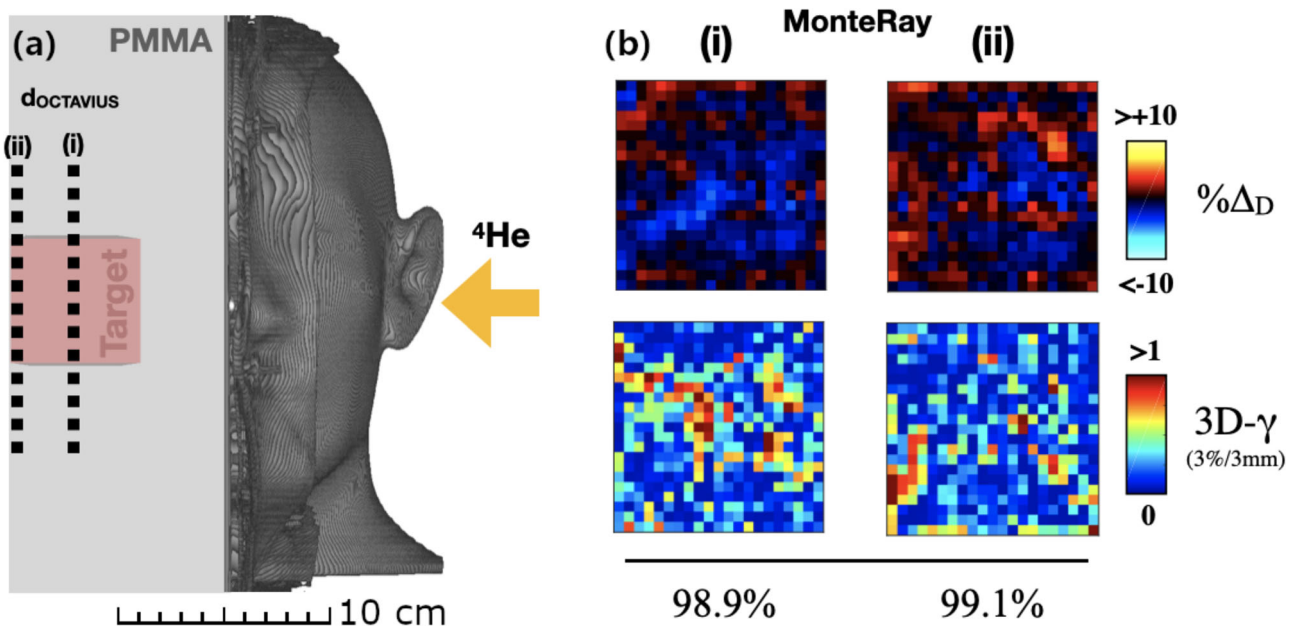

FIGURE 4 Panel (a) Schematic of experimental setup used for acquiring the data. 2D lateral slices were obtained at the locations marked (i) and (ii), corresponding to one slice in the middle of the SOBP and one near the distal edge. Panel (b) Comparison of MonteRay simulated doses against measurements in terms of relative dose difference (top row) and 3D-γ index (bottom row) for slices (i) and (ii). Computed 3D-γ passing rates for the two slices are given below

plates were used to position the OCTAVIUS detector (see Section 2.5.2) at depths of 7 and 10 cm behind the phantoms backplate. In Figure 4a, a schematic of the experimental setup can be seen. MonteRay simulations were carried out with 2% of the plan's total particle number. For comparison with previously reported results,[35] global 3D-γ index analysis was performed at 3%/3 mm.

2.5.5 | Patient plan

The patient plan was generated using the clinical TPS RayStation 10A (RaySearch Laboratories, Stockholm, Sweden) with an anonymized patient dataset representative of a meningioma treatment. Optimization was carried out on the PTV ($\sim$112 cm^3) with a target dose of 54 GyRBE. For the initial parameters of the optimization, two beams and a hexagonal spot pattern with 2.4 mm spot spacing and an energy spacing of 3.1 mm were chosen. The minimum number of particles per spot was set to 150000. The final plan included energies ranging from 87 to 150 MeV/u. In accordance with Bauer et al.,[36] FLUKA simulations were carried out with 1% of the total number of particles to reach a statistical uncertainty of around 1%, while MonteRay simulations were run with 2% of the total number of particles, resulting in a similar dose uncertainty of 1.1%.

For comparison with MonteRay, local 3D-γ analysis was carried out using the python package pymedphys (version 0.37.1) with a 2%/2 mm criterion and a low dose threshold of 5%. Prior to computing the 3D$-\gamma$ values, the dose computed by MonteRay was interpolated trilinearly to match the reference dose grid of the FLUKA simulation.

3 | RESULTS

3.1 | Pristine Bragg peaks – depth dose distributions

In total, 15 measured IDDDs with energies ranging from 50 to 200 MeV/u were compared with simulations performed in MonteRay. Before computing dose differences, MonteRay computed doses were shifted along the beam direction to match the measurements in terms of range (R_{80}). The shifts applied ranged from 0 mm to 0.12 mm, with a mean of 0.05 mm across all compared energies. For the analysis of relative errors ϵ (Equation 18), the high gradient region after the BP was omitted. In Figure 5a, IDDDs of six exemplary energies are displayed and in Figure 5b detailed relative error distributions are given in terms of box plots with individual relative dose differences indicated through black dots. Agreement of simulated to measured dose distributions was good with errors ranging from $+-1\%$ at lower to $+-3\%$ at higher energies. Averaging over all the measurements, mean relative errors between 0.3% and 1.4% were observed for the different energies. The maximum observed relative error was -2.7% at the highest energy of 201.7 MeV/u. Looking at the displayed curves in Figure 5a, we see that MonteRay tends to

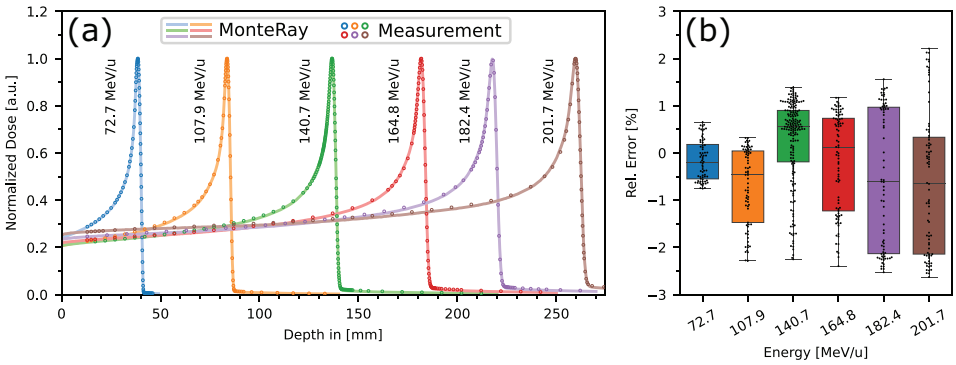

FIGURE 5 Panel (a) Normalized IDDDs for six beam energies are shown. Dose simulated by MonteRay is shown as solid lines while measurements are indicated through circles. Panel (b) The dose difference in percent is quantified using standard box plots. Bottom, middle and top bars of the boxes represent 25%, 50%, and 75% percentiles. The whiskers extend up to the minimum/maximum values. Dose differences from individual measurements are indicated through black dots

underestimate the dose in the entrance and rising part of the BP compared to the peak itself.

3.2 | Pristine Bragg peaks – lateral dose distributions

In total, lateral dose distributions of beams at 10 quasi-monoenergetic energies were compared against simulations. Prior to comparison, pre-processing steps were necessary. As shown in Section 3.1, small differences in range between MonteRay simulations and measurements were observed. To allow comparison of absolute dose in the high gradient BP region despite of this, alignment of the 2D dose distributions along the beam axis was necessary. For this, 1D depth dose distributions were extracted along the central axis, and a curve fit between measured and simulated dose distributions was performed, allowing the shift as a free parameter. The so obtained shifts were between 2 mm and 3.4 mm. Then, for each energy and for each available measured profile at that energy, the FWHM was determined through a gaussian fit for both measurements and simulated doses, making sure to account for the previously determined shift when selecting dose distributions at given depths. Here, day-to-day variations in beam width, ranging from −15 to +25%,[34] have to be considered. To account for this, the FWHM values were matched at the entrance, ensuring that observed differences do not stem from the starting conditions. In Figure 6a, the computed FWHM values are displayed for the highest energy of 201.7 MeV/u. For this energy, the differences in FWHM are between 0 mm and −0.3 mm. In Figure 6b,c, 1D dose distributions at a depth of 41.59 mm (first measurement) and 258.39 mm (measurement at BP) for 201.7 MeV/u are shown. In Figure 6d the differences in FWHM for all observed energies and depths are displayed in a box plot. Black dots indicate individual computed FWHM differences. Across all comparisons, the maximum differences observed were +0.2 mm/−0.37 mm.

3.3 | Spread out Bragg peaks

After remaining range uncertainties (<0.4 mm) were corrected for, SOBPs simulated with MonteRay were compared to measurements. Since the ionization chambers are not arranged in a rectilinear grid, a direct comparison of extracted 1D dose distributions is not possible. Instead, the dose obtained by MonteRay was interpolated on a 3D grid and dose values at exact 3D locations were extracted from the interpolant for comparison. Measurements located in the high gradient region of the SOBP and at the distal end were excluded during analysis. For plotting and comparison, 1D dose distributions were generated from the measurements by averaging over all values within the 6 × 6 cm^2 central region at a certain depth. In Figure 7a, depth dose distributions of the three SOBPs are shown while panels b), c), and d) show lateral dose distributions extracted from the central region of the three SOBPs. Considering each measurement individually, dose differences between −1%/−2.4%/−1.8% and +1.5%/+1.8%/3.6% for the SOBPs at 5 cm/12.5 cm/20.0 cm depth were observed. Averaged over all individual measurements, mean absolute dose differences were 0.7%, 0.7%, and 1.4%, respectively. Qualitatively, the lateral dose distributions show good agreement between MonteRay simulated doses and measured values.

3.4 | Anthropomorphic phantom

The two-dimensional dose distributions recorded with the OCTAVIUS detector are displayed in Figure 4b for the two depths, mid-SOBP (i) and near the distal edge of the SOBP (ii). In the upper row of Figure 4b, dose

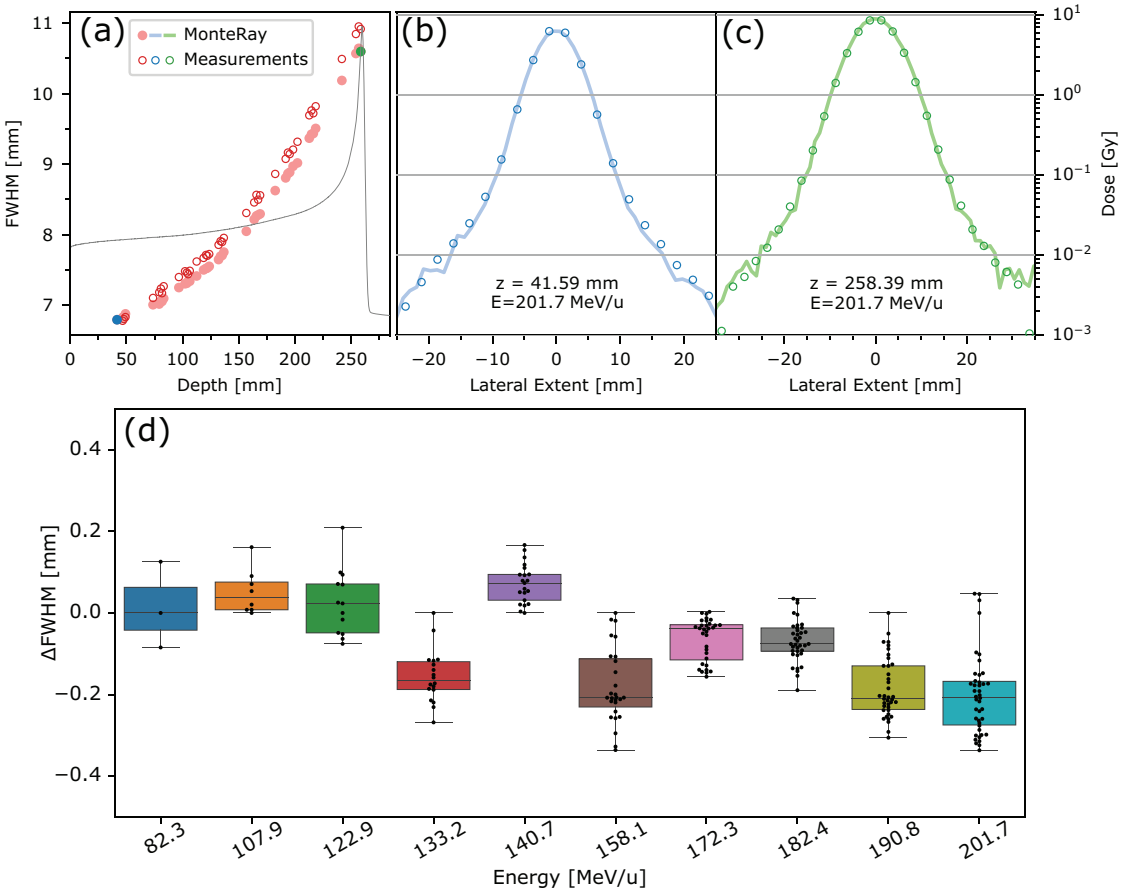

FIGURE 6 Top row: For a beam energy of 201.7 MeV/u, FWHM values computed from measurements and from MonteRay simulations are displayed in panel (a) MonteRay results are shown as solid red circles and measurements are indicated by rings. For orientation, the light grey line shows the corresponding depth-dose-profile. Blue and green circles indicate the locations of the lateral 1D dose distributions in panels (b) and (c), respectively. Panel (d) Boxplots show the distribution of FWHM differences between MonteRay and measurements. Boxes indicate standard 25%, 50%, and 75% percentiles while whiskers indicate minimum/maximum values. Black dots inside boxes indicate FWHM differences at individual depths

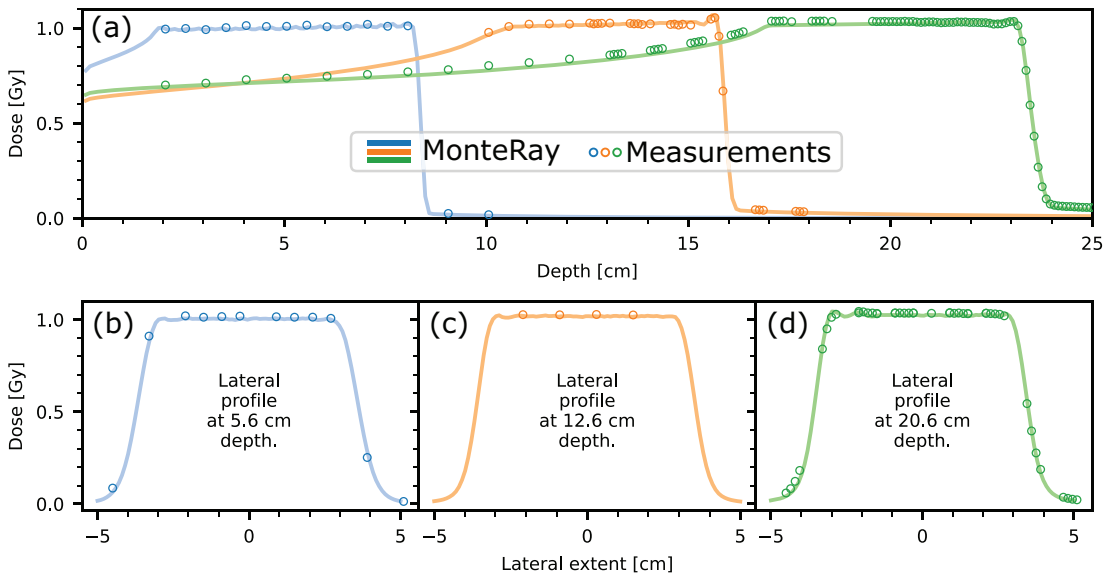

FIGURE 7 Top row: Depth dose distributions averaged over the 6 × 6 cm^2 central region of the SOBP are shown for MonteRay simulations (solid lines) and measurements (circles) for three different SOBP depths of 5 cm, 12.5 and 20 cm. Bottom row: Lateral dose distributions extracted from the central region of the three SOBPs at depths of 5.6 cm (b), 12.6 cm (c), and 20.6 cm (d) are shown

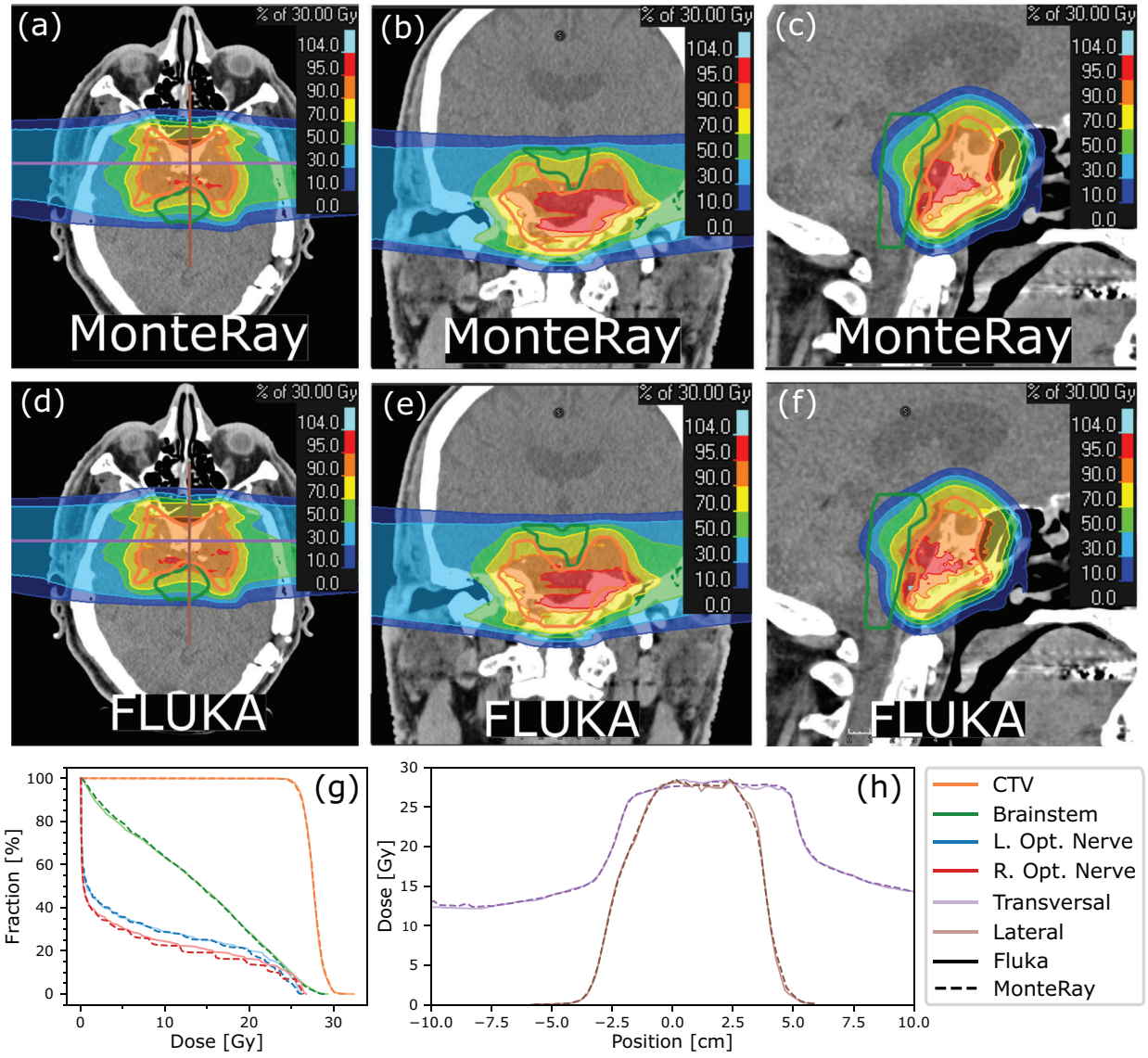

FIGURE 8 In panels a–f, 2D dose distributions calculated with MonteRay (top row) and with FLUKA (bottom row) are shown. The left, center and right columns correspond to axial, coronal and sagittal 2D dose distributions, respectively. In panel g, DVHs computed from FLUKA and MonteRay for the CTV, the Brainstem and the left/right optical nerves are shown. In panel h, line profiles (lateral and transversal) extracted from the depth dose distributions at the indicated locations in panel a and d are shown

differences in percent between MonteRay and measurements are shown. In the lower row, computed 3D-γ values are shown with computed passing rates written below. For the mid-SOBP (distal edge) slice, minimum dose differences were −4.5% (−4.4%) while maximum dose differences were 3.4% (4.1%). Averaging the absolute relative error over all voxels, values of 1.2% (1.2%) were obtained. For both slices, approximately 99% of all pixels passed the 3%/3 mm 3D-γ criterion.

3.5 | Patient plan

In panels a) to f) of Figure 8, resulting simulated doses for the patient plan are shown. Axial, coronal and sagittal slices are displayed in the left, center and right column, respectively. MonteRay doses are given in the top row (a-c) while FLUKA doses are given in the center row (d-f). Visual inspection of 2D profiles yielded good agreement and computed 2%/2 mm 3D-γ passing rates of 98.6% confirm this. For further analysis, dose volume histograms (DVH) for several regions of interest (CTV, brain stem, left optical nerve, right optical nerve) were computed and are displayed in panel g). The contours of the CTV (orange) and the brainstem (green) are indicated through solid lines in panels a) to f). Analysis of the DVHs in terms of D2%/D50%/D98% for the CTV and in terms of D1%/D2%/D5% for different organs at risk (OAR) was performed and is summarized in Table 1. For the CTV, excellent agreements within −0.1%

TABLE 1 Comparison of MonteRay and FLUKA patient plan dose calculations in terms of D2%, D50%, and D98% for the CTV and D1%, D2%, and D5% for the OARs

	D2			D50			D98		
ROI name	**FLUKA [Gy]**	**MR [Gy]**	**Diff. [%]**	**FLUKA [Gy]**	**MR [Gy]**	**Diff. [%]**	**Fluka [Gy]**	**MR [Gy]**	**Diff. [%]**
CTV	29.9	29.9	−0.1	27.6	27.7	−0.2	25.3	25.2	0.7
	D1			**D2**			**D5**		
ROI Name	**Fluka [Gy]**	**MR [Gy]**	**Diff. [%]**	**FLUKA [Gy]**	**MR [Gy]**	**Diff. [%]**	**FLUKA [Gy]**	**MR [Gy]**	**Diff. [%]**
Chiasma	27.3	27.4	−0.2	27.1	27.3	−0.5	27.0	27.2	−0.4
Brainstem	28.0	27.9	0.4	27.6	27.4	0.5	26.4	26.2	0.7
Left optical nerve	25.9	25.7	0.7	25.8	25.7	0.6	25.6	25.0	2.4
Right optical nerve	26.5	26.4	0.4	26.4	26.2	0.9	26.2	25.7	2.0
Brain	27.8	27.8	0.2	27.0	26.9	0.4	20.1	19.7	2.3

TABLE 2 End-to-end runtimes of MonteRay and FLUKA for 10^6 helium ions incident on a voxelized water geometry. The standard error of the mean is used as a measure of uncertainty and was calculated from five samples

Energy [MeV/u]	FLUKA time [s]	MonteRay time [s]	Speedup
50	777 ± 2	13.6 ± 0.4	57 ± 2
100	1653 ± 3	50.6 ± 0.5	32.7 ± 0.3
150	2976 ± 5	119.8 ± 0.3	24.9 ± 0.1
200	4730 ± 14	230 ± 1	20.6 ± 0.1

to 0.7% in these metrics was found. For the OARs differences in D1%/D2%/D5% were between −0.5% and 2.4%. Finally, in panel h) extracted 1D line profiles (position indicated through violet and brown lines in panels a) and d)) are shown for MonteRay and FLUKA. Again, good agreement can be observed.

3.6 | Runtime comparisons

End-to-end runtimes of MonteRay were compared to those of FLUKA on a sample problem with 50–200 MeV/u helium ions incident on a voxelized water tank geometry with a grid-spacing of $1 \times 1 \times 1$ mm^3. To obtain accurate runtimes, five runs with 10^6 primary particles each were timed. All runs were performed on a single core of an otherwise idle Intel i7-9700k processor. In Table 2, run times of FLUKA and MonteRay and computed speedups are summarized. The tracking rates for helium ions varied from 4300 to 74000 primaries per second for MonteRay with speedups approximately ranging from 20 to 60.

4 | DISCUSSION

In this work, the extension of MonteRay for the simulation of helium ion beams was presented and the accuracy and speed of the engine assessed. Dosimetric comparisons were performed on a variety of scenarios like pristine Bragg peaks, SOBPs and anthropomorphic targets. Measurements and FLUKA computations served as references and MonteRay achieved good accuracy on all scenarios.

Comparisons of depth-dose profiles of helium ion beams in water showed agreement within ± 3% against measurements. This is comparable to dose-differences previously reported for FLUKA in similar scenarios.[4] In comparison, previously reported results of MonteRay with proton beams revealed errors within −3% to +1% over the HIT therapeutic range.[17] This regression can possibly be explained by uncertainties in nuclear interaction cross sections. While recent data on cross sections of helium ions by Horst et al.[31] were taken into account, the large uncertainties reported could impact the accuracy of dose distribution predictions, possibly explaining in part the differences in terms of dose distributions observed here. Additionally, the lack of experimental data in terms of double differential secondary fragment spectra motivates future studies on interaction cross sections of helium ions. One promising candidate for this could be the FOOT project.[38]

Moving on to more complex scenarios, MonteRay calculations were performed on an anthropomorphic head phantom and an exemplary patient plan. Comparing the former against measurements and the latter against FLUKA simulations, excellent agreement was found. On the anthropomorphic phantom case, 3D-γ passing rates were ∼99%, matching those previously reported for FLUKA and exceeding those previously reported for an in-house analytical dose engine (93%).[36] The improved accuracy of MonteRay may hint at the necessity of using MC based dose calculation algorithms for helium ion therapy in highly heterogenous targets compared to classic analytical dose engine. Also, MC-computations could improve the dose prediction accuracy compared to analytical dose engine when beam modifiers such as range shifters are needed for treatment.[16] Regardless, extensive analysis will have to be performed to truly

understand whether a helium ion MC engine is needed in clinical practice or if an analytical algorithm, like the one featured in the TPS currently used at the HIT facility (RayStation), is sufficient.

The FLUKA comparisons for the patient plan have shown good agreement in terms of 3D-γ passing rates (>98%) and dose differences, with clinically relevant metrics like DVHs matching well.

In this work, a new and improved multiple coulomb scattering model for MonteRay was introduced. It does not rely on empirically determined constants to deal with different material, particle types or step sizes. Instead, Molière's scattering distribution was approximated making use of the fact that it is approximately proportional to θ^{-4} for large scattering angles θ. Sampling from the so derived distribution can be performed quickly using inverse transform sampling and all quantities necessary are computed analytically starting from basic material properties, like atomic composition or density. To benchmark the scattering models accuracy, comparisons of simulated lateral line profiles with measurements were carried out. Good agreements in FWHM within $\pm$ 0.4 mm, corresponding to a relative difference of $\pm$ 5%, at all evaluated energies and depths were observed. A downside of the newly developed approach is that the evaluation of the equations presented in Section 2.3.2 is cost intensive. Despite efforts to accelerate the computation of the necessary quantities χ_c and B (see section 2.3.2), for example, by pre-computing material constants, ~15%–20% of the total computational time, is spent in the scattering routine. This is caused by the need to evaluate expressions (e.g., Equation 15) which contain computationally costly transcendental function calls. Future work will focus on further accelerating these parts, for example by using suitable approximations to further simplify calculations of material constants.

Similarly, the energy loss straggling calculations based on the work of Chibani et al.[20] present another computational bottleneck with another 10%–20% of the computational time spent there. Consequently, development of faster energy loss straggling algorithms would be of great interest for the future acceleration of MC simulations.

Finally, general purpose MC simulations are still the gold standard for dose computation but are limited in clinical use due to time constraints. To that end, the development of MonteRay focused not only on accuracy but also on speed to make it clinically viable. As a result, MonteRay achieved runtimes 20–60 times faster than FLUKA on identical hardware. Like other recent fast MC engines, these speedups are made possible by a simplified treatment of physics. This includes approximations for the energy loss based on the work of Chibani et al.,[21] the newly developed multiple scattering model and the use of pre-computed inelastic nuclear interaction databases. These databases, generated using the powerful and time-tested nuclear models contained within FLUKA, allow MonteRay to avoid detailed computation of complex inelastic nuclear interaction processes. As a bonus, MonteRay will be able to directly make use of future improvements made to FLUKA's interactions models.[7] In addition to this, the database driven approach has the advantage to be easily extensible to other types of particles, and therefore, MonteRay can potentially be extended towards the simulation of carbon ion beams.

Qin et al[39] have previously shown that accurate carbon ion dose calculation based on nuclear interaction databases extracted from GEANT are possible. Further work on MonteRay will intend to see how using FLUKA databases performs, especially since de Simoni et al.[27] recently reported on their implementation of carbon ion inelastic nuclear interactions based on a phenomenological model, also achieving accurate dose predictions.

5 | CONCLUSION & OUTLOOK

The extension of the dose calculation engine MonteRay to include helium ion beams has shown that fast MC simulation of ^{4}He-ion treatment plans is possible. Good accuracy against measurements and FLUKA simulations were achieved with runtimes approximately 20–60 times faster than FLUKA. While these speedups are good, the goal is to accelerate MonteRay even further to improve usability. A promising avenue for this is GPU acceleration, which has proven successful in several other MC engines.

Having the capability of simulating helium ions, MonteRay can serve as a fast and accessible tool for ongoing and future research projects, starting with the upcoming clinical trial using helium ions at HIT as well as foreseen helium ion FLASH investigation, helium ion spot-scanning hadron arc therapy[39,40] or, with a possible extension towards carbon ions in mind, multi-ion therapy.[41,42]

The inclusion of carbon ions in MonteRay is expected soon, as the modern C++ codebase and reuse of the successful database driven approach for modeling nuclear interactions will speed up the process.

Finally, a clinically viable dose engine for helium ions will require a variable RBE model and future development of MonteRay will focus on implementing LET/RBE weighting of dose.

ACKNOWLEDGMENTS

The authors acknowledge financial support through the German Federal Ministry of Education and Research (BMBF) (Grant number: 13GW0436A).

CONFLICT OF INTEREST

The authors have no conflicts of interest to declare.

REFERENCES

1. Castro JR, Quivey JM. Clinical experience and expectations with helium and heavy ion irradiation. *Int J Radiat Oncol Biol Phys*. 1977;3:127-131. doi:10.1016/0360-3016(77)90238-3
2. Saunders W, Castro JR, Chen GT, et al. Helium-ion radiation therapy at the Lawrence Berkeley Laboratory: recent results of a Northern California Oncology Group Clinical Trial. *Radiat Res Suppl*. 1985;8:S227-34.
3. Castro JR, Chen GTY, Blakely EA. Current considerations in heavy charged-particle radiotherapy: a clinical research trial of the university of California Lawrence Berkeley laboratory, northern California oncology group, and radiation therapy oncology group. *Radiat Res*. 1985;104(2):S263. doi:10.2307/3576656
4. Tessonnier T, Mairani A, Brons S, et al. Helium ions at the heidelberg ion beam therapy center: comparisons between FLUKA Monte Carlo code predictions and dosimetric measurements. *Phys Med Biol*. 2017;62(16):6784-6803. doi:10.1088/1361-6560/aa7b12
5. Knäusl B, Fuchs H, Dieckmann K, Georg D. Can particle beam therapy be improved using helium ions? A planning study focusing on pediatric patients. *Acta Oncol*. 2016;55(6):751-759. doi:10.3109/0284186X.2015.1125016
6. Tessonnier T, Mairani A, Chen W, et al. Proton and helium ion radiotherapy for meningioma tumors: a Monte Carlo-based treatment planning comparison. *Radiat Oncol*. 2018;13(1):2. doi:10.1186/s13014-017-0944-3
7. Mairani A, Mein S, Blakely EA, et al. Roadmap: helium ion therapy. *Phys Med Biol*. 2022;67(15). doi:10.1088/1361-6560/ac65d3
8. Tessonnier T, Böhlen TT, Ceruti F, et al. Dosimetric verification in water of a Monte Carlo treatment planning tool for proton, helium, carbon and oxygen ion beams at the Heidelberg Ion Beam Therapy Center. *Phys Med Biol*. 2017;62(16):6579-6594. doi:10.1088/1361-6560/aa7be4
9. Ferrari A, Sala PR, Fasso A, Ranft J. FLUKA: a multi-particle transport code. 2005. doi:10.2172/877507
10. Böhlen TT, Cerutti F, Chin M, et al. The FLUKA code: developments and challenges for high energy and medical applications. *Nucl Data Sheets*. 2014;120:211-214. doi:10.1016/j.nds.2014.07.049
11. Agostinelli S, Allison J, Amako K, et al. Geant4—a simulation toolkit. *Nucl Instrum Methods Phys Res A*. 2003;506(3):250-303. doi:10.1016/S0168-9002(03)01368-8
12. Sato T, Iwamoto Y, Hashimoto S, et al. Features of particle and heavy ion transport code system (PHITS) version 3.02. *J Nucl Sci Technol*. 2018;55(6):684-690. doi:10.1080/00223131.2017.1419890
13. Mein S, Choi K, Kopp B, et al. Fast robust dose calculation on GPU for high-precision 1H, 4He, 12C and 16O ion therapy: the FRoG platform. *Sci Rep*. 2018;8(1):14829. doi:10.1038/s41598-018-33194-4
14. Fuchs H, Alber M, Schreiner T, Georg D. Implementation of spot scanning dose optimization and dose calculation for helium ions in Hyperion. *Med Phys*. 2015;42(9):5157-5166. doi:10.1118/1.4927789
15. Widesott L, Lorentini S, Fracchiolla F, Farace P, Schwarz M. Improvements in pencil beam scanning proton therapy dose calculation accuracy in brain tumor cases with a commercial Monte Carlo algorithm. *Phys Med Biol*. 2018;63(14):145016. doi:10.1088/1361-6560/aac279
16. Lysakovski P, Ferrari A, Tessonnier T, et al. Development and benchmarking of a monte Carlo dose engine for proton radiation therapy. *Front Phys*. 2021;9:655. doi:10.3389/fphy.2021.741453
17. Jiang H, Paganetti H. Adaptation of GEANT4 to Monte Carlo dose calculations based on CT data. *Med Phys*. 2004;31(10):2811-2818. doi:10.1118/1.1796952
18. Parodi K, Ferrari A, Sommerer F, Paganetti H. Clinical CT-based calculations of dose and positron emitter distributions in proton therapy using the FLUKA Monte Carlo code. *Phys Med Biol*. 2007;52(12):3369-3387. doi:10.1088/0031-9155/52/12/004
19. Schneider W, Bortfeld T, Schlegel W. Correlation between CT numbers and tissue parameters needed for Monte Carlo simulations of clinical dose distributions. *Phys Med Biol*. 2000;45(2):459-478. doi:10.1088/0031-9155/45/2/314
20. Chibani O. New algorithms for the Vavilov distribution calculation and the corresponding energy loss sampling. *31st Nucl Sci Symp, 16th Symp on Nucl Power Syst*. 1998;45(5):2288-2292. doi:10.1109/23.725266
21. Gert Moliere. Theorie der Streuung schneller geladener Teilchen II Mehrfach-und Vielfachstreuung. *Zeitschrift für Naturforschung A*. 203;(2):78-97. https://www.degruyter.com/document/doi/10.1515/zna-1948-0203/html
22. Kuhn SE, Dodge GE. A fast algorithm for Monte Carlo simulations of multiple Coulomb scattering. *Nucl Instrum Methods Phys Res A*. 1992;322(1):88-92. doi:10.1016/0168-9002(92)90361-7
23. Gottschalk B, Koehler AM, Schneider RJ, Sisterson JM, Wagner MS. Multiple Coulomb scattering of 160 MeV protons. *Nucl Instrum Methods Phys Res, Sect B*. 1993;74(4):467-490. doi:10.1016/0168-583X(93)95944-Z
24. Fano U. Inelastic collisions and the molière theory of multiple scattering. *Phys Rev*. 1954;93(1):117-120. doi:10.1103/PhysRev.93.117
25. Scott WT. The theory of small-angle multiple scattering of fast charged particles. *Rev Mod Phys*. 1963;35(2):231-313. doi:10.1103/RevModPhys.35.231
26. Simoni Mde, Battistoni G, Gregorio Ade, et al. A data-driven fragmentation model for carbon therapy GPU-Accelerated Monte-Carlo dose recalculation. *Front Oncol*. 2022;12. doi:10.3389/fonc.2022.780784
27. Ranft J. Estimation of radiation problems around high-energy accelerators using calculations of the hadronic cascade in matter. *Part Accel* 1972;3:130-131. https://s3.cern.ch/inspire-prod-files-a/aa63ebed9dad980c37c221a107b81d89
28. Tripathi RK, Cucinotta FA, Wilson JW. Accurate universal parameterization of absorption cross sections. *Nucl Instrum Methods Phys Res, Sect B*. 1996;117(4):347-349. doi:10.1016/0168-583X(96)00331-X
29. Tripathi RK, Cucinotta FA, Wilson JW. Accurate universal parameterization of absorption cross sections III – light systems. *Nucl Instrum Methods Phys Res, Sect B*. 1999;155(4):349-356. doi:10.1016/s0168-583x(99)00479-6
30. Horst F, Aricò G, Brinkmann K-T, et al. Measurement of He 4 charge-and mass-changing cross sections on H, C, O, and Si targets in the energy range 70-220 MeV/u for radiation transport calculations in ion-beam therapy. *Phys Rev C*. 2019;99(1):14603.
31. Tessonnier T, Mairani A, Brons S, Haberer T, Debus J, Parodi K. Experimental dosimetric comparison of 1H, 4He, 12C and 16O scanned ion beams. *Phys Med Biol*. 2017;62(10):3958-3982. doi:10.1088/1361-6560/aa6516
32. Besuglow J, Tessonnier T, Kopp B, Mein S, Mairani A. The evolution of lateral dose distributions of helium ion beams in air: from measurement and modeling to their impact on treatment planning. *Front Phys*. 2022;9:3-3. doi:10.3389/fphy.2021.797354
33. Karger CP, Jäkel O, Hartmann GH. A system for three-dimensional dosimetric verification of treatment plans in intensity-modulated radiotherapy with heavy ions. *Med Phys*. 1999;26(10):2125-2132. doi:10.1118/1.598728
34. Tessonnier T, Marcelos T, Mairani A, Brons S, Parodi K. Phase space generation for proton and carbon ion beams for external users' applications at the heidelberg ion therapy center. *Front Oncol*. 2015;5:297. doi:10.3389/fonc.2015.00297
35. Mein S, Kopp B, Tessonnier T, et al. Dosimetric validation of Monte Carlo and analytical dose engines with raster-scanning 1H, 4He, 12C, and 16O ion-beams using an anthropomorphic phantom. *Phys Med*. 2019;64:123-131. doi:10.1016/j.ejmp.2019.07.001

36. Bauer J, Sommerer F, Mairani A, et al. Integration and evaluation of automated Monte Carlo simulations in the clinical practice of scanned proton and carbon ion beam therapy. *Phys Med Biol*. 2014;59(16):4635-4659. doi:10.1088/0031-9155/59/16/4635
37. Battistoni G, Toppi M, Patera V, Collaboration TF. Measuring the impact of nuclear interaction in particle therapy and in radio protection in space: the FOOT experiment. *Front Phys*. 2021;8. doi:10.3389/fphy.2020.568242
38. Qin N, Pinto M, Tian Z, et al. Initial development of goCMC: a GPU-oriented fast cross-platform Monte Carlo engine for carbon ion therapy. *Phys Med Biol*. 2017;62(9):3682-3699. doi:10.1088/1361-6560/aa5d43
39. Mein S, Kopp B, Tessonnier T, et al. Spot-scanning hadron arc (SHArc) therapy: A proof of concept using single- and multi-ion strategies with helium, carbon, oxygen, and neon ions. *Med Phys*. 2022;49(9):6082-6097. doi:10.1002/mp.15800
40. Mein S, Tessonnier T, Kopp B, et al. Spot-scanning hadron arc (SHArc) therapy: a study with light and heavy ions. *Adv Radiat Oncol*. 2021;6(3):100661. doi:10.1016/j.adro.2021.100661
41. Kopp B, Mein S, Dokic I, et al. Development and validation of single field multi-ion particle therapy treatments. *Int J Radiat Oncol Biol Phys*. 2020;106(1):194-205. doi:10.1016/j.ijrobp.2019.10.008
42. Inaniwa T, Kanematsu N, Shinoto M, Koto M, Yamada S. Adaptation of stochastic microdosimetric kinetic model to hypoxia for hypo-fractionated multi-ion therapy treatment planning. *Phys Med Biol*. 2021;66(20). doi:10.1088/1361-6560/ac29cc

How to cite this article: Lysakovski P, Besuglow J, Kopp B, et al. Development and benchmarking of the first fast Monte Carlo engine for helium ion beam dose calculation: MonteRay. *Med Phys*. 2023;50:2510–2524. https://doi.org/10.1002/mp.16178

3.3 Development and validation of MonteRay, a fast Monte Carlo dose engine for carbon ion beam radiotherapy

Authors: **Peter Lysakovski**, Benedikt Kopp, Thomas Tessonnier, Stewart Mein, Alfredo Ferrari, Thomas Haberer, Jürgen Debus, Andrea Mairani
Publication status: Published (25 September 2023)
Journal reference: Medical Physics
DOI: https://doi.org/10.1002/mp.16754
Authors' contributions: **PL** is the first author of this publication. **PL**, BK and AM were responsible for the conceptual design of the Monte Carlo engine. **PL**, BK, and AM developed the source code of the Monte Carlo engine. **PL** generated the materials database, including elastic and inelastic nuclear cross sections. AF developed the code for the generation of inelastic nuclear databases from FLUKA. **PL** generated the inelastic nuclear databases. **PL** generated all Figures besides Figure 6 which was generated by SM. **PL**, TT, and AM worked on the analysis of data. TT, AM, and SM collected and provided experimental data used in this work. TT computed and provided the patient plan and SOBP plans. AF provided technical guidance for the generation of inelastic nuclear databases. JD and TH provided clinical direction during project development, manuscript writing and project administration and funding acquisition.

Received: 18 June 2023 | Revised: 25 August 2023 | Accepted: 11 September 2023

DOI: 10.1002/mp.16754

RESEARCH ARTICLE

MEDICAL PHYSICS

Development and validation of MonteRay, a fast Monte Carlo dose engine for carbon ion beam radiotherapy

Peter Lysakovski[1,2] | **Benedikt Kopp**[1] | **Thomas Tessonnier**[1,3] | **Stewart Mein**[1,3,4,5,6] | **Alfredo Ferrari**[1] | **Thomas Haberer**[1] | **Jürgen Debus**[1,5,7] | **Andrea Mairani**[1,3,8]

[1]Heidelberg Ion-Beam Therapy Center (HIT), Department of Radiation Oncology, Heidelberg University Hospital, Heidelberg, Germany

[2]Faculty of Physics and Astronomy, Heidelberg University, Heidelberg, Germany

[3]Clinical Cooperation Unit Translational Radiation Oncology, German Cancer Consortium (DKTK) Core-Center Heidelberg, National Center for Tumor Diseases (NCT), Heidelberg University Hospital (UKHD) and German Cancer Research Center (DKFZ), Heidelberg, Germany

[4]Division of Molecular and Translational Radiation Oncology, Heidelberg Faculty of Medicine (MFHD) and Department of Radiation Oncology, Heidelberg University Hospital (UKHD), Heidelberg, Germany

[5]Heidelberg Institute of Radiation Oncology (HIRO), National Center for Radiation Oncology (NCRO), Heidelberg University Hospital (UKHD), Heidelberg Faculty of Medicine (MFHD) and German Cancer Research Center (DKFZ), Heidelberg, Germany

[6]Department of Radiation Oncology, University of Pennsylvania, Philadelphia, Pennsylvania, USA

[7]Clinical Cooperation Unit Radiation Oncology, German Cancer Consortium (DKTK) Core-Center Heidelberg, National Center for Tumor Diseases (NCT), Department of Radiation Oncology, Heidelberg University Hospital (UKHD) and German Cancer Research Center (DKFZ), Heidelberg, Germany

[8]Medical Physics, National Centre of Oncological Hadrontherapy (CNAO), Pavia, Italy

Correspondence
Andrea Mairani, Heidelberg Ion-Beam Therapy Center (HIT), Department of Radiation Oncology, Heidelberg University Hospital, Heidelberg, Germany.
Email: Andrea.Mairani@med.uni-heidelberg.de

Funding information
German Federal Ministry of Education and Research (BMBF), Grant/Award Number: 13GW0436A

Abstract

Background: Monte Carlo (MC) simulations are considered the gold-standard for accuracy in radiotherapy dose calculation; so far however, no commercial treatment planning system (TPS) provides a fast MC for supporting clinical practice in carbon ion therapy.

Purpose: To extend and validate the in-house developed fast MC dose engine MonteRay for carbon ion therapy, including physical and biological dose calculation.

Methods: MonteRay is a CPU MC dose calculation engine written in C++ that is capable of simulating therapeutic proton, helium and carbon ion beams. In this work, development steps taken to include carbon ions in MonteRay are presented. Dose distributions computed with MonteRay are evaluated using a comprehensive validation dataset, including various measurements (pristine Bragg peaks, spread out Bragg peaks in water and behind an anthropomorphic phantom) and simulations of a patient plan. The latter includes both physical and biological dose comparisons. Runtimes of MonteRay were evaluated against those of FLUKA MC on a standard benchmark problem.

Results: Dosimetric comparisons between MonteRay and measurements demonstrated good agreement. In terms of pristine Bragg peaks, mean errors between simulated and measured integral depth dose distributions were between –2.3% and +2.7%. Comparing SOBPs at 5, 12.5 and 20 cm depth, mean absolute relative dose differences were 0.9%, 0.7% and 1.6%

respectively. Comparison against measurements behind an anthropomorphic head phantom revealed mean absolute dose differences of $1.2\% \pm 1.1\ \%$ with global 3%/3 mm 3D-γ passing rates of 99.3%, comparable to those previously reached with FLUKA (98.9%). Comparisons against dose predictions computed with the clinical treatment planning tool RayStation 11B for a meningioma patient plan revealed excellent local 1%/1 mm 3D-γ passing rates of 98% for physical and 94% for biological dose. In terms of runtime, MonteRay achieved speedups against reference FLUKA simulations ranging from 14× to 72×, depending on the beam's energy and the step size chosen.

Conclusions: Validations against clinical dosimetric measurements in homogeneous and heterogeneous scenarios and clinical TPS calculations have proven the validity of the physical models implemented in MonteRay. To conclude, MonteRay is viable as a fast secondary MC engine for supporting clinical practice in proton, helium and carbon ion radiotherapy.

KEYWORDS
carbon ions, dose calculation, fast Monte Carlo, radiotherapy

1 | INTRODUCTION

In radiotherapy, carbon ions can offer advantageous dose distributions for clinics that seek new-age treatments for inoperable diseases with poor prognosis using conventional radiation therapy or chemotherapy.[1] Currently, 14 facilities using carbon ion beams are in operation and further seven are either under construction or in planning.[2] Treatment planning systems (TPS) for carbon ions that are used in clinics use analytical dose calculation algorithms for calculating physical and biological dose distributions.[3–8] These typically rely on external databases (based on Monte Carlo [MC] simulations or experimental data) to describe the interaction of carbon ion radiation in water in terms of depth-dose distributions, lateral dose distributions and nuclear fragment spectra.[6,7] Conventional MC simulations like FLUKA,[9,10] GEANT[11] or PHITS[12] are the gold standard when it comes to accuracy but their detailed modeling of particle interactions with matter comes at the cost of increased runtime. In two recent works, fast MC dose engines for carbon ions have been developed.[13,14] However, these have been validated only against predictions of general-purpose MC codes without any dosimetric verification in a clinical facility against measurements. Further, neither of these works have presented any comparisons in terms of biological dose, a key quantity in carbon ion beam radiotherapy.

Recently, the MC engine MonteRay was presented for the fast calculation of proton and helium ion beam dose distributions.[15,16] In this work, the extension of MonteRay towards carbon ion beams is presented. The implemented physical models for electromagnetic and nuclear interactions will be explained in detail. For verification, dosimetric comparisons against measurements in homogeneous and heterogeneous scenarios were performed. To evaluate the accuracy of MonteRay in a clinical scenario, both physical and biological dose distributions of an exemplary meningioma case were compared with dose predictions computed with the clinically used TPS RayStation (RaySearch Laboratories).

2 | METHODS AND MATERIALS

Some parts of MonteRay, like the implementation of energy loss straggling or multiple Coulomb scattering, have already been presented in previous work.[15,16] These will only be described briefly here. Besides changes specific to carbon ion beams, for example the addition of new inelastic nuclear interactions, some general changes to the code will be described below. For example, this includes the implementation of geometry handling routines.

2.1 | Transport and geometry

During the simulation of carbon ion beams, primary carbon ions and fragments produced in nuclear interactions are transported. This includes the following particles: ^{1}H, ^{2}H, ^{3}H, ^{3}He, ^{4}He, ^{6}Li, ^{7}Li, ^{8}Li, ^{9}Li, ^{11}Li, ^{7}Be, ^{8}Be, ^{9}Be, ^{10}Be, ^{11}Be, ^{8}B, ^{10}B, ^{11}B, ^{12}B, ^{11}C and ^{12}C. All of these undergo energy loss and scattering due to electromagnetic interactions (Section 2.2) but only a subset is able to undergo nuclear interactions themselves (see Section 2.3). For the definition of the simulation environment, elemental compositions, mass densities and nuclear interaction cross sections are defined for 42 different compounds following an approach similar to previous works.[16–19] Both inelastic and elastic cross sections of particles undergoing nuclear interactions were extracted from FLUKA and tabulated for energies ranging from 0.1 MeV/u to 500.1 MeV/u. For treatment

plan recalculations, TPS-specific lookup tables are used for the conversion of Hounsfield units (HU) to stopping power ratios (SPR).

Besides nuclear interaction cross sections, per-element fragmentation spectra are needed for the simulation of nuclear interactions. For each particle undergoing nuclear interactions, these were computed for the following thirteen elements: ^{1}H, ^{12}C, ^{14}N, ^{16}O, ^{23}Na, ^{24}Mg, ^{31}P, ^{32}S, ^{35}Cl, ^{40}Ar, ^{39}K, ^{40}Ca and ^{48}Ti. For two elements, Nickel and Tungsten, no nuclear interaction cross sections are currently included since they are only used in modelling the HIT specific beamline and don't occur in the human body in significant amounts.

In previous versions of MonteRay, phase-space files of the beam at the isocenter were used for initializing primary particles. This had the downside of having to generate the phase-space in advance. Especially the inclusion of beam shaping devices like a range shifter or a ripple filter was problematic as it required multiple sets of phase-spaces to be available at runtime. To improve flexibility in terms of supported geometries, this phase-space based approach has been superseded by a model of the HIT beamline together with a simple parametrization of the beam before the beamline, consisting of a single gaussian in terms of energy spread and position. This was made possible through the implementation of geometry handling routines based on the principle of constructive solid geometry, similar to PENGEOM[20] or the FLUKA implementation. This makes it possible to define a simulation environment composed of simple shapes such as planes, rectangles or cylinders combined through Boolean expressions to form more complex shapes. During initialization of the simulation, the user-provided Boolean expressions that define the world are read in, transformed into their conjunctive normal form and from them, a reduced order binary decision diagram is constructed using the algorithm described by Andersen.[21] During transport, this tree-like structure is traversed to determine which region a particle is currently in, and which region the particle's trajectory will intersect next.

For performance reasons, the geometry of the beam monitoring system, whose FLUKA model consists of hundreds of primitive shapes, was approximated through a single slab of material with equivalent mean elemental composition and density. Only the tungsten wires that are part of the multiwire proportional chambers were modeled explicitly as their influence on the depth dose distribution is visible for low energies, especially without a ripple filter.[6] Similarly, while it is possible to implement the ripple filter using a combination of triangular prisms and rectangles, this would require the calculation of many intersections to traverse it. Instead, the ripple filter was modeled via a set of piecewise linear functions which define a polygon that is periodic along the x-axis and infinitely extended along the y-axis. With this implementation, the traversal of the ripple filter requires only two intersections for most primary particles.

The continuous energy loss of charged particles due to the interaction with atomic electrons is modeled via the mean stopping power of water which was extracted from FLUKA assuming an ionization potential of water of 77 eV. This is in line with the value used by Parodi et al.[6] The stopping power in other materials is assumed to be equal to that of water besides a constant, particle independent factor, the so-called SPR.

Now, let E_m denote the particle's kinetic energy divided by the particles atomic mass m_a. As a function of E_m, the stopping power $S_w(E_m)$ of a particle in water is approximately independent of the particle's atomic mass, and particles with identical atomic numbers have similar stopping powers. Consequently, the tabulation of stopping powers in MonteRay was not done for individual particles but for atomic numbers one to six, covering all particle species transported in MonteRay. In addition to the stopping power, the quantity $R_w(E_m)$ was pre-computed and tabulated

$$R_w\ (E_m) = \int_0^{E_m} \frac{dE'_m}{S_w\left(E'_m\right)}\ . \tag{1}$$

This can be used as a way of computing the traversed pathlength Δx of a particle that starts with an energy E_m^{start} and ends at with energy E_m^{end} since:

$$\Delta x\ = \int_{E_m^{\text{start}}}^{E_m^{\text{end}}} \frac{dE'_m}{S_w\left(E'_m\right)}\ = \left(R_w\left(E_m^{\text{end}}\right) - R_w\left(E_m^{\text{start}}\right)\right). \tag{2}$$

As the step size in MonteRay is defined in terms of energy lost (not distance traveled) this quantity is crucial in estimating the range of the particle. The advantage of using R_w over S_w for the estimation of Δx lies in the fact that the particle loses energy over the step and R_w allows to take this into account since the integral is implicitly included as according to Equation (2). Both R_w and S_w are among the most frequently accessed quantities in MonteRay (owing to the energy scoring approach presented below) and as a result, a fast computation of them is critical. For this purpose, they are approximated through piecewise 4th order polynomial fits which allow an accurate tabulation with few bins (40 currently), ergo few memory accesses. This approach was also used to tabulate biological data and linear energy transfer (LET) tables used for the calculation of biological dose and LET. These quantities, too, are frequently accessed since they are needed whenever scoring occurs.

During particle transport, the particle takes a sequence of discrete steps. At the end of each step, the particle loses energy (Section 2.2.1) and is deflected

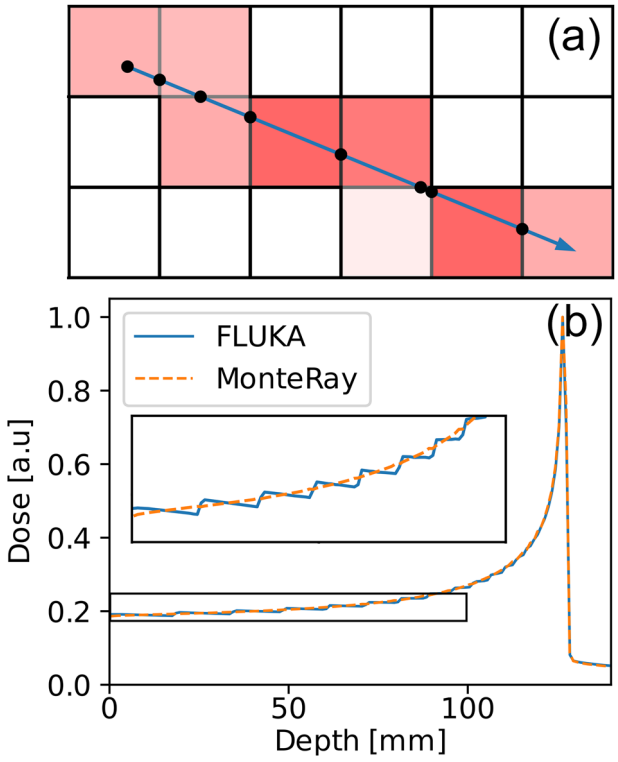

FIGURE 1 (a) Schematic visualization of scoring in MonteRay. An exemplary 2D scoring grid is shown with a single particle step (blue arrow). Shades of red indicate the dose deposited (white = low dose, red = high dose). Black dots show intersections with the scoring grid. The stopping power is recomputed at every intersection. (b) Depth dose distribution of 250 MeV/u carbon ions incident on water with a fractional energy loss of 10% in both MonteRay and FLUKA. Inside the figure, a zoomed in section is included to better show the sawtooth pattern observed when one does not recompute the stopping power in each scoring bin.

(Section 2.2.2) due to electromagnetic interactions. If a scoring grid is defined at the particle's location, the energy lost during the step is recorded in that scorer. For this, it is distributed across the scorer's voxels in proportion to the length of the particles track in each voxel. For this voxel traversal, an algorithm based on the work of Amanatides and Woo[22] is used. A schematic of the scoring process is given in (Figure 1a). There, the arrow indicates the path traveled by a particle in a single step, that is energy loss, deflection and nuclear interactions would only be handled at the beginning and end of the arrow. At each intersection with the scoring grid, indicated through black dots, the stopping power is evaluated using the previously described polynomial interpolator. In principle this will allow MonteRay to have larger steps without distorting the deposited dose. Qualitatively, this is demonstrated in (Figure 1b) where both FLUKA and MonteRay depth dose distributions of 250 MeV/u carbon ions in water with a fractional energy loss of 10% are shown. A distinct sawtooth pattern appears in the FLUKA dose but recalculation of the stopping power in each scoring cell allows to avoid this pattern while still taking large steps.

In this work, the step-size was chosen as follows. Firstly, a hard limit in terms of the length of the step is imposed by:

1. The distance to the boundary of the region the particle is currently in which is determined using the new geometry routines.
2. The distance to the next nuclear interaction, sampled from an exponential distribution using the mean free path tabulated for each particle and compound.

Next, a limit in terms of the energy that may be lost by the particle in one step is imposed. For the simulations presented here, the energy loss fraction f was chosen such that

1. it is at least 2% (similar to the step size used by FLUKA when default settings for hadron therapy are chosen);
2. it is at most 25% (this limit was also chosen by Qin et al.[13]);
3. within this range the energy loss fraction is chosen such that the step length of the particle in water is approximately equal to the voxel size of the scoring grid Δx_g.

It is then given by the following equation

$$f = \min\left(0.25, \max\left(0.02, \frac{\Delta x_g S_w(E_m)}{E}\right)\right). \quad (3)$$

The implemented voxel traversal algorithm is able to detect when a particle has insufficient energy to leave the voxel in which it is currently in and aborts transport, depositing all the particle's energy in that voxel.

Energy deposition is recorded as MeV per Voxel during simulation but eventually is converted to Gy when writing the output to a file. No calibration in terms of absolute dose was done for the results presented in this work and dose values reported are a direct consequence of physical interactions by the number of particles specified in the irradiation plan.

2.2 | Electromagnetic interactions

2.2.1 | Energy loss straggling

Energy loss straggling is simulated based on the method described in Chibani[23] and applied in Lysakovski et al.[15] using the Gaussian, the log-normal and the Landau distribution. As an example of the reproduction of energy loss distributions by MonteRay, in (Figure 2a), the energy loss distribution of 300 MeV/u ^{12}C ions is shown for

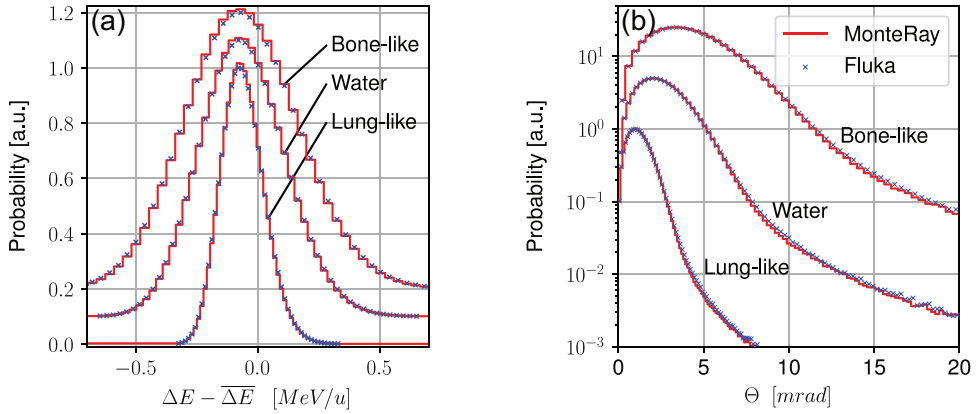

FIGURE 2 Distributions of (a) the energy loss relative to the mean energy loss and (b) the polar scattering angle Θ are shown for 1 cm of three materials (Bone-like, Water and Lung-Like). For visual purposes, the curves in panel (a) are offset by 0.1 from another while the maxima of the curves in panel (b) are normalized to 1, 5 and 25.

MonteRay and FLUKA. Three different materials (water, bone-like and lung-like) with a thickness of 1 cm with MonteRay step sizes of 1 mm are shown.

2.2.2 | Multiple Coulomb scattering

Broadening of the beam is caused by elastic collisions of beam particles with atomic electrons. After traversing a certain thickness of matter, the distribution of polar scattering angles θ of the particle is approximately described by a distribution derived by Molière.[24] MonteRay's approximation of Molière's distribution has been described in detail in Lysakovski et al.[16] No modifications were required to extend it from protons and helium ions to carbon ions. This is a clear strength of the model employed. Briefly, it uses two separate functions to approximate the small angle and asymptotic large angle parts of Molière's distribution in terms of the scaled angle $\vartheta = \theta/(\chi_c B^{1/2})$

$$f(\vartheta) \approx f_{\text{ray}}(\vartheta) + f_{\text{ruth}}(\vartheta) \tag{4}$$

where B is a measure for the average number of collisions occurring along the path Δx and χ_c is called the characteristic angle. The small angle part of Molière's distribution can be approximated by a Rayleigh distribution, corresponding to the first term in Molière's expansion

$$f_{\text{ray}}(\vartheta) = 2\vartheta \exp\left(-\vartheta^2\right) \tag{5}$$

For the asymptotic large part MonteRay uses

$$f_{\text{ruth}}(\vartheta) = \begin{cases} \frac{2}{B\vartheta^3}, & \vartheta \geq \sqrt{2} \\ 0, & \vartheta < \sqrt{2} \end{cases}. \tag{6}$$

The angle ϑ can be sampled from this distribution using inverse transform sampling but to convert ϑ to the true polar angle θ, the material, particle and path length dependent quantities χ_c and B must be computed. MonteRay's computation of these constants is based on the summary given by Gottschalk et al.[25] and was described in Lysakovski et al.[16] This approach is used for all ions in MonteRay and no particle or energy dependent scaling factors had to be introduced like it was done for goCMC[13] or FRED[14] for carbon ions. In (Figure 2b), the angular distributions of 300 MeV/u ^{12}C ions traversing 1 cm of water, a lung-like material and a bone-like material are shown. The MonteRay simulations were performed with a fixed step size of 1 mm using 10 million particles histories.

2.3 | Nuclear interactions

In MonteRay, carbon ions undergoing inelastic nuclear interactions create a wide range of secondary particles: ^{1}H (proton), ^{2}H (deuteron), ^{3}H (triton), ^{3}He, ^{4}He, ^{6}Li, ^{7}Li, ^{8}Li, ^{9}Li, ^{11}Li, ^{7}Be, ^{8}Be, ^{9}Be, ^{10}Be, ^{11}Be, ^{8}B, ^{10}B, ^{11}B, ^{12}B, ^{11}C and ^{12}C. For performance reasons, only a subset of these can undergo nuclear interactions (both elastic and inelastic) themselves. In the version presented here, this was: ^{1}H, ^{2}H, ^{3}H, ^{3}He, ^{4}He, ^{6}Li, ^{7}Li, ^{7}Be, ^{10}B, ^{11}B, ^{12}B, ^{11}C and ^{12}C.

The final list of particles that undergo nuclear interactions in MonteRay was determined in an iterative fashion by comparing (a) the fragmentation spectrum to FLUKA simulations (see Figure 3a and b) and by comparing simulations of pristine Bragg peaks to measurements and matching their shape (see Section 3.1). Increased accuracy through the inclusion of more nuclear interactions had to be balanced with a) the requirement of compute resources to create the pre-computed databases and (b) the influence on the runtime itself.

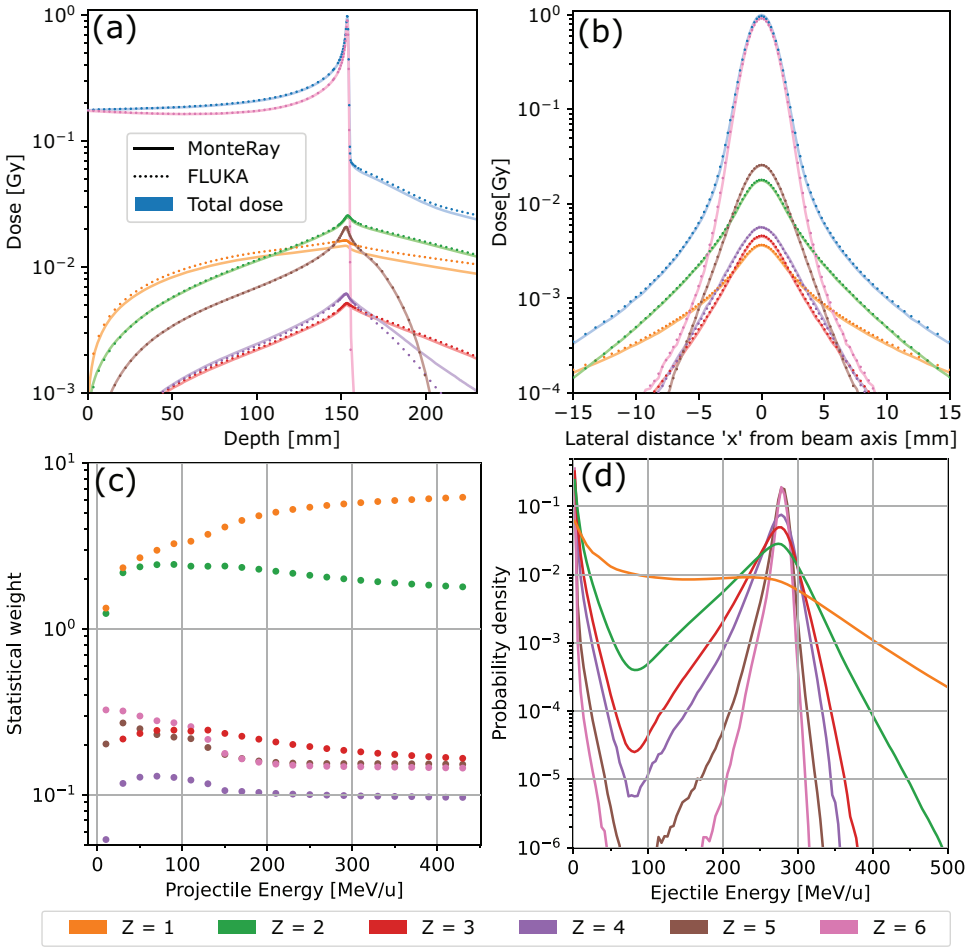

FIGURE 3 In panel (a), integrated depth dose distributions of 280 MeV/u carbon ions incident on water are shown for MonteRay (solid lines) and FLUKA simulations (dots). Besides the total dose (blue), individual contributions of particles with atomic numbers between one and six are shown. Similarly in panel (b), lateral distributions shortly before the BP are displayed. Lateral dose scoring was done in a 1 cm slice along the y-direction, that is perpendicular to the plotted axis. The legend from panel (a) applies. In panel (c), the statistical weights used by MonteRay during inelastic nuclear particle production are shown as a function of projectile energy for interactions between 12C and 16O. In panel (d), the distribution of ejectile energies for the interaction of 280 MeV/u 12C ions with 16O is shown. The angular part of the distribution was integrated over. The color scheme below the figure applies to all panels and indicates the colors used for particle groups with distinct atomic numbers Z.

Regarding the later, Section 3.5 showcases the impact of nuclear model extent on the runtime. In (Figure 3a and 3b), depth dose distributions and lateral distributions of 280 MeV/u carbon ions for MonteRay and FLUKA simulations are shown with the total dose (blue) broken down into the contributions of particles with atomic numbers one to six.

2.3.1 | Elastic nuclear interactions

For protons, elastic nuclear interactions with all ten elements are handled as described previously.[15] For the other particles that undergo nuclear interactions, elastic nuclear interactions are only considered when the target element is hydrogen. This approach is in line with MonteRay's treatment of helium ions. As presented in Lysakovski et al,[16] elastic nuclear events of particles with hydrogen are handled by shifting the frame of reference such that the hydrogen atom can be considered as the projectile. With this, the interaction process can use the same formalism as previously presented for protons,[15] based on the work of Ranft et al.[26] Afterwards, the resulting particles are boosted back into the initial frame of reference and transport continues.

2.3.2 | Inelastic nuclear interactions

In particle therapy, inelastic nuclear scattering events generate the mixed radiation field. High fidelity MC simulations like FLUKA have elaborate models implemented inside to treat these interactions. To avoid costly calculations, MonteRay instead employs a pre-computed

TABLE 1 List of all particle types that can undergo nuclear interactions in MonteRay and the range of projectile energies for which inelastic interaction tables were computed. In the third column, the list of possible secondary particles for each projectile type is given.

Projectile Name	Projectile Energy Range	Possible secondaries
^{1}H	10–500 MeV/u	^{1}H, ^{2}H, ^{3}H, ^{3}He, ^{4}He
^{2}H	40, 80, …, 480 MeV/u	Same as ^{1}H
^{3}H	40, 80, …, 480 MeV/u	Same as ^{1}H
^{4}He	10–500 MeV/u	Same as ^{1}H
^{6}Li	40, 80, …, 480 MeV/u	Same as ^{1}H + ^{6}Li
^{7}Li	40, 80, …, 480 MeV/u	Same as ^{6}Li + 7Li
^{7}Be	40, 80, …, 480 MeV/u	Same as ^{7}Li + ^{7}Be
^{10}B	10–500 MeV/u	Same as ^{7}Be + ^{8}Li, ^{9}Li, ^{11}Li, ^{8}Be, ^{9}Be, ^{10}Be, ^{11}Be, ^{8}B, ^{10}B
^{11}B	10–500 MeV/u	Same as ^{10}B + ^{11}B + ^{11}C
^{11}C	10–500 MeV/u	Same as ^{11}B
^{12}C	10–430 MeV/u	Same as ^{11}C + ^{12}C

database of nuclear event probabilities. As previously described for protons[15] and helium ions,[16] this database is based on nuclear models used internally by FLUKA. While for proton and helium ions only the production of ^{1}H, ^{2}H, ^{3}H, ^{3}He and ^{4}He was necessary, carbon ions generate a wider set of secondary particles which in turn themselves can undergo nuclear interactions. Consequently, the existing database was extended for the simulation of carbon ions and now consists of approximately 60000 individual 100 × 100 tables, corresponding to a memory footprint of about 2.4 gigabytes. This easily fits into main memory, even when MonteRay is run across multiple threads since the database is shared between all threads of a CPU. Each of the 60000 tables corresponds to a combination of projectile type, projectile energy, target element and ejectile type. The possible elements (^{1}H, ^{12}C, ^{14}N, ^{16}O, ^{23}Na, ^{24}Mg, ^{31}P, ^{32}S, ^{35}Cl, ^{40}Ar, ^{39}K and ^{40}Ca) are the same for all interacting particles, but the projectile energy ranges and possible ejectile particle types vary. For example, for primary carbon ions (^{12}C), the database covers a projectile energy from 10 to 430 MeV/u (corresponding to the maximum energy available at HIT) and the production of all available particle types is possible. Protons on the other hand cover an energy range from 10 to 500 MeV/u and only the production of ^{1}H, ^{2}H, ^{3}H, ^{3}He and ^{4}He is possible. For some infrequent particle types like ^{7}Li, the number of projectile energies was reduced to reduce the time necessary to generate these tables. In Table 1, a summary of all available nuclear interaction tables is given. For the handling of proton and ^{4}He ion beams, photons and neutrons were assumed to be dosimetrically irrelevant and they were neither transported nor produced. Like done by Qin et al,[13] the production and transport of neutrons was also ignored in MonteRay for the simulation of carbon ions. As will be discussed later, neutrons do impact the dose deposition of carbon ions and ignoring them does lead to an underestimation of the dose, especially at higher energies. As will be shown, MonteRay achieves good agreements nonetheless and the omission of neutrons is mainly visible through the lack of $Z = 1$ particles (compare Figure 3a).

If an inelastic nuclear interaction is determined to take place during particle transport, the tables corresponding to the current projectile, projectile energy (rounded to the nearest table's energy) and target element are selected. Each selected 100 × 100 table (corresponding to an ejectile particle type) now encodes a probability distribution in angle and energy from which the ejectile's properties can be sampled. The average number of particles that are produced per inelastic interaction is very low for some ejectiles and in order to keep the runtime small, the same approach as described by Qin et al.[13] was chosen to determine whether a secondary particle is actually produced. For this, the particle's weight is first split into a fractional and an integer part. If the integer part is not zero, a secondary with weight equal to the integer part is spawned. Additionally, a random number between 0 and 1 is sampled and if the fractional part is larger than this number, another secondary with weight 1 is sampled. For projectile energies below the lowest available table's energy, MonteRay randomly chooses whether a nuclear interaction takes place or not. In (Figures 3c and d), examples of the data contained in the nuclear interaction database are presented. In panel c), the average number of secondary particles with atomic numbers one to six as a function of the projectile's energy is shown for primary carbon ions impinging on ^{16}O. In (Figure 3d), the energy distribution, that is, the angular part of the database was integrated, of secondary particles produced by 300 MeV/u ^{12}C ions incident on ^{16}O is shown.

2.4 | Benchmarks

2.4.1 | Pristine Bragg peaks

As an initial clinical benchmark, measured integrated depth dose distributions (IDDD) were compared against MonteRay simulations. Measurements were recorded at HIT using a PEAKFINDER water column (PTW, Freiburg) with the measurement setup previously described by Tessonnier et al.[27] For this comparison, a total of 16 recorded IDDDs (6 with a ripple filter, 10 without a ripple filter) with energies ranging from 100 to 430 MeV/u were available. To match the detectors shape in MonteRay, it was modelled as a water cylinder with a radius of 4.08 cm. Due to the sharp BP of carbon ions and the high spatial resolution of the measured data

(0.05 mm in the BP region), scoring along the beam's direction was performed at a resolution of 0.1 mm, much higher than one would typically use in a patient plan calculation. The pristine Bragg peak measurements were used as a benchmark during development. Initial simulation results were used to adjust the beams initial momentum spread in a semi-automatic optimization procedure in which MonteRay simulations with different momentum spreads were compared against data, similar how previously momentum spread was adjusted for FLUKA simulations.[6,28]

For the comparison of measured doses to simulated doses, the IDDDs were normalized such that simulations and measurements match at the first measured depth of 16 mm in water. As a metric of agreement, the symmetric relative error was computed:

$$\varepsilon_{\text{rel}} = 200 \left(\frac{d_1 - d_2}{d_1 + d_2} \right) [\%] \tag{7}$$

2.4.2 | Spread out Bragg peaks

MonteRay simulations were compared against measured SOBPs in water centered at depths of 5, 12.5 and 20 cm. For all three depths, irradiation plans were optimized for uniform target doses of 1 Gy covering cubic volumes of $3 \times 3 \times 3$ cm^3 and $6 \times 6 \times 6$ cm^3. Across all plans, the energies of the SOBPs ranged from 98 MeV/u to 362 MeV/u. The data, previously used for comparisons with FLUKA simulations by Tessonnier et al,[29] was acquired using a three-dimensional array of 24 PinPoint ionization chambers (TM31015, PTW Freiburg). The array of ionization chamber was described in detail by Karger et al.[30]

2.4.3 | Anthropomorphic phantom

An anthropomorphic head phantom (Alderson phantom Radiology Support Devices, Long Beach, California, USA) was used to verify MonteRay in heterogeneous conditions. A detailed description of irradiation plan generation and data collection was given in Mein et al.[31] In summary, a FLUKA-based treatment planning tool was used to optimize for a $6 \times 6 \times 6$ cm^3 cubic uniform dose of 1 Gy centered 7 cm behind the phantoms backplate. The plan included energies ranging from 215 MeV/u to 346 MeV/u. Two sets of measurements have been performed. One in water, using the previously mentioned three-dimensional array of 24 PinPoint ionization chambers (TM31015, PTW Freiburg), and one behind a stack of PMMA plates that were used to position a 2D-ionization chamber array (OCTAVIUS, PTW Freiburg) covering the distal part of the SOBP (Figure 6a). The 2D detector consists of an array of 977 ionization chambers with a size of $2.3 \times 2.3 \times 0.5$ mm^3. MonteRay simulations were carried out with 2% of the plan's total particle number. For comparison with previously reported results,[31] global 3D-γ index analysis against OCTAVIUS data was performed at 3%/3 mm and 2%/2 mm.

2.4.4 | Patient plan

The patient plan was generated using the clinical TPS RayStation 11B (RaySearch Laboratories, Stockholm, Sweden) with an anonymized patient dataset representative of the re-irradiation treatment of a meningioma tumor with carbon ions. Optimization was carried out on the PTV (~105 cm^3) with a target dose of 42 Gy (RBE) in 14 fractions. For the initial parameters of the optimization, three beams and a hexagonal spot pattern with 2.4 mm spot spacing and an energy spacing of 3.1 mm (water equivalent depth) were chosen. The minimum number of particles per spot was set to 15 000. The final plan included energies ranging from 88 to 274 MeV/u. The plan was biologically optimized using the modified microdosimetric kinetic model (mMKM)[32] assuming a tissue characterized with $(\alpha/\beta)_{\text{ph}} = 2$ Gy and $\beta = 0.025$ Gy^{-2}. Final dose calculation in RayStation and MonteRay was performed on a 1 mm^3 grid. For MonteRay recalculation, the mMKM database was used for runtime calculations of the mixed radiation field parameters as described in details in Bauer et al.[33] Due to the high dose grid resolution (1 mm), higher than usually employed in clinical practice (2 mm), MonteRay calculations were carried out with 30% of the total number of particles in the plan to reach a mean relative uncertainty of 2% (a dose threshold of 5% was used for uncertainty calculation).

For comparison of computed dose distributions between MonteRay and RayStation, local 3D-γ analysis of both physical and biological dose was carried out with a 1%/1 mm and 2%/2 mm criterion and a lower dose threshold of 5% using the pymedphys python package (version 0.37.1). To ensure convergence and to estimate the variance of gamma passing rates, the simulations were repeated ten times in MonteRay (each simulation having 30% of the plans total number of particles).

3 | RESULTS

3.1 | Pristine Bragg peaks

Measured IDDDs with energies ranging from 100 to 430 MeV/u were compared with simulations performed in MonteRay. Prior to dosimetric comparisons, range differences between MonteRay simulations and

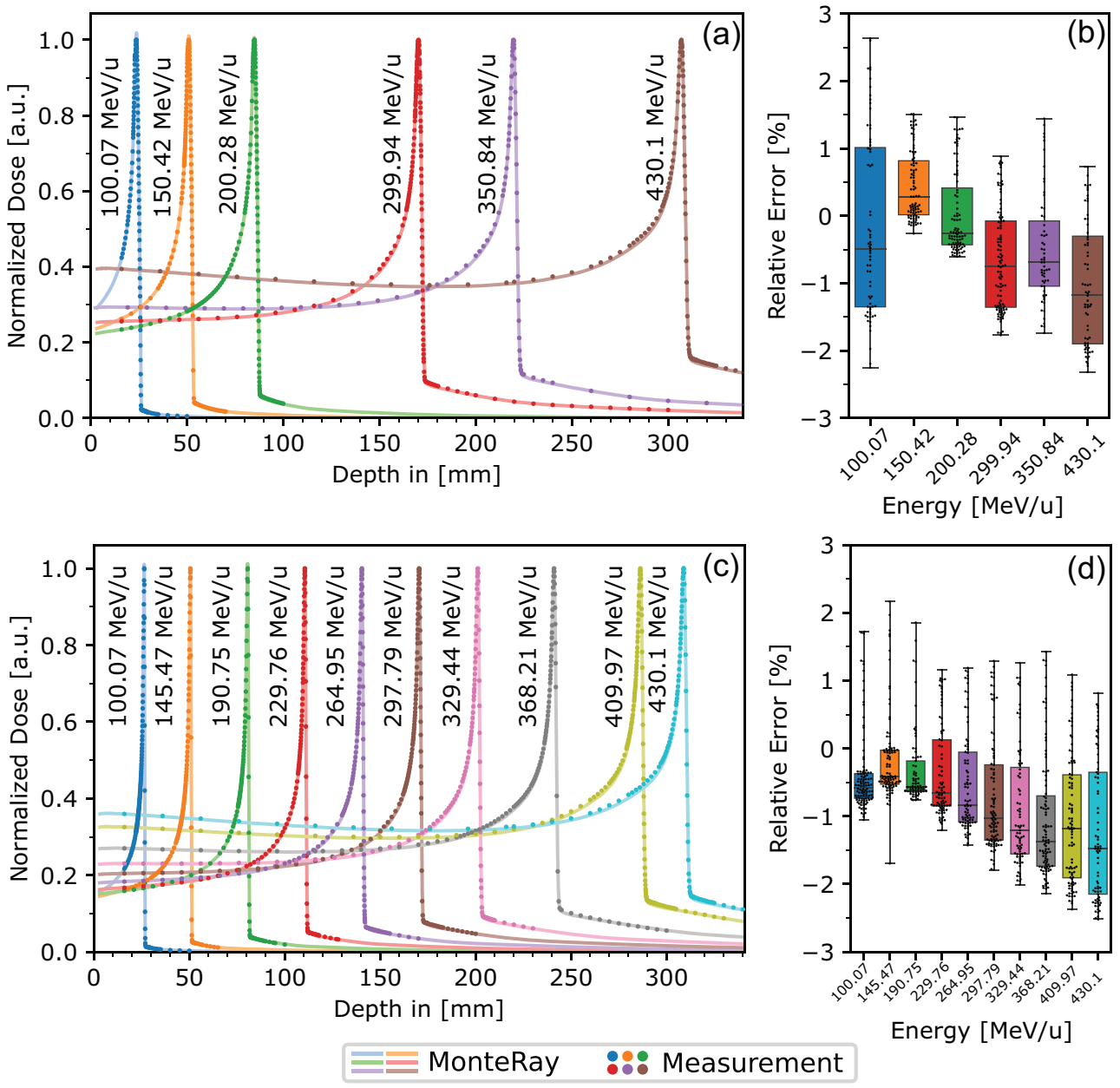

FIGURE 4 Panel (a): Normalized IDDDs for six quasi monoenergetic beams with a ripple filter in the beamline are shown. Doses simulated by MonteRay are shown as solid lines while measurements are indicated through circles. Panel b): The dose difference in percent is shown using standard box plots. The bottom, middle and top bars of the boxes represent 25%, 50% and 75% percentiles. The whiskers extend up to the minimum/maximum values. Individual dose differences are indicated through black dots. Panel (c): Like in panel (a), IDDDs of individual pencil beams are shown but now without a ripple filter present. Panel (d): Dose differences in percent for the IDDDs without a ripple filter are shown. IDDD, depth dose distributions.

measurements were estimated by computing the depth at which the curves have fallen to 80% of the maximum dose (the R_{80} value). Across all 16 compared BPs, the differences in range were between 0.02 and 0.3 mm, with a mean of 0.1 mm. Using these values, relative dose differences (see, Equation 7) were computed after MonteRay computed doses were shifted to match the measurements in terms of range. The high gradient region after the R_{80} point was excluded for analysis in terms of relative errors. In (Figure 4a), simulated and measured IDDDs for the six cases with a ripple filter are shown and in (Figure 4b) corresponding relative errors are shown as standard box and whisker plots with individual relative errors shown through black dots. With a ripple filter, excellent agreement across the 6 IDDDs was seen with errors ranging from −2.3% to 2.7% with average absolute relative errors between 0.5% and 1.2%. For the ten cases without a ripple filter (Figure 4c and d),

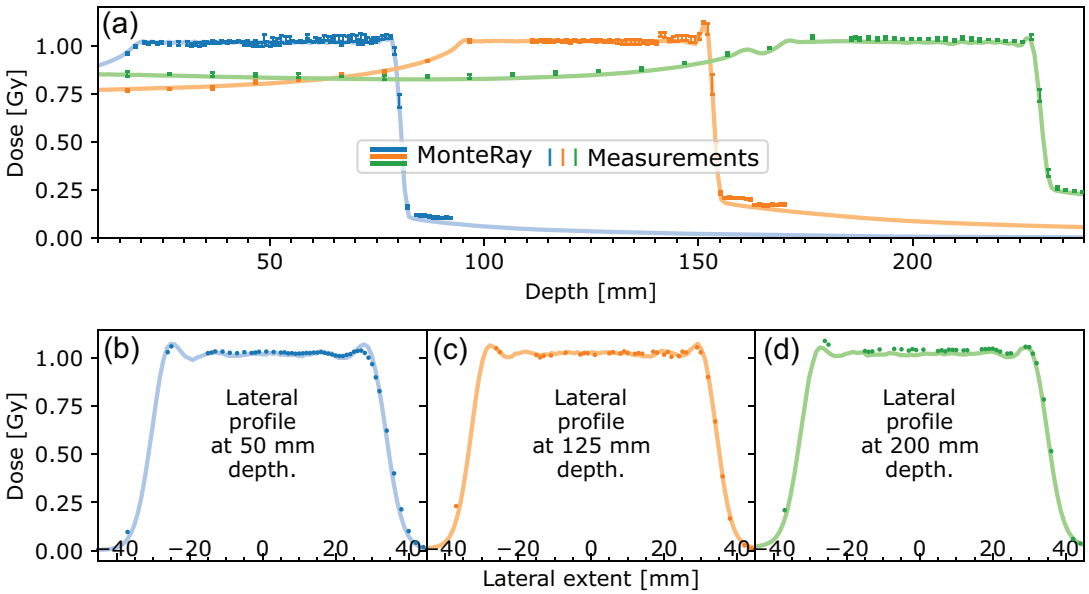

FIGURE 5 Top row: depth dose distributions averaged over the 6×6 cm^2 central region of the SOBP are shown for MonteRay simulations (solid lines) and measurements (dots) for three different SOBP depths of 5, 12.5 and 20 cm. Error bars indicated the variance of measured doses for each depth since multiple detectors were located at each depth. Bottom row: lateral dose distributions extracted from the central region of the three SOBPs at depths of 5.6 cm (b), 12.6 cm (c) and 20.6 cm (d) are shown.

errors ranged between −2.5% and 2.2% with mean absolute relative errors ranging from 0.5% to 1.4%.

3.2 | Spread out Bragg peaks

After correction of remaining range uncertainties (< 0.14 mm), SOBPs simulated with MonteRay were compared to measurements. For plotting and comparison, 1D depth-dose distributions were generated from the measurements by averaging over all values within the 6×6 cm^2 (or 3×3 cm^2) central region at a certain depth. In (Figure 5a), depth dose distributions of the three $6 \times 6 \times 6$ cm^3 SOBPs are shown while panels (b), (c) and (d) show lateral dose distributions extracted from the central region of the three SOBPs. Considering each recorded depth individually, dose differences between −2.8%/−3.3%/−2.5% and +1.3%/+1.0%/−0.7% for the SOBPs at 5 cm/12.5 cm/20.0 cm depth were observed. Averaged over all individual measurements, mean absolute dose differences were 0.9%, 0.7% and 1.6% respectively. For the 3 cm field size SOBPs, dose differences between −0.5%/−2.4%/−3.4% to +2.8%/+1.4%/−0.2% were seen. Mean absolute dose differences were 1.1%, 1.1% and 1.7% for the three depths, respectively. Qualitatively, the lateral dose distributions show good agreement between MonteRay simulated doses and measured values but a slight underestimation of dose at high depths can be seen.

3.3 | Anthropomorphic phantom

The results of the anthropomorphic phantom simulations are shown in panels (b) and (c) of (Figure 6). In panel (b), depth dose profiles extracted behind a heterogenous region of the phantom are shown. Simulated data (lines) from three different dose engines (FLUKA: black, FRoG: red, MonteRay: blue) and measured data (squares) are displayed. The HU values along the line profile are also graphed and show the heterogeneity of the phantom at that line profile location. Good agreement between MonteRay and measurements can be seen and the agreement of MonteRay to FLUKA is superior to that of the analytical dose calculation engine FRoG.

In (Figure 6c), dose differences in percent between MonteRay and OCTAVIUS measurements are shown and computed 3D-γ values are shown with computed passing rates written below. Averaging the absolute relative error over all voxels, values of $(1.2 \pm 1.1)\%$ were obtained. Approximately 99.3% and 96.8% of all pixels passed the 3%/3 mm and 2%/2 mm 3D-γ criterion, respectively. In comparison, previously reported results with FLUKA showed 3%/3 mm passing rates of 98.9%.

3.4 | Patient plan

In Figure 7, the results of the patient computation are shown. In panels (a) and (b), biological dose distributions in one axial slice are shown for RayStation

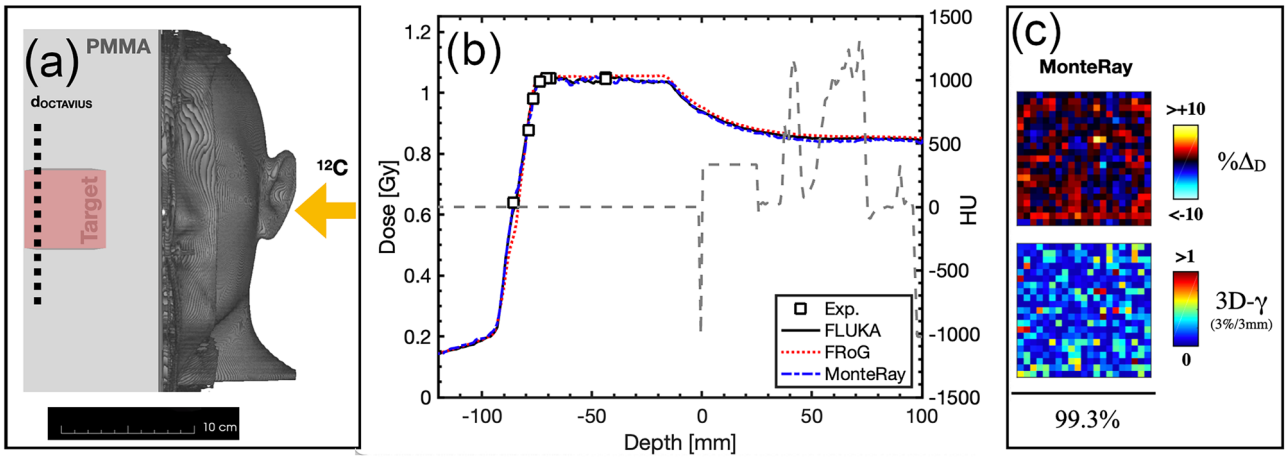

FIGURE 6 Panel (a): Schematic of the experimental setup used for acquiring the data. 2D lateral slices were obtained at the location marked with dashed line, corresponding to a slice near the distal edge of the SOBP. Panel (b): Depth dose profiles obtained with different dose calculation engines (FLUKA: black, FRoG: red, MonteRay: blue) are shown together with measurements obtained with an array of ionization chambers. The HU values along the extracted line profile are shown in light grey. Panel (c): Relative dose differences (top) and 3D-γ index for a 3%/3 mm criterion (bottom) are shown for the comparison of MonteRay simulations with 2D measurements.

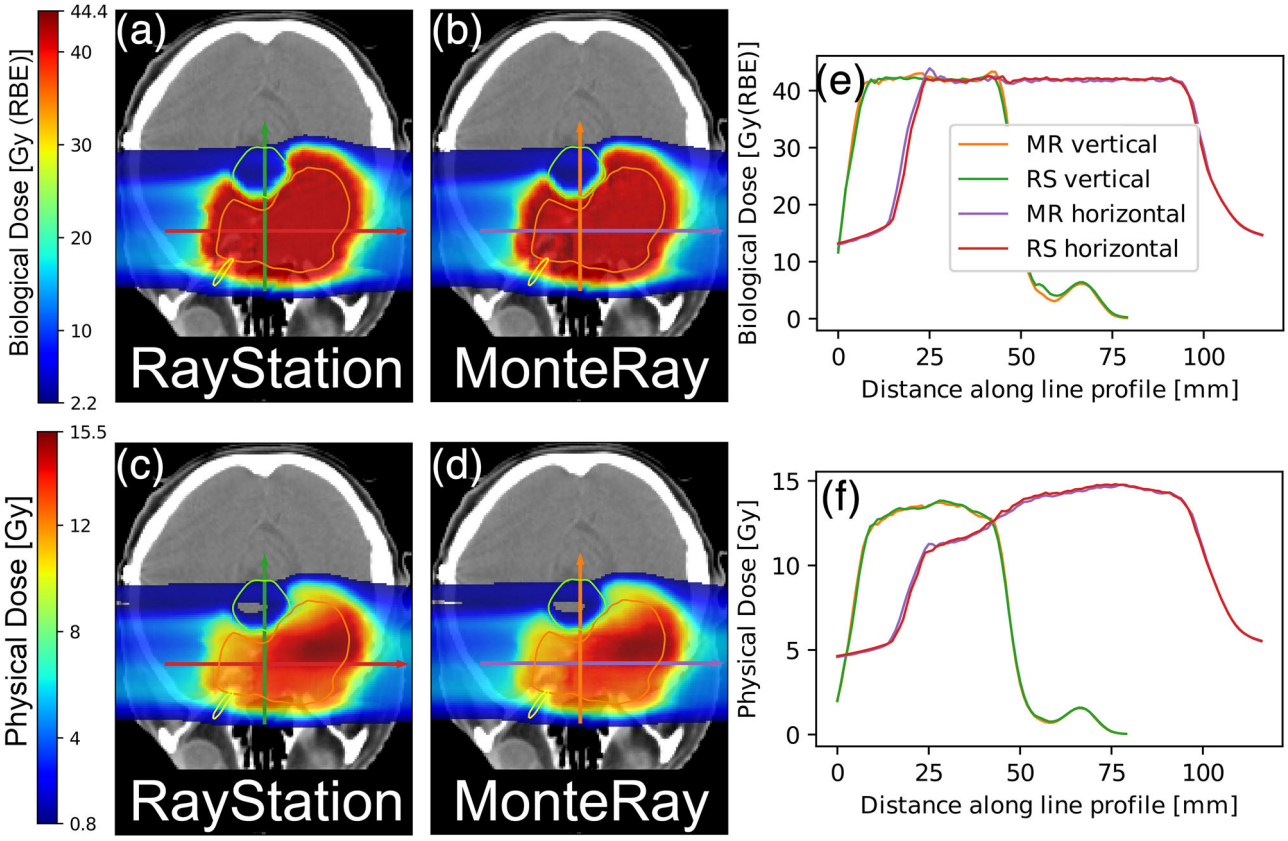

FIGURE 7 Comparison of MonteRay and RayStation computed doses for the exemplary meningioma case. In the top row, biological doses and in the bottom row, physical doses are shown. In panels (a) to (d), 2D dose distributions in an axial slice are shown for MonteRay and RayStation. Inside these panels, delineated structures of the brainstem (green), clinical target volume (CTV) (orange) and right optical nerve (yellow) are shown. The arrows mark the locations of extracted 1D line profiles which are visible in panels (e) and (f). In panel (e), line profiles of biological dose for MonteRay and RayStation are shown while physical dose profiles are shown in panel f).

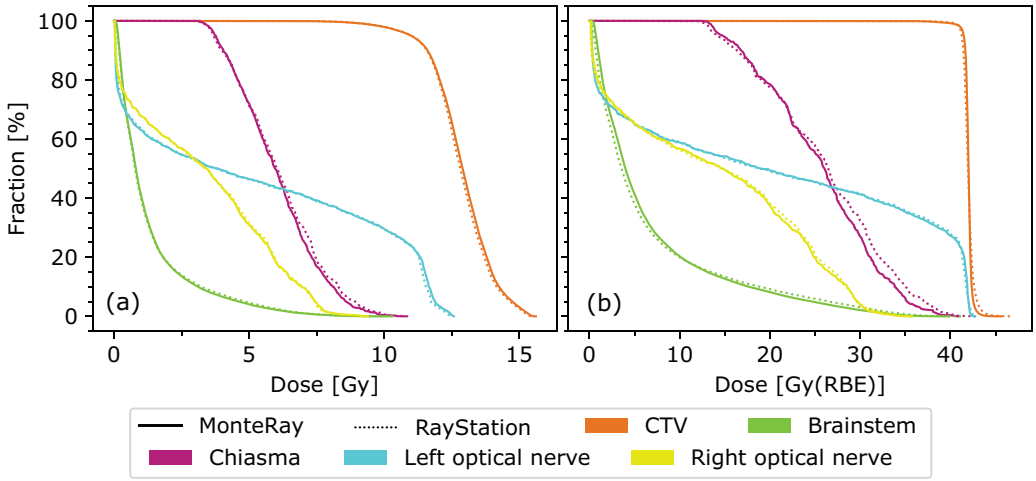

FIGURE 8 Dose volume histograms for physical (Panel (a)) and biological (Panel (b)) dose corresponding to the calculated doses displayed in Figure 7. MonteRay (RayStation) computations indicated through solid (dashed) lines. DVHs for the clinical target volume (CTV), Brainstem, Chiasma, left optical nerve and right optical nerve are shown. Contours of the CTV, Brainstem and right optical nerve in their corresponding colors are visible in Figure 7. DVHs, dose volume histograms.

and MonteRay. Likewise in panels (c) and (d), physical doses are shown. In panels (e) (biological) and (f) (physical), line profiles extracted from computed 3D dose distributions are displayed. The locations of the line profiles are indicated through color coded arrows in panels (a) to (d). Visual inspection of 2D and 1D dose profiles yielded good agreement in terms of biological and physical dose distributions. Using the 3D-γ metric for quantitative analysis and averaging over 10 runs (errors are given as standard deviations), yielded excellent 1%/1 mm (2%/2 mm) passing rates of 98.36 ± 0.04 % (99.40 ± 0.01 %) for physical and good passing rates of 93.90 ± 0.03 % (99.22 ± 0.03 %) for biological dose. Next, dose volume histograms (DVH) were computed for the clinical target volume (CTV), brain stem, left optical nerve and right optical nerve. They are displayed in Figure 8. The contours of the CTV, the brain stem and the right optical nerve are visible in panels (a) to (d) of Figure 8.

Qualitatively, Figure 8 shows good agreement between MonteRay simulations and RayStation predictions in terms of DVHs with differences more pronounced for biological dose than for physical dose. For a quantitative assessment, computed dose statistics (D1, D2, D50, D98, D99) are presented in Table 2.

3.5 | Runtime comparisons

End-to-end runtimes of MonteRay were compared to those of FLUKA on a sample problem with carbon ions incident on water with an energy range from 100 to 430 MeV/u. Benchmarks were performed on an Intel i7-9700k processor. Unless otherwise noted, the numbers reported are for single-threaded execution.

Besides the computational cost of the physical models implemented (for example for energy loss fluctuations or inelastic nuclear interactions), the performance of an MC code greatly depends on the step-size chosen. In MonteRay, the step-size is described by Equation 3. For the patient, SOBP and anthropomorphic phantom calculations presented here, the parameter Δx_g was 1 mm while for the pristine Bragg peaks, it was 0.1 mm. It is not possible to recreate this step size policy with FLUKA and so a direct comparison would be somewhat unfair. However, it is possible to run MonteRay with a step-size equal to that of FLUKA.

When running FLUKA with a certain requested fractional energy loss (either by explicitly setting it through the FLUKAFIX option or by using the default value of 2% for the hadron therapy option), FLUKA does not strictly adhere to this value. Instead, the fractional energy loss is about twice as high at low energies and slowly decreases with higher energies. For a fair comparison, the exact fractional energy loss as a function of a particle's energy was extracted from FLUKA with the default settings for hadron therapy (option HADROTHE) by using a feature of FLUKA (option USRDUMP) which allows to extract particle tracks step-by-step. In Figure 9, the fractional energy loss as a function of a particle energy per atomic mass is shown for protons, helium ions and carbon ions. This fractional energy loss, using a lookup table, was implemented in MonteRay for the sake of a fair comparison.

In Table 3, the runtimes of FLUKA, MonteRay with FLUKA step-sizes and MonteRay with step sizes according to Equation (3) are shown. The speedups observed were between 13.8 and 55.4 when recreating the step size of FLUKA and between 41.3 to 72.0 when using Equation (3) for the step size. As with previous

TABLE 2 Comparison of MonteRay and RayStation patient plan dose calculations in terms of D2%, D50% and D98% for the clinical target volume (CTV) and D1%, D2% and D5% for the OARs, both biological and physical dose results are shown.

Roi Name	D2			D50			D98		
	RS [Gy]	MR [Gy]	Diff. [%]	RS [Gy]	MR [Gy]	Diff. [%]	RS [Gy]	MR [Gy]	Diff. [%]
CTV Phys.	15.2	15.1	0.6	12.9	12.8	0.6	10.0	10.0	−0.2
	RS [GyRBE]	MR [GyRBE]	Diff. [%]	RS [GyRBE]	MR [GyRBE]	Diff. [%]	RS [GyRBE]	MR [GyRBE]	Diff. [%]
CTV Bio.	42.9	43.5	−1.4	42.0	42.0	0.1	41.1	41.0	0.1
	D1			**D2**			**D5**		
	RS [Gy]	MR [Gy]	Diff. [%]	RS [Gy]	MR [Gy]	Diff. [%]	RS [Gy]	MR [Gy]	Diff. [%]
Chiasma phys.	9.7	9.9	−1.7	9.3	9.4	−1.4	8.6	8.9	−3.8
Brainstem phys.	7.0	7.1	−1.8	6.2	6.3	−2.9	4.6	4.8	−4.5
Left optical nerve phys.	12.5	12.3	1.1	12.3	12.2	0.7	11.9	11.7	1.3
Right optical nerve phys.	8.2	8.2	−0.2	7.8	7.7	1.0	7.5	7.4	0.2
Brain phys.	12.4	12.4	0.4	11.1	11.1	−0.4	7.0	7.0	−0.2
	RS [GyRBE]	MR [GyRBE]	Diff. [%]	RS [GyRBE]	MR [GyRBE]	Diff. [%]	RS [GyRBE]	MR [GyRBE]	Diff. [%]
Chiasma bio.	38.5	39.8	−3.2	38.1	38.8	−1.9	35.2	37.1	−5.4
Brainstem bio.	32.7	34.4	−5.1	30.3	32.0	−5.5	24.6	26.5	−7.4
Left optical nerve bio.	42.2	42.4	−0.5	42.1	42.3	−0.4	42.0	42.0	−0.1
Right optical nerve bio.	32.3	33.1	−2.6	30.9	31.7	−2.8	29.7	29.6	0.5
Brain bio.	42.0	41.8	0.3	40.3	40.5	−0.6	24.2	24.5	−0.9

Abbreviations: MR, MonteRay; OARs, organs at risk; RS, RayStation.

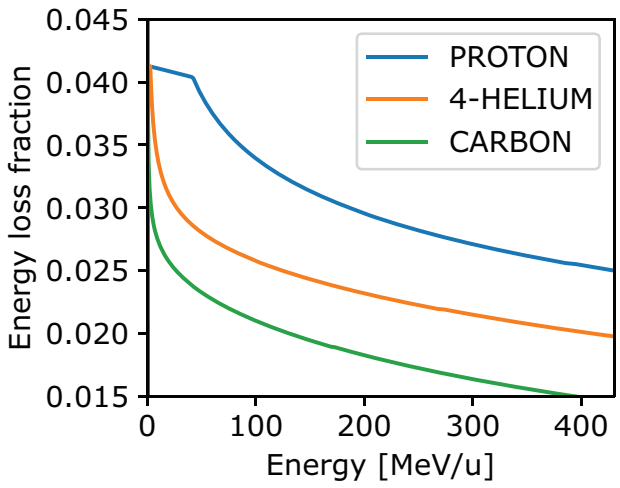

FIGURE 9 Actual step size (in terms of fractional energy loss) chosen by FLUKA for different primary particles when the defaults for hadron therapy are activated or the step size is manually set to 0.02 (2%) using the FLUKAFIX option.

versions of MonteRay, speedups increase with higher energies.

MonteRay transports a high variety of secondary particles and permits the reinteractions of more particles than previous fast carbon ion MC engines.[13,14] While this allows MonteRay to recreate the fragmentation spectrum of FLUKA well, it also has a performance penalty. To judge the impact of including a wide range of nuclear interactions, the runtime of MonteRay when only allowing for carbon ions to undergo nuclear interactions was measured. Moderate speedups compared to the base version (see Section 2.3) of 2, 5 and 16 % at 100 MeV/u, 250 MeV/u and 430 MeV/u were observed.

Finally, to judge the performance in MonteRay in real world scenarios, runtimes of a brain and a prostate treatment plan were measured when running MonteRay on all eight cores of the i7-9700k processor. Scoring and particle transport was performed on the CT grid ($1 \times 1 \times 3$ mm^3) and simulations were run until an average physical dose uncertainty of 2% in the high dose region (all voxels with dose >90% of the maximum dose) was reached. Statistical uncertainties were estimated using the sample standard deviation over the eight independent runs. In Table 4, the two plans are summarized (number of spots, number of fields, energy range, etc.)

TABLE 3 Single-threaded end-to-end runtimes of MonteRay and FLUKA for 10 million carbon ions incident on water. MonteRay runtimes are shown for two different step size policies. For the time in column two and speedup in column three, the step size of the particle was chosen according to Equation 3 while in columns four and five the step size was chosen to match FLUKA (as in Figure 9).

Energy [MeV/u]	FLUKA time [h]	MonteRay time [s] (Equation 3 SSP)	Speedup (Equation 3 SSP)	MonteRay time [s] (FLUKA like SSP)	Speedup (FLUKA like SSP)
100	1.8	159	41.3	475	13.8
250	8.5	682	44.8	1037	29.5
430	27.1	1355	72.0	1760	55.4

Abbreviation: SSP, step size policies.

TABLE 4 For benchmarking MonteRay's runtime in real world scenarios, two clinical plans were simulated until a statistical uncertainty of 2% was reached.

	Brain	Prostate
Number of spots	18806	13718
Number of fields	3	2
Minimum energy [MeV/u]	88.8	283.76
Maximum energy [MeV/u]	273.9	369.6
Total number of primaries in plan	810 million	1185 million
Primary fraction simulated	8%	3.5%
Number of simulated primaries	65 million	41 million
Runtime	862 s	1050 s

Note: The brain plan is equivalent to the one described in Section 2.4.4. The table summarizes the properties of the plans and shows their runtimes.

and their runtimes reported. For the brain case, already presented in Section 3.4, the simulation time for 65 million primaries was 862 s and for the prostate plan the runtime was 1050 s.

4 | DISCUSSION

In this work, the extension of MonteRay for the simulation of carbon ion beams was presented and the accuracy and speed of the engine assessed. Dosimetric comparisons were performed on a variety of scenarios like pristine Bragg peaks, SOBPs and anthropomorphic targets. MonteRay achieved good accuracy in all scenarios.

Comparisons of depth-dose profiles of carbon ion beams in water showed good agreement within less than ± 3% against relative measurements obtained with a PEAKFINDER water column. When evaluated against similar data, previously reported results of MonteRay with proton and helium ion beams were at −3% to +1% and −3% to +3%, respectively,[15,16] that is, according to this metric, the dose calculation with carbon ions is similarly accurate as the helium ion dose calculation.

Moving on to cases including more than one pencil beam, SOBPs of different sizes ($3 \times 3 \times 3$ cm^3 and $6 \times 6 \times 6$ cm^3) at different depths (5 cm, 12.5 and 20 cm) were simulated and compared to measurements. Here, MonteRay achieved dose differences ranging from approximately −3% to +1% with a tendency to underestimate the dose at high energies. This underestimation will be discussed in more detail below as it is related to an underestimation of dose delivered by particles with atomic number $Z = 1$ (see Figure 3a) and possibly ties into the differences observed with biological dose.

To benchmark MonteRay in scenarios with heterogeneities, calculations were performed on an anthropomorphic head phantom and compared against measurements. Excellent agreement was found with 3D-γ passing rates (3%/3 mm) of 99.3%, similar to the 98.9% previously reported for FLUKA.[31] Computed 2%/2 mm passing rates on this case were 96.8%, acceptable considering that measurements are the source of the reference dose. Comparisons with depth-dose profiles showed that MonteRay achieves dose prediction with a similar accuracy to FLUKA even in highly heterogeneous geometries.

In the future it is planned to use MonteRay as an in-silico plan verification tool in clinical practice. With this in mind, a patient case representative of a meningioma treatment was selected, and dose distributions obtained with MonteRay were compared to dose distributions computed by the clinical TPS RayStation. Besides physical dose distributions, biological dose distributions using the mMKM biological model were computed. Looking at physical dose first, comparisons in terms of 3D-γ passing rates yielded excellent passing rates of 98.36% ± 0.04% and 99.40% ± 0.01% for a 1%/1 mm and 2%/2 mm passing criterion, respectively. Passing rate for biological dose calculation were slightly worse with 93.90% ± 0.03% (1%/1 mm) and 99.22% ± 0.03% (2%/2 mm). Similarly, the agreement of DVHs (Figure 8) and dose statistics (Table 2) were good, with bigger differences observed for biological than for physical dose. Higher discrepancy in the biological dose is expected since it depends not only on the accuracy of the physical dose but also requires an accurate modeling of the mixed

radiation field. The latter, as noted by Tessonnier et al.[34] when investigating helium ions, is not necessarily represented accurately in the analytical algorithm of the TPS. It is possible that the detailed treatment of nuclear fragments in MonteRay allows it to predict biological dose more accurately. Yet, some discrepancies, mostly for particles with atomic number $Z = 1$, remain when contributions of secondary fragments to the total dose are compared against FLUKA simulations. Indeed, for the highest clinically used energy (430 MeV/u) the underestimation of $Z = 1$ dose reaches 20% near the BP. In comparison, the dose of particles with $Z = 6$ is replicated to within $\pm$1% and the dose of particle with $Z = 2$ matches to within $\pm$4% up to the BP.

Investigating the origin of this underestimation of particles with $Z = 1$, we concluded that is caused by the lack of neutron production and transport in MonteRay, similar how it was done by Qin et al.[13] If included, the neutrons could undergo nuclear interactions themselves to produce other particles, like protons. In principle, the generation of neutrons would be possible in MonteRay as their yield in nuclear interactions was tabulated similarly to other particles (see Section 2.3). But since neutrons don't carry an electrical charge, their transport would differ from that of all other particles currently included in MonteRay. As a result, they cannot be trivially implemented. Instead, other ways to account for the missing neutrons could be chosen in the future. For example, increasing the statistical weight of all protons produced in nuclear interactions by 15% appeared promising in increasing the dose of $Z = 1$ particles to match that of FLUKA while not influencing the runtime of the program. In the future, the validity of this approach will have to be investigated in more detail and it was not used for this work.

However, one should put these observed differences into perspective. Even comparisons between traditional MC engines like FLUKA and GEANT4 show considerable differences in the distributions of secondary particles. For example, Robert et al.[35] investigated FLUKA and GEANT4 simulations of 260 MeV/u carbon ion beams incident on a PMMA target and found large differences in both yield and energy spectra of secondary particles. The yields of protons and neutrons, in terms of secondaries leaving the target, differed by 14% and 17%, respectively. Similarly, Böhlen et al.[36] investigated FLUKA and GEANT4 simulations for carbon ion beams and observed differences in the yield of secondary fragments of several tens of percent. In their conclusion, the authors attempt to estimate the relevance of these differences for clinical practice. Only considering the observed discrepancies in terms of proton fluences, they estimate an error in biological dose of approximately 4%. They note, similar to the conclusion reached for helium ion simulations in MonteRay,[16] that the available measurements used to derive nuclear interaction models are few and come with large statistical uncertainties. To improve dose prediction in hadron therapy, experiments like FOOT[37] are needed. Since MonteRay uses databases generated from FLUKA, it could benefit easily from any future improvements made to the FLUKA interaction models.

By using simpler sampling techniques for energy loss and multiple coulomb scattering and by using pre-computed databases to handle inelastic nuclear interactions, MonteRay was able to achieve speedups against FLUKA ranging from 14 to 72, depending on the energy and the way that step sizes are computed. The runtime comparisons also included two patient plans. Firstly, the meningioma case presented in Section 2.4.4 and another plan representative of a prostate tumor. Runtimes, as summarized in Table 4, were 14 and 18 min, respectively. The required runtimes for simulating 10 million primary particles for these two cases were thus 133 s and 256 s. For comparison, Qin et al.[13] report 10 million primary particle runtimes of approximately 219 s and 251 s for similar cases using their GPU accelerated MC engine, that is MonteRay running on 8 CPU cores achieved similar runtimes. In comparison, De Simoni et al.[14] report higher tracking rates using their GPU accelerated MC algorithm. For a single beam of 300 MeV/u carbon ions, they achieve runtimes of 0.4 μs per primary which would correspond to 4 s per 10 million primaries. However, they do not report runtimes for patient plan calculations, so a direct comparison is not possible.

Finally, besides the run time improvements against FLUKA, the impact of different nuclear models on the runtime was studied. It was found that extending the range of nuclear interactions from only carbon ions (as was done in FRED and GOCMC) to the wide range of particles included in MonteRay led to a modest slow-down of 15% at the highest energy. This seems acceptable considering that this allows an accurate representation of FLUKA's fragmentation spectrum while still achieving satisfactory speedups.

5 | CONCLUSION AND OUTLOOK

The extension of the dose calculation engine MonteRay to include carbon ion beams has shown that fast MC simulation (14 to 72 times faster than FLUKA) of carbon ion treatment plans is feasible while maintaining good accuracy in clinical settings. GPU acceleration of MonteRay is planned in order to further gain a substantial speed-up. MonteRay is the only experimentally verified fast MC engine that is capable of simulating protons, helium ions and carbon ions and MonteRay can serve as a fast and accessible secondary dose engine for in-silico patient verification[33] in a clinical setting and for future developments in particle therapy,[34,35,36] in general. Finally, the ability to simulate particle transport in geometries directly within MonteRay, as opposed to rely-

ing on a phase-space, will allow an easier adaptation to other facilities.

ACKNOWLEDGMENTS

The authors acknowledge financial support through the German Federal Ministry of Education and Research (BMBF) (Grant number: 13GW0436A).

Open access funding enabled and organized by Projekt DEAL.

CONFLICT OF INTEREST STATEMENT

The authors have no conflicts of interest to declare.

REFERENCES

1. Durante M, Loeffler JS. Charged particles in radiation oncology. *Nat Rev Clin Oncol*. 2010;7(1):37-43. doi:10.1038/nrclinonc.2009.183
2. PTCOG—Facilities in Operation. Accessed September 21, 2023. https://www.ptcog.site/index.php/facilities-in-operation-public
3. Inaniwa T, Kanematsu N, Hara Y, et al. Implementation of a triple Gaussian beam model with subdivision and redefinition against density heterogeneities in treatment planning for scanned carbon-ion radiotherapy. *Phys Med Biol*. 2014;59(18):5361-5386. doi:10.1088/0031-9155/59/18/5361
4. Inaniwa T, Kanematsu N. A trichrome beam model for biological dose calculation in scanned carbon-ion radiotherapy treatment planning. *Phys Med Biol*. 2015;60(1):437-451. doi:10.1088/0031-9155/60/1/437
5. Inaniwa T, Kanematsu N, Hara Y, Furukawa T. Nuclear-interaction correction of integrated depth dose in carbon-ion radiotherapy treatment planning. *Phys Med Biol*. 2015;60(1):421-435. doi:10.1088/0031-9155/60/1/421
6. Parodi K, Mairani A, Brons S, et al. Monte Carlo simulations to support start-up and treatment planning of scanned proton and carbon ion therapy at a synchrotron-based facility. *Phys Med Biol*. 2012;57(12):3759-3784. doi:10.1088/0031-9155/57/12/3759
7. Mein S, Choi K, Kopp B, et al. Fast robust dose calculation on GPU for high-precision 1H, 4He, 12C and 16O ion therapy: the FRoG platform. *Sci Rep*. 2018;8(1):14829. doi:10.1038/s41598-018-33194-4
8. Choi K, Mein SB, Kopp B, et al. FRoG-A new calculation engine for clinical investigations with proton and carbon ion beams at CNAO. *Cancers (Basel)*. 2018;10(11):395. doi:10.3390/cancers10110395
9. Ferrari A, Sala PR, Fasso A, Ranft J. FLUKA: A Multi-Particle Transport Code. 2005. doi:10.2172/877507
10. Böhlen TT, Cerutti F, Chin M, et al. The FLUKA code: developments and challenges for high energy and medical applications. *Nuclear Data Sheets*. 2014;120:211-214. doi:10.1016/j.nds.2014.07.049
11. Agostinelli S, Allison J, Amako K, et al. Geant4—a simulation toolkit. *Nucl Instrum Methods Phys Res A*. 2003;506(3):250-303. doi:10.1016/S0168-9002(03)01368-8
12. Sato T, Iwamoto Y, Hashimoto S, et al. Features of particle and Heavy Ion Transport code System (PHITS) version 3.02. *J Nucl Sci Technol*. 2018;55(6):684-690. doi:10.1080/00223131.2017.1419890
13. Qin N, Pinto M, Tian Z, et al. Initial development of goCMC: a GPU-oriented fast cross-platform Monte Carlo engine for carbon ion therapy. *Phys Med Biol*. 2017;62(9):3682-3699. doi:10.1088/1361-6560/aa5d43
14. d SimoniM, e, G Battistoni, de GregorioA, et al. A data-driven fragmentation model for carbon therapy GPU-Accelerated Monte-Carlo dose recalculation. *Front Oncol*. 2022;12:780784. doi:10.3389/fonc.2022.780784
15. Lysakovski P, Ferrari A, Tessonnier T, et al. Development and benchmarking of a Monte Carlo dose engine for proton radiation therapy. *Front Phys*. 2021;9:655. doi:10.3389/fphy.2021.741453
16. Lysakovski P, Besuglow J, Kopp B, et al. Development and benchmarking of the first fast Monte Carlo engine for helium ion beam dose calculation: MonteRay. *Med Phys*. 2022;50(4):2510-2524. doi:10.1002/mp.16178
17. Jiang H, Paganetti H. Adaptation of GEANT4 to Monte Carlo dose calculations based on CT data. *Med Phys*. 2004;31(10):2811-2818. doi:10.1118/1.1796952
18. Parodi K, Ferrari A, Sommerer F, Paganetti H. Clinical CT-based calculations of dose and positron emitter distributions in proton therapy using the FLUKA Monte Carlo code. *Phys Med Biol*. 2007;52(12):3369-3387. doi:10.1088/0031-9155/52/12/004
19. Schneider W, Bortfeld T, Schlegel W. Correlation between CT numbers and tissue parameters needed for Monte Carlo simulations of clinical dose distributions. *Phys Med Biol*. 2000;45(2):459-478. doi:10.1088/0031-9155/45/2/314
20. Almansa J, Salvat-Pujol F, Díaz-Londoño G, Carnicer A, Lallena AM, Salvat F. PENLGEOM —A general-purpose geometry package for Monte Carlo simulation of radiation transport in material systems defined by quadric surfaces. *Comput Phys Commun*. 2016;199:102-113. doi:10.1016/j.cpc.2015.09.019
21. Andersen H.R. An Introduction to binary decision diagrams, Lecture notes, available online, IT University of Copenhagen, 1997.
22. Amanatides J, Woo A. A fast voxel traversal algorithm for ray tracing. *Eurographics*. 1987;87:3-10.
23. Chibani O. New algorithms for the Vavilov distribution calculation and the corresponding energy loss sampling. *31st Nucl Sci Symp, 16th Symp on Nucl Power Syst*. 1998;45(5):2288-2292. doi:10.1109/23.725266
24. Molier. Theorie der Streuung schneller geladener Teilchen II Mehrfach-und Vielfachstreuung. *Zeitschrift für Naturforschung A*. 203(2):78-97. https://www.degruyter.com/document/doi/10.1515/zna-1948-0203/html
25. Gottschalk B, Koehler AM, Schneider RJ, Sisterson JM, Wagner MS. Multiple Coulomb scattering of 160 MeV protons. *Nucl Instrum Methods Phys Res, Sect B*. 1993;74(4):467-490. doi:10.1016/0168-583X(93)95944-Z
26. Ranft J. Estimation of radiation problems around high-energy accelerators using calculations of the hadronic cascade in matter. *Part Accel*. 1972;3:129-161. https://s3.cern.ch/inspire-prod-files-a/aa63ebed9dad980c37c221a107b81d89
27. Tessonnier T, Mairani A, Brons S, Haberer T, Debus J, Parodi K. Experimental dosimetric comparison of 1H, 4He, 12C and 16O scanned ion beams. *Phys Med Biol*. 2017;62(10):3958-3982. doi:10.1088/1361-6560/aa6516
28. Tessonnier T, Marcelos T, Mairani A, Brons S, Parodi K. Phase space generation for proton and carbon ion beams for external users' applications at the Heidelberg ion therapy center. *Front Oncol*. 2015;5:297. doi:10.3389/fonc.2015.00297
29. Tessonnier T. Treatment of low-grade meningiomas with protons and helium ions. Dissertation, LMU München: Fakultät für Physik, 2017. doi:10.5282/edoc.20602
30. Karger CP, Jäkel O, Hartmann GH. A system for three-dimensional dosimetric verification of treatment plans in intensity-modulated radiotherapy with heavy ions. *Med Phys*. 1999;26(10):2125-2132. doi:10.1118/1.598728
31. Mein S, Kopp B, Tessonnier T, et al. Dosimetric validation of Monte Carlo and analytical dose engines with raster-scanning 1H, 4He, 12C, and 16O ion-beams using an anthropomorphic phantom. *Phys Med*. 2019;64:123-131. doi:10.1016/j.ejmp.2019.07.001
32. Chen Y, Li J, Li C, Qiu R, Wu Z. A modified microdosimetric kinetic model for relative biological effectiveness calculation. *Phys Med Biol*. 2017;63(1):15008. doi:10.1088/1361-6560/aa9a68

33. Bauer J, Sommerer F, Mairani A, et al. Integration and evaluation of automated Monte Carlo simulations in the clinical practice of scanned proton and carbon ion beam therapy. *Phys Med Biol*. 2014;59(16):4635-4659. doi:10.1088/0031-9155/59/16/4635
34. Tessonnier T, Ecker S, Besuglow J, et al. Commissioning of Helium ion therapy and the first patient treatment with active beam delivery. *Int J Radiat Oncol Biol Phys*. 2023;116(4):935-948. doi:10.1016/j.ijrobp.2023.01.015
35. Robert C, Dedes G, Battistoni G, et al. Distributions of secondary particles in proton and carbon-ion therapy: a comparison between GATE/Geant4 and FLUKA Monte Carlo codes. *Phys Med Biol*. 2013;58(9):2879-2899. doi:10.1088/0031-9155/58/9/2879
36. Böhlen TT, Cerutti F, Dosanjh M, et al. Benchmarking nuclear models of FLUKA and GEANT4 for carbon ion therapy. *Phys Med Biol*. 2010;55(19):5833-5847. doi:10.1088/0031-9155/55/19/014
37. Battistoni G, Toppi M, Patera V; The FOOT Collaboration. Measuring the impact of nuclear interaction in particle therapy and in radio protection in space: the FOOT experiment. *Front Phys*. 2021:8. doi:10.3389/fphy.2020.568242

How to cite this article: Lysakovski P, Kopp B, Tessonnier T, et al. Development and validation of MonteRay, a fast Monte Carlo dose engine for carbon ion beam radiotherapy. *Med Phys*. 2024;51:1433–1449.
https://doi.org/10.1002/mp.16754

Chapter 4

Discussion

In this work and the accompanying publications, the development and validation of a fast MC dose calculation engine for protons (section 3.1 [37]), helium ions (section 3.2 [38]) and carbon ions (section 3.3 [39]) has been presented. The developed computer program, named MonteRay, can compute dose distributions of clinical plans in voxelized geometries based on CT images or in artificial geometries, e.g., a water tank for QA purposes. As presented in the three publications, this can be done with a high degree of accuracy and speed when compared to traditional MC engines like FLUKA. Depending on the particle type and energy, the speedups achieved by MonteRay over FLUKA ranged from approximately 15x to 70x.

In this section, the individual publications will be discussed briefly, and in between, different parts of MonteRay will be discussed in more detail. For example, the transport of particles in magnetic fields or the implemented nuclear interaction model.

Fast Proton Dose Calculation

In the first publication, the development and evaluation of MonteRay for protons was presented, and the ability to perform accurate dose calculation was shown. The agreement when compared to measurements performed at HIT was excellent for integrated depth dose distributions, lateral profiles and SOBPs. For example, comparisons against SOBPs at depths of 5, 12.5 and 20 cm showed mean (averaged over all ionization chambers) absolute dose differences between 0.7 % and 1.0 %, similar to results reported previously with FLUKA [123]. Relative errors on measured pristine BPs were below 3.5 % for all energies, similar to the maximum relative error of 3 % reported in the commissioning of another fast proton MC engine [124], and to those of full MC codes [125] when evaluated on similar data.

In terms of runtime, using a homogeneous water phantom with a $2 \times 2 \times 2$ mm^3 scoring grid resolution and a beam energy of 150 MeV (an identical benchmark was used by Schiavi et al. [30]), MonteRay achieved tracking rates of $\approx$ 30000 particles per second, a 30-fold speedup compared to FLUKA simulations.

Dose Calculation in Magnetic Fields

Besides standard dose calculations, comparisons of MonteRay against FLUKA were also presented when a homogeneous magnetic field was present. Comparisons of MonteRay on a patient case, with and without a magnetic field, showed excellent agreement against FLUKA with local 2 %/2 mm 3D-γ-index pass rates of 99.98 % and 98.9 %, respectively. At that time, MonteRay was the first fast MC engine to include this capability. By now, another fast MC engine by Li et al. [33] and an analytical engine by Duetschler et al. [126] have presented fast dose calculation algorithms capable of taking homogeneous magnetic fields into account. To the best of the author's knowledge, no fast MC or analytical engines with the ability to transport particles in inhomogeneous fields exist. This shortcoming will need to be addressed in the future, since fast dose calculation engines will be a key component of future MRI-guided adaptive radiotherapy workflows [127].

One particular issue in the simulation of charged particles in magnetic fields of a realistic MRI scanner is the large spatial extent of the magnetic field, possibly requiring the simulation to start much further away from the patient CT to take the effect of the fringe field into account. For example, Fuchs et al. [128] found that it was necessary to include the effect of the magnetic field up to a strength of 50 mT for an accurate prediction of the particle's trajectory. This translated to an additional extent of 40 cm before the isocenter, effectively doubling the distance particles need to be transported, considering that treatment depths are typically less than 30 cm. To avoid this, innovative methods will need to be devised to account for the magnetic field's effect more time-efficiently.

Fast Helium Ion Dose Calculation

Shortly after the submission of the first publication, a patient at HIT received the world's first treatment with actively scanned helium ion beams [5]. At that time, no fast MC-based dose calculation algorithm for helium ions existed, and an analytical dose calculation algorithm was used for treatment planning. But, as mentioned in the first chapter, MC-based algorithms may offer better dosimetric accuracy. In particular for helium ions, Fuchs and Georg [11] have argued that

MC-based algorithms, as a more versatile alternative to analytical algorithms, will be expected to dominate the field in the future, especially when it comes to exploratory research like FLASH or mini-beam therapy.

Motivated by this and the developments at HIT, the second publication presented the inclusion of helium ions in MonteRay, making it the first fast helium ion dose engine in the world - achieving speedups up to a factor of 60 over FLUKA simulations. Dosimetric comparisons proved the accuracy of MonteRay and the validity of the chosen approach to handle nuclear interactions for helium ions, namely the use of nuclear databases extracted from FLUKA. In comparisons against lateral profiles, pristine BPs and SOBPs, MonteRay showed excellent agreement against measurements, comparable to FLUKA results in similar scenarios [22]. Comparisons in heterogeneous scenarios behind an anthropomorphic phantom (previously used in [129]) were performed, and with 3D-γ passing rates of 99 %, MonteRay matched previous results with FLUKA and exceeded those of an in-house analytical dose engine [129].

A New Approach to Handle Multiple Coulomb Scattering

Additionally, a new approach to handle MCS was introduced in the second publication, which is able to handle the scattering of different particle types and energies without relying on tabulated data. Instead, it is a direct approximation to Molière's theory of multiple scattering (see subsubsection 2.4.1.3). The validity of this approach was demonstrated in comparisons against measurements of lateral profiles, where computed lateral dose distributions were compared against measurements. In terms of the FWHM, maximum disagreements were within -0.37 mm/+0.2 mm for all energies and depths.

The advantage of this approach to MCS is that it models both the small angle Gaussian core of the distribution and the heavy large angle tail without requiring any finely tuned parameters; all quantities are computed from basic physical properties of the material (density, elemental composition) and the particle (energy, mass). In contrast, many fast particle therapy MC codes rely on a simple single Gaussian distribution using either Highland's (Equation 2.36) or Rossi & Greisen's (Equation 2.37) parametrization. But, a lot of its simplicity is lost since the free parameter E_s has to be fine-tuned to achieve good agreement against conventional MC engines [25, 28, 36, 35]. In particular, the authors of the only other two fast carbon ion engines, FRED [36] and goCMC [35], had to introduce energy (goCMC and FRED) or particle type (FRED) dependent tuning factors to Highland's ap-

proximation. While Schiavi et al. [30] have reported the implementation of a large angle term similar to the one used here, their model also relied on fitted parameters that had to be determined from comparisons to Geant4, and which depended on the simulation's step size, the target material and the particle's energy. The downside of MonteRay's MCS model are the computational costs associated with estimating the parameters of Molière's distribution. In the future, it may be worth investigating if a simpler computation of the parameters χ_c and B is possible, for example by assuming an average $\overline{Z}$ and $\overline{A}$ instead of looping over all elements in the compound.

Fast Carbon Ion Dose Calculation

In the third publication, MonteRay was extended to include carbon ions. This finally allowed MonteRay to simulate all three particle types used clinically at HIT: protons, helium ions and carbon ions. As before, MonteRay achieved excellent agreement against measurements of physical dose distributions like SOBPs, and additionally, it was shown that biological dose, a necessity for helium & carbon ion therapy, could be computed accurately. For this, a patient plan optimized and computed with the clinical TPS Raystation based on the mMKM biological model was used. Biological dose comparisons between MonteRay and RayStation showed local 3D-γ passing rates of 93.90 % ± 0.03 % (1 %/1 mm) and 99.22 % ± 0.03 % (2 %/2 mm). These passing rates were lower than those observed for physical dose comparisons (98.36 % ± 0.04 % and 99.40 % ± 0.01 %). One possible explanation for this was already given for a similar case by Tessonnier et al. [5], where larger differences for biological dose than for physical dose were observed when comparing two analytical dose engines against FLUKA predictions. They suggested that this might be because the two analytical algorithms did not account for the lateral variation of the particle spectrum and hence, the biological effect. Indeed, recent results by Bazani et al. [130], where the trichrome model of Inaniwa et al. [131] was implemented inside the clinical TPS RayStation, showed better agreement against FLUKA simulations in terms of biological dose. By modeling the particle spectrum directly, based on FLUKA databases, MonteRay does not have this limitation. As could be seen in Figure 3 of the third publication, MonteRay accurately models both depth-dose and lateral dose distributions of the individual fragments. To establish the exact influence of the nuclear model on the accuracy of biological dose predictions, and to decide what range of secondary particles is truly necessary, further studies with MonteRay will be necessary.

MonteRay's Nuclear Interaction Model

Compared to the developments to support helium ions, the inclusion of carbon ions required a much larger extension of the nuclear interaction databases; in their final version, they consisted of over 60000 individual tables, each encoding the probability of a certain particle being produced in a certain nuclear interaction at a certain energy and direction.

The nuclear model in MonteRay is very extensive when compared to the two other published fast carbon ion engines, FRED [36] and goCMC [35]. In total, 11 different particle types are allowed to undergo inelastic nuclear interactions with all 13 elements included in MonteRay (see section 2.5). On the other hand, FRED and goCMC only consider interactions of carbon ions. FRED goes even further and ignores nuclear interactions of carbon ions that were produced in nuclear interactions themselves (secondary carbon ions). The range of supported target elements is also limited to hydrogen, carbon and oxygen. While this, and the limited particle spectrum, may be a valid approximation for the computation of physical dose, neither FRED nor goCMC have presented comparisons of biological dose against established codes in patient geometries. However, Qin et al. have presented the capability of performing biological dose optimization without direct comparisons [58], and Simoni [132] has reported (3 %/2 mm) 3D-γ passing rates of 93.1 % for biological dose comparisons against FLUKA for low energy SOBPs in water. Additionally, the nuclear interaction model of FRED is limited to 300 MeV/u, well below the maximum energies of facilities like HIT (430 MeV/u) [46], the Italian National Centre for Oncological Hadron therapy (400 Mev/u) [133] or the MedAustron facility (400 MeV/u) [134].

During the development of MonteRay, the choice of which particles are allowed to undergo nuclear interactions was made based on comparisons of dose distributions against FLUKA. In these comparisons, not only the total dose was considered but also the contributions of particles grouped by their atomic number Z. Two such comparisons are shown in Figure 4.1, where 430 MeV/u carbon ions, the highest energy available at HIT, are incident on water. In panel a), reinteractions were disabled, and only primary carbon ions were allowed to undergo nuclear interactions. In panel b), the full MonteRay nuclear interaction model was enabled. As can be seen, the inclusion of reinteractions has a significant impact on the contribution of individual fragments to the total dose. Based on these comparisons, it was found necessary to include inelastic nuclear interactions of a wide range of particles. For example, the interaction of ^{11}C was deemed to be

necessary since otherwise, as visible in Figure 4.1, a noticeable bump in the dose contribution of particles with Z=6 (isotopes of carbon) is present. This bump is also clearly visible in the total dose, and Qin et al. [35] have also observed this bump, attributing it to dose deposited by ^{11}C. Curiously, they also observe this bump on simulations with Geant4, hinting at a possible discrepancy between the FLUKA and Geant4 nuclear interactions models.

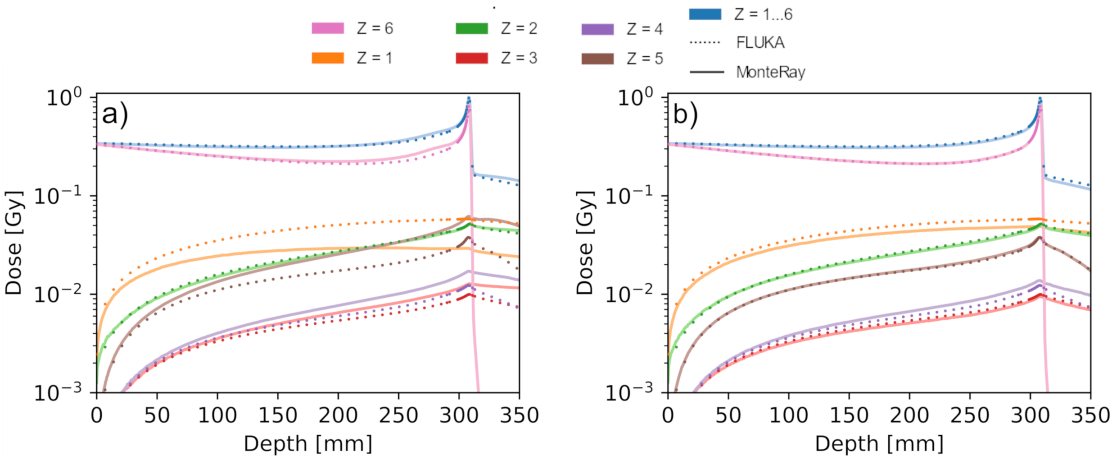

Figure 4.1: Depth-dose distributions of 430 MeV/u carbon ions incident simulated with MonteRay and FLUKA. In panel a), only primary carbon ions were allowed to undergo nuclear interactions in MonteRay. In panel b) the full MonteRay nuclear interaction model was enabled.

While MonteRay did achieve excellent agreements across all three particle species, some discrepancies remain. For example, as already discussed in [39], MonteRay underestimates the dose deposition of light fragments ($Z = 1$) when simulating carbon ions and when comparing to FLUKA. At 430 MeV/u, this discrepancy reaches 20 %. At the same time, the contribution of the heaviest particles ($Z = 6$) is reproduced to within 1 % when compared to FLUKA. This underestimation may stem from the omission of neutrons in MonteRay. These neutrons could undergo nuclear interactions, primarily producing low mass fragments. While this approximation is common in fast MC engines [35, 27, 135, 28, 37], we have observed discrepancies for helium [38] and carbon ions [39]. While the implementation of neutron transport in MonteRay could be possible, it will have to be seen whether this is truly necessary for a fast MC engine and if the gain in accuracy would warrant the penalty in performance. As already discussed in [39], an approach wherein the proton yield in nuclear interactions is increased by some factor might be more suitable.

Nuclear interaction models are an important part of MC engines and as outlined in the introduction, they greatly impact the dose distribution. At the same time, their treatment is challenging both in terms of theory and computational implementation. In nuclear interactions, a wide range of possible scenarios must be considered, including elastic collisions, fusion of nuclei or the fragmentation of the target or projectile. A great deal of work has been put into developing models that cover these interactions. The FLUKA code, a conventional MC engine, includes nuclear interaction models that have been finely tuned to match experimental data. This also includes data of specific interest to radiotherapy, for example in a recent work by Aricò et al. [102], the nuclear interaction models of FLUKA for helium ions were tuned to better reproduce data in the therapeutic energy range.

The main idea behind MonteRay was to make use of existing models, benefiting from decades of work, done by many people. This is an advantage over custom models like the one presented by Simoni et al. [36]. Another benefit is that MonteRay's nuclear interaction model can easily be extended towards other projectile types, target types or even energy ranges, if the need arises. One downside of MonteRay's approach is that the nuclear interaction model of FLUKA is not open-source and no outside validation of the model is possible. Another disadvantage is the size of the nuclear databases, taking up about 2.4 GB in memory. In particular, this is an inconvenience when installing MonteRay since this data has to be somehow transferred or downloaded. Loading the databases into main memory, on the other hand, is not a problem. On a modern system (e.g. Intel i7-9700k with an CT1000P1SSD8 SSD) this takes less than two seconds, and the data can be shared by all threads of a CPU.

One must further point out that the nuclear models inside FLUKA are not perfect and nuclear interaction modeling is not a solved topic in itself. Even between traditional MC engines like FLUKA and Geant4, considerable differences can be observed. As discussed in [39], studies by Robert et al. [136] or Böhlen et al. [137] show significant differences between FLUKA and Geant4 when it comes to nuclear interaction models. Böhlen et al. also estimated the impact of these discrepancies on the biological dose to be at ≈ 5 %. Tying this back to the earlier discussion on biological dose computation by MonteRay - likely MonteRay estimates are within the errors due to uncertainties in nuclear models. This, in part, lies in the fact that no physical models exist that describe nuclear interactions across the whole energy range relevant for radiotherapy from first principles. Instead, empirical models which are fit to measurements have to be

used. Where measurements are sparse or missing, interpolation between data is necessary. To improve nuclear interaction models in the context of light ion radiotherapy, further studies are needed to reduce uncertainties of macroscopic cross-sections and fragmentation spectra. One promising candidate is the FOOT experiment which aims to study, among other things, the fragmentation of helium and carbon ions [138].

Runtime of MonteRay - Is a GPU Implementation Necessary?

The observed speedups when comparing MonteRay against FLUKA are between 15 and 70, depending on the energy and ion type. Besides runtimes on artificial cases, in the third publication, runtimes for clinically relevant cases, a head and a prostate case, were reported for carbon ions, which are the most demanding particle in terms of computational time. Running on 8 cores (Intel i7-9700k), it took 14 and 18 minutes, respectively, to produce dose estimates with a statistical uncertainty below 2 % in the high dose region. Considering the number of cores available in modern systems, and the linear scaling of MonteRay's throughput with the number of cores [37], one can argue that runtimes well below 5 minutes are possible on modern many-core systems. For example, systems with 48 cores have been used for dose calculation by Grevillot et al. [23], and IBA Dosimetry, a medical technology company, suggests this configuration for their myQA iON software [24].

MonteRay's fast runtime and the speedups against FLUKA have been achieved without the use of additional hardware like Graphics Processing Units (GPUs). Because of this, MonteRay does have a lower speed when compared to MC engines that do use a GPU to accelerate simulations. The gain in speed when using GPUs is mostly a result of their architecture. While modern, high-end CPUs may have core counts up to 128, modern GPUs typically come with several thousand cores. While individual GPU cores are weaker than individual CPU cores, the sheer number of them allows to achieve impressive speedups for certain tasks. However, one must be careful when comparing CPU algorithms against GPU algorithms in terms of runtime. This point was also raised by Lee et al. [139] in their work titled "Debunking the 100X GPU vs. CPU myth: an evaluation of throughput computing on CPU and GPU" where the authors show that for some algorithms, the performance gap between CPUs and GPUs is much smaller when both CPU and GPU code is properly tuned. For example, one must consider CPU multithread-

ing when comparing CPU and GPU runtimes, since the parallelization of MC simulations is trivial, owing to the fact that no inter-thread dependencies must be taken into account. For example, Simoni et al. [36] report that "the observed gain in processing time, when comparing to the FLUKA full MC, was nearly a factor 2000" while comparing single core CPU execution times against GPU execution times. Similarly, Franciosini et al. [140], developing a GPU accelerated electron MC engine, report "observing a gain in processing time from 200 to 5000"[1] while comparing runtimes on a single core of a mid-range CPU (Intel Core i5-10400) with a high-end GPU (NVIDIA RTX 3090). More reasonable comparisons can be found in the works of Qin et al. [35] and Fracchiolla et al. [141]. The former, for their carbon ion MC engine, report GPU vs. CPU runtimes that are closer to one another. For example, the simulation time of 400 MeV/u carbon ions was $\approx$ 600 seconds on an Intel Xeon E5-2640 CPU and $\approx$ 50.4 seconds on an NVIDIA GeForce GTX 1080 GPU, a 12-fold speedup. Similar runtime differences can be found in the work of Fracchiolla et al. [141], where both the CPU and GPU versions of the RayStation proton MC engine were compared over an extensive set of 440 patient cases. For their comparison, the authors used[2] a dual socket Intel Xeon E5-2687W v3 CPU [142] with ten physical cores each, and an Nvidia RTX6000 GPU. The median GPU execution time over all 440 was reported at 7.1 s, while the median CPU execution time was 110 s, a 15-fold speedup.

Despite being slower, a CPU MC engine may offer several advantages over a GPU engine. Firstly, software development for GPUs is more challenging than for CPU codes, and to maximize performance, developers must carefully deal with GPU specific issues like warp divergences, shared memory conflicts and synchronization. An interesting work on this topic was published by van Werkhoven et al. [143], titled "Lessons Learned in a Decade of Research Software Engineering GPU Applications". In this work, the authors discuss some downsides of GPU acceleration, with a focus on research software development. One particular point the authors raise is software sustainability, which is "the capacity to endure and preserve the function of a system over an extended period of time" [144]. They argue, that supporting GPU applications might be at risk after a research collaboration ends since they require "advanced technical knowledge and specialized programming languages". A demotivating fate for a software that may have taken

[1] For the latter number, the authors likely refer to comparisons to Geant4, which is slower than FLUKA

[2] The exact CPU configuration was not mentioned in the publication [141] but kindly provided by Dr. Fracchiolla in private E-Mail communication (March 2024)

years to develop.

Some fast MC programs, e.g. RayStation [140], also maintain both CPU and GPU versions of their code. This allows thorough testing of the GPU code, where errors due to the GPU implementation can be clearly distinguished from errors that come from the MC implementation itself. As such, the CPU version of MonteRay can be seen as a necessary step for a possible future GPU version.

MonteRay as a Secondary Dose Engine for Quality Assurance Purposes

One point that has not been discussed yet is the potential benefit of using MonteRay in a clinical context for dose verification purposes. To ensure that the correct dose is delivered to the patient, HIT uses a comprehensive QA protocol that was described by Jäkel et al. [145]. Among other things, this protocol currently includes daily dosimetric measurements of standard plans (e.g. SOBPs) and patient plans in a water phantom. This amounts to a significant cost, both in terms of beam time and personnel time. Just the beamtime, i.e. active irradiation time, required for the daily measurements for patient plan verification, is estimated to be over 50 hours per year[3]. The purpose of these dosimetric measurements is to ensure that the dose calculated by the TPS is correct, at least when measured in a water phantom. In the future these measurements could be replaced by a secondary dose calculation engine, provided it is independent from the primary dose calculation engine. Using MonteRay in this way would allow to reduce the time spent on QA measurements, freeing up personnel and beam time. This is also a possible first step for the use of MonteRay at other facilities. To enable this, methods for automatically commissioning MonteRay's particle source for other facilities are needed, and have recently been under development.

[3]Estimate from private correspondence with Julian Horn, taking into account the yearly number of patients (≈ 650), the average number of fields per plan (≈ 2) and the average beam time required per field ($\approx 2.5 \frac{\text{min}}{\text{field}}$)

Chapter 5

Conclusion & Outlook

Particle therapy is an important tool in our arsenal of cancer treatment options, and there is a long list of research topics that have the goal of improving it even further. For example, MRI guided adaptive radiotherapy, helium ion beam therapy, multi-ion treatments and many more [127, 11, 146]. None of these research topics can be feasibly addressed without accurate dose calculation, and to allow researchers and clinicians to be productive in their work, dose calculation should be fast. In this thesis, the development and verification of MonteRay, a fast dose calculation engine for protons, helium ions and carbon ions was described and the capability of MonteRay to achieve fast and accurate dose calculation demonstrated.

In this final section, some current and future work will be presented. This includes both work under revision, work performed by the author of this thesis and work that was performed by other researchers with the help of MonteRay.

Electron Dose Calculation

In a master's thesis at the BioPT research group, concurrent to this thesis, the extension of MonteRay for electron dose calculation was presented [40]. Since then, this work has been extended to allow for the simulation of electron dose distributions in heterogeneous scenarios, and a publication detailing this is currently under review [41]. One example from this publication is shown in Figure 5.1. There, dose distributions of MonteRay and FLUKA are shown and compared for an 8×8 cm^2, 10 MeV electron field impinging on an anthropomorphic head phantom (Alderson phantom Radiology Support Devices, Long Beach, CA, USA). As can be seen, MonteRay closely matches the dose distribution of FLUKA, with 3 %/2 mm local

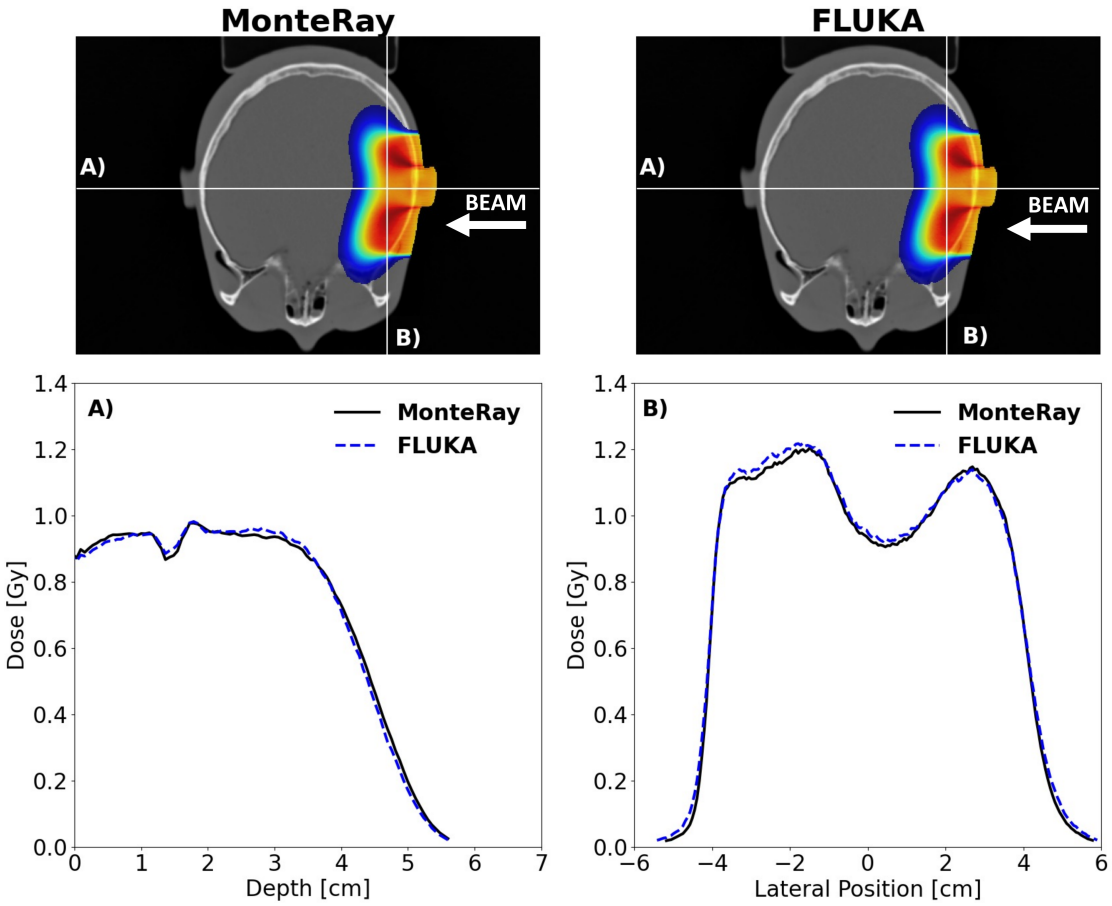

Figure 5.1: Dose distributions of MonteRay and FLUKA are shown for an 8×8 cm^2, 10 MeV electron field impinging on an anthropomorphic phantom. In the bottom panels, dose profiles at locations **A** and **B**, indicated in the upper panels, are shown. Figure taken from and to be published in [41].

3D-γ passing rates[1] of 99.4 %. For 10 MeV electrons, the dose calculation with MonteRay was 13 times faster than FLUKA. To tie back to the previous discussion on CPU vs GPU computation, FRED for electrons [140], report a 90-fold speedup for electrons. Thus one could reason, that MonteRay running on only 8 CPU cores is similarly performant as FRED for 10 MeV electrons.

Dose Optimization and Very High Energy Electron Therapy

A fast MC by itself can already serve as an important research tool, but to be used in a similar fashion as a TPS, a dose optimizer is needed. This has been achieved in an ongoing master's thesis by Aaron Osburg [42], in which a GPU based optimization algorithm was developed and coupled to MonteRay. In the future,

[1] This criterion was chosen to be consistent with Franciosini et al. [140]

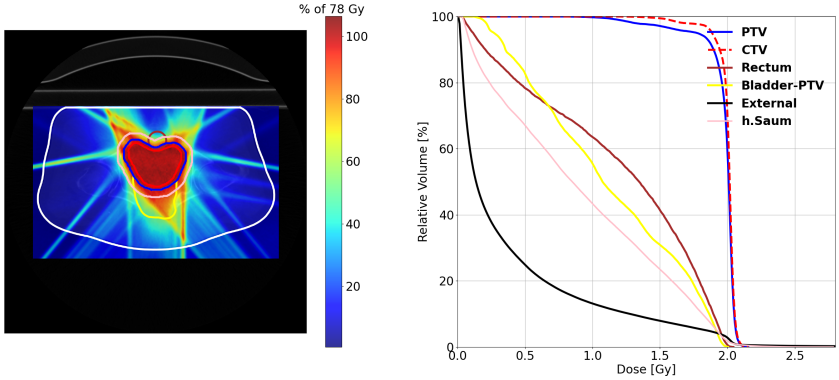

Figure 5.2: Example of ongoing work of VHEE planning in MonteRay. In the left panel, the forward dose calculation of an optimized 9 field electron plan is shown. In the right panel, dose volume histograms for this plan are displayed. Figure courtesy of Prof. Dr. Andrea Mairani.

this capability will be used to investigate the use of very high energy electron (VHEE) beams, a treatment modality currently under investigation due to the possibility of achieving healthy tissue sparing through the FLASH effect [147]. With the support of protons, helium ions, carbon ions and electrons, MonteRay, coupled with the optimizer, will allow the comparison of these treatment modalities in a single framework. An example of this ongoing work is shown in Figure 5.2. For this figure, an exemplary prostate patient was optimized with 9 VHHE fields, and in the left panel, the resulting dose distribution is shown. In the right panel dose volume histograms for the PTV, CTV and some organs at risk are shown. As can be seen, the interplay between MonteRay and the newly developed optimizer is capable of producing treatment plans for VHEEs that achieve good target coverage and sparing of organs at risk. Future work will aim to quantify the quality of these plans and to compare them to ion plans.

Beam Commissioning

For MC dose calculations it is common to use a parametrization of the beam's properties, e.g. its energy spectrum or its lateral spread, to initialize particles. With the goal of making MonteRay usable at different facilities, a commissioning framework has been created that semi-automatically generates a parametrization of the beam model based on measured data, like depth-dose distributions, lateral profiles and absolute dosimetric measurements. In Figure 5.3, the results of fitting depth-dose-distributons of protons at HIT (left column) and at a cyclotron based facility by IBA (right column) are shown. The later data was already used

for commissioning in [148]. In the top row, measured and simulated depth-dose distributions are shown. In the bottom row, comparisons of them in terms of the relative error are shown as boxplots. The high gradient region after the R_{80} point was excluded from this analysis. As can be seen, with the new unified beam parametrization model, consisting of a double gaussian energy spectrum, MonteRay is able to model the shape of depth-dose distributions for both facilities well, achieving relative errors within less than ±3% for most curves.

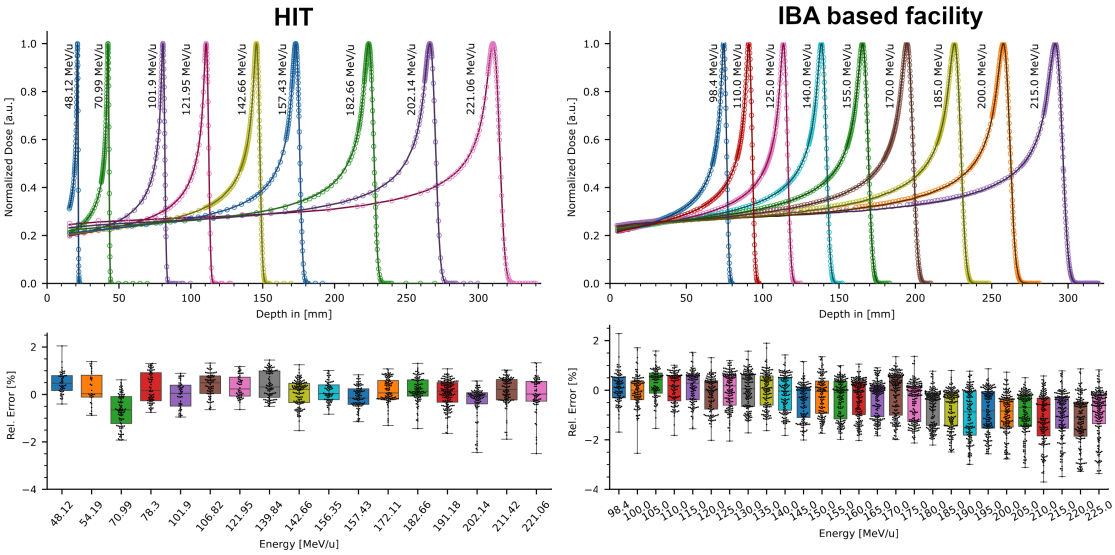

Figure 5.3: Result of the commissioning of MonteRay's beam model for the HIT (left) and a cyclotron based facility by IBA (right). In the top row, measured depth-dose distributions (circles) are compared to simulated depth-dose distributions (solid lines). In the bottom row, boxplots showing the relative differences between simulations and measurements, up to the high gradient region (R_{80}), are shown. For visual purposes, not all depth-dose distributions included in the bottom row are shown in the top row.

MonteRay - A Future Open Source Dose Engine?

In the realm of particle therapy, there is a lack of fast open source codes. Indeed, a literature search for open source MC engines only reveals two for proton therapy, MCsquare [28] and MOQUI [32], and none for helium or carbon ions. The author of this thesis strongly believes in the importance of open source software and the benefits it brings. As such, MonteRay has been developed with the goal of eventually making it available to the community as an open source project.

Towards this goal, a python interface for MonteRay is currently under de-

velopment. This interface will allow users to easily set up and run MonteRay simulations in a python environment, e.g. Jupyter notebooks. This will make it easier for users to interact with MonteRay and to analyze the results of their simulations without having to tediously write MonteRay configuration files (see Figure 2.20). Together with MonteRay's native dicom support and with the semi-automatic commissioning framework currently under development, this will make MonteRay a powerful tool for researchers and clinicians alike.

List of All Publications

Articles Used for This Thesis

- **Peter Lysakovski**, Alfredo Ferrari, Thomas Tessonnier, Judith Besuglow, Benedikt Kopp, Stewart Mein, Thomas Haberer, Jürgen Debus and Andrea Mairani. "Development and benchmarking of a Monte Carlo dose engine for proton radiation therapy." Frontiers in Physics (2021): 655.

- **Peter Lysakovski**, Judith Besuglow, Benedikt Kopp, Stewart Mein, Alfredo Ferrari, Thomas Tessonnier, Thomas Haberer, Jürgen Debus and Andrea Mairani. "Development and benchmarking of the first fast Monte Carlo engine for helium ion beam dose calculation: MonteRay." Medical Physics 50, no. 4 (2023): 2510-2524.

- **Peter Lysakovski**, Benedikt Kopp, Thomas Tessonnier, Stewart Mein, Alfredo Ferrari, Thomas Haberer, Jürgen Debus and Andrea Mairani. "Development and validation of MonteRay, a fast Monte Carlo dose engine for carbon ion beam radiotherapy." Medical Physics (2024).

Conference Contributions

- **Peter Lysakovski**, Benedikt Kopp, Judith Besuglow, Stewart Mein, Thomas Tessonnier, Alfredo Ferrari, Thomas Haberer, Jürgen Debus, Andrea Mairani. MonteRay: A fast Monte Carlo engine for helium ion dose calculation, Oral Presentation, 60th Annual Meeting of the Particle Therapy Co-Operative Group (PTCOG), 2022.

- **Peter Lysakovski**, Benedikt Kopp, Stewart Mein, Thomas Tessonnier, Alfredo Ferrari, Thomas Haberer, Jürgen Debus, Andrea Mairani. MonteRay: A fast Monte Carlo dose calculation engine for carbon ions and more, Oral

Presentation, 61st Annual Meeting of the Particle Therapy Co-Operative Group (PTCOG), 2023.

Bibliography

[1] E. Rutherford. "Collision of α particles with light atoms. IV. An anomalous effect in nitrogen". In: *Philosophical Magazine* 90.S1 (2010), pp. 31–37. ISSN: 1478-6435. DOI: 10.1080/14786431003659230.

[2] R. R. Wilson. "Radiological use of fast protons". In: *Radiology* 47.5 (1946), pp. 487–491. ISSN: 0033-8419. DOI: 10.1148/47.5.487.

[3] Harald Paganetti et al. "Roadmap: proton therapy physics and biology". In: *Physics in Medicine & Biology* 66.5 (2021). ISSN: 1361-6560. DOI: 10.1088/1361-6560/abcd16.

[4] Tanja Eichkorn et al. "Carbon Ion Radiation Therapy: One Decade of Research and Clinical Experience at Heidelberg Ion Beam Therapy Center". In: *International journal of radiation oncology, biology, physics* 111.3 (2021), pp. 597–609. DOI: 10.1016/j.ijrobp.2021.05.131. URL: https://www.sciencedirect.com/science/article/pii/S0360301621006751.

[5] Thomas Tessonnier et al. "Commissioning of Helium Ion Therapy and the First Patient Treatment With Active Beam Delivery". In: *International journal of radiation oncology, biology, physics* 116.4 (2023), pp. 935–948. DOI: 10.1016/j.ijrobp.2023.01.015.

[6] Ainaz Sourati, Ahmad Ameri, and Mona Malekzadeh. "Acute side effects of radiation therapy". In: *Cham: Springer* (2017).

[7] Christian P. Karger. "Der Strahlentherapie-Prozess". In: *Medizinische Physik*. Ed. by Wolfgang Schlegel et al. Lehrbuch. Berlin: Springer Spektrum, 2018, pp. 399–404. ISBN: 978-3-662-54801-1. DOI: 10.1007/978-3-662-54801-1_19. URL: https://link.springer.com/chapter/10.1007/978-3-662-54801-1_19.

[8] Wolfgang Schlegel, Christian P. Karger, and Oliver Jäkel. *Medizinische Physik: Grundlagen - Bildgebung - Therapie - Technik*. Lehrbuch. Berlin:

Springer Spektrum, 2018. ISBN: 978-3-662-54800-4. DOI: 10.1007/978-3-662-54801-1.

[9] A. Mairani et al. "The FLUKA Monte Carlo code coupled with the local effect model for biological calculations in carbon ion therapy". In: *Physics in medicine and biology* 55.15 (2010), pp. 4273–4289. DOI: 10.1088/0031-9155/55/15/006.

[10] S. Muraro, G. Battistoni, and A. C. Kraan. "Challenges in Monte Carlo Simulations as Clinical and Research Tool in Particle Therapy: A Review". In: *Frontiers in Physics* 8 (2020). DOI: 10.3389/fphy.2020.567800.

[11] Andrea Mairani et al. "Roadmap: helium ion therapy". In: *Physics in Medicine & Biology* 67.15 (2022). ISSN: 1361-6560. DOI: 10.1088/1361-6560/ac65d3.

[12] Ahmad Neishabouri et al. "Long short-term memory networks for proton dose calculation in highly heterogeneous tissues". In: *Medical Physics* 48.4 (2021), pp. 1893–1908. ISSN: 2473-4209. DOI: 10.1002/mp.14658.

[13] R. Mohan and J. Antolak. "Monte Carlo techniques should replace analytical methods for estimating dose distributions in radiotherapy treatment planning". In: *Medical Physics* 28.2 (2001), pp. 123–126. ISSN: 2473-4209. DOI: 10.1118/1.1344208.

[14] Lamberto Widesott et al. "Improvements in pencil beam scanning proton therapy dose calculation accuracy in brain tumor cases with a commercial Monte Carlo algorithm". In: *Physics in Medicine & Biology* 63.14 (2018), p. 145016. ISSN: 1361-6560. DOI: 10.1088/1361-6560/aac279.

[15] R. Kohno et al. "Clinical implementation of a GPU-based simplified Monte Carlo method for a treatment planning system of proton beam therapy". In: *Physics in medicine and biology* 56.22 (2011), N287–94. DOI: 10.1088/0031-9155/56/22/N03.

[16] Harald Paganetti. "Range uncertainties in proton therapy and the role of Monte Carlo simulations". In: *Physics in medicine and biology* 57.11 (2012), R99–117. DOI: 10.1088/0031-9155/57/11/R99.

[17] Sheng Huang et al. "Validation and application of a fast Monte Carlo algorithm for assessing the clinical impact of approximations in analytical dose calculations for pencil beam scanning proton therapy". In: *Medical Physics* 45.12 (2018), pp. 5631–5642. ISSN: 2473-4209. DOI: 10.1002/mp.13231.

[18] A. Ferrari et al. *FLUKA: A Multi-Particle Transport Code*. Office of Scientific and Technical Information (OSTI), 2005. DOI: 10.2172/877507.

[19] T. T. Böhlen et al. "The FLUKA Code: Developments and Challenges for High Energy and Medical Applications". In: *Nuclear Data Sheets* 120 (2014), pp. 211–214. ISSN: 00903752. DOI: 10.1016/j.nds.2014.07.049.

[20] S. Agostinelli et al. "Geant4—a simulation toolkit". In: *Nuclear Instruments and Methods in Physics Research Section A: Accelerators, Spectrometers, Detectors and Associated Equipment* 506.3 (2003), pp. 250–303. ISSN: 0168-9002. DOI: 10.1016/S0168-9002(03)01368-8. URL: https://www.sciencedirect.com/science/article/pii/S0168900203013688.

[21] Tatsuhiko Sato et al. "Recent improvements of the particle and heavy ion transport code system – PHITS version 3.33". In: *Journal of Nuclear Science and Technology* 61.1 (2024), pp. 127–135. DOI: 10.1080/00223131.2023.2275736.

[22] T. Tessonnier et al. "Helium ions at the heidelberg ion beam therapy center: comparisons between FLUKA Monte Carlo code predictions and dosimetric measurements". In: *Physics in Medicine & Biology* 62.16 (2017), pp. 6784–6803. ISSN: 1361-6560. DOI: 10.1088/1361-6560/aa7b12.

[23] L. Grevillot et al. "The GATE-RTion/IDEAL Independent Dose Calculation System for Light Ion Beam Therapy". In: *Frontiers in Physics* 9 (2021). DOI: 10.3389/fphy.2021.704760.

[24] *IBA Dosimetry: myQA iON - Patient QA*. 17/01/2024. URL: https://www.iba-dosimetry.com/product/myqa-ion-pt.

[25] Matthias Fippel and Martin Soukup. "A Monte Carlo dose calculation algorithm for proton therapy". In: *Medical Physics* 31.8 (2004), pp. 2263–2273. ISSN: 2473-4209. DOI: 10.1118/1.1769631.

[26] Xun Jia et al. "GPU-based fast Monte Carlo dose calculation for proton therapy". In: *Physics in medicine and biology* 57.23 (2012), pp. 7783–7797. DOI: 10.1088/0031-9155/57/23/7783.

[27] H. Wan Chan Tseung, J. Ma, and C. Beltran. "A fast GPU-based Monte Carlo simulation of proton transport with detailed modeling of nonelastic interactions". In: *Medical Physics* 42.6 (2015), pp. 2967–2978. ISSN: 2473-4209. DOI: 10.1118/1.4921046.

[28] Kevin Souris, John Aldo Lee, and Edmond Sterpin. "Fast multipurpose Monte Carlo simulation for proton therapy using multi- and many-core CPU architectures". In: *Medical Physics* 43.4 (2016), p. 1700. ISSN: 2473-4209. DOI: 10.1118/1.4943377.

[29] Nan Qin et al. "Recent developments and comprehensive evaluations of a GPU-based Monte Carlo package for proton therapy". In: *Physics in medicine and biology* 61.20 (2016), pp. 7347–7362. DOI: 10.1088/0031-9155/61/20/7347.

[30] A. Schiavi et al. "Fred: a GPU-accelerated fast-Monte Carlo code for rapid treatment plan recalculation in ion beam therapy". In: *Physics in medicine and biology* 62.18 (2017), pp. 7482–7504. DOI: 10.1088/1361-6560/aa8134.

[31] Daniel Maneval, Benoît Ozell, and Philippe Després. "pGPUMCD: an efficient GPU-based Monte Carlo code for accurate proton dose calculations". In: *Physics in medicine and biology* 64.8 (2019), p. 085018. DOI: 10.1088/1361-6560/ab0db5.

[32] Hoyeon Lee et al. "MOQUI: an open-source GPU-based Monte Carlo code for proton dose calculation with efficient data structure". In: *Physics in medicine and biology* 67.17 (2022). DOI: 10.1088/1361-6560/ac8716.

[33] Shijun Li et al. "A GPU-based fast Monte Carlo code that supports proton transport in magnetic field for radiation therapy". In: *Journal of applied clinical medical physics* 25.1 (2024), e14208. DOI: 10.1002/acm2.14208.

[34] Martin Janson et al. "Treatment planning of scanned proton beams in RayStation". In: *Medical dosimetry : official journal of the American Association of Medical Dosimetrists* 49.1 (2024), pp. 2–12. DOI: 10.1016/j.meddos.2023.10.009.

[35] Nan Qin et al. "Initial development of goCMC: a GPU-oriented fast cross-platform Monte Carlo engine for carbon ion therapy". In: *Physics in medicine and biology* 62.9 (2017), pp. 3682–3699. DOI: 10.1088/1361-6560/aa5d43.

[36] Micol de Simoni et al. "A Data-Driven Fragmentation Model for Carbon Therapy GPU-Accelerated Monte-Carlo Dose Recalculation". In: *Frontiers in oncology* 12 (2022), p. 780784. ISSN: 2234-943X. DOI: 10.3389/fonc.2022.780784.

[37] Peter Lysakovski et al. "Development and Benchmarking of a Monte Carlo Dose Engine for Proton Radiation Therapy". In: *Frontiers in Physics* 9 (2021). DOI: 10.3389/fphy.2021.741453.

[38] Peter Lysakovski et al. "Development and benchmarking of the first fast Monte Carlo engine for helium ion beam dose calculation: MonteRay". In: *Medical Physics* 50.4 (2023), pp. 2510–2524. ISSN: 2473-4209. DOI: 10.1002/mp.16178.

[39] Peter Lysakovski et al. "Development and validation of MonteRay, a fast Monte Carlo dose engine for carbon ion beam radiotherapy". In: *Medical Physics* (2023). ISSN: 2473-4209. DOI: 10.1002/mp.16754.

[40] Luisa Rank. "Development and Verification of an Electron Monte Carlo Engine for Applications in Intraoperative Radiation Therapy". Master's thesis. Karlsruhe, Germany: Karlsruhe Institute of Technology, Institute of Experimental Particle Physics, 2023.

[41] Luisa Rank et al. "Development and Verification of an Electron Monte Carlo Engine for Applications in Intraoperative Radiation Therapy". In: *Medical Physics* (Under review).

[42] Aaron Osburg. "Development of a GPU-accelerated Fluence Optimizer for Particle Therapy". Master's thesis. Heidelberg, Germany: Heidelberg University, Faculty of Physics and Astronomy, Manuscript in preparation.

[43] H. Eickhoff et al. "The GSI Cancer Therapy Project". In: *Strahlentherapie und Onkologie* 175 Suppl 2.2 (1999), pp. 21–24. ISSN: 1439-099X. DOI: 10.1007/BF03038880. URL: https://link.springer.com/article/10.1007/bf03038880.

[44] Gerhard Kraft. "History of the heavy ion therapy at GSI". In: (2013), pp. 1–17. URL: https://three.jsc.nasa.gov/articles/Krafts_GSI.pdf.

[45] Oliver Jäkel, Gerhard Kraft, and Christian P. Karger. "The history of ion beam therapy in Germany". In: *Zeitschrift fur medizinische Physik* 32.1 (2022), pp. 6–22. DOI: 10.1016/j.zemedi.2021.11.003. URL: https://www.sciencedirect.com/science/article/pii/S0939388921001082.

[46] Stephanie E. Combs et al. "Particle therapy at the Heidelberg Ion Therapy Center (HIT) - Integrated research-driven university-hospital-based radiation oncology service in Heidelberg, Germany". In: *Radiotherapy and oncology : journal of the European Society for Therapeutic Radiology and Oncology* 95.1 (2010), pp. 41–44. ISSN: 0167-8140. DOI: 10.1016/j.radon

c.2010.02.016. URL: https://www.sciencedirect.com/science/article/pii/S016781401000109X.

[47] Corporate Communication & Press Office Heidelberg University Hospital. *Heidelberger Ion Beam Therapy Center*. 3/02/2024. URL: https://www.klinikum.uni-heidelberg.de/fileadmin/hit/dokumente/121019KV_SS_HITImage_engl_web_ID17763.pdf.

[48] S. Incerti et al. "The Geant4-DNA project". In: *International Journal of Modeling, Simulation, and Scientific Computing* 01.02 (2010), pp. 157–178. ISSN: 1793-9623. DOI: 10.1142/S1793962310000122.

[49] M. Scholz and G. Kraft. "Calculation of Heavy Ion Inactivation Probabilities Based on Track Structure, X Ray Sensitivity and Target Size". In: *Radiation Protection Dosimetry* 52.1-4 (1994), pp. 29–33. ISSN: 0144-8420. DOI: 10.1093/oxfordjournals.rpd.a082156.

[50] Taku Inaniwa et al. "Treatment planning for a scanned carbon beam with a modified microdosimetric kinetic model". In: *Physics in Medicine & Biology* 55.22 (2010), pp. 6721–6737. ISSN: 1361-6560. DOI: 10.1088/0031-9155/55/22/008.

[51] A. Mairani et al. "Optimizing the modified microdosimetric kinetic model input parameters for proton and 4He ion beam therapy application". In: *Physics in Medicine & Biology* 62.11 (2017), N244–N256. ISSN: 1361-6560. DOI: 10.1088/1361-6560/aa6be9. URL: https://pubmed.ncbi.nlm.nih.gov/28384125/.

[52] Stephen Joseph McMahon. "The linear quadratic model: usage, interpretation and challenges". In: *Physics in Medicine & Biology* 64.1 (2018), 01TR01. ISSN: 1361-6560. DOI: 10.1088/1361-6560/aaf26a.

[53] A. E. Nahum. "Condensed-history Monte-Carlo simulation for charged particles: what can it do for us?" In: *Radiation and Environmental Biophysics* 38.3 (1999), pp. 163–173. ISSN: 1432-2099. DOI: 10.1007/s004110050152. URL: https://link.springer.com/article/10.1007/s004110050152.

[54] Alex F. Bielajew. "History of Monte Carlo". In: *Monte Carlo Techniques in Radiation Therapy*. CRC Press, 2021, pp. 3–15. DOI: 10.1201/9781003211846-2. URL: https://www.taylorfrancis.com/chapters/edit/10.1201/9781003211846-2/history-monte-carlo-alex-bielajew.

[55] Martin J. Berger. "Monte Carlo calculation of the penetration and diffusion of fast charged particles". In: *Methods in Computational Physics* 135 (1963).

[56] H. Paganetti et al. "Accurate Monte Carlo simulations for nozzle design, commissioning and quality assurance for a proton radiation therapy facility". In: *Medical Physics* 31.7 (2004), pp. 2107–2118. ISSN: 2473-4209. DOI: 10.1118/1.1762792.

[57] Luis Peralta and Alina Louro. "AlfaMC: A fast alpha particle transport Monte Carlo code". In: *Nuclear Instruments and Methods in Physics Research Section A: Accelerators, Spectrometers, Detectors and Associated Equipment* 737 (2014), pp. 163–169. ISSN: 0168-9002. DOI: 10.1016/j.nima.2013.11.026.

[58] Nan Qin et al. "Full Monte Carlo-Based Biologic Treatment Plan Optimization System for Intensity Modulated Carbon Ion Therapy on Graphics Processing Unit". In: *International journal of radiation oncology, biology, physics* 100.1 (2018), pp. 235–243. DOI: 10.1016/j.ijrobp.2017.09.002. URL: https://www.sciencedirect.com/science/article/pii/S0360301617338488.

[59] L. Su et al. "WE–C–BRB–08: A GPU/CUDA Based Monte Carlo Code for Proton Transport: Preliminary Results of Proton Depth Dose in Water". In: *Medical Physics* 39.6Part26 (2012), p. 3945. ISSN: 2473-4209. DOI: 10.1118/1.4736101.

[60] John Amanatides, Andrew Woo, et al. "A fast voxel traversal algorithm for ray tracing". In: *Eurographics*. Vol. 87. 1987, pp. 3–10.

[61] John David Jackson. *Classical electrodynamics*. 3. ed., [Nachdr.] Hoboken, NY: Wiley, ca. 2009. ISBN: 9780471309321.

[62] H. Bethe. "Zur Theorie des Durchgangs schneller Korpuskularstrahlen durch Materie". In: *Annalen der Physik* 397.3 (1930), pp. 325–400. ISSN: 0003-3804. DOI: 10.1002/andp.19303970303.

[63] F. Bloch. "Zur Bremsung rasch bewegter Teilchen beim Durchgang durch Materie". In: *Annalen der Physik* 408.3 (1933), pp. 285–320. ISSN: 0003-3804. DOI: 10.1002/andp.19334080303.

[64] Frank Herbert Attix. *Introduction to Radiological Physics and Dosimetry*. 1. Auflage. Weinheim: Wiley-VCH, 2008. ISBN: 9783527617142. URL: https://ebookcentral.proquest.com/lib/kxp/detail.action?docID=7076127.

[65] P. Mayles, A. Nahum, and J.C Rosenwald. *Handbook of radiotherapy physics: Theory and practice*. New York, London: Taylor & Francis, 2007. ISBN: 9781420012026.

[66] John R. Sabin, Jens Oddershede, and Stephan P.A. Sauer. "On the Determination of the Mean Excitation Energy of Water". In: *Theory of Heavy Ion Collision Physics in Hadron Therapy*. Elsevier, 2013, pp. 63–77. ISBN: 0065-3276. DOI: 10.1016/b978-0-12-396455-7.00003-0.

[67] L. E. Porter and D. I. Thwaites. "Physical state effects on the mean excitation energy of water as determined from alpha particle stopping-power measurements". In: *Physical Review A* 25.6 (1982), pp. 3407–3410. ISSN: 0556-2791. DOI: 10.1103/physreva.25.3407.

[68] Michael Dingfelder et al. "Electron inelastic-scattering cross sections in liquid water". In: *Radiation Physics and Chemistry* 53.1 (1998), pp. 1–18. ISSN: 0969-806X. DOI: 10.1016/s0969-806x(97)00317-4.

[69] Martin J. Berger, J S. Coursey, and M A. Zucker. "ESTAR, PSTAR, and ASTAR: Computer Programs for Calculating Stopping-Power and Range Tables for Electrons, Protons, and Helium Ions (version 1.21)". In: (1999). URL: https://www.nist.gov/publications/estar-pstar-and-astar-computer-programs-calculating-stopping-power-and-range-tables-0.

[70] Giuseppe Battistoni et al. "The FLUKA Code: An Accurate Simulation Tool for Particle Therapy". In: *Frontiers in oncology* 6 (2016), p. 116. ISSN: 2234-943X. DOI: 10.3389/fonc.2016.00116.

[71] K. Parodi et al. "Monte Carlo simulations to support start-up and treatment planning of scanned proton and carbon ion therapy at a synchrotron-based facility". In: *Physics in Medicine and Biology* 57.12 (2012), pp. 3759–3784. ISSN: 0031-9155. DOI: 10.1088/0031-9155/57/12/3759.

[72] David Robert Grimes, Daniel R. Warren, and Mike Partridge. "An approximate analytical solution of the Bethe equation for charged particles in the radiotherapeutic energy range". In: *Scientific Reports* 7.1 (2017), p. 9781. ISSN: 2045-2322. DOI: 10.1038/s41598-017-10554-0.

[73] Lev Davidovich Landau. "On the energy loss of fast particles by ionization". In: *J. Phys.* 8 (1944), pp. 201–205. URL: https://cds.cern.ch/record/216256.

[74] E. A. Uehling. "Penetration of Heavy Charged Particles in Matter". In: *Annual Review of Nuclear Science* 4.1 (1954), pp. 315–350. ISSN: 0066-4243. DOI: 10.1146/annurev.ns.04.120154.001531.

[75] P. V. Vavilov. "IONIZATION LOSSES OF HIGH-ENERGY HEAVY PARTICLES". In: *Originating Research Org. not identified* Vol: 5 (1957). URL: https://www.osti.gov/biblio/4311507.

[76] S. M. Seltzer and M. J. Berger. "Energy Loss Straggling of Protons and Mesons: Tabulation of the Vavilov Distribution". In: *Studies in Penetration of Charged Particles in Matter* 39 (1964), p. 187.

[77] O. Chibani. "New algorithms for the Vavilov distribution calculation and the corresponding energy loss sampling". In: *IEEE Transactions on Nuclear Science* 45.5 (1998), pp. 2288–2292. ISSN: 0018-9499. DOI: 10.1109/23.725266.

[78] Kurt Siegfried Kölbig and Benno Schorr. "A program package for the Landau distribution". In: *Comput. Phys. Commun.* 31.CERN-DD-83-18 (1983), pp. 97–111.

[79] Gert Moliere. "Theorie der Streuung schneller geladener Teilchen II Mehrfach- und Vielfachstreuung". In: *Zeitschrift für Naturforschung A* 3.2 (1948), pp. 78–97. ISSN: 0932-0784. DOI: 10.1515/zna-1948-0203.

[80] S. Goudsmit and J. L. Saunderson. "Multiple Scattering of Electrons". In: *Physical Review* 57.1 (1940), pp. 24–29. ISSN: 0031-899X. DOI: 10.1103/PhysRev.57.24.

[81] H. S. Snyder and W. T. Scott. "Multiple Scattering of Fast Charged Particles". In: *Physical Review* 76.2 (1949), pp. 220–225. ISSN: 0031-899X. DOI: 10.1103/PhysRev.76.220.

[82] H. W. Lewis. "Multiple Scattering in an Infinite Medium". In: *Physical Review* 78.5 (1950), pp. 526–529. ISSN: 0031-899X. DOI: 10.1103/PhysRev.78.526.

[83] H. A. Bethe. "Molière's Theory of Multiple Scattering". In: *Physical Review* 89.6 (1953), pp. 1256–1266. ISSN: 0031-899X. DOI: 10.1103/PhysRev.89.1256.

[84] Gert Moliere. "Theorie der Streuung schneller geladener Teilchen I. Einzelstreuung am abgeschirmten Coulomb-Feld". In: *Zeitschrift für Naturforschung A* 2.3 (1947), pp. 133–145. ISSN: 0932-0784. DOI: 10.1515/zna-1947-0302.

[85] B. Gottschalk et al. "Multiple Coulomb scattering of 160 MeV protons". In: *Nuclear Instruments and Methods in Physics Research Section B: Beam Interactions with Materials and Atoms* 74.4 (1993), pp. 467–490. ISSN: 0168-583X. DOI: 10.1016/0168-583X(93)95944-Z. URL: https://www.sciencedirect.com/science/article/pii/0168583X9395944Z.

[86] U. Fano. "Inelastic Collisions and the Molière Theory of Multiple Scattering". In: *Physical Review* 93.1 (1954), pp. 117–120. ISSN: 0031-899X. DOI: 10.1103/PhysRev.93.117.

[87] William T. Scott. "The Theory of Small-Angle Multiple Scattering of Fast Charged Particles". In: *Reviews of Modern Physics* 35.2 (1963), pp. 231–313. ISSN: 0034-6861. DOI: 10.1103/RevModPhys.35.231.

[88] Hu Beilai. "Estimation of particle losses due to multiple scattering". In: *Nuclear Instruments and Methods in Physics Research Section B: Beam Interactions with Materials and Atoms* 61.4 (1991), pp. 522–526. ISSN: 0168-583X. DOI: 10.1016/0168-583x(91)95332-8.

[89] Virgil L. Highland. "Some practical remarks on multiple scattering". In: *Nuclear Instruments and Methods* 129.2 (1975), pp. 497–499. ISSN: 0029-554X. DOI: 10.1016/0029-554X(75)90743-0. URL: https://www.sciencedirect.com/science/article/pii/0029554X75907430.

[90] Bernard Gottschalk. *Radiotherapy Proton Interactions in Matter*. URL: http://arxiv.org/pdf/1804.00022.

[91] Bruno Rossi and Kenneth Greisen. "Cosmic-Ray Theory". In: *Reviews of Modern Physics* 13.4 (1941), pp. 240–309. ISSN: 0034-6861. DOI: 10.1103/RevModPhys.13.240.

[92] *Open-MCsquare source code on GitLab*. 1/03/2024. URL: https://gitlab.com/openmcsquare/MCsquare/-/blob/1f5deb1906a6a9beb77590bd64fbb5394593e060/src/include/compute_EM_interaction.h#L24.

[93] Byron P. Roe. *Probability and Statistics in Experimental Physics*. Second Edition. Undergraduate Texts in Contemporary Physics. New York, NY: Springer, 2001. ISBN: 9781468492965. DOI: 10.1007/978-1-4684-9296-5.

[94] Sebastian E. Kuhn and Gail E. Dodge. "A fast algorithm for Monte Carlo simulations of multiple Coulomb scattering". In: *Nuclear Instruments and Methods in Physics Research Section A: Accelerators, Spectrometers, Detectors and Associated Equipment* 322.1 (1992), pp. 88–92. ISSN: 0168-9002.

DOI: 10.1016/0168-9002(92)90361-7. URL: https://www.sciencedirect.com/science/article/pii/0168900292903617.

[95] Marco Durante and Harald Paganetti. "Nuclear physics in particle therapy: a review". In: *Reports on progress in physics. Physical Society (Great Britain)* 79.9 (2016), p. 096702. DOI: 10.1088/0034-4885/79/9/096702.

[96] Joseph F. Janni. "Energy loss, range, path length, time-of-flight, straggling, multiple scattering, and nuclear interaction probability". In: *Atomic Data and Nuclear Data Tables* 27.4-5 (1982), pp. 341–529. ISSN: 0092-640X. DOI: 10.1016/0092-640X(82)90005-5. URL: https://www.sciencedirect.com/science/article/pii/0092640X82900055.

[97] P. Sigmund. "Particle Penetration and Radiation Effects. General Aspects and Stopping of Swift Point Particles". In: *Springer series in solid state sciences* 151 (2006).

[98] Johannes Ranft. "Estimation of radiation problems around high-energy accelerators using calculations of the hadronic cascade in matter". In: *Part. Accel.* 3 (1972), pp. 129–161.

[99] J.-J. Gaimard and K.-H. Schmidt. "A reexamination of the abrasion-ablation model for the description of the nuclear fragmentation reaction". In: *Nuclear Physics A* 531.3-4 (1991), pp. 709–745. ISSN: 0375-9474. DOI: 10.1016/0375-9474(91)90748-U. URL: https://www.sciencedirect.com/science/article/pii/037594749190748U.

[100] R. Serber. "Nuclear Reactions at High Energies". In: *Physical Review* 72.11 (1947), pp. 1114–1115. ISSN: 0031-899X. DOI: 10.1103/PhysRev.72.1114.

[101] K. Gunzert-Marx et al. "Secondary beam fragments produced by 200 MeV/u carbon ions in water and their dose contributions in carbon ion radiotherapy". In: *New Journal of Physics* 10.7 (2008), p. 075003. DOI: 10.1088/1367-2630/10/7/075003.

[102] G. Aricò et al. "Developments of the nuclear reaction and fragmentation models in FLUKA for ion collisions at therapeutic energies". In: *CERN Proc* 1 (2019), pp. 321–326. URL: https://cds.cern.ch/record/2669357.

[103] A. Ferrari and P. R. Sala. "A new model for hadronic interactions at intermediate energies for the FLUKA code". In: *Proceedings of the MC93 International Conference on Monte Carlo Simulation in High-Energy and Nuclear Physics*. Ed. by P. Dragovitsch, S.L. Linn, and M. Burbank. Singapore: World Scientific, 1994, p. 277.

[104] V. Andersen et al. "The FLUKA code for space applications: recent developments". In: *Advances in Space Research* 34.6 (2004), pp. 1302–1310. ISSN: 0273-1177. DOI: 10.1016/j.asr.2003.03.045. URL: https://www.sciencedirect.com/science/article/pii/S0273117704002054.

[105] Heinz Sorge, Horst Stöcker, and Walter Greiner. "Poincaré invariant Hamiltonian dynamics: Modelling multi-hadronic interactions in a phase space approach". In: *Annals of Physics* 192.2 (1989), pp. 266–306. ISSN: 0003-4916. DOI: 10.1016/0003-4916(89)90136-x.

[106] Francesco Cerutti et al. "Low energy nucleus–nucleus reactions: the BME approach and its interface with FLUKA". In: *Proc. 11th Int. Conf. Nuclear Reaction Mechanisms*. 2006.

[107] *FLUKA: USRBDX*. 13/09/2023. URL: http://www.fluka.org/content/manuals/online/USRBDX.html.

[108] W. Schneider, T. Bortfeld, and W. Schlegel. "Correlation between CT numbers and tissue parameters needed for Monte Carlo simulations of clinical dose distributions". In: *Physics in Medicine and Biology* 45.2 (2000), pp. 459–478. ISSN: 0031-9155. DOI: 10.1088/0031-9155/45/2/314.

[109] E. Frieden. "The chemical elements of life". In: *Scientific American* 227.1 (1972), pp. 52–60. ISSN: 0036-8733. DOI: 10.1038/scientificamerican0772-52.

[110] Katia Parodi et al. "PET/CT imaging for treatment verification after proton therapy: a study with plastic phantoms and metallic implants". In: *Medical Physics* 34.2 (2007), pp. 419–435. ISSN: 2473-4209. DOI: 10.1118/1.2401042.

[111] Eike Rietzel, Dieter Schardt, and Thomas Haberer. "Range accuracy in carbon ion treatment planning based on CT-calibration with real tissue samples". In: *Radiation Oncology* 2.1 (2007), p. 14. ISSN: 1748-717X. DOI: 10.1186/1748-717X-2-14. URL: https://ro-journal.biomedcentral.com/articles/10.1186/1748-717x-2-14.

[112] T. Haberer et al. "The Heidelberg Ion Therapy Center". In: *Radiotherapy and oncology : journal of the European Society for Therapeutic Radiology and Oncology* 73 Suppl 2 (2004), S186–90. ISSN: 0167-8140. DOI: 10.1016/s0167-8140(04)80046-x.

[113] U. Weber and G. Kraft. "Design and construction of a ripple filter for a smoothed depth dose distribution in conformal particle therapy". In: *Physics in Medicine and Biology* 44.11 (1999), pp. 2765–2775. ISSN: 0031-9155. DOI: 10.1088/0031-9155/44/11/306.

[114] F. Bourhaleb et al. "Monte Carlo simulations of ripple filters designed for proton and carbon ion beams in hadrontherapy with active scanning technique". In: *Journal of Physics: Conference Series* 102 (2008), p. 012002. ISSN: 1742-6588. DOI: 10.1088/1742-6596/102/1/012002.

[115] L. Grevillot, M. Stock, and S. Vatnitsky. "Evaluation of beam delivery and ripple filter design for non-isocentric proton and carbon ion therapy". In: *Physics in Medicine & Biology* 60.20 (2015), pp. 7985–8005. ISSN: 1361-6560. DOI: 10.1088/0031-9155/60/20/7985.

[116] Andrew S. Glassner. *An introduction to ray tracing*. Transferred to digital print. San Francisco, Calif.: Morgan Kaufmann, 2007. ISBN: 9780122861604.

[117] Ronald Goldman. "Intersection of two lines in three-space". In: *Graphics gems*. 1990, p. 304.

[118] GitHub. *google/googletest: GoogleTest - Google Testing and Mocking Framework*. 10/03/2024. URL: https://github.com/google/googletest.

[119] *Boost C++ Libraries*. 10/03/2024. URL: https://www.boost.org/.

[120] Matthew McCormick et al. "ITK: enabling reproducible research and open science". In: *Frontiers in Neuroinformatics* 8 (2014), p. 13. ISSN: 1662-5196. DOI: 10.3389/fninf.2014.00013. URL: https://www.frontiersin.org/articles/10.3389/fninf.2014.00013/full.

[121] Marco Eichelberg et al. "Ten years of medical imaging standardization and prototypical implementation: the DICOM standard and the OFFIS DICOM toolkit (DCMTK)". In: *SPIE Proceedings*. Ed. by Osman M. Ratib and H. K. Huang. SPIE, 2004. ISBN: 0277-786X. DOI: 10.1117/12.534853.

[122] *SQLite Home Page*. 9/03/2024. URL: https://www.sqlite.org/.

[123] T. Tessonnier et al. "Experimental dosimetric comparison of 1H, 4He, 12C and 16O scanned ion beams". In: *Physics in Medicine & Biology* 62.10 (2017), pp. 3958–3982. ISSN: 1361-6560. DOI: 10.1088/1361-6560/aa6516.

[124] Jan Gajewski et al. "Commissioning of GPU–Accelerated Monte Carlo Code FRED for Clinical Applications in Proton Therapy". In: *Frontiers in Physics* 8 (2021). DOI: 10.3389/fphy.2020.567300.

[125] Zi-Yi Yang et al. "Inter-comparison of Dose Distributions Calculated by FLUKA, GEANT4, MCNP, and PHITS for Proton Therapy". In: *EPJ Web of Conferences* 153 (2017), p. 04011. DOI: 10.1051/epjconf/201715304011.

[126] Alisha Duetschler et al. "A fast analytical dose calculation approach for MRI-guided proton therapy". In: *Physics in Medicine & Biology* 68.19 (2023), p. 195020. ISSN: 1361-6560. DOI: 10.1088/1361-6560/acf90d.

[127] Aswin Hoffmann et al. "MR-guided proton therapy: a review and a preview". In: *Radiation oncology (London, England)* 15.1 (2020), p. 129. DOI: 10.1186/s13014-020-01571-x.

[128] Hermann Fuchs et al. "Commissioning a beam line for MR-guided particle therapy assisted by in silico methods". In: *Medical Physics* 50.2 (2023), pp. 1019–1028. ISSN: 2473-4209. DOI: 10.1002/mp.16143.

[129] Stewart Mein et al. "Dosimetric validation of Monte Carlo and analytical dose engines with raster-scanning 1H, 4He, 12C, and 16O ion-beams using an anthropomorphic phantom". In: *Physica medica : PM : an international journal devoted to the applications of physics to medicine and biology : official journal of the Italian Association of Biomedical Physics (AIFB)* 64 (2019), pp. 123–131. DOI: 10.1016/j.ejmp.2019.07.001.

[130] Alessia Bazani et al. "Effects of nuclear interaction corrections and trichrome fragment spectra modelling on dose and linear energy transfer distributions in carbon ion radiotherapy". In: *Physics and imaging in radiation oncology* 29 (2024), p. 100553. DOI: 10.1016/j.phro.2024.100553.

[131] T. Inaniwa and N. Kanematsu. "A trichrome beam model for biological dose calculation in scanned carbon-ion radiotherapy treatment planning". In: *Physics in Medicine & Biology* 60.1 (2015), pp. 437–451. ISSN: 1361-6560. DOI: 10.1088/0031-9155/60/1/437.

[132] Simoni Micol. "Development of tools for quality control on therapeutic carbon beams with a fast-MC code (FRED)". Doctoral thesis. Rome, Italy: University of Rome, 2020. URL: https://iris.uniroma1.it/bitstream/11573/1545155/1/Tesi_dottorato_DeSimoni.pdf.

[133] S. Giordanengo et al. "The CNAO dose delivery system for modulated scanning ion beam radiotherapy". In: *Medical Physics* 42.1 (2015), pp. 263–275. ISSN: 2473-4209. DOI: 10.1118/1.4903276.

[134] Markus Stock et al. "Development of Clinical Programs for Carbon Ion Beam Therapy at MedAustron". In: *International journal of particle therapy* 2.3 (2016), pp. 474–477. DOI: 10.14338/IJPT-15-00022.1.

[135] Andries N. Schreuder et al. "Validation of the RayStation Monte Carlo dose calculation algorithm using realistic animal tissue phantoms". In: *Journal of applied clinical medical physics* 20.10 (2019), pp. 160–171. DOI: 10.1002/acm2.12733.

[136] C. Robert et al. "Distributions of secondary particles in proton and carbon-ion therapy: a comparison between GATE/Geant4 and FLUKA Monte Carlo codes". In: *Physics in Medicine & Biology* 58.9 (2013), pp. 2879–2899. ISSN: 1361-6560. DOI: 10.1088/0031-9155/58/9/2879.

[137] T. T. Böhlen et al. "Benchmarking nuclear models of FLUKA and GEANT4 for carbon ion therapy". In: *Physics in Medicine & Biology* 55.19 (2010), pp. 5833–5847. ISSN: 1361-6560. DOI: 10.1088/0031-9155/55/19/014.

[138] Giuseppe Battistoni et al. "Measuring the Impact of Nuclear Interaction in Particle Therapy and in Radio Protection in Space: the FOOT Experiment". In: *Frontiers in Physics* 8 (2021), p. 568242. DOI: 10.3389/fphy.2020.568242. URL: https://www.frontiersin.org/articles/10.3389/fphy.2020.568242/full.

[139] Victor W. Lee et al. "Debunking the 100X GPU vs. CPU myth". In: *Proceedings of the 37th annual international symposium on Computer architecture*. New York, NY, USA: ACM, 2010. DOI: 10.1145/1815961.1816021.

[140] G. Franciosini et al. "GPU-accelerated Monte Carlo simulation of electron and photon interactions for radiotherapy applications". In: *Physics in Medicine & Biology* 68.4 (2023). ISSN: 1361-6560. DOI: 10.1088/1361-6560/aca1f2.

[141] Francesco Fracchiolla et al. "Clinical validation of a GPU-based Monte Carlo dose engine of a commercial treatment planning system for pencil beam scanning proton therapy". In: *Physica medica : PM : an international journal devoted to the applications of physics to medicine and biology : official journal of the Italian Association of Biomedical Physics (AIFB)* 88 (2021), pp. 226–234. DOI: 10.1016/j.ejmp.2021.07.012.

[142] *Intel Xeon Processor E5-2687W - Product Specifications*. 5/03/2024. URL: https://www.intel.com/content/www/us/en/products/sku/64582/intel-xeon-processor-e52687w-20m-cache-3-10-ghz-8-00-gts-intel-qpi/specifications.html.

[143] Ben van Werkhoven, Willem Jan Palenstijn, and Alessio Sclocco. "Lessons Learned in a Decade of Research Software Engineering GPU Applications". In: *Computational Science – ICCS 2020*. Ed. by Valeria V. Krzhizhanovskaya et al. Vol. 12143. Springer eBook Collection. Cham: Springer International Publishing and Imprint Springer, 2020, pp. 399–412. ISBN: 978-3-030-50435-9. DOI: 10.1007/978-3-030-50436-6{\textunderscore}29.

[144] Patricia Lago et al. "Framing sustainability as a property of software quality". In: *Communications of the ACM* 58.10 (2015), pp. 70–78. ISSN: 0001-0782. DOI: 10.1145/2714560.

[145] O. Jäkel et al. "Quality assurance for a treatment planning system in scanned ion beam therapy". In: *Medical Physics* 27.7 (2000), pp. 1588–1600. ISSN: 2473-4209. DOI: 10.1118/1.599025.

[146] Benedikt Kopp et al. "Development and Validation of Single Field Multi-Ion Particle Therapy Treatments". In: *International journal of radiation oncology, biology, physics* 106.1 (2020), pp. 194–205. DOI: 10.1016/j.ijrobp.2019.10.008. URL: https://www.sciencedirect.com/science/article/pii/S0360301619338799.

[147] Maria Grazia Ronga et al. "Back to the Future: Very High-Energy Electrons (VHEEs) and Their Potential Application in Radiation Therapy". In: *Cancers* 13.19 (2021). ISSN: 2072-6694. DOI: 10.3390/cancers13194942.

[148] Stewart Mein et al. "How can we consider variable RBE and LETd prediction during clinical practice? A pediatric case report at the Normandy Proton Therapy Centre using an independent dose engine". In: *Radiation Oncology* 17.1 (2022), p. 23. ISSN: 1748-717X. DOI: 10.1186/s13014-021-01960-w. URL: https://ro-journal.biomedcentral.com/articles/10.1186/s13014-021-01960-w.

Acknowledgements

My first and foremost thanks goes to **Prof. Dr. Andrea Mairani**. I could not have asked for a better supervisor. He always made me feel like my work mattered, pushed me in the right direction and was there to offer help or advice when I needed it. I am very grateful for the opportunity to work with him.

I am very grateful to **Prof. Dr. Dr. Jürgen Debus** for the opportunity to work under his guidance, for the acquisition of funding and for evaluating this thesis.

I want to thank **Prof. Dr. Oliver Jäkel** for his willingness to be a referee of this thesis, and I would like to thank **Prof. Dr. Lauriane Chomaz** and **Prof. Dr. Jörg Jäckel** for being part of the final examination committee.

Next, I would like to thank **Alfredo Ferrari** for helpful discussions, providing insights and assistance to the workings of FLUKA, and for the opportunity to use the FLUKA nuclear interaction models in this work.

Thomas Tessonnier, has my sincere gratitude for his constant help and advice, but also for lending me an open ear when things were not going as planned.

A big thanks goes to **Benedikt Kopp**, for his invaluable contributions to the development of MonteRay, for the mountainbiking trips and above all for introducing me to the BioPT group.

A special thanks goes to my close colleagues at HIT: **Aaron**, **Celine**, **Filipa**, **Friderike**, **Hailey**, **Hans**, **Judith**, **Luisa**, **Mac**, **Maria**, **Nish**, **Saleh**, **Selver** and **Yasmin**. I'm grateful for the fun times we had in the office and the support I have received from you. The lunch discussions, bike trips, bouldering sessions, camping trips, Tropikel concerts and one or the other beer that we've had together made this time so much more enjoyable.

This thesis was made possible through funding by the **German Ministry of Education and Research (BMBF)** under the grant number **13GW0436A**.

Последнее, но не менее важное: я благодарен моим родителям **Антонина Морланг** и **Владимир Лысаковский**. С тех пор, как я себя помню, они всегда отдавали все ради меня, и в конечном итоге именно они вели меня по этому пути. Я благодарен за их риск и жертву, которые они понесли, приехав в эту страну, и за все их труды, благодаря которым я получил возможность учиться и достигать своих целей.

Всё что не (ни) делается, к лучшему.

Eidesstattliche Erklärung

Hiermit versichere ich, dass ich diese Arbeit selbständig verfasst habe und keine anderen als die angegebenen Quellen und Hilfsmittel verwendet habe.

Heidelberg, den _____ _____